2013

Fatigue Performance Assessment of Refurbished Orthotropic Deck for a Signature Bridge under Simulated Site-Specific Loading

Nirab Kumar Manandhar
Lehigh University

Fatigue Performance Assessment of Refurbished Orthotropic Deck for a Signature Bridge under Simulated Site-Specific Loading

by

Nirab Kumar Manandhar

A Thesis
Presented to the Graduate and Research Committee
of Lehigh University
in Candidacy for the Degree of
Master of Science

in

Structural Engineering

Lehigh University

September 2013

This thesis is accepted and approved in partial fulfillment of the requirements for the Master of Science.

_____

Date

_____

Dr. Sougata Roy
Thesis Advisor
ATLSS Engineering Research Center,
Lehigh University

_____

Dr. Richard Sause
Thesis Advisor
Department of Civil and Environmental
Engineering, Lehigh University

_____

Dr. Sibel Pamukcu
Chairperson
Department of Civil and Environmental
Engineering, Lehigh University

ACKNOWLEDGEMENT

The author would like to express his sincere gratitude to his thesis advisors, Dr. Sougata Roy and Dr. Richard Sause, for their valuable guidance and insight of this research. The author particularly appreciates the effort put forward by Dr. Roy in helping him to complete his thesis. The research in this thesis was conducted in ATLSS Engineering Research Center at Lehigh University, and the efforts of the laboratory staffs in the successful completion of the project are greatly appreciated. The author appreciates the support of the fellow graduate students Ratna Shailendra Deo Alapati and Michael Molina, who worked on this project, and helped the author compile and present data effectively. Furthermore, the author would like to thank Dr. Christopher C. Higgins from Oregon State University for providing the MATLAB code used for digital image rectification. Finally, the author would like to thank his parents and friends for all the support they provided throughout this process.

CONTENTS

LIST OF TABLES

LIST OF FIGURES

ABSTRACT

After a comprehensive study of the site specific loading, it was decided to replace the 45 year old distressed concrete filled steel grid deck at the upper level of the signature suspension bridge with a steel orthotropic deck that is integral with the floor system and the stiffening truss. In view of the high volume of truck traffic on the deck, and the concerns of increased possibility of fatigue cracking from a large number of welded connections in the orthotropic deck, the design and fabrication of the replacement orthotropic deck details needed to be verified for infinite fatigue life, i.e., 75 years' service life without any fatigue cracking under site specific loading.

A full size prototype of a quarter of the deck between the panel points of the stiffening truss, and including one floor beam and two stringers was fatigue tested in at the ATLSS Engineering Research Center, Lehigh University. This study, identified as Phase 1 and reported by Alapati (2012), demonstrated that the proposed replacement deck design did not meet the fatigue design requirements of 75 years' service life. The prototype exhibited premature fatigue cracking of the intermediate subfloor beam-to-rib weld at the cutout termination, and the internal bulkhead plate-to-rib welds at the intermediate subfloor beam. Based on these findings, it was recommended to reduce the stresses at the critical details below their respective constant amplitude fatigue thresholds (CAFT) for achieving a 75 years' service life under site specific loading. Accordingly, deck design was revised where the cutout for the ribs at the intermediate subfloor beams was enlarged at the rib termination, and the thickness of the subfloor beam web was increased from $^{5}/_{8}$ in. (16 mm) to $^{7}/_{8}$ in. (22 mm). In addition, the number of subfloor beams between the floor beams was also increased from four to five, which reduced the

spacing between the subfloor beams from 12 ft. $4^1/_2$ in. (1.257 m) to 8 ft. 3 in (2.515 m). The thickness of the full depth bulkhead plates inside the ribs was increased from $^5/_{16}$ in. (8 mm) to $^5/_8$ in. (16 mm). The welded connection between the bulk-head plate and the rib over the top 7 in. (175 mm) critically stressed region was fabricated as a complete joint penetration weld, which ensured adequate penetration at the weld root and increased the fatigue resistance of this cruciform detail.

The fatigue performance of the refurbished deck was evaluated by full size prototype testing of the modified Phase 1 specimen, where the intermediate floor beam was replaced to incorporate the improved design. Similar to the Phase 1 testing, the test setup simulated the global boundary conditions including the supporting floor framing. The deck was fatigue tested using four stationary overhead hydraulic actuators positioned centrally in the transverse direction. In the longitudinal directions the actuators were positioned in concentric and eccentric configuration about the intermediate subfloor beam and were loaded in paired sequence simulating the passage of the tandem axle of an AASHTO fatigue truck across the intermediate subfloor beam. Three additional under deck actuators were used to simulate continuity boundary conditions. The deck was tested for 5 million cycles at a load level of 3.45×HS15 (=3×0.75×HS20 or the HL-93 fatigue truck) including impact, which was considered equivalent to 75 years' service life under site specific loading. The deck was instrumented to evaluate its response, with majority of the instrumentation concentrated around the critical welded details in the intermediate subfloor beam.

No fatigue cracking was found in the deck upon completion of the testing. The Phase 2 study verified that the refurbished deck would provide a 75 years' service life

under site specific loading. With the design improvements, the stresses at the fatigue critical details reduced significantly compared to the original deck tested in Phase 1. The measured stress ranges at all details except at the cutout edge were at or below the constant amplitude fatigue threshold (CAFT) of their respective detail categories.

3D Finite Element analyses of the deck were performed to understand the complex behavior of the deck under localized and moving wheel loads, and to verify the measured response under static and dynamic loading conditions. Multi-level submodel analyses were performed to assess the fatigue performance of the critical connection details, and to assess the fatigue strength of the rib-to-subfloor beam and rib-to-bulkhead plate weld connection at the cutout termination using local stress based approaches. The hot spot stress obtained at the rib-to-subfloor beam and the rib-to-bulkhead plate weld toes were compared against the FAT 100 curve as per IIW recommendations. The notch stress approach used by Roy and Fisher (2005) for assessing constant amplitude fatigue threshold (CAFT) of welded connections was also implemented to predict the fatigue performance of the rib-to-subfloor beam connection detail.

1 INTRODUCTION

1.1 Background

After a comprehensive study of the site specific loading, it was decided to replace the 45 years old distressed concrete filled steel grid deck at the upper level of a signature suspension bridge with a steel orthotropic deck (Alapati 2012). Due to light weight and inherent redundancy resulting in better structural efficiency, orthotropic deck was a natural choice for rehabilitating the long span bridge as it increased the longevity by reducing sustained load on the primarily load carrying elements. A thin wearing surface providing improved riding quality could further help in reducing the dead load. In addition the modular deck system would facilitate accelerated construction in constrained urban environment. One of the primary reasons for selecting an orthotropic deck was to provide minimum 75 years' service life with minimum maintenance and improved life cycle cost.

In view of the site-specific high Average Daily Truck Traffic (ADTT), often consisting of overload vehicles however, in-service fatigue cracking from a large number of welded connections in the deck was a concern. To accommodate the limitations on vertical clearance, the proposed deck consisted of relatively shallow closed trapezoidal ribs and subfloor beams. In addition, the subfloor beams were made integral with the existing floor system rendering the deck span two-way in contrast to conventional design of orthotropic deck systems. Cutouts were provided in the subfloor beams at the rib intersections for the pass through ribs and the ribs were provided with full depth internal bulkheads at the subfloor beam intersections. These introduced additional stress

concentrations in the load bearing subfloor beams making the welded connections susceptible to fatigue cracking. Accordingly, the design and fabrication of the replacement orthotropic deck details had to be verified for infinite fatigue life, i.e. no fatigue cracking in-service during the design life of the bridge.

A full size prototype of a quarter of the deck between the panel points of the stiffening truss, and including one floor beam and two stringers was fatigue tested in 2009 at the ATLSS Engineering Research Center, Lehigh University. This study, identified as Phase 1 was reported and described by Roy et al. (2012) and Alapati (2012). The study demonstrated that the proposed replacement deck design did not meet the fatigue design requirements of 75 years' service life. The prototype exhibited premature fatigue cracking of the intermediate subfloor beam-to-rib weld at the cutout termination, and the internal bulkhead plate-to-rib welds at the intermediate subfloor beam. Based on these findings, it was recommended to reduce the stresses at the critical details below their respective constant amplitude fatigue thresholds (CAFT) for achieving a 75 years' service life under site specific loading. It was recommended to reduce the stresses in the intermediate subfloor beams by modifying the cutout geometry (increasing the cutout radius), and/or increasing the thickness of the subfloor beam web, and/or reducing the spacing between the subfloor beams. It was also recommended to increase the thickness of the bulkhead plate, and to use at least a partial penetration groove weld for the bulkhead plate-to-rib connection over the highly stressed regions, for ensuring adequate fusion at the weld root and improving the fatigue resistance of the cruciform connection by preventing fatigue crack growth through the weld throat. Fatigue testing of the refurbished deck, incorporating these design changes, was also recommended for

verifying infinite life performance.

Following the recommendations of the Phase 1 study, the design of the replacement deck was revised. To reduce the high stresses in the subfloor beams and the bulkhead plates, the cutout was enlarged at the rib termination. The stresses were further reduced by increasing the thicknesses of the subfloor beam from $^{5}/_{8}$ in. (16 mm) to $^{7}/_{8}$ in. (22 mm). In addition, the number of subfloor beams between the floor beams was also increased from four to five, which reduced the spacing between the subfloor beams from 12 ft. $4^{1}/_{2}$ in. (3.772 m) to 8 ft. 3 in. (2.515 m). The thickness of the bulkhead plate was increased from $^{5}/_{16}$ in. (8 mm) to $^{5}/_{8}$ in. (16 mm). The welded connection between the bulkhead plate and the rib over the critically stressed region was specified as a complete joint penetration weld, which ensured adequate penetration at the weld root and increased the fatigue resistance of this cruciform detail.

1.2 Previous Studies

A preliminary search on steel orthotropic deck revealed more than 100 publications. These publications span a wide range of areas such as application, case studies, evaluation of in-service fatigue cracking and retrofit, etc. However, fatigue resistance of different welded details in orthotropic decks of varied configurations has not been established by laboratory testing, where the boundary effects have been adequately accounted for. Only a handful of such tests in the United States provided data on rib-to-deck plate weld detail and the rib-to-floor beam connections with cutout of particular geometric configuration, which were not readily applicable to the orthotropic deck details for the subject bridge.

Significant research had been done on fatigue resistance of welded details of orthotropic decks in the United States, Netherlands, Germany, and in Japan. Outside the United States, the researches were limited to experimental and analytical evaluation of fatigue performance of orthotropic decks that exhibited distress in service and developing effective retrofit details. In the United States, fatigue resistances of orthotropic decks have been mostly evaluated by testing full size prototypes of the replacement orthotropic decks for signature bridges in the laboratory. These tests were carried out with realistic simulation of boundary conditions, moving loads and fabrication effects. Most of these tests were conducted in ATLSS Engineering Research Center, Lehigh University.

Before the current testing of the prototype replacement deck, the other tests conducted at the ATLSS Engineering Research Center were for the Williamsburg Bridge in New York City (Tsakopoulos and Fisher 2003, Kaczinsky et al. 1997), and for the Bronx Whitestone Bridge in New York City (Tsakopoulos and Fisher 2005), with realistic simulation of boundary conditions, moving loads and fabrication effects. These studies primarily focused on the rib-to-floor beam connections with continuous ribs and a cutout provided in the floor beam under the soffit of the rib. In these replacement orthotropic decks, the intermediate subfloor beams were not connected to the main load carrying members, and essentially acted as diaphragms.

From the test conducted on the prototype of replacement orthotropic deck for the Williamsburg Bridge, it was concluded that a combination of full penetration weld and fillet weld at the rib-to-subfloor beam was more fatigue resistant than just a fillet welded connection that stopped short of the cutout. The combination consisted of 4 in. (102 mm) full penetration weld adjacent to the termination of the cutout and the rest fabricated with

fillet welds. The fatigue resistance of this weld option was defined by AASHTO LRFD as Category C fatigue design curve.

The next study was carried out on the prototype of replacement deck for the Bronx-Whitestone Bridge. In this, the replacement orthotropic deck design incorporated the improvements identified from the Williamsburg Bridge deck testing and the bulkhead plate was replaced with two internal stiffeners at the rib-to-floor beam connection. The load level was equivalent to 3×HS15 and 4.6×HS15 (where HS15 is the AASHTO fatigue truck) including 15% impact for each of the two phases of testing. Even with the application of the maximum stress range in the random variable spectrum determined from field measurements by Connor and Fisher (2001) and Connor et al. (2003), the only fatigue cracking was observed at the deck plate at the floor beam locations. This test demonstrated the effectiveness of the design improvements adopted in the prototype replacement decks of these two bridges.

In the current study, bulkhead plates are provided as the continuation of the subfloor beams inside the ribs. Therefore, the rib-to-floor beam connection and the rib-to-bulkhead plate connections form a cruciform detail. In Phase 1 study, toe cracking at the rib-to-subfloor beam connection and root cracking at rib-to-bulkhead plate were observed (Alapati 2012).

1.3 Objectives of Current Study

The objective of this study were

(i) to assess the fatigue performance of the refurbished deck incorporating the aforementioned design changes by full scale prototype testing simulating the passage of the AASHTO tandem axle loading,

(ii) to determine the response of the refurbished prototype deck under static and rolling wheel loads,

(iii) to characterize the behavior and response of the refurbished prototype deck by 3D Finite Element Analyses and laboratory measurements, and

(iv) to determine the fatigue strength the critical connection details using local stress based approaches, and

(v) to assess the fatigue performance of the critical connection details.

1.4 Study Approach

In order to achieve objectives of this study, the following approach was adopted. The Phase 1 deck specimen was refurbished. During the fabrication process, recommended modifications from the Phase 1 study were incorporated. Since the intermediate subfloor beam was the component most vulnerable to fatigue failure, the entire middle panel of the specimen containing the intermediate subfloor beam, associated deck plate and five internal ribs was replaced by a new panel. The new deck panel was fabricated and replaced as per the recommendations from Phase 1. In this process the deck length was also decreased, ultimately decreasing the span length between the subfloor beams.

The deck was instrumented using more than 180 sensors at critical locations for obtaining stress and displacement data. The global vertical displacements of the prototype deck under load were simulated by three actuators located under the floor beam and the two stringers. The deck response was determined under a rolling tandem axle bogie load moved across the deck at a slow rate (Crawl Test). The refurbished deck was then tested under simulated passage of the tandem axles of the AASHTO fatigue truck.

The fatigue testing was conducted using four actuators loaded in series for three loading steps mimicking the passage of the tandem wheel axles of a notional fatigue design truck. The wheel loads were simulated using 4 hydraulic actuators to generate constant amplitude load ranges of 41.4 kips at each actuator. The load was transferred from each actuator to the spreader beam fitted with 10 in (254 mm) × 20 in (508 mm) rubber foot prints at each ends in contact with the deck surface. However, as it was realized later on that due to the absence of unloading step, the deck elements under study weren't experiencing a complete stress cycle. So, the fatigue test was repeated by including an unloading step after each loading cycle.

This full-scale prototype was also used as a full scale mock up to develop critical information on construction issues related to fabrication and deck installation. After completion of fatigue tests, the response and performance of the deck were evaluated from the experimental results.

In addition, 3D finite element analysis (FEA) of the deck were performed to understand the complex behavior of the deck under localized and moving wheel loads and to verify the measured response under static and dynamic loading conditions.

Multi-level sub model analyses were performed at the ribs 3 and 7 cutout terminations to determine the fatigue strength of the critical welded details. Local stress based approaches were then used for assessing the fatigue performances of the rib-to-subfloor beam and the rib-to-bulkhead plate welded connections.

1.5 Outline

This thesis contains nine chapters and an appendix. The first chapter introduces the background, the study objectives and approach taken to achieve the objectives of the

study.

The second chapter describes in detail the modifications made to the prototype deck that was tested in the Phase 1 experimental program. This chapter provides details of the modifications, fabrication, installation and the final modified version of the refurbished deck specimen.

The third chapter contains the finite element analysis of the prototype deck and describes the behavior of the deck under wheel load. The critical components and details of the deck are identified and further submodel analyses were performed at ribs 3 and 7 cutout termination locations. Local stress based approaches adopted for the assessment of fatigue critical detail is also introduced in this chapter.

The fourth chapter presents the results obtained from finite element analyses. The behavior and responses of the deck components like the deck plate, subfloor beams, and bulkhead plates are discussed in detail. The fatigue critical connections at the rib-to-subfloor beam and rib-to-bulkhead plate are assessed based on local stress based approaches.

The fifth chapter provides the details on the instrumentation methods, and modifications made to the existing test setup from Phase 1 testing. In addition, the details of tests conducted including the loadings and procedures are provided in this chapter.

The sixth chapter discusses the crawl test results, including the behavior and response of the prototype deck when the crawl truck was rolled longitudinally along the deck.

The seventh chapter discusses the static test results. The response of important deck elements and fatigue critical details under loading are described in this chapter.

The eighth chapter discusses the fatigue test results and performances of fatigue critical deck elements under the fatigue loading. It provides an assessment of fatigue testing with regards to intermittent static tests conducted throughout the Phase 2 testing. Additionally, the assessment of fatigue critical details are provided based on experimental and FEA results.

The final chapter presents the observations of the Phase 2 testing, its conclusions, and recommendations based on the study.

2 DECK MODIFICATION

The modification of the Phase 1 deck for the Phase 2 testing is detailed in this chapter. This includes the modification plan for cutting and replacing the middle portion of the Phase 1 deck containing the intermediate subfloor beam (SFB) with a refurbished segment. The intermediate SFB in this segment incorporated the design improvements recommended after the Phase 1 study. In the modification process the length of the deck was also reduced.

2.1 Modification Plan

In view of paucity of funds and limited time available, it was envisaged to modify the Phase 1 deck for the Phase 2 study. Since the recommended design improvements were limited only to the SFBs, and the intermediate SFB was found to be more critical than the end SFBs in the Phase 1 study (Alapati 2012), it was decided to concentrate the modification around the intermediate subfloor beam.

Details of the Phase 1 prototype deck is provided in Alapati (2012). The Phase 1 prototype deck was 33 ft. 10 in. (10.312m) long and 22 ft. $2^1/_4$ in. (6.763 m) wide, and consisted of six deck panels including one typical cantilevered panel, one typical inner panel between two stringers, and part of a typical deck panel between another two stringers that was included as a cantilevered segment. These panels were 27 ft. $9^1/_2$ in. (8.471 m) long and included two intermediate SFBs. Other three part panels were of corresponding width, but 6 ft. $0^1/_2$ in. (1.842 m) long and included only the end SFB. The deck panels were joined by field splices. The cantilevered segments to the west were 5 ft. $2^1/_8$ in (1.578 m) wide. The inner segments were 11 ft. 4 in. (3.454m) wide. The

cantilevered segments to the east were 5 ft. 8 in. (1.727 m) wide. The inner segments had five ribs and the cantilevered segments had two ribs each. Thus, the prototype deck consisted of nine longitudinal ribs, three transverse SFBs spaced at 12 ft. $4^1/_2$ in. (3.772 m) including one typical end SFB on the floor beam and two typical intermediate SFBs, and two longitudinal stringer extensions (SEs). The end SFB over the floor beam was identified as SFB1 and the two intermediate SFBs were identified as SFB2a and SFB2b. The stringers extensions coinciding with the stringers A and B were identified as SE-A and SE-B respectively. The ribs were numbered 1 through 9 from west to east, with ribs 3 to 7 located between SE-A and SE-B. A typical section of the Phase 1 deck is reproduced in Figure 1.

To reduce the spacing between the SFBs in the Phase 2 refurbished deck, it was planned to remove 6 ft. $1^1/_4$ in. (1.861 m) lengths of the Phase 1 deck (including the ribs, the deck plate and the stringer extension) on either side of SFB2a over its entire width and replace it with a deck segment of 4 ft. $1^1/_2$ in. (1.257 m) length. This modification plan retained the general symmetry in the longitudinal direction of the deck about SFB2a and reduced the overall length of the deck to 25 ft. 6 in. (7.772 m). The cutlines on the deck plate and the stringer extensions are shown in Figures 2 and 3.

Since SFB2a between SE-A and SE-B (Bay B in Figure 2) was most critically stressed (Alapati 2012), it was planned to fabricate a new deck segment containing five ribs and a redesigned SFB2a for the replacement deck segment over Bay B only. It was decided to discard portion of the removed Phase 1 deck between SE-A and SE-B, trim the stringer extensions and the outer bays of the deck (in bays A and C) equally on both sides of SFB2a to matching length with the new deck segment and retain them as parts for the

replacement deck segment. The deck segments were to be connected by welded deck plate and bolted rib and SE splices.

2.2 Cutting and Staging of Existing Deck

The Phase 1 deck was cut transversely along the cutlines shown in Figures 2 and 3 using a plasma torch, except the deck plate to the east of Stringer B, which was flame cut. The cutting of deck plate was semi-automated by using a plasma torch that moved transversely across the deck mounted on a guide track. The ribs and the SEs were cut manually with a handheld plasma torch. The cutlines on either side of SFB2a were at 6 ft. $1^1/_4$ in. (1.861 m) on the deck plate, and at 6 ft. $2^1/_2$ in. (1.892 m) on the ribs and SEs (Figure 4). This resulted in $1^1/_4$ in. (31.7 mm) projections or lips in the deck plates of the retained north and south deck segments (see further discussion later).

The interior cut deck segments containing SFB2a was removed and the south deck segment was shifted north by 8 ft. 3 in. (2.515 m) leaving a gap of 3 ft. $11^1/_2$ in. (1.207 m) between them for the replacement deck segment (Figure 5). The gap was 2 in. (51 mm) less than the length of the replacement segment which created a 1 in. (25 mm) overlap on both transverse deck plate splices. This precautionary measure was devised for accurate joint preparation for the transverse deck plate splice between the segments.

The stringer extensions A and B along with the exterior bays (bays A and C) were cut away from the removed Phase 1 deck segment as discussed above, by cutting the deck plate in the Bay B parallel to the ribs at 2 in. (51 mm) offset from the SEs. These cut lines are shown in Figure 4. In the Phase 1 deck, the longitudinal deck plate splices were located at 2 in. (51 mm) east of both the SEs. The west deck plate splice to the east of SE-A was located in Bay B, and the east deck splice to the east of SE-B was located in Bay

C. The deck segment in Bay A was separated by air arc removal of the longitudinal deck plate splice to the east of SE-A. The deck segment in Bay C was separated by plasma cutting of the deck plate 2 in. (51 mm) west of SE-B. The middle cut piece was discarded and the two side segments were then trimmed to 4 ft. $1^1/_2$ in. (1.257 m) length (parallel to the ribs) symmetrically about SFB2a (Figure 6). Similar to the previous transverse cuts, the deck plate of the trimmed segments on each side was cut $1^1/_4$ in. (32 mm) longer than the ribs so that it could be finished to a 1 in. (25 mm) projection or lip in the final replacement segment. As explained earlier, the deck projections were provided for match cutting of the deck plate and accurate joint preparation for the final transverse deck splice.

The exterior cut segments (bays A and C) were shipped to Haberlee Steel Inc. (HSI), Souderton, PA, the fabricator of the Phase 1 prototype deck and also the replacement deck segment. The interior cut segment containing SFB2a and ribs 3 and 7 were retained in the ATLSS Laboratory for metallographic and post-mortem studies (Alapati 2012).

2.3 Fabrication of New Deck and Replacement Deck Segment

A new deck segment of 11 ft. × 4 ft. $1^1/_2$ in. (3.353 m × 1.257 m) plan dimension, and comprising five ribs and an intermediate SFB was fabricated by HSI. Following the recommendations of Phase 1 testing, the thickness of the SFB and the bulkhead plate were increased to $^7/_8$ in. (22 mm) and $^5/_8$ in. (16 mm), respectively. The geometry of the cutout was modified with an increased radius at the cutout termination on the rib of $1^1/_2$ in. (38 mm). The details of the modified rib-to-subfloor beam connection are shown in Figure 7.

The five rib segments (ribs 3 to 7) were cut from a single rib that was available from the Phase 1 prototype deck fabrication. The ribs were prepared for rib-to-rib bolted splices and the rib-to-deck plate welds. Similar to the Phase 1 prototype, the ribs were connected to the deck plate with a specified 80% partial joint penetration (PJP) welds. The ribs were welded to the deck plate in down position i.e., the ribs were inverted onto the deck plate during welding. In order to minimize distortion from weld heat input, both sides of the ribs were welded simultaneously by SAW process using an automatic gantry. Any weld blow-through was repaired and weld melt-through were controlled. The quality of the rib-to-deck weld fabrication including the extent of weld penetration was assessed using Phased Array Ultrasonic Testing (PAUT). Very few sections had less than specified penetration therefore they were not repaired and accepted as is.

Prior to welding the ribs to the deck plate, the bulkhead plates were welded inside the ribs providing continuity to the subfloor beams. To avoid any fatigue cracking from the weld throat that was found in the Phase 1 testing (Alapati 2012), the rib-to-bulkhead plate welds were fabricated using both sided PJP welds over 7 in. (178 mm) length from the top of the bulkhead plate (Figure 7). The rest of the bulkhead plate was fillet welded on both sides to the rib wall. The geometry of the bulkhead plate also dictated the convenience of fillet welding (Figure 7).

The subfloor beams were welded to the ribs and deck plate only after the ribs were welded to the deck plate. The rib-to-subfloor beam connections employed PJP welds everywhere, except adjacent to the cutout termination on the rib wall, where a 4 in. (102 mm) long CJP weld was employed (Figure 7) to achieve complete fusion of the weld root. A run off tab was prepared on the SFB web to avoid fabrication flaws at the

weld termination. The tab was later removed by air carbon arc and ground off to the cutout profile (Figure 7) using a cylinder plug style grinding stone. The SFB2a-to-deck plate welds were $^{5}/_{16}$ in. (8 mm) back to back fillet welds.

The retained exterior deck segments (bays A and C) which were cut out of the removed Phase 1 were connected to the new deck segment by longitudinal CJP deck plate splices. The refurbished deck section was shipped to the ATLSS Laboratory for installation.

2.4 Installation of Refurbished Deck Section

The refurbished deck section was installed in ATLSS Laboratory in the gap between the remnants of the existing panels discussed in section 2.2 and shown in Figure 5. As discussed earlier, a 1 in. (25 mm) lip was provided in the deck plate of the existing segments on either side of the gap, i.e., the gap at the deck plate was 2 in. (51 mm) too short. The refurbished deck was inserted in the gap overlapping the existing deck plates by 1 in. (25 mm) on either side. The overlapped portions of the existing deck plates were match cut against the new deck plate for accurate fit up and tighter joint preparation for the CJP transverse deck splice. The deck plates were spliced across the entire width by CJP welds with steel backing bars left in place using SAW process. The welding was performed semi-automatically, using a portable self-propelled welder mounted against a guide (Figure 8). All the welded connections were inspected by AWS certified UT Level II welding inspector (Figure 9). The plan view of the refurbished deck section is shown in Figure 10. The ribs and the SEs were spliced by slip critical bolted connections using A325 bolts of 1 in. (25 mm) diameter, according to the typical rib splice details used in the Phase 1 deck. All bolts were tightened using a calibrated hydraulic torque wrench on

a Skidmore Wilhelm tester for $^{3}/_{8}^{th}$ turn of the nut. The details of the bolted splices are shown in Figure 11.

The bolt holes were drilled against the splice plates as templates. However, due to the non-uniform cut made using the handheld torch the inside column of the bolts could not be installed for Rib 3 north splice on the existing deck segment. The gap between the ribs was too wide, which resulted in insufficient edge clearance for installing the bolts.

2.5 Description of Modified Prototype Deck

The plan view of the modified prototype deck is shown in Figure 10. The spacing between the SFBs reduced to 8 ft. 3 in. (2.515 m), and the length of the deck was reduced to 25 ft. 6 in. (7.772 m). The width of the deck remained 22 ft. $2^{1}/_{8}$ in. (6.760 m).Other features of the deck remained same as the Phase 1 deck. Refer Alapati (2012) for the deck details.

For ease of referencing, two transverse sections Y-Y and U-U are identified on the deck as shown in Figure 10. The section Y-Y is located at mid-span between SFB1 and SFB2a, at 4 ft. $1^{1}/_{2}$ in. (1.257 m) north of SFB2a. This section coincides with mid-span section Z-Z in Phase 1 (Roy et. al. 2012). The section U-U was located at 2 ft. $0^{3}/_{4}$ in (0.629 m) south of SFB2a. Section U-U coincides with the south transverse splice in the refurbished deck.

Internal full depth bulkhead plates were provided in the ribs at the intersections with SFB2a. The bulkhead plates were $^{5}/_{8}$ in. (16 mm) thick. The bulkhead plates were not attached to the deck plate, instead a $^{5}/_{16}$ in. (8 mm) gap was provided between the top of the bulkhead plate and the underside of the deck plate (Figure 7).

2.6 Test Plan

The full size prototype deck, refurbished as described earlier, was tested in the laboratory. The deck was oriented in the north-south directions, and will be referred to accordingly in the subsequent sections. The test setup from the Phase 1 testing (Alapati 2012) was retained including the floor beam and stringers A and B as part of the floor framing to reproduce realistic boundary conditions. Additional details of the test setup including the rationale for the setup are provided by Alapati (2012).

In the laboratory setup, the west end of the floor beam was fixed to the reaction wall and the east end was supported vertically by a floor mounted actuator. The stringers cantilevered from the floor beam on the north and the south sides by 3 ft. $3^1/_2$ in. (1.003 m) and 27 ft. 4 in. (8.331 m), respectively. The north ends of the north side stringers were unsupported while the south ends of the south side stringers were supported vertically by floor mounted actuators. These actuators were displacement controlled and were used to simulate the global continuity boundary conditions.

Similar to the Phase 1 study (Alapati 2012) the deck was tested to a loading condition that simulated the passage of a tandem axle of the HL-93 notional truck of the AASHTO LRFD Bridge Design Specifications (2010). This was achieved by loading the deck with four overhead actuators that were loaded alternately in pairs. The actuators were separated by 2 ft. $0^3/_4$ in. (0.629 m) similar to half the distance between the axles of the notional truck in tandem configuration. The actuators were attached to a spreader beam, which represented each axle of the tandem. The spreader beams distributed the load to the deck through a 10 in. (0.254 m) wide by 20 in. (0.508 m) long loading pads at each end, simulating the tire contact of wheel pairs on each side of an axle as per

AASHTO (2010). The transverse distance between the loading pads was 6 ft. (1.829 m) identical to the distance between the wheels of the HL-93 notional truck. The longitudinal position and the loading sequence of the actuators were decided by conducting crawl tests, where a bogie having AASHTO tandem configuration was rolled across the deck, such as to produce the maximum effects at the critical connections of SFB2a. The transverse load disposition for the tests was decided based on the Phase 1 study in which a load disposition concentric with Rib 5 or centrally between SE-A and SE-B resulted in the critical stresses at the SFB2a (Alapati 2012). The details of loading are further described in sections 5.4 and 5.6.

3 FINITE ELEMENT ANALYSIS OF PROTOTYPE DECK

The details on Finite Element Analyses (FEA) performed for the prototype deck specimen is provided in this chapter. The FEA simulated the laboratory test, and accordingly the test plan is discussed along with the boundary and loading conditions used to imitate the laboratory testing. These results of the FEA along with the fatigue assessment of connection details are presented in Chapter 4

3.1 Analysis Plan

FEA of the refurbished prototype orthotropic deck were performed to understand the behavior of the deck specimen under wheel loads, to identify the most critically stressed regions of the deck and to assess the fatigue performance of the critical welded connections based on local stresses. Per AASHTO Bridge Design Specifications, fatigue design of steel bridges is performed using nominal stress versus life (S-N) curves that were mostly developed based on fatigue test results of beam specimens having different detail categories of differing notch severity. Nominal stresses are typically determined using simple strength of material calculations based on applied loading and nominal section properties, but considering the gross geometric changes at a section, which locally magnify or decrease the nominal stress. Because of the complex geometries and distribution of stresses in orthotropic decks, however, nominal stresses in orthotropic deck elements cannot be easily defined or computed. As such, the traditional nominal stress based fatigue design provisions of the AASHTO Specifications are not readily applicable to the orthotropic deck details. Accordingly, fatigue performance of orthotropic decks needs to be assessed using local stress based approaches requiring

advanced analyses, verified by full scale testing in the laboratory.

Detailed three dimensional (3D) models of the prototype deck (Figures 12 and 13) were developed in ABAQUS (Dassault Systèmes 2010), a commercially available FEA software. At first, a global model of the test setup including the prototype deck along with the supporting stringers and the floor beam was analyzed. For easier correlation with the laboratory test setup, the FE models are also described with reference to north, south, east and west directions. The global FE model was analyzed for the crawl and the static test load dispositions, which allowed calibration of the FE models against experimental results. The analyses identified high stress concentrations in the SFBs (particularly in SFB2a) at the cutout terminations in the vicinity of the rib-to-subfloor beam welded connections and at the rib-to-bulkhead plate welded connections, which could lead to fatigue cracking. Quantification of these stress concentrations was necessary for accurate assessment of the connection fatigue performance.

Obtaining converged FE solutions at the high stress concentration regions require finer mesh size. Considering the size of the 3D model of the full size specimen, a finer mesh would enormously increase the number of elements and would result in prohibitive computing time. In addition, the complex geometric features at the cutout terminations including the welds would complicate the meshing technique. Moreover, fatigue cracking usually originates from the toe or the root of a welded connection due to inherent notch like discontinuities that act as stress raisers. These stress concentrations are localized and sharply dissipate away from the weld notches, creating steep stress gradient. As the radii of curvature at the notch decreases, the elastic stress concentration at the notch theoretically tends to infinity. Thus, stress concentration around weld notches becomes

dependent on mesh refinement.

Accordingly, multilevel submodels of the fatigue critical welded connections at SFB2a were analyzed to accurately study the variation of local stresses. The global model was analyzed including all structural features except the welds. The weld details were included in the submodels to account for the stiffening effect of the weld bead, and the weld toe notch effect. However, the notch at the weld root was not modeled, since weld root notches tend to be less critical. Since the detailed modeling of local region causes negligible effect on the overall solution, the submodel analyses of these local regions provide accurate solutions. The submodels were analyzed based on the displacement solution of the previous level model. The global solution of the first level submodel was not significantly influenced by the weld details, and therefore was expected to provide results consistent with the global model.

Fatigue cracking occurred at the cutout termination on Rib 3 and at the bulkhead plates of ribs 3 and 7 at SFB2a in Phase 1 testing (Alapati 2012). FEA of th Phase 1 deck showed high stress concentration at these locations (Alapati 2012). Global FE analyses of Phase 2 deck also showed high stress concentrations at the same locations in SFB2a. Subsequently, multilevel submodels of the fatigue critical welded connections at SFB2a were analyzed with refined mesh sizes (Figure 14).

The sizes of the submodels were reduced at each level (Figure 14) and the mesh sizes were also progressively refined. The submodels focused on the areas of high tensile stress concentration at SFB2a-to-rib connections near the cutout termination, i.e. to the east of Rib 3 and to the west of Rib 7. The submodels were analyzed for the same load cases as the global model. The first level submodel (SM1) included a part of the

prototype deck in between the SEs containing SFB2a. FEA results of SM1 showed high stresses at the cutouts for ribs 3 and 7 adjacent to the rib-to-subfloor beam and the rib-to-bulkhead plate welds. Two second level submodels (SM2) were developed, at the intersections of SFB2a with ribs 3 and 7 respectively, which included the individual ribs and parts of SFB2a. To obtain converged stresses at the SFB2a-to-rib weld toe, further four levels of submodel analyses were performed with the introduction of a finite radius at the weld toe. As shown in Figure 14, SM3 was developed from SM2, SM4 was developed from SM3, SM5 was developed from SM4 and SM6 was developed from SM5.

3.2 Introduction to Local Stress Approaches

The local stress based approaches are used for assessing fatigue performance of welded joints where due to complex geometry of the connection, a nominal stress cannot be easily defined. In these approaches, the fatigue performance is assessed based on a stress at or in the vicinity of the weld that is obtained by measurement or advanced FE analyses. Since fatigue cracking from the weld toe is more critical for an adequately designed weld, the subsequent discussion on local stress-based approaches is limited to weld toe applications. The variation of the normal stress on the surface of a plate perpendicular to a weld toe is shown in Figure 15. Significant stress gradient and stress concentration exists around the weld toe. Away from the weld, the nominal stress in the plate varies linearly. Approaching the weld toe the stress variation increases nonlinearly. The local stress at the weld toe notch having a zero notch radius is theoretically infinite. However, in reality a non-zero radius exists at the weld toe notch, which results in a high but finite elastic stress concentration at the weld toe. These locations of high stress

concentration that are susceptible to fatigue cracking are also called ‘hot-spot’.

The fatigue crack initiation at the weld toe is directly associated with the total stress at the weld toe notch, called the notch stress. Estimation of notch stress by FEA is very sensitive to the mesh density, as the local stress asymptotically approaches the theoretical stress with decreasing mesh size. Thus, extra computational effort is needed for obtaining the converged notch stress at the weld toe.

The local stress, excluding the non-linear (asymptotically approaching) stress peak caused by the weld toe notch is called the structural stress. The structural stress is usually obtained by extrapolating the converged stresses at reference points ahead of the weld toe. This extrapolated stress at the weld toe is often referred in literature as the “hot-spot” stress. The reference points chosen for extrapolation are such that they are far enough to be influenced by the weld toe discontinuity, but affected by the connection discontinuity. Thus, the hot-spot stress obtained from extrapolation represents the geometric effect of the connecting elements or the connection geometry and is also called the “geometric stress”. Appropriate local stresses in conjunction with a calibrated S-N curve or the material endurance limit can provide quantitative assessment of finite and infinite life resistance of connection details.

3.2.1 Hot Spot Stress Approach

The hot spot stress depends on the global dimension, geometry and loading parameters of the components at the welded connection. The method of determining the hot spot stresses was initially developed for strain gauge application, which later on was adopted for use with FEA results. The hot spot stresses are determined by measuring the surface stresses at two or three reference points in the vicinity of the hot spot under

consideration, and extrapolating them to the weld toe. The stresses normal to the weld toe are considered for this purpose. The reference points lie on a path normal to the weld toe at the hot spot. This line is termed as the evaluation line originating at the hot spot. This hot-spot stress is used in conjunction with a "master" S-N curve, for predicting the fatigue life of the connection detail.

Several recommendations for estimating the hot-spot stress exist in the offshore, ship building and automobile industries (Radaj and Sonsino 1998, Hobbacher 2005, DNV 2010, ABS 2010) that differ in the FE modelling , the stresses to be considered, the extrapolation points, and the resistance curves to be used. A local stress-based approach using the stress at a singular reference point on the surface ahead of the weld toe, was originally developed and successfully applied for fatigue cracking at the weld toe of tubular structures in the offshore industry (Marshall and Wardeiner 2005), where significant out-of-plane bending arises at the connections to maintain compatibility of deformation between the components. These hot spot structural stress approach were later promoted for welded joints of plate type structures (Marshall and Weidnier 2005). The parametric study for in plane weld notches were performed by Fricke and Bogdan (2001) with coarse mesh modelling. Isoparametric elements having mid-side nodes and element length x (x = 10 mm was used for the study) was used for determining hot spot stress by linear extrapolation of stresses over reference points 0.5x and 1.5x away from the hot spot. The study showed the hot spot stresses obtained from this procedure could be compared to the International Institute of Welding (IIW) fatigue class FAT 100 and FAT 90 (corresponding to AASHTO Category B` and C) for non-load carrying and load carrying welds, respectively. This study did not relate x with the thickness of the plate.

However Healy (2004) proposed a fixed element size equal to the thickness of the plate (t) for obtaining consistent results at the mid-side (half the edge length of the mesh element) stress. A relatively coarse mesh size of $t \times t$ was recommended in view of making practical application to large scale structures computationally less expensive. The mid-side stress at the $0.5t$ with a coarse mesh was found to be larger than the stresses obtained from FEA with a finer mesh. This larger stress was considered to be helpful in compensating the any error associated with extrapolation. The ship building societies recommended the use of stress extrapolation using evaluation points at distances of $0.5t$ and $1.5t$ from the weld toe along the evaluation line (Radaj 2006) for $t \times t$ mesh size. This method was incorporated into IIW (Hobbacher 2007) guidelines for estimating hot spot stresses for coarse meshed ($t \times t$ mesh size) FE models.

The methodologies recommended by IIW (Hobbacher 2005) are used for the current study and presented further. IIW terms the local stress as Structural Hot Spot Stress. Two types of hot spot are defined by IIW depending on their location on the plate and their orientation with respect to the weld toe. The hot spots located on a plate surface is identified as “Type a”, and the hot spots located at a plate edge is identified as “Type b” (Figure 16). Different extrapolation methodologies are recommended depending on the type of hot spot as well as the FE modelling. The extrapolated hot spot stresses are used in conjunction with the IIW fatigue class (FAT) S-N plots (Hobbacher 2007).

The two point linear stress extrapolation method, in which the non-linear surface stress obtained on the evaluation line is linearized by extrapolating to the weld toe, is recommended for type ‘a’ hot spots. When using relatively fine meshed FE models with shell or solid elements, the size must be limited to 0.4t where t is the thickness of the

plate. IIW (Hobbacher 2007) provides the expression for linear extrapolation using two reference points at 0.4t and 1.0t ahead of the hot spot:

$$\sigma_{hs} = 1.67 \cdot \sigma_{0.4t} - 0.67 \cdot \sigma_{1.0t} \tag{1}$$

where, σ_{hs} is the structural hot spot stress to be determined, $\sigma_{0.4t}$ is the surface stress at a distance $0.4t$ and $\sigma_{1.0t}$ is the surface stress at the distance $1.0t$.

For relatively coarse FE models of shell or solid elements, a mesh density of t × t is recommended with the extrapolation points located at 0.5t and 1.5t. The extrapolated hot spot stress is then obtained as:

$$\sigma_{hs} = 1.5 \cdot \sigma_{0.5t} - 0.5 \cdot \sigma_{1.5t} \tag{2}$$

When the increase in structural stresses along the evaluation line towards the hot spot is highly non-linear, a quadratic extrapolation is recommended (Hobbacher 2006) for plate structures with three reference points at $0.4t$, $0.9t$, and $1.4t$:

$$\sigma_{hs} = 2.52 \cdot \sigma_{0.4t} - 2.24 \cdot \sigma_{0.9t} + 0.72 \cdot \sigma_{1.4t} \tag{3}$$

where, $\sigma_{0.4t}$, $\sigma_{0.9t}$ and $\sigma_{1.4t}$ are the surface stresses at the distances $0.4t$, $0.9t$, and $1.4t$, respectively.

For type ‘b’ hot spots, the stress distribution is not dependent on the plate thickness because of which reference points at absolute distances of 4 mm, 8 mm, and 12 mm are used for quadratic extrapolation (Hobbacher 2006). For this method, the element length is required to be less than 4mm. The extrapolation equation is given as:

$$\sigma_{hs} = 3 \cdot \sigma_{4\,\mathrm{mm}} - 3 \cdot \sigma_{8\,\mathrm{mm}} + \sigma_{12\,\mathrm{mm}} \tag{4}$$

where, $\sigma_{4\ mm}$, $\sigma_{8\ mm}$ and $\sigma_{12\ mm}$ are the surface stresses at the distances 4 mm, 8 mm and 12 mm, respectively.

Recently, local stress based fatigue design guidelines for orthotropic decks were incorporated into the AASHTO LRFD Bridge Design Specifications (AASHTO 2012, Kozy et. al. 2010). These recommendations are identical to the IIW (Hobbacher 2005) recommendations for determining structural hot spot stress using a relatively coarse mesh of solid or shell elements. The local stress for fatigue design is termed in the specification as the local structural stress. In the specification commentary, it has been suggested to use this local stress in conjunction with the AASHTO Category C design curve, without any distinction for finite and infinite life assessment.

Although not explicitly recognized by the IIW recommendations, it should be noted that the fatigue assessment of welded connections using the hot spot stress have been calibrated against fatigue cracking at the weld toes of small-scale cruciform and T-connections. As such, the hot spot stress approach can only be used for predicting finite life. This method cannot be used for assessing fatigue cracking from weld root and specifically for infinite life design (i.e. no fatigue crack growth at all).

3.2.2 Notch Stress Approach

The notch stress is the maximum local stress at the root of a notch obtained from the converged FEA results assuming linear-elastic material behavior and fictitious non zero radius at the notch root. The severity of this effective notch stress concentration affects the crack initiation at a notched component and can be used to determine the fatigue resistance by comparing with the material endurance limit of an unnotched component.

The notch stress approach can be used for assessing infinite life resistance of welded connections. The fatigue effective local stress at the weld toe notch is compared against the endurance limit of the material to supress the possibility of cyclic crack initiation or propagation. A notch of 0.04 in (1 mm) radius is introduced at the toe of the nominal weld geometry, and the converged maximum (tensile) surface stress at the center of the rounded notch is used as the notch stress for assessment of infinite life fatigue resistance. The fictitious notch radius was proposed by Radaj (2006) based on a modified formulation of Neuber's fatigue notch factor equation including multiaxial stress state at the weld toe, such that the same fatigue effective notch stress is obtained as for a weld toe without a notch radius. This approach was successfully used by Roy and Fisher (2005) for assessing constant amplitude fatigue threshold (CAFT) of welded connections as:

$$S_r = \frac{1\text{-R}}{2\text{K}_\text{f}}\left[-\sigma_R + \sqrt{\sigma_R^2 + \frac{8}{1-R}S_f^2}\right] \; ksi \tag{5}$$

where, S_r is the nominal stress range, R is the ratio of minimum and maximum stresses in a fatigue stress cycle, K_f is the fatigue notch factor, S_f is the endurance limit of the material, and σ_R is the residual stress.

Based on the empirical relationship proposed by Peterson (1959), the fatigue notch factor at the weld toe notch (K_f) used in Equation (4) can be written as a function of the theoretical notch stress concentration (K_t), the material constant (a) and the notch root radius (r) (Banantine et. al. 1990).

$$K_f = 1 + \frac{K_t - 1}{\left(1 + \frac{a}{r}\right)} \tag{6}$$

The theoretical stress concentration factor (K_t) is defined as the ratio of maximum stress at a discontinuity (σ_{max}) and the nominal stress in a component (σ_{nom}).

The material constant a can be estimated from the ultimate strength of the material, F_u as follows (Banantine et. al 1990):

$$a = \left[\frac{300}{F_u(ksi)}\right]^{1.8} \times 10^{-3} in \tag{7}$$

3.3 Details of Global Model

The above deck and the under deck views of the global model are shown in Figures 12 and 13 respectively. The Phase 2 global model was developed by R.S. Deo Alapati by appropriately modifying (discussed in Chapter 2 earlier) the Phase 1 global model. The global model contained the prototype deck, the stringers and the floor beam replicating the laboratory test arrangement, and was modeled according to the design drawings (provided by the designer of the replacement deck). The deck plate and the ribs were modeled as an integral unit. The subfloor beams, the stringer extensions, the stringers and the floor beams were modeled as separate parts. The welded connections in individual parts were considered as monolithic and were not detailed separately. The welded and the bolted connections between the parts were modeled as tie constraints, which rigidly connected the mating surfaces of the connected components by enforcing same displacement at the interface nodes.

3.4 Details of Submodels

Six levels of submodels were analyzed. Progression of these submodels from the global model is shown in Figure 14 for Rib 7. The results for SM1 indicated that the stresses at the cutout for Rib 7 were more critical than those at Rib 3. Accordingly, the submodels at Rib 7 were only analysed. The progression of submodels for Rib 3 was

similar but handed. The six levels of submodels were identified as SM1, SM2, SM3, SM4, SM5 and SM6. The submodel SM1 was derived from the global model, and was developed by R.S Deo Alapati. The submodel analyses employed displacement based submodeling where each submodel was analyzed by the displacement solution of the global model (for SM1) or the previous level submodel (for the other submodels) at the common interface. The weld details were included in the submodels as per the nominal size indicated in the design drawings. In SM1, SM2, and SM3, the weld toe was modeled as a sharp corner without any notch radius. The weld toe notch for SM4, SM5 and SM6 was rounded with 0.04 in. (1 mm) radius. These four submodels were developed for assessing infinite life fatigue performance of the rib-to-subfloor beam welded connection using notch stress approach. In addition, SM2 was reanalyzed as SM2A as per the AASHTO recommended meshing guidelines presented in section 3.2.1. Any lack of fusion (LOF) at the root of the fillet and PJP welds were not modeled; instead a complete fusion was assumed for all welds. The results obtained from all submodels were compared by overlaying the contour plots of maximum principal stress for each submodel as shown in Figures 17 and 18. These plots demonstrated the consistency in the results obtained from the various levels of submodel, and verified the approach of submodel analyses including the size of the submodels and the accuracy of the solutions.

3.4.1 Submodel 1 (SM1)

The first level submodel (shown in Figure 19) included a 6 ft. (1.829 m) length of the prototype deck symmetric about SFB2a. In the transverse direction, the model was 11 ft. 3 in. (3.429 m) wide containing ribs 3 to 7 between the stringer extensions symmetrically about Rib 5. The length of the submodel was chosen such as to minimize

the boundary effects due to the applied loads on the deck as discussed later in section 3.8. The connection angles between the subfloor beam and the stringer extensions, and the splice plates that provided continuity to the bottom flange of the subfloor beam at the stringer extensions were included in this model (Figure 14). The bolted connections at the connection angles between SE and the SFB2a, and between the splice plates and the SFB2a were modeled as tie constraints.

3.4.2 Submodel 2 (SM2)

Figure 14 shows the 3D view of the second level submodel at Rib 7. The submodels were 10 in. × 25 in. × 22.6 in (0.254 m × 0.635 m × 1.829 m) as shown in Figure 20. The submodels were symmetric about the respective rib centerline. The length of the submodels along the ribs was chosen such as to entirely accommodate the 10 in. (254 mm) long load pad. The width of the submodel in the transverse direction was chosen such that the local areas of interest at the weld details were sufficiently away from the edges of the model and therefore not interfered by the discontinuities at the boundary.

3.4.3 Submodel 3 (SM3)

The third level submodel considered the half of SM2 towards the centerline of the SFB2a as shown in Figure 14 for SM3 of Rib 7. The submodel was 10 in. × 12.5 in. × 22.6 in (0.254 mm × 0.318 mm × 1.829 mm) as shown in Figure 20.

3.4.4 Submodel 4 (SM4)

The fourth level submodel derived from SM3 included a rectangular portion of the highly stressed region of SFB2a around the cutout termination on Rib 7 as shown in Figure 14. The submodel was 9 in. × 7 in. × 8 in. (229 mm × 178 mm × 203 mm) as

shown in Figure 20. A 0.04 in. (1 mm) rounding was introduced in this level of submodel at the subfloor beam-to-rib weld toe as per the protocols for notch stress based fatigue assessment discussed in section 3.2.2.

3.4.5 Submodel 5 (SM5)

The fifth level submodel included a smaller portion near the cutout termination (Figure 14), where the peak stress concentration was observed in SM4. The submodel was 2.5 in. × 2.0 in. × 1.5 in. (64 mm × 51 mm × 38 mm) as shown in Figure 20. This submodel also included the 0.04 in. (1 mm) rounding at the weld toe that was introduced in SM4.

3.4.6 Submodel 6 (SM6)

As shown in Figure 14, the sixth level submodel was derived from SM5 containing a small portion of the rib-to-SFB2as weld and the SFB2a web at the cutout termination where it exhibited the peak stress concentration in SM5 (Figure 14). The edges of SM6 were aligned parallel and perpendicular to the rib-to-SFB2a weld to simplify meshing of the complex geometry including portions of the weld, the SFB2a web, the cutout and the 0.04 in (1 mm) notch rounding. The size of the submodels was 1.88 in. × 1.13 in. × 1.41 in. (48 mm × 29 mm × 36 mm) as shown in Figure 20.

3.4.7 Submodel 2A (SM2A)

The second level submodel was reanalyzed with a mesh size as recommended yby the AASHTO LRFD Bridge Design Specifications (discussed in section 3.2.1). This submodel was identified as SM2A.

3.5 Material Properties

Widely accepted linear elastic material properties of steel were used for analysis. The modulus of elasticity and Poisson's ratio of steel were assumed as 29000 ksi (2.0×10^5 MPa) and 0.3, respectively.

3.6 Boundary Conditions

Similar to the Phase 1 studies (Alapati 2012), the boundary conditions for the global model replicated the boundary conditions of the laboratory test setup. These boundary conditions are shown in Figures 12 and 13. One end of the floor beam (the east end in the laboratory) and the ends of the stringers (the south end in the laboratory) were assigned displacement boundary conditions. In the laboratory testing, the under deck actuators were used to vertically displace the ends of the stringers and the floor beam. The top and bottom clevises of these actuators were arranged such as to allow in plane displacements and rotations but to restrain the out-of-plane displacements of the stringers and the floor beam. Consistent boundary conditions were assigned in the FE model to the nodes of the floor beam and stringers that were covered by the actuator clevises (Figures 12 and 13).

In the laboratory setup, SFB1 was supported by the floor beam that was fixed to the reaction wall on the west end with a wall fixture, which in turn was anchored to the strong wall. Initially, it was believed that the wall fixture would behave as “encastre” or fully fixed. During the Phase 1 studies (Alapati 2012), the global FE model was calibrated against the static test results. It was determined that the test setup provided less than full fixity to the floor beam at the west wall and a higher reaction at the propped end. Accordingly, an in plane rotational spring (i.e. the rotation about Z axis as shown in

Figure 13) of 20×10^6 kip/rad (3.5×10^6 kN/rad) stiffness was assigned as a boundary condition to the global model at the west (wall) end of the floor beam. The Phase 2 model was analyzed for the same boundary condition at the wall fixture.

For the crawl test simulation, downward vertical displacements of 0.03 in. (1 mm) and 0.125 in. (3 mm) were specified at the ends of the floor beam and the stringers, respectively, same as the displacements imparted during the laboratory testing. These displacements were held constant for the entire crawl test.

The vertical displacements specified at the stringer and floor beam ends (at the under deckactuator locations) for the static test simulation are provided in section 5.5.1 for the respective loading steps (described later in section 3.8).

As discussed earlier, all submodels were analyzed for displacement boundary conditions, which were derived from the solutions of the respective previous level models at the common interfaces.

3.7 Element Type and Meshing

3.7.1 Choice of Elements

The models were meshed using 3D continuum solid hexahedron elements. Although the tetrahedral elements are geometrically versatile and are very convenient for automatic meshing of complex shapes, hexahedral elements were used for their higher accuracy and convergence rate. It is also recommended by ABAQUS (Dassault Systèmes 2010) that first-order tetrahedral elements be avoided for stress analyses as these elements are overly stiff and exhibit slow convergence with mesh refinement. An extremely fine mesh is generally needed to obtain accurate results with these elements

near stress concentrations, which would add significant large computational costs for large models.

Each hexahedral element had 20-nodes and three displacement degrees of freedom per node. The element formulation implemented isoparametric second order serendipity type interpolation functions and Gauss integration with Gauss points corresponding to eight reduced integration Barlow points (Dassault Systemès 2010). In ABAQUS this element is identified as C3D20R. The C3D20R element was used as it is known to provide accurate results for three dimensional stress analyses and is effective in capturing stress concentration effects (Dassault Systemès 2010).

Isoparametric elements possess intrinsic coordinate (or reference coordinate) system for formulating element stiffness matrix (Cook et. al. 2002). The physical element in the real coordinate system is mapped to the reference element in the reference coordinate system. The relationship between these two coordinate systems is defined by the Jacobian matrix. The nodal points of the element are used to define both the element geometry and the element displacement using identical shape functions (hence isoparametric). By suitable choice of constants in the shape function, these elements can show the correct rigid-body and constant strain modes required for the patch test. Thus, convergence in results is obtained with mesh refinement.

A fully integrated element uses all the available Gauss points and determines all the stiffness coefficients of the element stiffness matrix (Logan 2007). This increases the accuracy of the numerical integration; however, the higher accuracy overestimates the element stiffness and results in lesser deformation than the true solution. As a result, spurious shear strains develop in parts of the model that should not have any shear strain

and the accuracy of solution decreases. The energy that should induce bending is then lost in developing the spurious shear strain.

The reduced integration element with incomplete polynomials underestimates the stiffness matrix by introducing rigid body modes. The number of internal constraints is decreased, causing softening effect and increasing the accuracy of the solution. In second-order isoparametric elements the stresses are calculated at the integration points and are most accurate at these locations. At other locations, the stresses are interpolated (inside) or extrapolated (to the surface) linearly.

A fully-integrated twenty-node, three-dimensional element requires twenty seven gauss points. The reduced integrated version of the same element with eight gauss points reduces the required computational effort to less than 30% of the effort required with fully-integrated element. This advantage played an important role in selecting the element type as the deck specimen including the test setup could be modeled using more accurate second order solid elements and could be analyzed effectively with comparatively less computational resources.

The disadvantage of reduced-integrated element is that, the element stiffness matrix becomes rank deficient, i.e. the number of linearly independent rows or the rank of the matrix is less than the number of rows of the matrix. The use of too few gauss points in reduced-integrated element may produce instability, spurious singular mode, zero energy or hourglass mode. The deficiency in rank or the zero energy mode results in a number of different configurations of the element having same internal energy. It causes the element to deform in a shape like an hourglass without any associated energy, hence known as the hourglass mode. This mode can propagate through regularly shaped

elements and this nonphysical response can grow in an unbounded way unless controlled, causing numerical instability. For example, with the C3D20R elements, this mode can propagate in single stack of elements. Since the models were meshed using automatically generated non-uniform meshes, the freedom of propagation was limited and the manifestation of the spurious modes was not a concern with the chosen element type. As such no special technique was employed to control the hourglass mode (Dassault Systemès 2010).

3.7.2 Details of Meshing

All models were meshed using automatic structured meshing algorithm in ABAQUS. The models were partitioned as necessary to facilitate the meshing as per the chosen algorithm. The minimum seed (desired or target) lengths for automatic mesh generation are presented in Table 1. A 1 in. (24.5 mm) mesh size was used for the global model. For the six levels of submodels, SM1 to SM6, the mesh sizes were progressively reduced by half. A nominal mesh size of $^{7}/_{8}$ in. (22.2 mm), same as the thickness of the subfloor beam web, was used for SM2A as per the recommendations of the AASHTO Specifications (AASHTO 2010). Details of the number of elements, nodes, degrees of freedom and desired edge length of elements (l) for the global model and the submodels are presented in Table 1. The aspect ratio (the ratio of the longest to the shortest edge of an element), face angle (also known as corner angle) and edge length of the elements checked for quality prior to the final analysis of the model. The results of the element quality checks are presented in Tables 2 to 4. The definition of the aspect ratio and the corner angle are depicted in Figure 21 for a schematic of a 2D element.

Isoparametric elements with high aspect ratio and very large or small face angles

are known to degrade the accuracy of a FEA solution. Following the recommendations of ABAQUS (Dassault Systemès 2010), elements with an aspect ratio greater than 10, with a small face angle less than 10°, and with a large face angle greater than 160° were avoided as much as possible as demonstrated in Tables 2 and 3. The number of elements with face angles smaller than 10° and greater than 160° were less than 1% except for SM4 and SM5 with number of elements having angles greater than 160° as 1.5% and 2.6%, respectively.

Except for SM5 and SM2A, only less than 2% of the elements in the submodels had an aspect ratio greater than 10. For SM5 and SM2A, respectively 17% and 6% of the elements had an aspect ratio greater than 10 however, only about 4% and 2% of the elements had aspect ratio greater than 15.

The number of elements with edge lengths varying more than 25% and 50% of the desired lengths are presented in Table 4. The tabulated element quality check show that only a small percentage of elements do not satisfy the recommended criterion for the aspect ratio and the face angles. In the global model, the elements with a large aspect ratio and sharp internal angles were mostly located at the termination of the cutout in the subfloor beams and the flares in stringer extensions. The less than desirable elements in the stringer extensions were not of a concern as these elements were far from the critical regions of the deck to cause any significant effect. The critically stressed SFB cutouts were reanalyzed using element sizes that progressively decreased with increased level of sub-modeling. In the submodels, the elements with sharp face angles and high aspect ratios were restricted to the sharp termination of the cutout at the end of rib-to-SFB2a weld and the rib-to-deck plate welded connections (Figure 22). For the more refined

submodels (SM4, SM5 and SM6), the elements with larger aspect ratio were located along the rib-to-SFB2a weld toe that was rounded with a 0.04 in (1 mm) radius (Figure 23). For SM2A, the size of element was decided as per AASHTO specification based on the thickness of SFB2a which was $^{7}/_{8}$ in. (22 mm). Due to the presence of cutouts, welds and ribs that were thinner than SFB2a, more elements in this submodel had higher aspect ratio. However, the elements with small or large internal angles and large aspect ratios did not affect the solution at the cutout termination significantly, as the very few distorted elements were surrounded by elements of high quality, which primarily controlled the solution.

3.8 Loading

3.8.1 Loading for Crawl Test Simulation

The global model of the prototype deck was analyzed to simulate the crawl test in the laboratory. Similar to the Phase 1 study (Alapati 2012), the test truck was simulated by four rectangular load patches, spaced center to center at 4 ft. (1.219 m) in the longitudinal direction (parallel to the ribs) and 6 ft. (1.829 m) in transverse direction. The load from each wheel pair was distributed uniformly over a 10 in. (254 mm) long (parallel to the ribs) and 20 in. (508 mm) wide rectangular load patch as recommended by the AASHTO LRFD Bridge Design Specification (AASHTO 2012). For the test truck, a transverse gap of approximately 1 in. (25 mm) existed in the middle of each wheel pairs. In addition, the tire contact areas and the amount of pressure exerted by each of the wheel pairs were not even (Alapati, 2012). For simplicity in FE modeling, however, the gap was ignored in the idealized rectangular wheel contact. The total load applied during the crawl

test in the laboratory was 53.8 kip (239.3 kN) including the weight of the truck and the billets as elaborated further in section 5.3. This load was applied on the FE model as a uniform pressure of 67 psi (462.8 kPa) on each of the four simulated tire contact areas or load patches.

Rolling of the test truck was simulated by analyzing the global model for five load cases, each representing a discrete truck position in the longitudinal direction (Figures 24 and 25). Each consecutive load cases were separated by 2 ft. 0-$^{3}/_{4}$ in. (0.629 m). The load dispositions were chosen such as to simulate the passage of an AASHTO tandem axle over SFB2a from one span to the other, providing the most critical stresses in the intermediate subfloor beam which was the primary focus of this phase of the study.

3.8.2 Loading for Static and Fatigue Test Simulation

FE model of the deck was analysed for the same loading sequence as the laboratory static and fatigue tests. The longitudinal load disposition for the static and fatigue tests were decided based on the crawl test results as discussed earlier and also in detail in section 5.5. During the laboratory testing, two pairs of alternate actuators were loaded sequentially to simulate the passage of a tandem axle. The actuators were positioned concentric with Rib 5. Load was applied to the deck using spreader beams and loading blocks that simulated truck axles and wheels, respectively. The underside of the loading blocks was fitted with rectangular rubber patches simulating rubber tires. A transverse gap of approximately 1 in. (25 mm) was provided in the middle of the rubber patches simulating a pair of wheels.

The global FE model was analyzed for discrete load positions same as the actuators during the static test. The load was distributed uniformly over a 10 in. (254

mm) long and 20 in. (508 mm) wide rectangular load patch (AASHTO 2012). For simplicity in modeling, the load at each simulated wheel contact with the deck was applied uniformly over a rectangular patch of 10 in × 20 in (254 mm × 508 mm) that did not consider the 1 in (25 mm) gap.

Figure 26 shows the disposition of the load patches on the global model simulating the static test. Each row represented one spreader beam (or one axle of the tandem) with the rubber patches at the ends. These load patches (LPs) are identified in the figure with respect to the respective actuator identifier (see section 5.5.1). For example, the load patches under actuator #3 is identified as LP-3. The rows of load patches were spaced 2 ft 0 $^{3}/_{4}$ in (0.629 m) apart in the longitudinal direction. The FEA was performed in three load steps (LSs) replicating the loading protocols for the laboratory tests.

(i) Load Step LS-0: A pressure of 7.5 psi (51.7 kPa) was applied on each load patches corresponding to the minimum load of 3 kip (13.3 kN) at each actuator, simulating the dead load effect as explained in section 5.5.5.

(ii) Load Step LS-1: A pressure of 110 psi (765.3 kPa) was applied on each of the four load patches LP-3 and LP-5 generating a total applied load of 88.8 kip (395.0 kN). The minimum load of 1.5 kip (6.7 kN) was applied on each of the remaining load patches, LP-4 and LP-6. The load position for LS-1 was similar to that of LC-2 in the crawl test simulation.

(iii) Load Step LS-2: A pressure of 110 psi (765.3 kPa) was applied on each of the four load patches LP-4 and LP-6 generating a total applied load of 88.8 kip (395.0 kN). The minimum load of 1.5 kip (6.8 kN) was applied on each of the

remaining load patches, LP-3 and LP-5. The load position for LS-2 was similar to that of LC-3 in crawl test loading simulation.

3.9 Analysis

The FE models were analyzed on a distributed memory computer cluster of 10 nodes, each having eight central processing units (cpu). All analyses were linear elastic performed using a direct linear equation solver that converged in a single increment. The direct linear equation solver employed a sparse, direct, Gauss elimination method that determined an exact solution of the system of linear equations (up to machine precision).

4 FINITE ELEMENT ANALYSIS RESULTS

The behavior of the ribs, the deck plate, the subfloor beams and the bulkhead plates inside the ribs, as obtained from the FEA, are discussed in this chapter. These responses are compared with those of Phase 1 deck. Finally, fatigue assessment of the rib-to-SFB2a and the rib-to-bulkhead plate welded connections using the local stress based approaches are presented.

4.1 Discussion of FEA Results

4.1.1 Response of the Ribs and the Deck Plate

The contour plots of maximum principal stresses on deformed configuration of the deck for LS-1 and LS-2 of the static test simulation (section 3.8.2) are shown in Figures 27 and 28, respectively. As expected, a two way deformation of the deck was observed. High stresses and deformation of the deck plate were noted locally under the load patches. The response of the deck plate and the ribs were evaluated by investigating the variation in normal stresses and displacements along two longitudinal sections: one between ribs 3 and 4 (section 1-1), and another along the centreline of Rib 4 (section 2-2); and the transverse section Y-Y. These sections are shown in Figure 26. The longitudinal sections 1-1 and 2-2 were chosen as they were located or close to the west load patches. The response of the deck plate along other similar sections mirrored about Rib 5 in the vicinity of the east load patches located in between ribs 6 and 7 and at the centreline of Rib 6 were also similar. However, the sections 1-1 and 2-2 were chosen compared to the other sections as they showed higher responses. Similarly, the transverse section Y-Y was selected as it was located in the middle of the north span and exhibited

higher response compared to the section U-U, although both were located under load patches.

Figure 29 presents the normal stress in the longitudinal direction on the top and the bottom face of the deck plate along section 1-1 for both LS-1 and LS-2. The west load patches covered parts of ribs 3 and 4 and the deck plate in between, as shown on the transverse section of the deck in the inset.

As seen in Figure 29, the stresses peaked under the load patches and diminished rapidly away from them. Under the load patches, the stresses on the top and the bottom surface of the deck plate were almost equal in magnitude but of opposite sign. Away from the loads, the stresses at the top and the bottom of the deck plate were of almost equal. This suggests that away from the wheel loads, the longitudinal stress in the deck plate was predominantly in-plane (membrane stress) due to global bending of the deck, and significant local bending of the deck plate occurred under the wheel loads giving rise to the high stress peaks of opposite sign. The membrane stress was compressive in general except at SFB2a, where tensile stress developed due to continuity of the deck plate over the subfloor beam. Due to the addition of the membrane stress, the stresses at the top surface of the deck plate were higher than the stresses on the bottom surface under the wheel loads. The local response of the deck plate under the wheel loads was similar in the span for both LS-1 and LS-2. At SFB2a under LP-5 in LS-1, however, the local bending of the deck plate was reduced as the deck plate was supported by the SFB web, which interrupted the local bending.

The variation of the longitudinal normal stresses on the top surface of the deck plate and on the soffit of the rib at section 2-2 are shown in Figure 30 for both LS-1 and

LS-2. The stresses on the deck plate were similar to the stresses at section 1-1, localized around the load patches due to localized bending, peaking under the load patches and diminishing rapidly away from them. At section 2-2, the stresses in the deck plate were lower compared to section 1-1, which was directly under the load pads. Section 2-2, although close to the load pads, was not directly under them. Rib 4 experienced higher stresses compared to Rib 3 because the rib was located farther from the stringer supports in the transverse direction. In addition, Rib 4 shared a larger portion of the patch load shown in the inset. Contrary to the localized response, however, the response of the rib was similar to that of a continuous beam subjected to concentrated loads, exhibiting primarily linear stress variation between the load points and the supports.

In LS-1, the maximum tensile stress in the rib soffit occurred at the maximum loaded section on the north span (section Y-Y). A small tensile stress developed in the south span due to the minimum load applied at LP-6. An almost zero stress was observed at SFB2a, since SFB2a deformed under the concentrated load from LP-5 acting as a flexible support rather than a rigid support. As such, the rib response was similar to that of a continuous beam on an elastic foundation. SFB1 was supported on a rigid floor beam and SFB2b was not directly loaded. Hence, compressive stresses developed in the rib soffit due to continuity moment at the rigid supports. In LS-2, tensile peak stresses were observed under LP-4 and LP-6 which were loaded to the maximum load. SFB2a was minimally loaded and therefore did not experience any noticeable deformation and acted as a rigid support for the continuous rib. As such, compressive stresses developed in the deck plate at SFB2a in addition to other subfloor beam locations.

Normal stresses in transverse direction on both the top and bottom faces of the

deck plate and the ribs at section Y-Y for LS-1, when LP-3 was loaded to the maximum is presented in Figure 31. Tensile stresses are plotted towards the top side of the deck plate and outer side of the ribs. Similarly, compressive stresses are plotted towards the bottom side of the deck plate and inner side of the ribs. Stresses were localized under the wheel loads (over ribs 3, 4, 6 and 7) where the deck plate underwent significant bending as is evident by almost equal stresses of opposite sign on the top and the bottom surfaces of the deck plate. Evidently, the deck plate supported on the rib walls behaved as a continuous beam on elastic foundations. On the bottom face of the deck at the rib-to-deck plate welded connections (of ribs 3, 4, 6 and 7), the transverse stresses normal to the weld axis were compressive. The compressive stresses were about 7.4 ksi (51 MPa) and 6.3 ksi (43 MPa) at ribs 3 and 7, and about 9.8 ksi (68 MPa) and 9.4 ksi (95 MPa) at ribs 4 and 6, respectively. Due to the presence of high tensile residual stresses at the weld toe and the weld root (almost close to the yield stress of the material), the welded connection would locally experience tensile stress ranges even when subjected to nominal compressive stresses under wheel loads, contributing to fatigue damage at this welded connection.

The deformation of the deck at section Y-Y in LS-1 of the static test simulations is presented in Figure 32. Significant distortion of ribs 3, 4, 6, and 7, and flexural deformation of deck plate were observed under the load patches. The distortion of the ribs was due to frame action between the ribs and the deck plate. This distortion introduced linearly varying stresses in the rib walls (Figure 31). Rib 5, which was not under the load patch, did not distort and the deck plate underwent hogging flexural deformation between ribs 4 and 6 as shown in Figure 32.

The vertical displacements of deck plate, along the transverse section Y-Y

coinciding with LP-3 (west) are shown in Figure 33. The deck section experienced maximum deflection in LS-1, when the load patches located at section Y-Y were loaded to the maximum. The floor beam was fixed to the wall at the west end and propped at the east end, and the other components of the deck were cantilevered off the floor beam. The east end of the floor beam and the south ends of the stringers were imparted displacement boundary condition consistent with the laboratory testing which pulled the deck lower. As a result, the deck section exhibited a global tilt towards east as observed in Figure 32 and 33. Figure 33 also shows that the deck experienced more local deformation in LS-1 compared to LS-2, because the load patches at section Y-Y were not loaded to the maximum in this load step. The displacements of the deck plate in LS-1 showed local valleys with kinks at the hard supports of the rib-to-deck connections over ribs 3 and 4 and ribs 6 and 7. As is more evident from Figure 32, the deck plate deformation was consistent with the rib distortion under direct loading at section Y-Y. Thus, a predominant local flexural deformation of the deck plate supported by the elastic rib walls was observed in the transverse direction under the wheel loads.

The vertical displacements of the deck plate along the longitudinal section 1-1 are shown in Figure 34 for LS-1 and LS-2, obtained at the soffit of the deck plate. The plots in each load step show that the maximum displacement was localized under the load patches, and the displacement

decreases rapidly away from the load patches. The presence of SFB2a provides extra stiffness at the SFB2a-section due to which even in LS-1 (when LP-5 was directly above SFB2a), the deck plate under LP-5 does not show maximum displacement like under other load patches. In LS-1, only the deck plate under LP-3 shows maximum local

displacement. In LS-2 the deck is loaded symmetrically about SFB2a and both the locations under load patches 4 and 6 show maximum local displacements. Hogging flexural deformation was observed at the deck plate between load patches 4 and 6 with SFB2a acting as an elastic support in between. Along the longitudinal direction, the displacements increased gradually from the north end to the south end of the deck. The north side of the deck rested on the floor beam that was fixed at the east end and was more rigid than the rest of the transverse section of the deck. Also during the modification of the Phase 1 deck, only the deck was made shorter. However, the lengths of the stringers and the location of their supports were left unchanged. As a result, the support condition of the deck was asymmetric in the longitudinal direction causing rigid body rotation towards the south coupled with local deformation. This rigid body rotation was more in LS-2 because the distance of loading load patches were farther from the floor beam than in LS-1.

The vertical displacements, on the soffit of deck plate and rib, along the longitudinal section 2-2 are shown in Figure 35. The displacement of the deck plate at this section was similar to that in section 1-1 except at SFB2a for LS-1. No noticeable displacement was observed at SFB2a in section 1-1 while at section 2-2, some displacement was observed at the deck plate. Unlike section 1-1, cutouts around the ribs were present at section 2-2 which decreased the stiffness of this section resulting in more displacement under the same load. The rib (Rib 4) followed the same displacement pattern as the deck plate, however the maximum displacements under the load patches were lower compared to the deck plate. The deck plates experienced direct loading by the load patches due to which it experienced more displacement than the rib.

The behavior and performance of ribs and deck plate at section Y-Y were also studied since this section was directly under loading by actuator #3 (LS-1 in Phase 2) in between SFB1 and SFB2a. Loading conditions in LS-1 for Phase 2 was similar to LS-3 for Phase 1 where loads were simultaneously applied at SFB2a and 4 ft. $1^1/_2$ in. (1.257 m) north of SFB2a. The behavior of the deck section was similar in both test phases. Maximum stresses and bending were observed directly under the loads i.e. at ribs 3, 4, 6 and 7 while stresses at rib 5 were nominal. However, the magnitude of stresses at the rib walls were observed to be higher in Phase 2 (Figure 31) compared to Phase 1 (Figures 83 and 84 by Alapati 2012).

In Phase 1 also, the location of the high stresses on the deck plate and the ribs were mainly under the load patches on the deck. The deformations were concentrated under the load patches and decreased rapidly away from them. Load steps 1 and 2 used in Phase 1 testing were eliminated in Phase 2 testing while LS-3 of Phase 1 matched with LS-1 of Phase 2 test. The normal stress in the longitudinal direction on the top and the bottom faces of the deck plates at sections 1-1 and 2-2 were similar in both Phase 1 and Phase 2 testing (refer to Figures 72 to 75 in Alapati 2012). The transverse section X-X in Phase 1 was at the same location as section Y-Y in Phase 2 with reference to SFB2a. The variation of transverse stress along these sections was similar, however, the stresses in Phase 2 were found to be higher than in Phase 1 (refer to Figure 79 in Alapati 2012). Section X-X also experienced maximum deformation when the load patches located at section X-X was loaded to the maximum (refer to Figure 81 in Alapati 2012). As such, the ribs under the load patches (ribs 3, 4, 6 and 7) experienced significant distortion.

4.1.2 Response of Intermediate Sub-floor Beam (SFB2a)

The deformed configurations of SFB2a is shown in Figures 36 and 37 for static test simulations under LS-1 and LS-2, respectively. The east end of the floor beam was displaced downwards matching the actuator displacement in the laboratory testing which resulted in a displaced profile similar to a propped cantilever. The subfloor beam essentially deformed as a beam spanning between the stringer extensions.

Since the subfloor beam was integral with the stringer extensions, the wheel loads were transferred to the stringer extension plates through the subfloor beam by shear as shown in Figure 38 reproduced from Alapati (2012). The contours of the maximum principal stress in SFB2a are shown in Figures 39 and 40 for LS-1 and LS-2, respectively. In both cases, the transfer of shear to the stringer extensions resulted in a tension field from the bottom (tension) flange of the subfloor beam to the top corner of the connection between the subfloor beam and the stringer extension. The maximum stresses occurred along the diagonal tension field at ribs 3 and 7: in the subfloor beam at the termination of the cutouts on the rib wall. Since the bulkhead plates inside the ribs at the subfloor beam locations provides continuity, a diagonal tension field also developed in the bulkhead plate from subfloor beam-to-rib cutout to the opposite upper corner of the bulkhead plate (Figure 41).

The presence of cutouts around the ribs caused bifurcation of the shear induced tensile stress fields resulting in regions of stress concentration around the cutout (Figures 39 and 40): one below the rib and another at the cutout termination on the rib. These stress concentration regions developed in the web of the subfloor beam, where the tension fields were approximately tangential to the cutouts. The radius of the cutout at the rib to

SFB2a interface was $1^1/_2$ in. (38 mm) while the radius of the cutouts under the ribs was $6^5/_8$ in. (168 mm) and therefore the stress concentrations at the cutouts under the ribs were lower compared to that at the cutout terminations at the weld toe (Figure 41).

The presence of weld toe notches at the rib-to-subfloor beam connections also contributed as stress raisers. The FEA results for SM2 (submodel containing both stress concentration locations at the cutout) showing the stress concentrations at the cutouts are presented in Figure 41. The maximum principal stress was determined at the cutout termination as 24.3 ksi (167.8 MPa) and at the edge of the cutout under the ribs as 11.2 ksi (77.2 MPa). However as is well known, the nominal fatigue resistance of base metal is higher than the welded connections. Hence the subfloor beam-to-rib welds, and the bulkhead plate to the rib welds were more susceptible to fatigue cracking. The behavior of the bulkhead plates are discussed later.

The maximum out-of-plane bending of the subfloor beam web due to the rotation of the rib was expected to occur at the rib-to-subfloor beam interface. This out-of-plane bending response was assessed with respect to the FEA results of SM5, which provided the most accurate estimate of the stress field in the region. Figure 42 shows the variation of the stress normal to the weld toe on the north and south faces of SFB2a at Rib 3 along a path normal to the weld toe that was tangential to the cutout. As is evident from the figure, the stresses were primarily in-plane. The out-of-plane stress component was minimal in LS 1 while no out-of-plane stress was detected for LS-2. The out-of-plane bending component in LS-1 was maximum at the weld toe and stayed constant for up to the distance of about 1 in (25 mm). As the distance further increased, it decreased rapidly and became primarily in-plane. For LS 2, there was no bending because the loading was

symmetric to SFB2a.

The responses of SFB2a were similar in both Phase 1 and Phase 2. The displacement profiles of SFB2a were similar in both phases. In Phase 1 also, maximum local deformation of the deck plate was seen under the load patches. The stress concentration regions were observed along the diagonal tension field at ribs 3 and 7 in the subfloor beam at the termination of the cutouts on the rib wall. From SM2 analysis in Phase 1, the maximum principal stress of 41.0 ksi (282.69 MPa) was observed at the cutout termination around Rib 3 in LS-3 static test simulation (Figure 99 in Alapati, 2012). From SM2 analysis in Phase 2, the maximum principal stress was observed to be 24.33 ksi (167.75 MPa) at the cutout termination around Rib 7 in LS-1 static test simulation. Hence, it shows that the modification of the deck helped reduce the maximum stress at the high stress concentration regions in SFB2a (Figure 41).

4.1.3 Response of End Sub-floor Beam (SFB1)

Figures 43 and 44 show the deformations of SFB1 in comparison to SFB2a. Since SFB1 was supported by the floor beam, the deformation of SFB1 was less compared to SFB2a. As discussed earlier, the east end of the floor beam was displaced downwards in order to match the boundary conditions of the laboratory test. Hence, a displaced profile similar to the propped cantilever was observed. LS1 caused higher stresses at SFB1 compared to LS-2 because the loading pads in LS-1 were closer to SFB1 than in LS-2. The contours of the maximum principal stress in SFB1 are shown in Figure 45 for LS-1. Similar to SFB2a, the maximum stress occurred at the termination of the cutouts in the subfloor beam and in the bulkhead plates at ribs 3 and 7. But as is evident, the stresses in SFB1 were much less compared to stresses in SFB2a because SFB1 was supported by the

stiff floor beam and the longitudinal disposition of the loading on the deck was eccentric towards SFB2a.

Similarly, in Phase 1 also the stresses in SFB1 were much less compared to those in SFB2a. The displacement profiles of SFB1 were also similar in both phases. However, in Phase 2 the stresses were even smaller because the loadings applied in Phase 2 were eccentric towards SFB2a. No loading was applied over SFB1. Hence, SFB1 in Phase 2 experienced very less deformation compared to Phase 1.

4.1.4 Response of the Bulkhead Plate

The bulkhead plates inside the ribs at the subfloor beam locations provided continuity to the subfloor beams. Contour plot of maximum principal stress at the Rib 7 bulkhead plate is shown in Figure 41 for LS-2 of static test simulation. As mentioned earlier in section 4.1.2, a diagonal tension field was developed in the bulkhead plate from subfloor beam-to-rib cutout to the opposite upper corner of the bulkhead plate resulting in stress concentrations at the connections along the tension field.

Figure 46 shows the variation of the maximum principal stress and the stress normal to the rib-to-bulkhead plate weld along the weld toe. The path originated at the top edge of the bulkhead plate and proceeded as indicated by the arrow. SM3 of Rib 7 under LS-2 was used for this plot because: (a) SM3 was the submodel with the highest mesh density that contained the entire path on the tension side of the rib-to-bulkhead plate connection; (b) LS-2 produced higher stress between the two load steps; and (c) Rib 7 showed higher stresses than Rib 3. Both the peak maximum principal stress and the maximum stress normal to the weld toe occurred at about 6.2 in (158 mm) from the top edge of the bulkhead plate, identified by point A. Except at the top edge of the bulkhead

plate, the normal and the maximum principal stresses were close. It implies that the direction of maximum principal stress was generally close to the normal to the weld toe except at the top edge of the bulkhead plate. In Figure 47 the normal stresses on both faces of the bulkhead plate are plotted for LS-2 along a path, originating from point A (as identified in Figure 46) and proceeding normal to the rib-to-bulkhead plate weld. A high stress of about 9.5 ksi (65.5 MPa) was noted at the weld toe that sharply decreased to about 5.8 ksi (40.0 MPa) within 0.2 in (5 mm) and then decreased at a reduced rate. The stress on the north and the south faces was almost equal in magnitude, which implies that the stress in the bulkhead plate was primarily in plane. The stress distribution was typical of local stresses adjacent to a weld toe. The gradual variation of the stress was due to the stress concentration effect of the cutout, where the rapid rise in the stress peak was due to the weld toe notch effect. In this context it may be noted that the weld toe in SM3 was modeled ideally as the sharp notch with zero radius. The local stress at the weld toe notch is theoretically singular. The finite stress at the weld toe obtained from the FEA results is only indicative, corresponding to the mesh density used for this model. This stress would increase asymptotically with increased mesh refinement.

Figure 48 shows the normal stress through the thickness of the bulkhead plate at Rib 7 rib-to-bulkhead plate weld toe as obtained from the FEA results of SM5. The results of SM5 were used for obtaining a more accurate variation through the thickness. It can be seen that the stress increased asymptotically approaching the weld toe at the plate surface and decreased rapidly inside the plate. For about half the thickness in the middle of the bulkhead plate, the stress remained constant. Also, higher stresses were observed for LS2 as compared to LS1. The variation of stress in Figure 48 also shows that the

stresses at the bulkhead plate were primarily in-plane.

The responses of the bulkhead plates were similar in Phase 1 and Phase 2. The maximum principal and normal stress, at the bulkhead plate-to-rib connection adjacent to cutout termination in Phase 1 and obtained from the SM2 analysis, were 18.7 ksi (128.8 MPa). This stress was almost twice of what was observed at the same location in Phase 2. The variation of stress normal to the rib-to-bulkhead weld toe was similar in both phases of testing (Figure 46 and see Figure 105 from Alapati 2012). Similar to Phase 2 observations, some out-of-plane bending was experienced by bulkhead plate when the loading applied on the deck was not symmetric to the respective subfloor beams. This bending was maximum at the weld toe and decreased away from the weld toe.

4.2 Assessment of Fatigue Resistance

4.2.1 Assessment using Hot Spot Stress Approach

The hot spot regions on SFB2a were recognized using FE analysis. Among the recognized hot spots, the hot spots at rib-to-SFB2a connection were considered more important in view of fatigue cracking. The rib-to-SFB weld toe detail at these ribs 3 and 7 cutout terminations had significant stress concentrations due to the global load effects and the presence of cutouts in their vicinity. Applying hot spot stress approach may get complicated when the hot spots for different loading cases have to be considered. However, in our case the hot spots for both the fatigue loading cases occurred at the same locations. Also the detail at the cutout terminations can be classified as into type ‘a’ and ‘b’ according to IIW (Hobbacher 2008). The hot spot located on the rib-to-SFB weld toe can be identified as type ‘a’, and the hot spot located at the cutout edge can be identified

as type ‘b’ as shown in Figure 49.

The variation of normal stress (S_{11}) along the weld toe showed that the maxima of this stress occurred at a distance of about 0.4 in. (10 mm) from the cutout termination on the rib (Figure 50). With this location as the plot origin, the variation of S_{11} obtained from all the submodel analyses along a path perpendicular to the weld toe (subsequently identified as the evaluation line) is shown in Figure 51. As mentioned in IIW (Hobbacher 2006), this detail can be evaluated as a fatigue class (FAT 100) detail. The thickness of SFB2a, *t*, was $^{7}/_{8}$ in. (22 mm). Accordingly, the distance of various reference points from the weld toe along the evaluation line for using Equations (1) and (3) to obtain the HSS were 0.4*t:* 0.35 in. (9 mm); 0.9*t:* 0.79 in. (20 mm); 1.0*t:* 0.88 in. (22 mm); and 1.4*t:* 1.23 in. (31 mm). The plot in Figure 51 demonstrates that except at the weld toe notch, S_{11} converged in SM2 at all the reference points for a mesh size of 0.25 in. (6 mm). Hence, SM2 results can be used for the hot spot stress extrapolation.

As is seen, the normal stress S_{11} did not change monotonously as is typically observed adjacent to toe of a welded connection (Figure 15), but exhibited a bimodal distribution. The stress peak due to the notch effect of the weld toe was observed, which decayed rapidly away from the weld toe consistent with the decay of the theoretically infinite stress ahead of a sharp notch. Due to the stress concentration effect of the cutout, however, the stress increased again to another peak. The combined stress concentration effect of the weld notch and the cutout geometry can be seen in the contour plot at the cutout termination on the rib wall in Figure 52. Along the evaluation line, the second stress peak occurred at a distance of about 0.9 in. (23 mm) away from the weld toe.

For the linear extrapolation method, the hot spot stress at the weld toe was

estimated using the FEA results of SM2 at 0.4*t* and 1.0*t* distance on a path perpendicular to the weld toe (Figure 53). One of the reference points was located at the top of the secondary stress peak while the other was located on the slope towards the weld. Using Equation (1), the hot spot stress at the weld toe was obtained as 10.9 ksi (75.2 MPa).

In view of a nonlinear stress variation the hot spot stress at the weld toe was also determined by a quadratic extrapolation using the stresses at 0.4*t*, 0.9*t* and 1.4*t* from the weld toe (Figure 54) and Equation (3). The reference points at 0.4*t* and 1.4*t* from the weld toe were located on either sides of the second peak, whereas the reference point at 0.9*t* was located in the vicinity of the second peak stress. The quadratically extrapolated hot spot stress was 6.7 ksi (46.2 MPa) as shown in Figure 54.

As per the AASHTO recommendations (AASHTO, 2010), the local structural stress or the hot spot stress at the weld toe was estimated from the results of SM2A for a $t \times t$ mesh, by linearly extrapolating the surface stresses at 0.5*t* and 1.5*t* distance from the weld toe on the evaluation line using Equation (2). This extrapolation is graphically presented in Figure 55. The reference points were located on either side of the second stress peak due to the cutout. As a result the local structural stress at the weld toe was influenced by the stress concentration resulting from the cutout geometry. The estimated stress at the weld toe based on the $t \times t$ mesh density in SM2A was 14.7 ksi (101.4 MPa).

Figure 56 presents the S-N design curve for the assessment of the hot spot stresses obtained from extrapolations recommended by IIW (Hobbacher 2005). The rib-to-SFB2a joint with bulkhead plate had formed a cruciform connection (Figure 57). The fatigue class (FAT) value of 100 with a slope of 3.0 was provided for the cruciform or T-joint with full penetration detail (Hobbacher 2005). This coincides with AASHTO Category B′

detail curve however, the constant amplitude fatigue limit (CAFL) knee point occurs at 10 million cycles. The hot spot stress obtained from quadratic extrapolation was a small number of 6.7 ksi (46.2 MPa), which was well below the CAFL. The hot spot stress obtained from linear extrapolation of 10.9 ksi (75.2 MPa) was exactly on the FAT 100 S-N curve. This suggests that the detail shows finite life and could crack at about 5 million fatigue cycles. As per AASHTO recommendations, the hot spot stress of 14.7 ksi (101.4 MPa) obtained from extrapolation was compared against AASHTO Category C design curve with CAFT at 10 ksi (68.95 MPa) in Figure 58. Since the extrapolated local structural stress range was well above the CAFT value, the subfloor beam-to-rib welded connection was expected to develop fatigue cracking at the weld toe at a (finite) design life of about 1.4 million cycles.

The occurrence of diagonal tension bands and weld toe notches at the rib-to-bulkhead plate connections caused stress concentrations on the bulkhead plates adjacent to the cutout (towards the transverse centerline of the deck) and on the opposite end of the diagonal. In section 4.1.4, the location of the maximum stress concentration in the region adjacent to the cutout was identified (Figure 46). The normal stress variation (S_{11}) along the path perpendicular to the weld toe (or the evaluation line) is presented in Figure 47.

The thickness of bulkhead plate was $^{5}/_{8}$ in. (16 mm). Since, the hot spot location of the bulkhead is also type ‘a’, it can be evaluated using Equation (1). The distance of various reference points from the weld toe along the evaluation line for using Equations (1) to obtain the HSS were 0.4t: 0.25 in. (6 mm) and; 1.0t: 0.63 in. (16 mm).

Unlike SFB-to-rib weld toe, the stress variation was steep when close to the weld

toe and linear after about 0.25 in. (6 mm) away from the weld toe. Therefore, these stress extrapolation points may be free of weld toe notch effect. As such the hot spot stress at this weld toe was estimated using the FEA results at 0.4t and 1.0t distance on a path perpendicular to the weld toe (Figure 59). The stresses at Rib 7 were considered for this study as it showed higher stresses during the FE analyses. Using Equation (1), the hot spot stress at the weld toe was obtained as 5.9 ksi (41 MPa). This stress is lower than the CAFL for the FAT 100 S-N curve. It suggests that the rib-to-bulkhead plate detail should show infinite life.

According to the definition provided by IIW (Hobbacher, 2006), the cutout edge of the SFB cutout detail can be considered a type 'b' hot spot. The maximum stress at this detail was observed at Rib 7 cutout. Therefore, Equation (4) was used for calculating the hot spot at the weld toe of this welded and ground smooth cutout detail. The stress variation was nonlinear and peaked before the weld toe (Figure 60). The extrapolated stress was similar to the FEA stress at the weld toe, which was 13.9 ksi (96 MPa). This hot spot stress at this cutout edge detail is recommended to be compared against FAT 90 plot as is shown in Figure 61. This assessment shows that this detail should develop fatigue cracking at about 1.6 million cycles.

4.2.2 Assessment using Notch Stress Approach

The prototype orthotropic deck tested and designed for this project was intended for infinite fatigue life. However the hot spot stress approaches provided only the finite life assessment of the fatigue critical detail connection. Therefore, the fatigue strength of the rib-to-SFB2a weld connection for infinite life was determined by the notch stress approach as described in section 3.2.2. The notch stresses were obtained for the submodel

analyses SM4, SM5 and SM6. As is displayed in Figure 62 the maximum notch stress value was observed as 25.63 ksi (177 MPa) for SM4, and the converged maximum notch stress value was obtained as 23.8 ksi (164 MPa) in SM5 and SM6. This converged notch stress value was then compared with the CAFT of welded connections for the infinite life fatigue resistance at the weld toe notch. This can be obtained from Equations (4) to (6) given in section 3.2.2.

The theoretical stress concentration factor (K_t) which is needed for solving Equation (5) is the ratio of maximum and the nominal stresses at the discontinuity. It is generally dependent on the connection geometry and the mode of loading. It is difficult, if not impossible, to define the nominal stress in orthotropic bridge deck near such complex connection geometries at the rib-to-subfloor beam connections. The situation is further complicated by the mode of loading (shear vs. normal) etc. As discussed in the previous section and shown in Figure 51, a well-defined nominal stress was not present at the rib-to-SFB connections. With respect to Figure 52, at the rib-to-SFB connection, the stress concentration was influenced by the stress concentration due to the cutout geometry. Therefore, the value of K_t could not be determined from the models analyzed so far.

The geometry of the rib-to-SFB weld connection and the cutout are the principal cause of stress concentration at the rib-to-SFB weld toe. The fatigue cracking at the weld toe usually initiates from micro-discontinuities and grows along the weld toe. Therefore, the mode of cracking is governed by the stress normal to it. The total effective stress concentration factor at the rib-to-SFB welded connection could therefore be considered as the product of each stress concentration factor due to the cutout and the weld toe

notch. Accordingly, it was envisaged to determine the stress concentration due to the cutout alone by the following methodology.

The effect of the stress concentration due to the weld toe geometry, K_{t1}, was determined from the model of a simple cruciform cross section at rib-to-SFB connection subjected to nominal stress. Model 1 was created for this purpose.

The effect of the stress concentration due to the cutout, K_{t2}, was determined by comparing the stress conditions with and without the cutout in similar models subjected to identical loading and boundary conditions. Model 2 and Model 3, representing the portion of SFB between SEs A and B were created for this purpose. Model 2 was modeled with the cutouts around the ribs while Model 3 was modeled without cutouts. These models were subjected to shear loading similar to loading at SFB2a. The maximum normal stresses along the weld toe location were the compared to obtain the stress concentration due to the presence of cutouts. Finally, the total stress concentration (Kt) at the rib-to-SFB connection detail was obtained as the product combination of these two stress concentrations ($K_{t1} \times K_{t2}$).

4.2.2.1 Model 1

Model 1 represented the cross section of the cruciform connection of bulkhead plate and SFB welded to the rib (Figure 63). SFB and bulkhead plate were the main load carrying members. The widths of rib, bulkhead plate, and SFB were $^5/_{16}$ in. (8 mm), $^5/_8$ in. (16 mm), and $^7/_8$ in. (22 mm), respectively with $^1/_4$ in. (6 mm) welds. The bulkhead plate and SFB were 5 in. (127 mm) long while the rib was 10 in. (254 mm) long. A rounding of 0.04 in. (1 mm) radius was made at the rib-to-SFB weld toe. The bulkhead plate, SFB, rib and weld parts were attached by applying tie constraints at their adjoining faces. In the

actual prototype deck, the rib-to-SFB welds were CJP while the rib-to-bulkhead plate welds were PJP. However in the FE models including Model 1, all the connection were monolithic.

The boundary conditions were assigned to the model at the free edges of all the members to allow a single degree of freedom parallel to the applied stress in the SFB and the bulkhead plate. The free end of the bulkhead plate was constrained in both X and Y directions. The free edges of the rib and the SFB were allowed to move only in X-direction by constraining Y-axis displacement as shown in Figure 63. A 10 kip (44.48 kN) load was applied at the free edge of SFB in the X-direction as shown in Figure 63.

4.2.2.2 Model 2

Model 2 contained the mid-plane section of the subfloor beam including the cutouts and the gap above the bulkhead plates (Figure 64). The gap between the bulkhead plates and the deck plate was $^{5}/_{16}$ in. (8 mm). As shown in the figure, the model was 11ft. 4 in. (3.454 m) wide and 1 ft. 9 $^{3}/_{8}$ in. (0.543 m) in depth.

The boundary conditions for this model closely emulated the SFB-to-SE connection. The edges of the SFB were fixed in the axial (X) and vertical (Y) directions as shown in Figure 64. A distributed load of 1 kip (4.45 kN) was applied over 20 in. (0.508 m) strips consistent with the load patches used for the analyses of the global model (see section 3.8).

4.2.2.3 Model 3

Model 3 was similar to Model 2 but without any cutouts around the ribs but including the including the gap at the top of the bulkhead plate. This model was analyzed for identical boundary conditions and loadings (

Figure 65).

4.2.2.4 Analysis Details

All three models were meshed with 2D continuum shell elements using automatic meshing algorithm in ABAQUS. An eight-node quadratic plane stress quadrilateral reduced integration element was used. The modulus of elasticity and Poisson's ratio of steel were assumed as 29000 ksi (2.0×10^5 MPa) and 0.3, respectively. These relatively simple models were run on the desktop personal computer having 1 cpu and 4 GB memory.

Model 1 was analyzed with mesh sizes of 0.1 in. (2.5 mm), 0.05 in. (1.3 mm), 0.025 in. (0.6 mm), and 0.0125 in (0.3 mm). The maximum stress at the weld toe notch converged at the mesh sizes of 0.025 in (0.6 mm) as shown in Figure 66.

Model 2 and Model 3 were analyzed with mesh sizes of 0.5 in (12.7 mm), 0.25 in. (6.4 mm), and 0.125 in (3.2 mm). The peak stress of Model 2 converged at 0.25 in (6.4 mm) mesh size as (Figure 67). The stresses of Model 3 converged for all three mesh sizes (Figure 68).

4.2.2.5 Results

Model 1 was used to determine the stress concentration factor due to the presence of weld. The maximum principal stress distribution in Model 1 is shown in Figure 69.

The stress normal to the weld toe is presented in Figure 66. It shows the nominal stress on SFB and the exponential increase of normal stress towards the weld toe. The converged maximum stress at the weld toe rounding was 26.0 ksi (179 MPa) for the nominal stress of 11.40 ksi (79 MPa) at the surface of SFB. The stress concentration factor (K_{t1}) due to the presence of weld is therefore, 2.3.

Model 2 and Model 3 were used to determine the stress concentration factor due to the presence of cutouts. The final results for these models showing the principal stress distribution are presented in Figures 70 and 71. The stresses normal to Rib 3 weld along the path of rib-to-SFB weld toe at Rib 3 tension side cutout are plotted in Figure 72 for Model 2 and Model 3.As the path originates from the edge of the cutout, the maximum stresses in Model 1 was observed 0.45 in. (11 mm) from the origin of the path. Maximum stress was observed at about 0.4 in. (10 mm) from the cutout edge in the previous analyses of 3-D models. So, the location of the maximum stress from the cutout edge was similar. The maximum normal stress in Model 2 was 6.5 ksi (45 MPa) and the corresponding normal stress at the same location in Model 3 was 0.65 ksi (5 MPa). Thus, the stress concentration factor (K_{t2}) due to the presence of the cutouts is 10.

The total effective stress concentration factor (K_t) at the rib-to-SFB connection is the product of K_{t1}.and K_{t2} i.e. 23. The value of 'a' for the 50 ksi steel was calculated from Equation (6) as 0.025 in (0.64 mm). As mentioned above in previous sections, the notch rounding of 0.04 in. (1 mm) was provided at the weld toe. By substituting these values in Equation (7) the calculated value of K_f was 16.8. Hence, the fatigue effective notch stress concentration reduced to about 73% of the notch stress concentration of the rounded weld toe.

$$K_f = 1 + \frac{K_t - 1}{\left(1 + \frac{a}{r}\right)} = 1 + \frac{23 - 1}{\left(1 + \frac{0.0157}{0.04}\right)} = 16.8$$

For as-welded connections, tensile residual stresses can be considered to be approximately equal to the yield stress of the material near the weld. It results in a local stress ratio in excess of 0.5. An endurance limit of 0.5 times the ultimate strength is assumed for structural steel. Thus, the relationship in Equation (4) can be further simplified for the local infinite life fatigue resistance, $(\Delta F)_l$ of the weld toe notch using the yield strength (F_y) and ultimate yield strength (F_u) of the material.

$$(\Delta F)_l = \frac{1}{2.92}\left[-F_y + \sqrt{F_y^2 + 4 \times F_u^2}\right] ksi \tag{7}$$

Since, the yield and ultimate strengths of the material are usually known, this expression is found to be more convenient to use. For ASTM A709 Gr. 50 steel, the nominal yield strength is 50 ksi (345 MPa) and a nominal ultimate strength is 65 ksi (448 MPa). The infinite life fatigue resistance can then be calculated by substituting these values in Equation (7):

$$(\Delta F)_l = \frac{1}{2.92}\left[-50 + \sqrt{50^2 + 4 \times 65^2}\right] ksi = 30.7\ ksi$$

Hence, the local infinite life fatigue resistance at the weld toe notch was obtained as 30.7 ksi (212 MPa). The applied local notch stress range (obtained from FEA) was less than the local fatigue resistance, which indicates infinite life for the SFB2a-to-rib weld detail at the cutout termination.

5 FULL SCALE LABORATORY TEST

This chapter provides the overview of the laboratory testing. It includes the instrumentation of the deck specimen and acquisition of data at the important locations of the deck in order to understand the behavior of the deck and assess its fatigue performance. Also briefly described are the modifications made to test setup for Phase 2 testing and the procedures followed for crawl, static and fatigue tests.

5.1 Instrumentation

5.1.1 Overview

Similar to the Phase 1 study (Alapati 2012), the refurbished prototype deck was densely instrumented to determine its global response and to measure the local stresses at the fatigue sensitive connection details. Most of the functioning strain gauges on the existing portions of the Phase 1 prototype deck were retained.

Based on the FEA studies (Chapters 3 and 4) of the prototype deck and the fatigue cracking observed in Phase 1 studies, fatigue performance of SFB2a in the improved design was the primary focus of the Phase 2 study. Accordingly, most of the strain gauges installed in this phase of the study were concentrated on SFB2a adjacent to the cutouts of ribs 3 and 7, and on the internal bulkhead plates of these ribs.

Stresses were measured using surface mounted, encapsulated metallic, bonded or welded electrical resistance strain gauges. The vertical displacements of the ribs and the deck plate were measured using linear variable displacement transformers (LVDTs). The instrumentation plans along with the FEA results used for deciding gauge placements are shown in Figures 73 to 93. A total of 181 data channels consisting of 85 uniaxial, and 96

rosette gauges, were used in Phase 2A for the fatigue test and the intermittent static tests. After the initial static test in Phase 2A, all the LVDTs were disconnected. For Phase 2B testing, 60 strain gauges on SFB1 retained from Phase 1 testing were monitored. Among these 60 gauges, 24 were rosette gauges and 36 were uniaxial gauges.

The strain gauges installed on the reused deck segments of Phase 1 were retained for Phase 2 testing. Due to the modifications, section Y-Y of Phase 1 deck was located at the mid span section between SFB1 and SFB2a in the Phase 2 deck (Figure 73). The strain gauges between SEs A and B present at transverse section Y-Y, and the gauges at floor beam to wall connection plates were reused in Phase 2 testing. The retained gauges at section Y-Y were located on the top and bottom faces of the deck plate and on the inner and outer faces of rib walls, abutting the rib-to-deck welds on either side of Rib 7. SFB2a was the most critical component of the deck and was studied in detail. The behaviors of the other two subfloor beams were not monitored initially, in Phase 2A testing. However, in Phase 2B the gauges on SFB1 were re-used to monitor the behavior of SFB1.

To capture the global response of the deck specimen, additional strain gauges were installed on the soffits of ribs 3 to 7 at section Y-Y, 4ft. $1^1/_2$ in. (1.257 m) north of SFB2a. Similar gauges were installed at section Z-Z which was the mid-span between SFB1 and SFB2a in Phase 1 deck. Phase 1 deck specimen did not have bolted rib connections. To monitor the slip critical bolted connections at splices south of SFB2a (section U-U), strain gauges were installed on the splice plates for ribs 3 to 7.

As section Z-Z was the mid-section between SFB1 and SFB2a in Phase 1, section Z-Z was provided with LVDTs at the soffits of deck plate and ribs between ribs 3 to 6.

Similarly, in Phase 2, LVDTs were installed at section Y-Y on the soffit of the deck plate and the ribs between ribs 3 and 6. The relative displacements measured by these LVDTs provided an assessment of deformation of the deck plate with respect to the ribs.

Each instrumentation channel including each uniaxial gauge and each element of rosette and strip gauges are identified by a unique four digit number. The first digit is used to identify the channels installed in a particular phase of study. For example, the strain gauge on SFB1 installed in Phase 1 was denoted as 1054, 1055, etc. and the strain gauge on SFB2a installed in Phase 2 was denoted as 2025, 2026, etc.

5.1.2 Details of Sensors

Strain gauges of uni-axial, and rosette configurations having different resistances and applicable temperature ranges were used. Most gauges had $^1/_4$ in. (6 mm) gauge length while some gauges installed at ribs 3 and 7 cutout terminations had $^1/_{25}$ in. (1 mm) gauge length. Details of strain gauges that were carried over with the parts of Phase 1 deck are provided in Phase 1 studies by Alapati (2012). On the deck plate, and the ribs, weldable uni-axial strain gauges were used. At the toe of the rib-to-bulkhead plate weld, high temperature weldable strain gauges were used. The strain gauges used on the SFBs were bondable strain gauges of uni-axial, strip and rosette types. The types of strain gauges installed during the Phase 2 study as well as those retained from Phase 1 were:

1. Vishay Micro Measurements CEA-06-250UW-350 uni-axial bondable gauges having 350Ω resistance and $^1/_4$ in. (6 mm) gauge length;
2. Vishay Micro Measurements LWK-06-W250B-350 uni-axial weldable gauges having 350Ω resistance and $^1/_4$ in. (6 mm) gauge length;
3. Vishay Micro Measurements LZN-NC-W250G uni-axial weldable (high temperature)

gauges having 120Ω resistance and $^1/_4$ in. (6 mm) gauge length;

4. Vishay Micro Measurements CEA-06-250UR-350 rosette (also called rectangular rosette) bondable gauges having 350Ω resistance and $^1/_4$ in. (6 mm) gauge length.
5. Texas Measurements FXV-1-11-002LE bondable strip gauges having five elements of $^1/_{24}$ in. (1 mm) gauge length and 120 Ω resistance oriented along the length of the strip at $^1/_{12}$ in. (2 mm) pitch.
6. Texas Measurements FRA-1-11-003LE bondable stacked rosette gauges of $^1/_{25}$ in. (1 mm) gauge length in rectangular configuration and having 120 Ω resistance.

The strain gauges were installed in accordance with the guidelines provided by the strain gauge manufacturers.

The LVDTs were Macro Sensors DC 750-1000, having a nominal displacement range of ±1 in. (±25 mm).

5.1.3 Instrumentation of Deck Plate

The FEA results of the prototype deck showed that the effects of loading on the deck plate were highly localized under the loading pads. The portion of the deck under the loading patches showed maximum deformation which rapidly decreased as the distance from loading increased (see section 4.1.1). Similarly, these locations under the loading pads (i.e. at ribs 3, 4, 6 and 7) also experienced high normal stresses in the transverse direction. On the bottom face of the deck at the rib-to-deck welded connections (of ribs 3, 4, 6 and 7), the transverse stresses were compressive (Figure 31). However, due to the possibility of high residual stresses at the rib-to-deck plate weld toe, these welded connections may locally experience tensile stress cycles under the resulting compressive stresses under the wheel loading. This may contribute to fatigue damage at

these welded connections.

Weldable uni-axial strain gauges of $^1/_4$ in. (6 mm) gauge length installed in Phase 1 on the top and the bottom surfaces of the deck plate at section Y-Y and retained for Phase 2 testing are shown in Figures 73 to 75. These strain gauges were installed on the deck plate at the rib-to-deck connections of Rib 7 in Phase 1. These gauges were used in order to observe the highly localized transverse stresses at rib-to-deck connections under direct loading by actuator #3 (placement of actuator #3 will be discussed later in section 5.4)

Along the centerline of SFB2a, strain gauge CH 2153 was installed on the deck plate above Rib 5 and was oriented in the transverse direction of the deck. The location of this gauge was similar to longitudinally oriented CH 1211 used in Phase 1 (Alapati 2012).

A pair of strain gauges (channels 2151 and 2152) was installed at section U-U for capturing local stresses at the transverse deck splice under the load pads. These gauges were longitudinally oriented abutting the deck splice weld and were located within the 1 in. (25 mm) gap between the west side rubber loading pads as shown in Figure 76.

Three LVDTs were installed under the deck plate at section Y-Y, for measuring the vertical displacement of the deck plate (Figure 74). These LVDTs were used only during the crawl tests and static tests prior to initiating the fatigue test, and were positioned similar to the Phase 1 testing (Alapati 2012). The LVDTs were identified as: channels 1375, 1377, and 1379 for those located between ribs 3 and 4, 4 and 5, and 5 and 6, respectively.

5.1.4 Instrumentation of Ribs

It was observed from the FEA results that at section Y-Y the rib section under the

wheel loads were distorted giving rise to linearly distributed stresses in the rib walls. Study of longitudinal stresses at the rib soffits showed that ribs under the loading pads that are farther away from the stringer extension supports experienced higher stresses than the others. Unlike the stresses on the deck plate or at the rib-to-deck connections, the longitudinal stresses at the rib soffits was similar to that of a continuous beam subjected to concentrated loads (Figure 35).

As discussed in the previous section, the gauges on the walls of Rib 7 at the rib-to-deck weld connection in section Y-Y were retained and used in Phase 2 testing (Figure 75). The strain gauges were present on both the internal and external faces of the rib walls in back-to-back configuration and were oriented along the depth of the rib wall. The internal gauges on both the rib walls were found to be non-functional when setting up for Phase 2 testing. These internal gauges were inaccessible and could not be replaced.

Uni-axial strain gauges of $^1/_4$ in (6 mm) gauge length were installed at the middle of the soffit of ribs 3, 4, 5, 6 and 7 (strain gauge channels 2155 to 2159, respectively) at section Y-Y (Figure 77). These gauges were installed at the midspan section between SFB1 and SFB2a and were comparable to the gauges installed at the midspan section Z-Z between SFB1 and SFB2a in Phase 1 (strain gauge channels 1222, 1217, 1219, 1220 and 1224, respectively). Prior to installation of these strain gauges, the paint on the soffit of the prototype deck was ground to bare steel at the strain gauge locations because section Y-Y lied on the part of the deck retained from Phase 1 which had a layer of paint on the underside.

At section Y-Y, three LVDTs were installed on the rib soffits next to the rib soffit gauges (Figure 74) for measuring the vertical displacements of the ribs. These LVDTs

were used only during the crawl tests and static tests prior to initiating the fatigue test. The LVDTs were positioned similar to the Phase 1 study at the mid span section between SFB1 and SFB2a (Alapati 2012). These LVDTs were identified as: channels 1374, 1376 and 1378 at ribs 3, 4 and 5, respectively.

5.1.5 Instrumentation of SFB2a

SFB2a was densely gauged around ribs 3 and 7 as shown in Figures 78 and 79. All the gauges except at the cutout face at mid thickness were installed back-to-back on both north and south sides of SFB2a web (Figures 80 to 83). Figures 80 and 81 show the north face of SFB2a at Rib 3 while Figures 82 and 83 show the south face of SFB2a at Rib 7. The channel numbers of the gauges installed on the north face are shown in parentheses.

The instrumentation of SFB2a was decided on the basis of FEA results. It showed high stress concentrations at ribs 3 and 7 cutouts (Figures 39 and 40): at the cutout terminations towards the mid-span of the subfloor beam and at the cutouts under the rib soffits. The cutout termination was also the SFB-to-rib weld termination detail. The presence of weld notch at this location meant it was a fatigue critical detail. In Phase 1 testing, fatigue cracking had occurred at the Rib 3 cutout termination (Alapati 2012). Hence, the cutout termination experiencing tensile stresses were extensively instrumented.

As shown in Figures 81 and 83, 1mm rosette gauges and strip gauges were to be installed on both faces of Rib 3 east and Rib 7 west cutout terminations. The stresses usually flow tangential to the curved edges in the presence of curved obstructions on their path. So, it was assumed that the maximum stresses at the cutout termination would be

tangential to the curvature at that location. The tangent direction was 55° with respect to the rib-to-SFB2a weld toe. Figure 84 shows the FEA principal stress measurements along the 55° path. The figure also shows the planned gauge placements. The rosette gauge was to be placed as close to the cutout termination to capture the maximum tensile stress at this high stress concentration location. One of the rectangular arms of the rosette gauge (identified as Gauge 1 in Figure 85) was planned to be installed at 55° with the weld toe such that it was tangential to the cutout edge. A strip gauge was to be placed aligned at 55° with the weld toe adjacent to the rosette gauge. Due to the presence of high stress gradient, this strip gauge was envisaged to capture the stress gradient in the direction of maximum principal stress and tangent to the cutouts. The variation in the direction of maximum principal stresses along the 55° path is also shown in the Figure 84.

Two additional bondable rosette gauges, $^{1}/_{4}$ in. (6 mm) in length, were provided at 5 in. (127 mm) and 6 in. (152 mm) from the deck soffit along the SFB2a-to-rib weld toe as shown in Figure 79 to determine the stress concentrations and principal stress direction at those locations. FEA results showed the maximum principal stresses along the rib-to-SFB2a weld toe to increase exponentially towards the cutout termination (Figure 86). These rectangular rosette gauges were installed close to the weld toe and oriented such that the perpendicular gauges of the rosettes were parallel and normal to the weld toe.

Along the mid thickness of the cutout edge, two strip gauges were provided – one starting at the weld toe and another $^{5}/_{8}$ in. (16 mm) away from weld toe (Figures 81 and 83). Each of these strip gauges consisted of five 1 mm gauges. FE analysis showed that maximum stresses at these cutout edges don't occur right at the cutout terminations but occurs some distance away from the termination before the stresses start decreasing

gradually (Figure 84). Thus, one strip gauge was placed right at the cutout termination while another was placed at the location of high stresses.

A uniaxial strain gauge (CH 2154) was installed on the soffit of the bottom flange of SFB2a, in the middle of Rib 5 (Figure 87). A similar gauge (CH 2153) was installed on the deck plate opposite to CH 2154 at the same section. The location and orientation of CH 2154 was similar to that of CH 1216 in Phase 1 (Alapati 2012).

5.1.6 Instrumentation of Bulkhead Plates of Ribs 3 and 7

In Phase 1, on each bulkhead plate at ribs 3 and 7, the strain gauges on the opposite diagonals that spanned between the cutout termination on the rib and the opposite top corner of bulkhead plate measured tensile and compressive stresses, respectively (Alapati 2012). Tensile stresses were measured at the gauges on the diagonals that passed through the cutout termination towards the mid span of the SFB. Compressive stresses were measured at the gauges on the diagonals that passed through the cutout termination towards the SEs. During Phase 1 post-mortem studies, fatigue cracks were discovered at the rib-to-bulkhead plate connections experiencing tensile stresses in ribs 3 and 7 (Alapati 2012). Hence, in order to better understand the nature of stress distribution in the bulkhead plates, an instrumentation plan as shown in Figure 79 was devised based on the FEA results.

From the FEA results it was observed that the principal stresses along the rib-to-bulkhead plate weld toe, towards the mid-span of the subfloor beam, was maximum at about 6 $^{1}/_{2}$ in. (165 mm) from the top edge of the bulkhead plate (Figure 88). The direction of the maximum principal stress was close to the direction normal to the weld toe. Thus, to assess the local stress concentration adjacent to the cutout termination, three

$^1/_4$ in. (6 mm) uniaxial strain gauges were provided on both faces of the bulkhead plate, abutting perpendicularly to the bulkhead plate-to-rib weld toe. These gauges were located at about 5 $^3/_8$ in. (137 mm), 6 $^1/_2$ in. (165 mm), and 7 $^5/_8$ in. (194 mm) from the top edge of the bulkhead plate along the weld toe as shown in Figure 79.

As shown in Figure 89, the stress normal to rib-to-bulkhead weld toe decreases away from the weld toe. Close to the weld toe where the uniaxial gauge was placed, the stresses are very high due to the notch effect. Due to the size constrains of the $^1/_4$ in. (6 mm) rectangular rosette gauges, a rosette gauge was installed at some distance away from the uniaxial gauge. It was provided 1 $^1/_4$ in. (31 mm) away from weld toe and $6^1/_2$ in. (165 mm) from the top of bulkhead plate parallel to the weld (Figures 79 and 89). As shown in Figure 79, one of the gauge arms of the rectangular rosette was aligned normal to the weld toe. This rosette gauge was placed to measure the stress at that location having diminished notch effect from the welded connection and also to assess direction of principal stresses in the bulkhead plates. Another rectangular rosette was installed on the centerline of the bulkhead plate at 3 $^7/_8$ in. (98 mm) from the top end of the bulkhead plate (Figure 79) to determine the direction of principal stresses in the diagonal tension band.

Three $^1/_4$ in. (6 mm) uniaxial gauges were installed near the top edge of the bulkhead plate on the diagonally opposite corner (along the tension band) as shown in Figure 79. The gauges were provided in a line subtending 35^0 with the top edge of the bulkhead plate. The variation of stress along this path is presented in Figure 90. The FEA results also showed that the direction of maximum principal stress was close to 35° from the horizontal. The first gauge was installed such that one of its top corners on the long

end touched the weld toe and another touched the top edge of the bulkhead plate. The second gauge was located with clear spacing of $^1/_4$ in. (6 mm) with the first gauge while the third gauge was installed abutting the second gauge (Figure 79).

All gauges were installed on both north face and south face of the bulkhead plates of ribs 3 and 7 (Figure 79). The identifications of the gauges are shown in Figures 80 and 82 for ribs 3 and 7, respectively. The gauges on the bulkhead plates were installed during deck fabrication. The SFB-to-rib and the rib-to-deck plate welding were done after the gauges were installed on the bulkhead plates. High temperature weldable strain gauges were used for the gauges abutting the bulkhead plate-to-rib weld toes (eg. channels 2001, 2002, 2003, 2024 on the north face of Rib 3 bulkhead plate) in anticipation of the high temperature that would develop during the welding of SFB-to-rib and rib-to-deck plate connections.

5.1.7 Instrumentation on Splice Plates

The bolted rib splices between the new and the existing deck segments were also instrumented to monitor any sudden changes at the slip critical bolted connections (Figure 87). Uniaxial strain gauges were installed on both the east and west splice plates of each rib aligned with the rib axis (Figure 91). These gauges on ribs 3 to 7 were numbered from 2160 to 2169.

5.1.8 Instrumentation of SFB1

The instrumentation of SFB1 was inherited from Phase 1 instrumentation (Alapati 2012). The strain gauges at SFB1 were installed around the cutouts, symmetrically on the east and west sides of ribs 2, 3, 7 and 8. Additional strain gauges were provided on the south face of bulkhead plates in ribs 3 and 7. Figures 92 and 93 show the arrangement of

gauges on the south face of SFB1. The strain gauges were installed in back-to-back configuration on the north and south face of the SFB1 web. The bulkhead plate gauges were present only on the south face. These gauges were oriented horizontally, at an angle of about 17° to the weld toe normal. The channel numbers of the gauges installed on the north face of SFB1 are shown in parentheses. Due to the limited number of available channels in the data logger, channels 1294, 1296, 1298, and 1307 at rib 7 were not connected.

5.2 Data Acquisition

Data were collected using programmable digital data loggers manufactured by Campbell Scientific Inc. (CSI). The data loggers were provided with nine CR 9051 analog input cards, which processed the output signal from the instruments. These input cards, also called analog-to-digital (AD) cards, convert the analog signal obtained from the sensors to digital storable format. The processed signals were then stored in a removable storage card from which the data could be downloaded to the computer. Each analog card could accommodate 14 data channels, where each data channel was a quarter of a Wheatstone Bridge circuit.

Two data loggers identified as DAQ1 and DAQ2 were employed for testing. The seven load cells were connected to DAQ1 and the six LVDTs used during the crawl tests and the initial static tests prior to the start of the fatigue test were connected to DAQ2. Input card 1 of DAQ1 consisted of one trigger input channel from controller, 7 actuator channels and 4 strain gauge channels connected to Rib 3 gauges. The data loggers collected data only when the trigger input from the controller was ‘ON’. All channels of input cards 2 to 6 and one channel of input card 7 in DAQ1 were also connected to Rib 3

gauges. Rest of the channels of input card 7 and all channels of input cards 8 and 9 of DAQ1 were connected to Rib 7 gauges. All channels of input cards 1 and 2, and six channels of input card 3 of DAQ2 were assigned to Rib 7 gauges. Rest of the deck plate and splice plate gauges were connected to channels 7 to 14 of input card 3, all channels of input card 4, and nine channels of input card 5 of DAQ2. The five LVDTs used at section Y-Y were connected to channels 10 to 14 of input card 5 and 1 channel of input card 6. The LVDTs were disconnected prior to start of fatigue test and their channels were freed. For Phase 2B testing, channels 10 to 14 of input card 5 and all channels of input cards 6 to 9 of DAQ 2 were assigned for the strain gauges on SFB1. Fatigue testing of the deck specimen involved one trigger, seven actuator and 116 strain gauge channels in DAQ 1 for both Phase 2A and Phase 2B testing; 65 strain gauge channels in DAQ2 for Phase 2A testing; and 125 strain gauge channels in DAQ2 for Phase 2B testing.

Five volts excitation was provided for all the $^1/_4$ in. (6 mm) uniaxial and rosette gauges while two volts excitation was provided to the 1mm rosette and strip gauges. In view of the relatively low frequency of testing, no real time filtering was used during data collection. For the crawl tests and the static tests, data was sampled at a frequency of 10 Hz and averaged over one second (i.e. 10 samples) before recording. For the fatigue tests, the data was collected at a frequency of 10 Hz without averaging. To reduce noise and spurious signals in collected data, the settling time was set at 100 μsecs and the integration time was set at 670 μsecs. The settling time is the time taken for the input or output channel to settle to its new value while switching between the channels when a change in signal occurs. The integration time is the time over which the input signal is averaged to reduce the noise caused due to random fluctuations in the signal.

Four sets of data were recorded during the fatigue test. In one set, the time history data for all channels were collected at 10 Hz for 5 minutes when triggered by a user. This data was collected during regular inspection of the fatigue test. The second set of data contained maximum and minimum response of the channels over each 15 minutes interval, which was collected programmatically by the logger at every fifteen minutes of an hour. A subset of this data, comprising the response of a few critical gauges, was recorded in the third set for monitoring during each test inspection. The fourth data set consisted of the results of a rainflow counter which counted the number of stress cycles (or loading cycles) and was recorded at every 10 minutes. This data was used as a redundant counter to the mechanical counter attached to actuator #3 and the digital counter in the load controller that were set up to count the number of load cycles during the fatigue tests. In Phase 2A, the strain gauges located on rib soffits at section Y-Y (channels 2154, 1217, 1219, 1220, 1222, 1224) were used for the rainflow counters. In Phase 2B, only the strain gauge channels 1220 and 1224 were retained for rainflow counting as the cycle counts from these gauges matched closely to the other counters.

5.3 Crawl Test

Similar to Phase 1 testing (Alapati 2012), three types of tests were performed on the prototype deck — crawl tests, static tests and fatigue tests. In the crawl tests, a bogie (test truck) representing the AASHTO tandem axle was rolled across the deck at a very slow speed to determine the response of the deck elements under the moving load. The total longitudinal distance traversed by the bogie was 17 ft. 11 in. (5.461 m). From Phase 1 testing, it was observed that the cutout and the internal bulkhead plates for ribs 3 and 7 at SFB2a were most critically stressed when the crawl truck was located centrally in the

transverse direction of the deck specimen (Alapati 2012). This was also confirmed by the FEA conducted by Alapati for different transverse load dispositions. The same transverse load position was also used for the Phase 1 static and fatigue tests. Accordingly, the transverse position of the crawl truck for the Phase 2 tests was aligned with the centerline of Rib 5, which was 11 ft. 5 in. (3.480 m) from the east edge of the prototype deck. The longitudinal load disposition and the protocols for the static and fatigue tests were developed based on the crawl test results.

5.3.1 Test Truck

The test truck represented the typical trailer axles of a tractor-semitrailer having tandem configuration conforming to HL-93 loading of the AASHTO LRFD Bridge Design Specifications. The details of the test truck are provided in the Phase 1 study (Alapati 2012). The truck consisted of two axles spaced 4 ft. (1.219 m) apart in the longitudinal direction. A pair of wheels was attached at the ends of each axle. In the transverse direction, the center-to-center distance between the wheel pairs was 6 ft. (1.829 m). Each wheel was fitted with retreaded truck tires pressurized to about 90 psi (620.5 kPa). According to the AASHTO LRFD Bridge Design Specifications the load from a wheel pair is specified to be distributed uniformly over rectangular contact area 10 in. (254 mm) long and 20 in. (508 mm) wide. To compare with the recommendations of the AASHTO Specifications, the tire contact for each wheel was measured on the laboratory floor before Phase 1 testing. The measurement showed that the actual tire contact dimensions did not match exactly with the specified contact dimensions (Alapati 2012).

5.3.2 Weight of Test Truck

As in Phase 1 testing (Alapati 2012), the truck was loaded with four steel billets placed in a configuration shown in Figure 94. The weights of the truck and each billet as measured by Alapati (2012) are shown in Table 5. The measurements were 26.5 kip (117.9 kN) at one axle and 27.3 kip (121.4 kN) at the other, resulting in a gross weight of 53.8 kip (239.3 kN). This load is equivalent to 2.24 times the rear axle weight of the AASHTO notional fatigue truck (0.75×HS20 or HS15).

5.3.3 Crawl Test Procedure

Similar to the Phase 1 testing (Alapati 2012), a guide truss was laid along the length of the deck concentrically aligned with Rib 5 to guide the test truck in a straight line (Figure 95). The guide truss was provided with brackets on the underside at the north and south ends, which were used to clamp the truss to the deck. The hydraulic winch was fitted to the south end of the guide truss and a pulley was set on the north end. The hydraulic winch and the pulley were used to roll the truck across the deck.

During the crawl test, the east end of the floor beam and the south ends of stingers A and B were displaced downward by 0.10 in. (2.54 mm), 0.07 in. (1.78 mm), and 0.07 in. (1.78 mm), respectively by the under deck actuators. These displacements were provided by the designer of the replacement bridge deck for the Phase 1 study. The designer advised to use the same displacements for the Phase 2 testing.

The test truck was lifted on to the deck using the overhead crane in the laboratory and was aligned with the guide truss at the south end of the deck. The center of the truck was aligned with Rib 5 centerline, 11 ft. 5 in. (3.353 m) from the east end of the deck. At this transverse position, the truck's wheels were located above ribs 3, 4, 6 and 7 as shown

in Figures 94 and 95.

Before initiating the crawl test, the LVDTs were balanced or zeroed to remove the offset caused by the electrical circuits. The strain gauges were also zeroed when the under deck actuators were displaced by $^{1}/_{8}$ in. (3 mm) vertically downward and no significant load was on the deck. When zeroing the channels even the truck was lifted off the deck using a crane. The data collection was started as soon as the strain gauges were zeroed. The truck was then set at the starting position for forward roll on the deck.

The truck was rolled in the forward (i.e. south to north) and then the reverse (i.e. north to south) directions. It was placed towards the south end of the deck specimen for a forward roll. At the start of the roll, the truck's center was at 3 ft. 9 $^{3}/_{4}$ in. (1.162 m) north from the south edge of the deck. The truck was placed such that its rear axles were as close to the edge as possible without having to risk it falling off the deck. The steel billets were lifted one by one and were placed on the truck in the desired configuration as shown in Figure 94 (view looking north). The collection of the data was stopped after the truck completed the reverse roll. The billets and then the truck were taken off the deck, and the under deck actuators were returned to zero position.

The data collection was manually synchronized with start and stop of the truck roll, and the times taken by the truck to complete the forward and reverse rolls were noted using a stop watch. The average speed in forward roll and reverse roll were 0.081 mph (0.130 km/h) and 0.089 mph (0.143 km/h), respectively. The strain gauge data obtained from this test were then converted into stress vs. distance plots.

5.4 Modified Test Setup

The front elevation view (looking north) and the side elevation view of the test

setup are shown in Figures 96 and 97, respectively. The front elevation view was similar to Phase 1 setup. The only changes made in Phase 2 test setup were the number and positions of the over the deck actuators. As mentioned before and discussed by Alapati portions of a floor beam and the stringers A and B were included as part of the test setup to reproduce realistic boundary conditions. The setup of the test specimen was similar to that of Phase 1 and no changes were made to the fixtures used in Phase 1 (see Alapati 2012 for details). The west end of the floor beam was fixed to the reaction wall using a wall fixture. The overhead actuators were supported by an arrangement of three parallel cross beams and one longitudinal beam (Figures 96 and 97). These cross beams were attached to the reaction wall using a wall column at the west end and to a floor column at the east end (Figure 96). The longitudinal beam, identified as the loading beam, was hung from the cross beams to support the overhead actuators.

Seven hydraulic actuators, four above the deck and three under the deck, were used for applying load to the prototype deck and for simulating boundary conditions. The overhead actuators were located 2 ft. $0^{3}/_{4}$ in. (0.629 m) apart based on the crawl test results. The actuators were numbered 3 to 6 starting at the north end because actuators #1 and #2 from Phase 1 test setup were removed and only actuators #3 to #6 were retained as necessary. These over the deck actuators were load controlled and were used for loading the specimen during fatigue and static testing. The under deck actuators at the east end of the floor beam and the south ends of the stringers were displacement controlled. These actuators under stringers A and B, and the floor beam were numbered 7, 8 and 9, respectively (Figure 97).

The primary goal of testing the refurbished orthotropic deck (in Phase 2) was to

determine the fatigue resistance of welded connections at the intermediate subfloor beam (SFB2a) of the deck. So, this was achieved by loading the deck with four overhead actuators (instead of six used in Phase 1), that were loaded sequentially in pairs. In Phase 1, the actuators were separated by a distance similar to the distance between the axles of the notional truck in tandem configuration (Alapati 2012) but in Phase 2 the actuators were separated by a distance similar to half the distance between the axles of the notional truck in tandem configuration. However, the actuators alternating in longitudinal positions were paired for loading. So, the distance between the loading actuators was similar to the distance between the tandem axles of HL-93 notional truck as in Phase 1.

The above deck loading simulated the passage of the AASHTO HL-93 notional truck in tandem configuration. The details of loading and the loading protocol are described in section 5.4. The overhead actuators represented axles of the tandem notional truck as these actuators were attached to a spreader beam and distributed the load to the deck through two loading pads placed 6 ft. (1.829 m) apart in the transverse direction. Each loading pad, 10 in. × 20 in. (254 mm × 508 mm) simulated the contact of a pair of wheels at each end of an axle of a truck since the transverse distance between the loading pads were identical to distance between the wheels as per the AASHTO LRFD Bridge Design Specifications.

The same hydraulic actuators and actuator controller used in Phase 1 were also used in Phase 2 testing. Three support columns were installed close to the propped cantilever ends of the floor beam and the stringers as a safety measure (Figure 98). The floor beam and the stringers rested on the support columns whenever the testing of the prototype deck was stopped and the actuators were not hydraulically live. The height of

support columns was designed 2 in. (51 mm) shorter than the height of the floor beams and stringers above the laboratory floor. This difference in height was compensated by shims. The shims were removed during testing, when the deck was supported by the live under-deck actuators.

5.5 Loading for Static and Fatigue Tests

5.5.1 Loading Arrangement

The loading arrangement for the static and fatigue tests was decided from crawl test results and consistent with the Phase 1 study (Alapati 2012). It was proposed to position the simulated tandem axles (actuators) centrally between SE-A and SE-B, to produce the most critical stresses at the rib-to-deck plate connection and the rib-to-subfloor beam connections. The longitudinal positions and loading sequence of the actuators were selected such as to produce maximum influence at the critical connections of SFB2a during the passage of crawl truck on the modified prototype deck.

In the longitudinal direction, the simulated tandem axles (actuators) were located as shown in Figure 97, with actuator #5 located centrally above SFB2a. Actuator #3 was positioned 4 ft. $1^1/_2$ in. (1.257 m) north of SFB2a, aligned with section Y-Y. Actuators #4 and #6 were positioned at 2 ft. $^3/_4$ in. (0.629 m) to the north and south of SFB2a, respectively. Thus, actuators #4 and #6 were located on the deck splice between the new and old deck segments. Actuators #3 and #4 were paired with actuators #5 and #6, respectively. This allowed the sequential loading by the actuators, simulating the passage of the truck axles.

As mentioned earlier, the load from each actuator was distributed through a

spreader beam into two rectangular load pads (simulating the wheel contacts with the deck plate) 10 in. (254 mm) long and 20 in. (508 mm) wide, and spaced 6 ft. (1.8 m) apart in transverse direction (as per AASHTO LRFD Bridge Design Specifications).

Similar to Phase 1 (Alapati 2012), each actuator was loaded to maximum load range 41.4 kip (184.1 kN). A minimum additional load of 3 kip (13.4 kN) was maintained by all actuators to simulate the dead load effects and to avoid loss of contact between the loading pads and the deck during testing. The vertical displacements specified at the stringer and floor beam ends, at the under the deck actuators, for the static test simulation are provided in Table 6.

5.5.2 Hydraulic Actuators

Seven hydraulic actuators were used for static and fatigue testing of the refurbished prototype deck (Figures 96 and 97). Four overhead actuators (actuators #3 to #6 from Phase 1) were used to load the prototype deck and three under deck actuators were used to simulate the boundary conditions. All these actuators were retained from Phase 1 testing. Refer to Alapati (2012) for further details.

5.5.3 Actuator Controller

All seven actuators and two hydraulic service manifolds (HSM) were simultaneously controlled by a MTS Flextest 100 digital controller. Similar to Phase 1 study, the overhead actuators (actuators #3 to #6) were operated under load control and the under deck actuators (actuators #7 to #9) were operated under displacement control. The loads and displacements of these actuators were monitored. Two hydraulic service manifolds (HSM) were used to regulate the flow between the pump and the actuators. Haversine (for static test) and sine (for fatigue test) wave forms were used as commands

for all actuators. The controller software was also equipped with digital interlocks for safety purposes. Refer to Alapati (2012) for further details.

5.5.4 Safety Features

Throughout the project, safety of life and the deck specimen itself was given a very high priority. For safe operation of the tests, several safety features were implemented. Mechanical limit switches were provided at each actuator and digital limit switches were activated in the controller. Proper protocols were established for conducting the tests and inspecting the deck specimen. Everyone entering the laboratory was required to wear hard hats, closed toe shoes, safety glasses and full pants. In the laboratory, all equipments were handled by skilled lab-technicians. The test specimen was setup and instrumented in the laboratory by experienced lab-technicians under close supervision. Once the entire test setup was completed, specific test protocols were prepared for proper execution of the tests. In order to avoid any accidents during testing and operating the test controllers, all the available safety features were adopted.

Digital limit and error detectors were set to monitor the load and displacement feedbacks and the error between the command and the feedback at each actuator channels. The limit detectors monitored sensor feedback signals and triggered error if the sensor signal exceeded the specified. The error detectors monitored the difference between command and feedback signals and triggers error if the sensor signal exceeds the specified. When tripped, these interlocks would shutdown the HSMs. These limit and error interlocks were set in view of fatigue testing such that the feedback signals were within the limit and the testing wasn't frequently interrupted.

Each actuator was provided with mechanical limit switches. These were adjusted

in place so as to limit the movement of the actuators within the operational range. These mechanical limit switches were set to shutdown the HSMs if the actuators displaced more than $^{3}/_{8}$ in. (10 mm) to prevent any accidental damage to the prototype deck. If in case the actuator tried to go beyond the range, it would activate the limit switch, which would trip fault and shutdown the test. This prevented any damage that could have been caused due to accidental overloading since it constrained the movement of actuators within the limit.

An emergency shutdown switch was also provided next to the controller, which could be used to shutdown the test manually during emergencies. The laboratory was also equipped with safety sensors for the pressure and temperature of hydraulic oil. Any irregularities detected by these sensors triggered instant shutdown of the system.

5.5.5 Loading Protocol

From the crawl test results, it was observed that maximum stresses were experienced by SFB2a when the centerline of the test truck was close to the centerline of SFB2a (see Chapter 6). The loading protocol simulated the passing of a tandem axle across the deck to subject the rib-to-deck plate, rib-to-bulkhead plate and the rib-to-SFB2a welds of the refurbished deck to the highest critical stresses.

The loading protocol is shown in Figure 99. Three load steps were defined in the loading protocol in which the sequential loading by actuators #3 to #6 is shown. In load step 0 (LS 0) of the loading protocol, all overhead actuators applied a uniform load 3 kip (13.4 kN). This minimum load was maintained by all actuators. In load step 1 (LS 1), actuators #3 and #5 were loaded to 44.4 kip (197.5 kN), whereas actuators #4 and #6 were maintained at 3 kip (13.4 kN). In load step 2 (LS 2), actuators #3 and #5 were unloaded to 3 kip (13.4 kN), whereas actuators #4 and #6 were loaded to 44.4 kip (197.5

kN). Subsequently the actuators #4 and #6 were unloaded to 3 kip (13.4 kN) for the static tests, returning to the load state of LS 0.

During Phase 2A of fatigue testing LS 2 was followed by LS 1 and the loading sequence was repeated. Since two actuators applied the maximum load and the other actuators were maintained at minimum load in each loading step, the total maximum load applied on the prototype deck at any time was 94.8 kip (421.7 kN). Further details on Phase 2A and 2B loading protocols is given in sections 5.6.4 and 5.6.5.

In each loading step the bottom actuators applied a displacement corresponding to the global vertical displacement of the bridge at the respective actuator locations (discrete boundaries) under the applied load. These displacements were provided by owner of the bridge for Phase 1 testing (Alapati 2012).

5.6 Test Procedure

5.6.1 Static Test

Static tests were performed on the deck following the loading protocol discussed earlier at a slow (or almost static) loading rate to determine the stresses and change in state of structure. The loading sequence for static test is shown in Figure 100. The load at each actuator was changed between the minimum and the maximum value in 5 seconds and the loads were held at the specified load steps for 10 seconds.

The static tests were performed prior to initiating the fatigue test and intermittently during the fatigue tests. The initial static tests were conducted to determine the base sate of the structure. Intermittent statics tests were performed on a weekly basis and after the laboratory events causing stoppage of testing. Intermittent static tests were

conducted at regular time intervals to determine the change in state of the deck with respect to the initial measured stresses at the strain gauges. The static test results are discussed in detail in Chapter 7.

5.6.2 Fatigue Test

The fatigue testing of the prototype deck was performed by repeated application of the loading sequence discussed in the loading protocol. The fatigue tests followed the same loading sequence as the static tests, but were conducted at as faster loading rate. In Phase 2A, the actuators applied load in 0.5 seconds as shown in Figure 101. Each actuator was cycled between the minimum and maximum loading at 1 Hz frequency. In Phase 2B, the loading protocol shown in Figure 102 was used and the actuators applied load in 1 second as shown in Figure 103. Each actuator was cycled between the minimum and maximum loading at 1.5 Hz frequency. Accordingly, the frequency of each load cycle (comprising the two load steps) was also 1 Hz in both, Phase 2A and Phase 2B.

The test was conducted uninterrupted 24 hours a day and seven days a week, except for interruptions due to routine checks, maintenance or significant events. To verify infinite life fatigue performance (a minimum 75 years service life under site specific loading) the prototype deck was targeted to be tested for 5 million load cycles without any fatigue cracking based on site specific Weigh in Motion (WIM) data.

5.6.3 Inspection Regimen and Event Details

The prototype deck was inspected regularly for fatigue damage using a 10× magnifying glass. The inspection plan is shown in Figure 104, identifying the different areas of the deck that were inspected at different time intervals. The critical deck elements like SFB2a and the rib-to-deck welds around the loaded region were inspected

at every four hour interval between 8:00 AM and 12:00 midnight. At the completion of each million fatigue cycles the guide truss for the load pads was removed, the area on the deck plate in the loaded area was cleaned, and the deck plate underneath the load pads was inspected for any fatigue cracking.

5.6.4 Nonconformance of Loading Protocol

The fatigue testing of the deck was initiated on December 20, 2010, and was completed on April 18, 2011. While analyzing the test results for preparation of the report an anomaly in the loading protocol was discovered for the completed fatigue testing. As is seen from Figures 99 and 101, during the fatigue test the load steps 1 and 2 were synchronized such that the loads in actuators #3 and #5 increased in LS 1 and the loads in actuators #4 and #6 decreased in LS 2 simultaneously. The actuator #5 was located on SFB2a and actuators #4 and #6 were located symmetrically about SFB2a. The actuators were spaced at 4 ft. 1 $^{1}/_{2}$ in. apart. With this loading protocol, SFB2a only partially unloaded as the actuators #3 and #5 unloaded in LS 1, prior to being loaded again by actuators #4 and #6 in LS 2. As a result, SFB2a was loaded to the level of desired maximum stress but did not unload to the level of desired minimum stress, subjecting the critical details in SFB2a to a stress range much less than the target. For example, a typical time history of stress measurements during the fatigue test at strain gauge CH 2065, located at the Rib 3 cutout termination, is shown in Figure 105 along with static test measurements at that gauge. The fatigue test protocol was slightly different than that for the static test. For the static test an initial step (LS 0) existed, where all actuators were loaded to the minimum load of 3 kip. Subsequently the actuators were loaded in load steps 1 and 2 as per the protocol and then completely unloaded. The fatigue tests were

also initiated by loading the actuators to a minimum load of 3 kip. However, subsequently loads were alternately applied in load steps 1 and 2 as per the protocol without any unloading step, which created the anomaly in the loading protocol.

Unfortunately, this anomaly in the loading protocol was not realized during the fatigue test, since the fatigue testing was conducted by primarily monitoring the loads at the actuators and the measurements at the strain gauges on the soffit of the ribs at section Y-Y. The minimum and the maximum loads at each actuator were correctly maintained during the entire fatigue test, which produced the desired maximum stress in the deck. Since the stresses measured in the initial step, when all actuators were loaded to a minimum load of 3 kip, were small, the maximum stress was close to the stress range. As such, attention was given to the maximum stress measurements at the monitored gauges. Moreover, the effect of the incorrect protocol was different at different locations. The response of SFB2a was significantly influenced by both load steps, and therefore the desired minimum stress was not achieved in SFB2a. However, the response of section Y-Y was influenced more significantly by actuator #3, which was located directly at this section. Thus, the minimum stress measured at this section was close to the target value. Since the gauges at the soffit of the ribs at this section were monitored during the fatigue test, the anomaly in the loading protocol could not be discerned. A typical time history of stress measurement at strain gauge CH 2156 on the soffit of Rib 4 at section Y-Y is shown in Figure 106 along with the static test measurements at that gauge.

Due to the anomaly in the loading protocol, the critical details in SFB2a were subjected to stress ranges, which were significantly less than their respective CAFT. It was determined that the fatigue test did not verify the infinite life performance of the

critical connection details in SFB2a, which was the primary objective of the test program. Accordingly, it was decided to conduct the fatigue test with the correct loading protocol. The fatigue test conducted using the incorrect loading protocol was identified as Phase 2A, and the fatigue test conducted using the corrected loading protocol was identified as Phase 2B.

5.6.5 Loading Protocol for Phase 2B

As noted earlier, the primary reason for the anomaly in the loading protocol was the missing unloading step after load steps 1 and 2. The loading protocol was corrected by introducing a load step 3 (LS 3) after LS 2 in which actuators #4 and #6 were unloaded to the minimum load and the actuators #3 and #5 were held at the minimum load. The corrected loading protocol for Phase 2B is shown in Figures 102 and 103. By introducing the unloading step, all the actuators were simultaneously at the minimum loads in LS 3 before beginning another loading cycle. As a result, SFB2a experienced the full desired stress range between the minimum and maximum load conditions in a complete load cycle.

During the Phase 2B fatigue testing each actuator was cycled between the maximum and the minimum load at 1.5 Hz, which resulted in a frequency of 1 Hz for the complete load cycle.

The fatigue test was again conducted on the prototype deck using the Phase 2B loading profile (Figure 103) uninterrupted 24 hours a day, 7 days a week. The test was carried out using all the same test setup and following the same inspection regimen as in Phase 2A. The static tests were also conducted on a weekly basis in order to keep track of the condition of the prototype deck.

6 RESULTS OF CRAWL TEST

As discussed in section 5.3, crawl tests were performed to characterize the response of the deck under different load dispositions in the longitudinal direction, and thereby identify the longitudinal position of the actuators that would produce the most critical stress condition for the fatigue test. The results of the crawl tests are discussed in this section in terms of the response characteristics of the various gauged components.

6.1 General

Total 185 data channels including 63 uni-axial strain gauges, 96 rosette strain gauges, 20 five-element strip gauges and six LVDTs were used for the crawl tests. All measurements were conducted within the nominal elastic range of the material. The strains measured at the uniaxial gauges were converted to stresses by multiplying with the widely accepted modulus of elasticity of 29000 ksi (2×10^5 MPa) for steel. The strains measured at the rosette gauges were transformed to principal stresses and individual stress components based on two-dimensional strain-transformation relationships along with the assumed modulus of elasticity and Poisson's ratio of steel as 29000 ksi and 0.3, respectively.

The crawl test results are presented as plots of strain gauge and/or LVDT measurements against the travel of the test truck. Considering the longitudinal symmetry of the prototype deck with respect to SFB2a, the travel of the test truck is presented on the X-axis or the abscissa as the distance of the truck centerline from SFB2a. The measured quantities (stresses or displacements) are presented on the Y-axis or the ordinate. The start and end points of travel for the test truck were 8 ft. 11 $^1/_2$ in. (2.731 m)

both to the south and north of SFB2a. Thus, the total distance travelled by the test truck in the crawl test was 17 ft. 11 in. (5.461 m). Identifying the centerline of SFB2a as the origin, the distance of the longitudinal centreline of the test truck to the south of SFB2a is presented as negative and the distance to the north of SFB2a is presented as positive. Tensile stresses are presented as positive. Downward displacements are presented as negative. The elevation and part section of the deck, including the location of the sensors and the plotted distance of the crawl truck from SFB2a, are shown on the plots as key. In addition, the longitudinal positions of the crawl truck corresponding to the maximum responses are also presented on the plots.

For comparison with measurements, the FEA results of the global model of the deck analyzed for the crawl test positions are also presented on the crawl test plots. The loadings applied on the FEA for crawl test was equivalent to the weight of the crawl truck (see sections 3.4 and 3.9.1 in FEA chapter for details). Similar to plotting the crawl test measurements, the FEA results are also plotted against the distance from SFB2a to the longitudinal centerline of the load patches for the corresponding load cases. The FEA results are presented for the gauges on the deck plate, at the rib-to-deck weld toe, at the cutout terminations, and on the bulkhead plates abutting the weld toe. The FEA results are not presented for the bulkhead plate gauges whose measurements were deemed inconsistent and unreliable during the testing.

It may be noted that the crawl tests were performed under a gross tandem axle weight of 53.8 kip (239.3 kN), which was equivalent to 2.24 times the rear axle load of the AASHTO notional fatigue truck (section 5.3.2). As discussed earlier in section 5.6.2, for verifying infinite life, fatigue testing of the deck was performed under a gross tandem

axle weight of 82.8 kip (368.3 kN), which was 3.45 times the rear axle weight of the AASHTO notional fatigue truck. Thus, during the crawl tests, the deck was tested at a load of about 65% the fatigue limit state loading, and as such similar prorated responses of the deck were expected.

Some of the instrument channels were common to both Phase 1 and Phase 2 testing. The transverse position of the crawl truck for Phase 1 Position 5 (Alapati 2012) was similar to the transverse position of the crawl truck in Phase 2 testing. Thus, for the common channels the measurements of Phase 2 crawl test could be compared to those of Phase 1crawl test Position 5. These measurements were also included in the relevant plots presented in this section. Although similar, the crawl test Position 5 in Phase 1 was not exactly identical to Phase 2 crawl test position due to which there could be some minor differences in the crawl test responses between Phase 1 and Phase 2.

6.2 Global Response of the Prototype Deck

The global response of the prototype deck is discussed in this section in terms of the measurements at the sensors underside the deck on sections Y-Y, U-U and centerline of SFB2a. Uniaxial strain gauges were installed on the soffit of the ribs at sections Y-Y, oriented in the longitudinal direction (Figures 73, 74 and 77). In addition, at section Y-Y, LVDTs were installed on the soffit of the ribs adjacent to the strain gauges, and on the deck plate in between the ribs (Figure 74). Two gauges oriented in the longitudinal direction were provided on the upper surface of the deck plate in between ribs 3 and 4 at section U-U (the south deck splice) (Figure 76): one on the north side and another on the south side of the splice. Two uniaxial strain gauges were provided on the deck plate and on the soffit of SFB2a at the centerline of rib 5, oriented in the transverse direction

(Figures 78 and 87).

6.2.1 Response of Ribs and Deck Plate

Variations of the vertical displacements and the normal stresses in the longitudinal direction, measured at the instruments between SE-A and SE-B on section Y-Y are plotted in Figures 107 to 109. Also plotted are the FEA results at the gauge locations corresponding to the simulated load positions. It may be noted that the plots show the responses with respect to the distance of the truck centerline from SFB2a, and therefore the peak responses are not aligned exactly with the sensor sections in elevation, but the wheels generally are. In some plots, the wheels were not exactly aligned with the sensor. This is because a constant speed of the truck could not be maintained throughout the crawl test but the plots were prepared assuming an average constant speed. Nevertheless, the wheels were quite close to the sensors when the responses peaked.

As seen from the plots, the response at a sensor changed with the longitudinal position of the test truck. The maximum displacement response occurred when the centerline of the crawl truck was above the sensors (Figures 107 and 108). The vertical displacement of the ribs measured at the LVDT channels 1374, 1376 and 1378 are shown in Figure 107 and the vertical displacement of the deck plate measured at the LVDT channels 1375, 1377 and 1379 are shown in Figure 108. The change in displacements at the gauged section with the travel of the test truck was generally constant, suggesting that the displacements were primarily due to the global deformation of the deck. The rib displacements generally exhibited a single peak with a plateau at the peak displacement. The maximum displacement occurred under the influence of both axles, when the truck was above the instrumented section. Similar displacements were also noted particularly at

the LVDTs under ribs 4 and 5, when the leading axle approached section Y-Y, creating the plateau in the displacement response. The maximum downward vertical displacement was measured at Rib 4 as 0.0621 in. (1.6 mm). Ribs 3 and 5 exhibited a more uniform variation in the measured displacement with the passage of the truck. The displacement of Rib 3, the rib closest to the stringer extension, was the least. When the truck was on the south side of SFB2a, the displacement at Rib 5 was larger than Rib 4 and the relative displacement between ribs 5 and 4 was larger than the relative displacement between ribs 4 and 3. Initially, the measured displacement at all ribs exhibited similar rate of change with the truck travel. The change in displacement at Rib 4 and the relative displacement between ribs 4 and 3, however, increased as the truck approached SFB2a. The Rib 4 displacement surpassed Rib 5 as the centerline of the truck crossed onto the north side of SFB2a, with the leading axle nearing the instrumented section Y-Y. Finally, as the leading axle of the truck was near SFB1, the displacement of Rib 5 again exceeded the displacement of Rib 4.

The displacement profiles of the deck plate (Figure 108) exhibited multiple peaks with valleys in between. Again, the peak response occurred under the resultant influence of both axles when the center of the crawl truck (for a roll from south to north, or forward roll) crossed the transverse section Y-Y and the local peak responses occurred when the axles were about the section. This displacement response characteristic was noted at all LVDTs irrespective of whether they were located on the wheel paths or not, and the peak responses of the deck plate were more discernible compared to the ribs. The maximum downward vertical displacement of the deck plate was measured as 0.0632 in (1.6 mm) between ribs 5 and 6 (CH 1379). The variation of the displacement measured at the CH

1377, located symmetrically with CH 1379 between ribs 4 and 5, was almost identical to channel 1379 but 0.004 in. (0.1 mm) lesser in amplitude. Although the deck was symmetrically loaded and the LVDTs were symmetrically located, the boundary condition of the deck was not symmetric. The floor beam supporting the deck was fixed at the west wall (towards Rib 3) and was supported by an actuator at the east (towards Rib 7), which provided a downward vertical displacement of 0.10 in (2.54 mm) during the crawl test (see section 5.3.3). Due to these boundary conditions, the floor beam acted like a propped cantilever with a settlement of the prop, resulting in more (rigid body) deflection of the deck towards the east. This deflection pattern is evident in the transverse deformed configuration of the deck shown in Figure 32, and is also consistent with the measurements. The displacement of deck plate around Rib 3, the rib closest to the stringer extension, was generally the least except when the truck was around section Y-Y. Initially, the measured displacement at all LVDTS under the deck plate exhibited similar rate of change with the truck roll. The change in displacement at CH 1375 under the wheel path increased as the leading axle approached SFB2a. The displacement at this channel surpassed the displacement at CH 1377 when the centerline of the truck crossed the instrumented section Y-Y. Finally, as the leading axle of the truck approached SFB1, the displacement at CH 1377 surpassed the displacement at CH 1375.

The vertical displacements of the ribs and the deck plate, obtained from the FEA results at the LVDT locations, are also shown on the plots. The displacement profiles were consistent with the transverse deformation of the deck obtained from FEA (shown in Figures 32 and 33), As is evident, the change in the rib and the deck plate displacements at LVDT channels 1375 and 1376 adjacent to the east wheel path was due

to the transverse shear and flexural deformation of the deck, which was localized around the wheel loads when the truck was at the mid span between the subfloor beams.

Figure 109 shows the variation of the longitudinal stresses in the ribs measured at the strain gauge channels 2155 to 2159 on the rib soffit. All strain gauges located on the ribs under the wheel paths (ribs 3, 4, 6 and 7) exhibited similar variation. Negligible compressive stresses were noted at these gauges, when the crawl truck was on the south side of SFB2a. The stresses gradually increased and became tensile as the leading axle approached SFB2a and peaked when the truck crossed over to the north side of the subfloor beam. Two peaks were noted in the longitudinal stress profiles with the peak response occurring under the leading or the trailing axle above the transverse section Y-Y. The distance between the peaks was almost equal to the spacing of the axles on the test truck, confirming that each axle of the tandem resulted in one peak of these typical "camel-back" responses. The plateau or valley between the peak responses was caused by the interaction of influences of the tandem axles, as the axle pair crossed the sensor. The maximum longitudinal stress was 3.4 ksi (23 MPa) tensile measured at CH 1217 in Rib 4, which was located under the west wheel path.

The gauge on the soffit of Rib 5 (CH 2157) showed a different response and the least stress among all. Since this rib was located away from the wheel paths, its deformation was controlled by transverse shear and flexural deformation of the deck due to the passage of the crawl truck. Initially this gauge also showed compressive stress when the truck was on the south side of SFB2a. However, the stress became tensile earlier than the other rib gauges, when the truck was still on the south side. The stress response exhibited only one peak when the leading axle and the centerline of the truck

were almost equidistant from the gauged section. These crawl test results verify the FEA results which demonstrated that the response of the rib was similar to that of a continuous beam subjected to concentrated loads. Also, the ribs that are away from the stringer extension but under the direct wheel loadings experienced higher stresses.

The vertical displacement of the ribs measured at the LVDT channels 1374, 1376 and 1378 and the vertical displacements of the deck plate measured at the LVDT channels 1375, 1377 and 1379 are plotted in Figures 110 and 111, respectively for crawl test Position 5 of the Phase 1 testing (Alapati 2012). These LVDT channels were located at section Z-Z (the mid-span section between SFB1 and SFB2a) in the Phase 1 prototype deck (Alapati 2012). The comparison of Phase 1 and Phase 2 maximum displacements for the mid-span section between SFB1 and SFB2a is presented in Figure 112. Since the LVDT CH 1377 located under the deck plate between ribs 4 and 5 malfunctioned during Phase 1 crawl tests, the measurements from this channel are not presented in Figures 111 and 112. In Phase 1 position 5, the maximum downward vertical displacement of the ribs and the deck plate were measured as 0.113 in. (2.9 mm) and 0.126 in. (3.2 mm) at channels 1376 and 1379, respectively. As shown in Figures 107, 108, 110, 111 and 112, the influence of the crawl truck is similar in both Phase 1 and Phase 2, however, the displacement is substantially reduced in Phase 2.

Figure 113 shows the longitudinal stresses in the ribs of the Phase 1 prototype deck, measured during the crawl test Position 5 at the strain gauge channels 1222, 1217, 1219, 1220 and 1224. These channels were also located at section Z-Z, on the soffit of ribs 3 to 7 (Alapati 2012). In Phase 1 Position 5, the maximum longitudinal stress in the ribs was 5.2 ksi (tensile) in Rib 6 (CH 1220), when the center of the truck was over

section Z-Z. The comparison of Phase 1 and Phase 2 maximum stresses experienced by rib soffit gauges at the mid-span section between SFB1 and SFB2a is presented in Figure 114. As it can be observed in the figure, the stresses at the ribs were comparatively lower in Phase 2. Especially, for the ribs directly under the wheels (ribs 4 and 6), the stresses were considerably reduced.

Uniaxial strain gauges channels 2151 and 2152 were installed on the upper surface of the deck plate at section U-U abutting the transverse deck splice, which was located 2 ft. $0^{3}/_{4}$ in. (0.629 m) south of SFB2a. During the crawl test, these gauges fell under the path of the west wheel pairs in the space between them. The stresses experienced by the gauges during the crawl test are plotted in Figure 115. It is evident that the maximum longitudinal stresses occurred when the axle of the truck was directly above the splice. The gauges measured the maximum stress under the trailing axle. The measured stresses were compressive when at least part of the truck was on the south side of SFB2a. Small tensile stresses were measured at these gauges when the trailing axle of the truck crossed SFB2a to the north side. The measurements showed that the stresses at the splices were due to the general global flexural deformation of the deck under the truck, which was further magnified by the local flexural deformation of the deck plate under the wheels. The maximum longitudinal stresses measured at channels 2151 and 2152 were respectively 1.3 ksi (9 MPa) compressive and 1.8 ksi (12 MPa) compressive. The FEA results, also plotted in the figure, were close to the experimental values when the axles weren't directly above the gauges. However, when the axles were directly above the gauges, the experimental values showed higher stresses compared to FEA results. The sharp variation of stresses under direct influence of the wheel loads may have been

caused by extremely localized stresses under load pads and the presence of transverse deck splice. The welded deck splice wasn't modeled in the FE model but was present in the actual deck specimen acting as a stress raiser. As it was verified by Alapati (2012) that large variation can be observed between test and FEA data for primary deck members, the stresses measured by the deck plate gauges may have been higher because the wheel of the test truck had shifted from the intended position. The truck could shift transversely due to the gap provided between the guide truss on the deck and the guide tubes on the test truck. The gap in between the guide truss and the guide tube was 2 in. (51 mm). Since the stresses on the deck plate are highly localized under the wheel loadings (which will also be verified from results in section 6.3), even a small shift in loading may cause large variation in local stresses on the deck plate.

As it can be seen in the plot, both the gauges (channels 2151 and 2152) experienced similar stresses throughout the roll except when the axles were directly above them. CH 2152 experienced maximum tensile stress soon after it experienced its maximum compressive stress under the trailing axles. CH 2151 on the other hand, experienced two compressive stress peaks under the influence of rear axles. When the truck was rolled along the deck, due to the presence of weld, some extra effort was required to roll the truck above the splice. The bump faced by the tires while getting across the weld and landing on the gauge could have caused the noise and spike in these gauge measurements.

6.2.2 Response of Intermediate Subfloor Beam (SFB2a)

Uniaxial strain gauges identified as channels 2153 and 2154 were provided on the deck plate at SFB2a and on soffit of SFB2a, respectively (Figures 78 and 87). These

gauges were located at the mid span of SFB2a in between SE-A and SE-B, and were oriented in the transverse direction. Plots showing the variation of stresses at these gauges, as the test truck rolled along the deck, are shown in Figure 116. A small compressive stress of almost constant magnitude (about 0.2 ksi) was recorded at the gauge on the deck plate (CH 2153), whereas the strain gauge at the soffit of SFB2a (CH 2154) exhibited a single modal response as the truck rolled along the deck, with the maximum response of 1.8 ksi (12 MPa) occurring when the truck centerline was around SFB2a. The measured stresses were primarily flexural stresses in SFB2a.

CH 2154 was installed at the same location where CH 1216 was located in Phase 1 prototype deck. Figure 117 shows the stresses measured by CH 1216 in Phase 1 crawl test in transverse Position 5 (Alapati 2012). The response of SFB2a was similar in both Phase 1 and 2, however, the stresses measured in Phase 2 was smaller compared to Phase 1. The maximum stress measured by CH 1216 in Phase 1 was 2.7 ksi (19 MPa) compared to maximum stress measured by CH 2154 in Phase 2.

6.3 Response of Rib-to-Deck Plate Connections

Responses of the rib-to-deck plate connections were measured in Rib 7 at section Y-Y, where uniaxial strain gauges were installed in back-to-back configuration on the deck plate and on the rib walls (Figures 73 and 75). These gauges were retained from the Phase 1 testing. On the deck plate, strain gauges were installed on the top and bottom faces, oriented in the transverse direction, normal to the rib-to-deck weld. On the rib walls, strain gauges were provided on both faces, oriented along the rib, normal to the rib-to-deck weld. The gauges on the internal surfaces of the rib walls were malfunctioning (section 5.1.4) since the installation of the refurbished deck, hence, are

not included in the discussion.

Figure 118 shows the normal stresses measured by the gauge at the rib-to-deck weld toe (CH 1371) along with the measurements by the gauges on the deck plate (channels 1362 and 1363) on the west of Rib 7. Channels 1371 and 1363 were back to back gauges while CH 1362 was installed transversely next to CH 1363 as shown in the figure. Figure 119 shows normal stresses measured at the gauge on the outer west face of rib wall (CH 1370) at the same location (section Y-Y). The stresses were insignificant until the test truck crossed SFB2a and approached the gauged section. Bimodal responses, manifesting the effects of each axle of the tandem, were noted when the axles were close to the gauged transverse section. This indicated that the transverse stresses and the deck response were highly localized under the wheels. The stresses measured by the gauges on the top of deck plate were in tension while the stresses measured on the deck soffit and the external rib walls were in compression. The stresses at the top and bottom gauges (channels 1363 and 1371) were of almost equal magnitude but opposite sign, indicating primarily local flexural deformation of the deck plate under the wheel loads, where the deck plate bent over the rib wall causing tensile and compressive stresses at the top and bottom of deck plate respectively.

At the west rib to deck weld toe of rib 7, the stresses under the rear axle was lower than the stresses under the front axle, although the wheel loads were of almost equal magnitude. This may have been compounded by the complex interaction of the global and local response of the deck. As the truck moved longitudinally towards the center of the span (between SFB1 and SFB2a), the global transverse deformation of the deck increased, which influenced the local bending of the west rib wall under the wheel

load (Figure 119). Similar phenomenon was also observed in Phase 1. Studies were performed by Alapati (2012) in order to understand this behavior. The dimension of the tire patches recommended by AASHTO and the measured tire patches were different and during the crawl test, a gap 2 in. (51 mm) between the guide truss and the guide tube was provided for the smooth rolling of the truck along the guided path. The truck could shift transversely due to the gap between the guide truss on the deck and the guide tubes on the test truck. From the study, it was verified that the lesser response of the rib-to-deck connection under the rear axle occurred due to non-uniform tire contact and local transverse shift in wheel positions since the response of primary members of the deck were highly sensitive to the transverse position of the wheel loads.

Figure 120 shows the transverse stresses measured at back-to-back gauges on the deck plate along with deck gauge adjacent to it on the east of rib 7 (channels 1360, 1361 and 1369) at section Y-Y. Figure 121 shows normal stresses measured at the gauge (CH 1368) on the outer east face of rib wall at the same location. These gauges were on the east side of Rib 7 which did not experience direct wheel loads as shown in the figures. Compared to the similar gauge channels on the west side of rib 7, the channels on the east side experienced smaller maximum stresses and primarily the global effect of the test truck. The deck plate region away from the direct tire contact responded to the center of the truck instead of individual truck axles and the peak stresses were noted when the center of the test truck was close to section Y-Y. When the truck was in the span north of SFB2a, gradually varying compressive and tensile stresses developed at the top and the bottom gauges, respectively. For the gauge on the external rib wall (CH 1368), a hump and a plateau of peak responses was caused by the interaction of influences of the tandem

axles, as the axle pair crossed section Y-Y. It experienced peak stress when the leading axle was at section Y-Y and saw rapid decrease in stress as soon as the trailing axle crossed the section.

In Phase 1, there weren't any gauges installed at the rib-to-deck plate connection in section Z-Z (mid-distance between SFB1 and SFB2a). However, channels 1371 and 1370 in Phase 2 can be compared to channels 1367 and 1366 in Phase 1 because both sets of gauges were located 4ft. $1^1/_2$ in. (1.257 m) north of SFB2a. Figures 122 and 123 also show bimodal responses for channels 1366 and 1367 in Phase 1 that was similar to Phase 2. As seen in Figures 118 and 122, the stresses measured by gauges abutting the weld toe on the deck plate are significantly lower in Phase 2 compared to Phase 1. For gauges abutting the weld toe on the rib walls the maximum stresses were lower in Phase 2 compared to Phase 1, however, the stress measured by these gauges under the influence of front axles was higher in Phase 2 compared to Phase 1 (Figures 119 and 123). In Phase 1 crawl test plots (Figure 122), it was observed that the rib-to-deck plate gauge (CH 1367) observed small tensile stress when the axles were not at the gauged section. This causes stress reversal during the passage of the truck and may play a vital role in fatigue cracking from the weld toe. However in Phase 2, no such tensile stress was observed (Figure 118). CH 1371 measured compressive stress throughout the roll and the stress was almost zero when the axles were not at the gauged section.

6.4 Response of Intermediate Subfloor Beam (SFB2a) at Rib Cutouts

The response of the intermediate subfloor beam SFB2a under the rolling tandem axle is presented in terms of the stresses measured at the gauges on the SFB2a web around the cutouts of ribs 3 and 7. The connections of SFB2a to ribs 3 and 7, adjacent to

the SEs, were the most critical due to which they were elaborately gauged as discussed in instrumentation section 5.1.5. The layout of strain gauges is shown in Figures 79 to 83.

Ninety degree rosettes were installed to the east and the west sides of ribs 3 and 7 cutouts of SFB2a in back-to-back configuration. These rosettes were installed abutting the rib-to-SFB2a weld toe and as close as possible to the cutout edge, to capture the high stress concentrations at the cutout regions. It was planned to orient one of the rosette arms parallel to the rib-to-SFB2a weld, and another arm in a direction normal to it. The objective was to obtain stresses normal to the weld toe, and the principal stresses and their directions from the rosette measurements.

Stacked rosette gauges of 1 mm gauge length were installed back-to-back on Rib 7 west and Rib 3 east cutout terminations. Inadvertently, these rosettes were installed in an arbitrary orientation. While this arbitrary orientation of rosettes did not have any impact on the principal stresses and their directions (due to invariance), the stresses normal to the weld toe could not be directly obtained from the measurements. The stresses normal to the weld toe were computed from the principal stresses by transformation. Rosette gauges of $^{1}/_{4}$ in. (6 mm) length were installed to the east of Rib 7 and to the west of Rib 3. These gauges were installed as planned.

The variations of principal stresses presented in Figures 124 to 127 show the complex response of SFB2a at the rib connections, as the test truck moved across the deck. The FEA results are also shown in the figures. Although, the FEA results do not exactly match the experimental results, they show similar trends and changes in stresses on both sides of the SFB2a web. Hence, the FEA results also justify the observed behavior of SFB2a. The principal stresses recorded by the back to back rosettes are

produced on the same plots to visually assess the in-plane and out-of-plane stress components. These plots show that for a single passage of the test truck, the rib-to-subfloor beam welded connection at the SFB2a cutout experienced only one stress cycle due to the resultant effect of the tandem axles. Since the SFBs were made integral with the SEs, these stress distributions indicated that SFB2a was subjected to shear forces under loading which resulted in diagonal tension and compression stress fields around ribs 3 and 7. In view of relatively small difference in the magnitude of stresses on the north and the south faces, it is evident that the stresses in the web of SFB2a were primarily in-plane, and the component of out-of-plane stress was insignificant.

The principal stresses measured by 1 mm rosette gauges to the east of rib 3 and west of Rib 7 cutouts are shown in Figures 124 and 125, respectively. The maximum and minimum principal stresses are presented in Table 7. The peak principal stress among these gauges was 9.81 ksi (68 MPa) observed on Rib 3 north face cutout termination. From the figures, it is observed that the stresses were mostly in-plane, when the truck was on the span north of SFB2a. Some out-of-plane bending of the web was noted as the truck rolled along the south of SFB2a and crossed on to the north span. The stresses measured by these gauges were tensile and peaked when the center of the truck or the trailing axles of the truck was in the vicinity of SFB2a. Tensile stresses on the north face were higher than the stresses on the south face, indicating some northward bending of the SFB2a web. This out-of-plane bending stress was larger at the rib-to-SFB2a connection to the east of Rib 3.

The principal stresses for compression side rosette gauges in SFB2a i.e. on the west of Ribs 3 and east of Rib 7 cutout terminations are shown in Figures 126 and 127.

The maximum and minimum principal stresses for these gauges are recorded in

Table **8**. The peak principal stress among these gauges was 6.21 ksi (43 MPa) observed on Rib 3 south face cutout termination. The SFB2a web experienced more out-of-plane bending when the test truck was on the south span. To the west of Rib 3, this bending reversed while to the east of Rib 7, the bending minimized as the truck moved onto the north span. The south face of the web experienced higher compressive stress than the north face indicating northward bending of the web. These responses indicate slight twisting of the SFB2a web at the SE connections.

The maximum and minimum principal stresses at the east side of Rib 3 and west side of Rib 7, 5 in. (127 mm) and 6 in. (152 mm) below the deck plate along the rib-to-SFB2a weld toe, measured by back-to-back $^{1}/_{4}$ in. (6 mm) rosette gauges are provided in Table 9. The stresses measured at these gauges were lower than the stresses measured by the 1mm gauges at the cutout terminations and the stresses decreased as the distance from the cutouts increased.

Adjacent to 1mm stacked rosettes, at Rib 3 east and Rib 7 west cutout terminations, 1mm strip gauges were installed on both north and south faces in order to observe the stress gradient at the cutout close to subfloor beam-to-rib weld toe. Among the group of 5 linearly arranged 1mm gauges present in the strip gauges, the stress plots for the north and south face gauges closest to the SFB2a-to-rib weld toe are shown in Figures 128 and 129 for ribs 3 and 7 locations, respectively. The stress profiles for all the remaining four gauges in the strip gauge set followed the similar trend to the ones shown in the figures. The maximum stresses measured for these gauges are recorded in Table 10. From these tables, it is observed that maximum stresses tend to decrease as the distance

from the SFB2a-to-rib weld toe increases.

On SFB2a cutout edges, at Rib 3 east and Rib 7 west cutout terminations, two strip gauges totaling ten 1mm gauges were installed at the mid thickness of the ground smooth cutout surfaces. These were installed in order to observe the stress gradient along the cutout edges. Figures 130 and 131 show the crawl test plots for cutout gauge channels 2065 to 2074 at Rib 3 east and 2140 to 2149 at Rib 7 west cutout edges, respectively. All these gauges experienced a similar stress profile. The maximum and minimum stresses for these cutout edge gauges from the crawl test are recorded in Table 11. On the cutout edge, maximum stress of 11.14 ksi (77 MPa) and 10.74 ksi (74 MPa) were observed at channels 2069 and 2143 at rib 3 and rib 7 locations, respectively and the stress profiles for these individual channels are plotted in Figures 132 and 133. According to the plots, for a single passage of the crawl truck the cutout edges at ribs 3 and 7 cutout terminations experienced only one stress cycle due to the resultant effect of the tandem axles and the maxima of the stresses occurred when the crawl truck was over SFB2a. The first gauge of these strip gauges were located right at the weld line referenced to the SFB2a-to-rib weld toe on the cutout edge. So, it is clear that along the cutouts, the maximum stress do not occur right at the SFB2a-to-rib weld toe (or cutout termination). The maximum stress occurs a small distance of about 0.4 in (10 mm) to 0.8 in (20 mm) away from the cutout termination, and then the stresses start to decrease along the surface of the cutout face.

6.5 Response of Bulkhead Plate at SFB2a

Uniaxial and rosette strain gauges were installed on the bulkhead plates of ribs 3 and 7 at SFB2a as shown in Figures 79, 80 and 82. These gauges were installed back-to-back on both north and south face of bulkhead plates. The uniaxial gauges adjacent to the

cutout termination were oriented normal to the rib-to-bulkhead plate weld toe, while the gauges adjacent to the top edge were oriented diagonal to bulkhead plate. Pairs of rosette gauges were also installed on the bulkhead plates: one close to the cutout and another close to the center of bulkhead plate in Ribs 3 and 7.

The uniaxial gauges were placed adjacent to the cutout termination and to the opposite top edge of the bulkhead plate (see Figure 79). These gauges were positioned in a diagonal that was generally aligned with the tension stress field in SFB2a at the rib cutout, as was discussed earlier in section 5.1.6. The strain gauges were installed to record the high tensile stresses on the bulkhead plates at the rib-to-bulkhead plate weld toes having high stress concentrations. The stresses measured by the uniaxial strain gauges on the bulkhead plates of the ribs are shown in Figures 134 to 140, as the crawl truck rolled across the deck. FEA results are also shown for the comparisons. The FEA results for the gauges were found to match with the experimental crawl test results. The maximum stresses measured by these gauges are tabulated in Table 12. Channels 2077 and 2099 in rib 7 were malfunctioning at the time of crawl test because these gauges were already damaged at the time of installing the deck specimen. The maxima of tensile stress recorded on the bulkhead plate at SFB2a, was 4.95 ksi (34 MPa) for channel 2087

Pairs of rosette gauges were installed on the bulkhead plates (back-to-back): one close to the cutout termination and another close to the center of bulkhead plate in Ribs 3 and 7 (section 5.1.6 and Figure 79). The stresses measured by the rosette strain gauges on the bulkhead plates of the ribs are shown in Figures 141 to 144. The maxima of the principal stresses measured by the rosette gauges are tabulated in Table 13. The principal stresses for the rosette gauges at the bulkhead plates were small and these gauges were

also found to be inconsistent over a longer period of time during the fatigue test. So, comparisons of these gauge results with FEA are not provided and only the qualitative results are discussed. At the rosette strain gauge located close to the cutout termination, the gauge along the diagonal of the bulkhead plate measured the maximum tensile stress. At the rosette gauge located centrally on the bulkhead plate, the diagonal gauge directed from the gauges located adjacent to the cutout termination to the opposite top corner, experienced maximum tensile stress while the gauge perpendicular to it, experienced maximum compressive stress. These results indicated presence of diagonal tension and compression stress fields in the bulkhead plate extending from the cutout terminations to the opposite top corners. Apparently, the bulkhead plates provided path for tension and compression stresses in the web of SFB2a adjacent to the rib cutouts. These complimentary stress fields were caused by the shear transfer of loads from the deck plate to the SEs through the SFB.

The stress profiles recorded by the strain gauge had one major stress cycle per truck passage measured due to the resultant effect of the tandem axles. At the gauges adjacent to the cutout termination and the rosette gauges, the plateau or valley at the peak responses was caused by the interaction of influences of the tandem axles, as the axle pair crossed SFB2a. So, the maxima of stresses at these gauges occurred when the truck centerlines were away from SFB2a. At the gauges adjacent to the top edge of bulkhead plates, however, the magnitude of stresses increased as the truck approached SFB2a and decreased as the truck moved away. The maxima occurred when the centerline of the truck coincided with SFB2a.

The unevenness in stress distribution in ribs 3 and 7 may have been caused because the transverse placement of crawl truck was not perfectly symmetric with ribs 3 and 7. The gauges were supposed to be placed back-to-back at the bulkhead location. However, there is a possibility that the gauges weren't perfectly back-to-back, which may cause minor systematic error in the measured data. However, in the stress plots, both ribs 3 and 7 bulkhead plate show some bending.

7 RESULTS OF STATIC TEST

Results of static tests and response of the Phase 2 prototype deck under fatigue limit state loading at a static loading rate are presented in this chapter. Static tests were performed initially at the onset of the fatigue testing, and intermittently at about every million cycles or following any significant event to evaluate any change in the structure state. The global response of the deck is presented in terms of the response of ribs, deck and intermediate subfloor beam under the loading steps. Then the responses of important elements critical to fatigue loading are presented. These are the rib-to-deck plate connections, the intermediate and end subfloor beams around the cutouts and the bulkhead plates.

7.1 Introduction

At the onset of Phase 2A testing, static tests were performed on November 1, 2010, before initiating fatigue testing of the deck specimen. Four trials were conducted for shakedown and to determine repeatability of the measurements. A static test was also performed at the onset of Phase 2B fatigue testing on September 28, 2011. No significant changes were noted in these measurements, so the results of only the final trial of static test for Phase 2A and Phase 2B are presented here. These static tests were conducted with a minimum load of 3 kip (13.4 kN) at each of the four overhead actuators to simulate the effect of permanent load.

Throughout both Phase 2A and Phase 2B fatigue testing, intermittent static tests were performed at about every million load cycles, or following any significant event. In

addition, during Phase 2B, intermittent static tests were performed every week for a closer monitoring of any changes in the state of the structure.

For the initial static test of November 1, 2010 a total of 194 data channels including seven actuators, 85 uniaxial strain gauges, 96 rosette strain gauges, and 6 LVDTs were used. In addition, outputs from the seven actuator load cells were recorded on seven data channels. Prior to initiating the fatigue test, the LVDTs were disconnected from the data logger. All strain gauges from at SFB1 were retained from Phase 1 testing, but they were not connected to the data logger and therefore were not monitored during the Phase 2A testing. In Phase 2B, 60 out of 64 strain gauge channels were reconnected to the data logger for monitoring. Details of instrumentation at SFB1 are provided in 5.1.8 and 5.2.

All measurements were conducted within the nominal elastic range of the material. A modulus of elasticity of 29,000 ksi (2×10^5 MPa) and a Poisson's ratio of 0.3 were assumed for converting the measured strains to stresses.

During Phase 2A fatigue testing, inconsistent data were noted at the strain gauge channels 2061 to 2074 after about 390,000 cycles (on January 13, 2011). These gauges were located on SFB2a at the cutout for Rib 3 and were connected to the AD card slot #6 of DAQ 1. Upon scrutiny it was determined that the AD card had malfunctioned. The data card was replaced and a static test was performed on January 17, 2011 which revealed that the initial static test measurements at these data channels were also affected. Accordingly, the initial static test measurements conducted on November 1, 2010 for these channels were replaced with the measurements from the static test performed on January 17, 2011. Comparing with the measurements at other channels it was concluded

that the state of the structure essentially remained unchanged over the 390,000 fatigue stress cycles.

7.2 Global Response of the Prototype Deck

The global response of the prototype deck is discussed in this section in terms of the measurements at the sensors underside the deck on section Y-Y and at SFB2a. Uniaxial strain gauges were installed on the soffit of the ribs at section Y-Y, oriented in the longitudinal direction (Figure 77). In addition, LVDTs were installed at section Y-Y on the soffit of the ribs adjacent to the strain gauges, and on the deck plate in between the ribs. A uniaxial strain gauge oriented in the transverse direction, was installed on the deck plate and on the soffit of SFB2a as shown in Figure 87.

The static test results are presented as plots of strain gauge and/or LVDT measurements along section Y-Y, against the distance measured from the west end of the deck. The measured quantities (stresses or displacements) are presented on the ordinate or the Y-axis, and the distance from the west end along the section is presented on the abscissa or the X-axis. In order to compare these measurements with the FEA results, the FEA values at the sensor locations are presented alongside the measured values. Also shown on the plots are: the plan of the deck with the section identified; the plot origin; the increasing direction of the abscissa; and the transverse section (section Y-Y) of the deck. The transverse disposition of simulated wheel loads or the load pads are indicated on the transverse section of the deck. The downward displacements measured at the LVDTs are presented as negative, and the tensile stresses measured at the strain gauges are presented as positive, and vice versa.

7.2.1 Response of Ribs and Deck Plate

The vertical displacements measured by the LVDTs at section Y-Y during the static test are plotted in Figure 145. The LVDTs were installed in between the stringer extensions on the soffit of ribs 3, 4, and 5, and on the soffit of the deck plate in between ribs 3 and 4, ribs 4 and 5 and ribs 5 and 6. The section was located under actuator #3 and recorded the maximum displacement in LS 1, when the actuators #3 and #4 were loaded to the maximum. These vertical displacements are compared with the FEA results in Figure 146. The FEA results and the measurements exhibited similar distribution across the section, however, FEA results were lesser than the measurements. It is expected since FEA tends to overestimate the stiffness matrix and hence underestimate the displacement solutions.

Although the loading was symmetric with respect to Rib 5 (the central rib between SE-A and SE-B), the displacements were not symmetric due to asymmetric boundary conditions and the presence of box floor beam as was discussed in previous chapter. The displacement pattern suggested reverse bending of the deck plate, which was seen from the FEA results (Figures 32 and 33) associated with the distortion of the rib sections under load at the transverse section. The west wheel load was spread across parts of ribs 3 and 4 and the deck plate in between the ribs, which caused the relatively larger local displacements of the deck plate between ribs 3 and 4. The displacement of Rib 3, however, was less due to its proximity to SE-A. The larger displacements of Rib 5 and the deck plate between ribs 5 and 6 were due to the global transverse deformation of the deck under the wheel loads. In fact, the maximum displacement over the transverse section was recorded at the soffit of the deck plate between ribs 5 and 6. The decrease in

vertical displacement of the deck plate between ribs 4 and 5 (CH 1377) indicated hogging flexural deformation of the deck in the transverse direction in between ribs 4 and 6.

The transverse distribution of the longitudinal stresses measured by the strain gauges on the soffit of ribs at section Y-Y is plotted in Figure 147. Tensile stresses developed at the bottom of the ribs under the simulated wheel loads. The maximum longitudinal stress was recorded in LS-1 when actuators #3 and #5 were loaded to the maximum. In LS-2, the stresses were significantly smaller suggesting the ribs primarily experienced local deformation under the wheel loads. The loads were positioned in the transverse direction such that each load patch spanned parts of two adjacent ribs (ribs 3 and 4, and ribs 6 and 7) and the deck plate in between. Since the loading and the deck section was generally symmetric, particularly in the portion between SE-A and SE-B, the transverse distribution of the longitudinal stress was also somewhat symmetric to Rib 5. Rib 4 experienced higher longitudinal stress compared to Rib 3 near the west wheel load. Similarly, near the east wheel load Rib 6 experienced higher longitudinal stresses compared to Rib 7. This indicated that ribs 4 and 6 experienced larger longitudinal deformation compared to ribs 3 and 7 respectively. This can be explained in view of the significantly larger longitudinal stiffness of the stringer extensions and the stringers that constrained longitudinal deformation of the ribs adjacent to them. Away from the loads, Rib 5 experienced less longitudinal deformation and hence less longitudinal stress. The load deformation characteristic of the orthotropic deck under wheel loads was also demonstrated by the FEA as shown in Figures 32 and 33, and by the vertical displacements discussed earlier.

The maximum longitudinal stresses measured in LS 1 are compared with the FEA results in Figure 148. The FEA results exhibited similar distribution pattern as the measurements, although they were found to be slightly higher than the measured stresses, especially at ribs 4, 6 and 7. The stress under Rib 5 was small hence, the difference was also small.

As shown in Figures 145 and 147, the deck plate at section Y-Y experienced the maximum displacement and the largest longitudinal stresses in LS-1 of the static test. In Phase 1, LS-3 caused the maximum displacement and the longitudinal stresses (Alapati 2012) at section Z-Z, the mid-section between SFB1 and SFB2a, similar to section Y-Y in Phase 2. In both cases i.e. LS-3 in Phase 1 and LS-1 in Phase 2, one of the loading actuators was right above SFB2a and another 4ft. $1^1/_2$ in. (1.257 m) north of SFB2a. This loading condition was more severe than the condition in which the loads were applied on SFB1 and 4ft. $1^1/_2$ in. (1.257 m) south of SFB1 (LS-2 in Phase 1) because of higher stiffness caused by the presence of the floor beam. Figure 149 shows the comparison of the maximum measured displacements between Phase 1 and Phase 2. While the transverse distribution of displacements showed similar trends, the maximum displacements in Phase 2 were reduced by about 15% to 22% in Phase 2. Comparison of the maximum measured longitudinal stresses at the rib soffit between Phase 1 and Phase 2 (Figure 150) showed that the stresses were increased by about 22% to 41% in Phase 2 except at Rib 5, where the stress decreased. As discussed earlier in section 6.2.1, increasing the number of intermediate subfloor beams or by reducing the span length between the SFBs produced a stiffer refurbished deck in Phase 2 that resulted in reduced displacement under the fatigue limit state loading.

7.2.2 Response of Intermediate Subfloor beam SFB2a

A uniaxial strain gauge of $^1/_4$ in. (6 mm) gauge length was installed on the soffit (underside of the bottom flange) of SFB2a at mid-span between the stringer extensions. This strain gauge (CH 2154) was oriented transversely, and was aligned with a similar strain gauge (CH 2153) at the top of the deck plate (Figure 87).

The maximum response at CH 2154 was recorded in LS-2, when the actuators #4 and #6 were loaded to the maximum. The maximum response at CH 2153 was recorded in LS-1, when the actuators #3 and #5 (located over SFB2a) were loaded to the maximum. The global response of the deck at the intermediate subfloor beam SFB2a, as measured by channels 2153 and 2154, are plotted in Figure 151 along with the response predicted by FEA results under LS 1. As expected, compressive and tensile stresses developed at the top of the deck plate and at the bottom flange of the subfloor beam due to flexural deformation in the transverse direction. The stresses on the deck plate were highly concentrated close to the applied loading as was observed in FEA. The load pads were significantly away from CH 2153 on the deck plate under the static test load configuration. Due to the composite action, the compressive stress on the deck plate was significantly smaller than the tensile stress as it was also noted during the crawl test (Figure 116).

The maximum stresses measured at channels 2153 and 2154 were -0.65 ksi (-5 MPa) in LS-1 and 2.79 ksi (19 MPa) in LS-2, respectively. The two loading steps didn't make significant difference for these channels as the stress measured in CH 2153 for LS-2 was -0.51 ksi (-3 MPa) in CH 2154 for LS-1 was 2.45 ksi (17 MPa). The location of

CH 2154 was comparable to CH 1216 in Phase 1. In Phase 1, CH 1216 measured maximum stress of 3.72 ksi (26 MPa) in LS-4 (Alapati 2012).

7.3 Response of Rib-to-Deck Plate Connections

The response of the rib-to-deck plate connections was measured in Rib 7 at section Y-Y, where uniaxial strain gauges were provided in back-to-back configuration on the deck plate and the rib walls as discussed in section 5.1.4. The strain gauges installed on the deck plate to the west of Rib 7 were under the east load pads of actuator #3. The internal rib gauges at section Y-Y were damaged during Phase 1 and were not available in Phase 2.

The stresses measured at each gauge during the static test conducted on November 1, 2010 are presented in Figure 152. The stresses measured on the back-to-back gauges on the deck plate are plotted in Figure 153, along with the crawl test measurements. The crawl test results were discussed earlier in section 6.3.

Since the crawl test results were plotted with respect to the distance of the centerline of the truck (i.e., the midpoint between the axles) from SFB2a, the static test results for each load step were plotted at the midpoint between the respective actuators simulating the tandem axles. The actuators were spaced 4ft. $1^1/_2$ in. (1.257 m) apart in the longitudinal direction, and the tandem axles of the crawl truck were spaced at 4ft. (1.219 m). Thus a difference of $1^1/_2$ in. (38 mm) existed between the data points from the two measurements. As discussed in section 5.3, the crawl tests were conducted at lower load level than the static tests. For a consistent evaluation, the static test results prorated to the load level of the crawl tests are also shown on Figure 153. Noting that the crawl test only consisted of the live load effects, the results for the initial load step of the static test (LS-

0), where all actuators were at the minimum load level of 3 kips (13.3 kN) were deducted from the respective load steps to remove the effects of the simulated permanent load. This produced the effect of only the moving tandem axles or the live load in each load step, corresponding to 41.4 kips (184.1 kN) per actuator (or simulated axle) or 82.8 kips (368.3 kN) for the simulated tandem axles. The deduced results were then scaled down or prorated to the total weight of the crawl truck, i.e, 53.75 kip (239.1 kN). The plots showed that the static test measurements matched well with the crawl test results. As discussed earlier, the maximum stresses in the deck plate at the gauged section occurred when actuator #3 at the section was loaded to the maximum in LS-1 on when one of the axles of the tandem was on the section. The static test measurements are compared with FEA results at Rib 7 in Figure 154 at section Y-Y for LS-1 when actuator #3 at section Y-Y was loaded to the maximum. Figure 154 is reproduced from Figure 31 by adding the static test measurements as dots at Rib 7 rib-to-deck connection regions. The FEA results corresponding to the gauge location are shown in the figure. Although the FEA results were slightly higher than static test measurements, they generally agreed well.

As discussed in chapters 4 and 6, the response of the deck was highly localized under the wheel loads. At the rib-to-deck plate connection to the west of Rib 7, the stresses measured on the top of deck plate were in tension (channels 1362 and 1363) while the stresses measured on the deck soffit (CH 1371) and on the external face of the rib wall (CH 1370) were in compression. The stresses of comparable magnitude but opposite signs on the top and bottom of the deck plate indicated primarily flexural deformation of the deck plate locally under the wheel loads, although the higher maximum stress in CH 1362 (5.6 ksi) than that in CH 1371 (3.2 ksi) suggested presence

of some membrane action. The deck plate bent over the rib walls in the transverse direction of the deck causing tensile and compressive stresses at the top and bottom of deck plate respectively. Unlike the west side, the east side of Rib 7 was not directly subjected to a wheel load. The stresses to the east of Rib 7 were of opposite signs compared to stresses on the west side, which suggested distortional deformation of the rib as was evident from the Figure 32.

The gauges at section Y-Y on the deck plate and the rib walls were retained from Phase 1 testing. These gauges were located at 4ft. $1^1/_2$ in. (1.257 m) south of SFB1 at section Y-Y of the Phase 1 deck. Strain gauges in a similar configuration were also installed at section X-X of the Phase 1 deck, which was 4ft. $1^1/_2$ in. (1.257 m) north of SFB2a. It should be noted that the section X-X and Y-Y in the Phase 1 deck were located at third span positions between SFB1 and SFB2a. Due to the deck modification, however, the section Y-Y in the Phase 2 deck was at mid-span between the SFBs and also at the same distance as section X-X from SFB2a and section Y-Y from SFB1. Also these sections were loaded directly by an actuator in both phases of testing. The maximum stresses measured at the gauges at section X-X and Y-Y during Phase 1 static test of January 29, 2009 are presented in Figures 155 and 156, respectively for comparison with the Phase 2 measurements at section Y-Y. Some of the strain gauges were dysfunctional and did not provide any measurements, however, the measurements at the functioning gauges could be compared.

As is evident, the stresses in the deck plate to the west of Rib 7 were comparable between the Phase 1 and Phase 2 testing. In Phase 1 testing, the stresses at the top and the bottom of the deck plate at section Y-Y (channels 1362 and 1371) were almost equal in

magnitude suggesting very small membrane action. In Phase 2 testing, however, the stress at the soffit gauge was reduced and the stress at the deck gauge was increased, suggesting a larger component of membrane stress compared to the flexural stress in the deck plate. The stress on the soffit of the deck plate at CH 1371 in Phase 2 testing was closer to the stress at CH 1367 on section X-X in Phase 1 testing. The stress on the outer face of the rib wall was reduced in Phase 2 testing. The stresses were also reduced at the gauges to the east of Rib 7 in Phase 2 testing compared to Phase 1. Apparently, the transverse bending of the deck or the distortion of the ribs under wheel loads was reduced in Phase 2 testing due to the reduced deformation resulting from a reduction in the span between the floor beams and increased membrane action.

7.4 Response of Intermediate Subfloor Beam SFB2a at Rib Cutouts

The response of the intermediate subfloor beam SFB2a is presented in terms of the stresses measured at the gauges on the SFB2a web around the cutouts for the ribs 3 and 7. From the results of Phase 1 study and the FEA results discussed in Chapter 4, it was determined that the welded connections of SFB2a to ribs 3 and 7, adjacent to the SEs, were the most fatigue critical. As such, SFB web around the cutout for these ribs, including the internal bulkhead plates were densely gauged as discussed in section 5.1.5. The instrumentation of SFB2a around ribs 3 and 7 cutouts is shown in Figure 79.

The maxima and range of stresses measured on November 1, 2010 at all the strain gauges installed on SFB2a around the cutouts for ribs 3 and 7 are presented in Figures 157 to 164, along with the locations of the strain gauges. Consistent with the crawl test and FEA results, the maximum stresses occurred in LS-2 when actuators #4 and #6, located symmetrically with respect to SFB2a, were loaded to the maximum. The figures

also show the stresses measured by the strain gauges installed on the bulkhead, which will be discussed in a later section.

Rosette gauges of 1 mm gauge length were installed back-to-back on SFB2a web adjacent to the cutout terminations west of Rib 7 and east of Rib 3 placed as close to cutout as possible. As explained in Appendix A, these rosettes were inadvertently installed in arbitrary orientations as shown in Figures 165 to 168. While this arbitrary orientation did not have any impact on the measured principal stresses and their directions (due to invariance), the stresses normal to the weld toe could not be directly obtained from the rosette measurements. As such, the stress normal to the weld toe was computed by transforming the principal stress in the direction normal to weld. Due to the arbitrary orientation of these rosette gauges, however, the direction of the principal stress with respect to the rib-to-SFB weld could not be directly established. The as installed location and orientation of these rosette gauges with respect to the cutout termination and rib-to-deck weld were determined from the photographs of the as installed gauges using an image rectification method discussed in Appendix A. The orientation of the rosette gauges, the directional and principal stresses at the rosette gauges, and the stresses normal to the rib-to-SFB weld toe are presented in Tables 14 and 15 for load steps 1 and 2, respectively. The tabulated quantities are illustrated in Figure 169. The stresses caused by individual load step were obtained by subtracting LS-0 measurements from load steps 1 and 2 measurements. Then, the principal and normal stress range calculations were performed using the stresses caused by load steps 1 and 2 without the permanent load effect simulated by LS-0. The maximum of normal stress range was calculated to be 10.2 ksi (70 MPa) at Rib 7 cutout on the north face.

Figures 170 and 171 show the principal stresses from static test measurements along with the measurements for crawl test at the 1 mm rosette gauges to the east and west of ribs 3 and 7, respectively. The stresses measured by the back to back rosettes on the north and the south faces are plotted on the same figure to visually assess the relative proportion of the in-plane and the out-of-plane stress components. As was noted in the previous sections, a $1^1/_2$ in (38 mm) difference existed between the data points from the static and the crawl test measurements due to the difference between the spacing of actuators and the tandem axle spacing. For a consistent evaluation, the static test results prorated to the load level of the crawl tests are also shown on the figures. The maxima of principal stresses at the rosette gauges occurred in LS-2, when actuators #4 and #6 were loaded to the maximum. At Rib 3, the prorated static test results for the gauge on the north face was consistent with the crawl test results, however for the gauge on the south face, the prorated static test results exceeded the crawl test measurements by more than 1 ksi (7 MPa). The southward bending of the SFB2a web at this location was smaller in the static test compared to the crawl test, as is evident from the lesser difference between the north and the south face results. The principal stresses at Rib 7 also exhibited similar trend, where, the prorated static test measurements for the gauges on the north face were consistent with the crawl test results. On the south face, the prorated static test measurements were about 1.5 ksi (10 MPa) higher compared to the crawl test. The static test measurements at this location showed primarily in plane stresses. These differences in the crawl and static test measurements observed at the cutout gauges may have been caused due to the combined effect of the discrepancies in the size and positions of the wheel loads. For static tests, loading pads of 10 in. × 20 in. (254 mm × 508 mm) were

used to simulate the contact of a pair of wheels on each side of the tandem axles. However, the measurements of the actual tire contact for the crawl truck did not exactly match with the above contact dimensions (Alapati 2012). As discussed earlier in section 6.2.1, a 2 in (51 mm) play existed between the guide truss and the guide tube of the test truck, and therefore the truck could shift transversely during the crawl test. The FE analyses were conducted with idealized tire patches consistent with the static test. Hence, as seen in the figures, the FEA and static test produced similar results. Thus, the static test load disposition generally produced consistent results with the crawl test.

Under ribs 3 and 7 each, a rosette was installed on the north and south faces of the SFB2a web, abutting the cutout. The rosettes were positioned towards the west and east sides of ribs 3 and 7 respectively, about $3^{7}/_{8}$ in. (98 mm) away from the centerline of the ribs (Figure 79). The stresses measured by these rosettes and the computed principal stresses in LS-2 are shown in Tables 16 and 17. The maximum principal stress was tensile and tangential to the cutout. The minimum principal stress normal to the free edge was naturally almost zero. The maximum principal stress measured under Rib 7 was 8.2 ksi (57 MPa) on south face gauge at Rib 7 cutout.

The strain gauges on SFB2a around the cutouts for ribs 3 and 7 are shown in Figures 159 and 160, respectively, overlaid on the contour of maximum principal stress as obtained from the FEA results of SM2 for LS-2. The measured stresses at the gauges are also shown in the figures. Note that the estimated principal stresses are presented for the rosette gauges. The principal stresses computed from the $^{1}/_{4}$ in (6 mm) rosette gauges installed back-to-back on the north and south faces of SFB2a web, and to the west and east sides of the cutouts at ribs 3 and 7, are shown in Tables 18 to 23 for LS-2 in Phase 2.

The layout of the rosette gauges and the direction of the larger (magnitude) principal stresses on the south face are also shown in the respective tables. Tensile stresses are defined as positive. The direction of principal stresses is presented with respect to the rosette arm perpendicular to the rib-to-subfloor beam weld. This angle is defined positive in the counter clockwise direction. The measured stresses were consistent with the stress distribution obtained from the FEA. The west side of Rib 3 and the east side of Rib 7 primarily experienced compressive stresses while the east side of Rib 3 and the west side of Rib 7 primarily experienced tensile stresses which were in agreement to the discussion presented in chapters 3 and 5 (FEA and Crawl test chapters).

As it is also observed from Tables 14 to 17, the stresses at the corresponding gauges on the north and south faces, and the principal stresses at the back-to-back rosettes, were of almost equal magnitude, indicating that the stresses in the web of SFB2a were primarily in-plane. Some difference existed between the directions of principal stresses at the north and south face rosettes, suggesting complex distribution of stresses with presence of some out-of-plane bending and/or twisting at the cutout terminations.

As discussed earlier, these rosette gauges were not installed at exactly same distance (as prescribed on the instrumentation plan) from the cutout termination which may have ultimately affected the results to certain extent. The magnitude of the stress measurements at the gauges on the east and west side cutout terminations of ribs 3 and 7 could not be compared due to two different kinds of gauges installed at different distances away from cutout terminations on the east and west side. However, the stress distributions indicated that SFB2a was subjected to shear forces under simulated wheel

loads, which resulted in diagonal tension and compression stress fields around ribs 3 and 7.

The measured distribution of principal stresses below and above the cutouts was consistent with the transfer of the simulated wheel loads from the deck to the SEs by shear in the SFB2a web similar to Phase 1 study. Assuming a simply supported beam, Figure 38 schematically shows the shear force and the bending moment diagrams in SFB2a when loaded by two distributed load patches that simulated one of the axles on the SFB, as in LS-1. Shear force is developed only between the distributed loads and the nearest supports for the symmetric load distribution within symmetric section between the SEs (Figure 38). In this shear span, a diagonal tension field would develop in the web from the bottom (tension) flange to the top corner of the support. In the SFB2a web, this tension field was interrupted by the rib cutouts. Because of the continuity provided by the bulkhead plate, a diagonal tension field developed above the cutout through the bulkhead plate, from the cutout termination on the rib to the stringer extension at the opposite top corner. Another branch of the tension field developed in the web of the subfloor beam under the cutout. As a result, high stress concentrations developed at the edge of the cutouts in the web of the subfloor beam, and in the bulkhead plates where the tension field was terminated. Due to the smaller cutout radius near the rib-to-subfloor beam connection, the stress concentration was significantly higher at this location compared to that under the ribs (refer to the principal stresses presented in Tables 14 to 17). Similar high stress concentration was also noted at the bulkhead-to-rib welded connection near the top corner, which will be discussed later.

Adjacent to the 1 mm rosettes at the cutout terminations to the east of Rib 3 and west of Rib 7, five element strip gauges of 1 mm gauge length were installed back-to-back on SFB2a web (Figures 81 and 83). The maximum and range of stresses measured at the gauges during the static test are tabulated in Figures 161 and 164 for both north and south faces. These stresses are plotted along with the FEA results in Figures 172 and 173. As seen in the figures, the stresses generally decreased as the distance from the cutout termination increased. The maximum stress of 15.7 ksi (108 MPa) and the maximum stress range of 14.5 ksi (100 MPa) were measured at CH 2052 on Rib 3 north face.

In Figures 161 and 164 respectively, the maximum stresses and stress ranges for the strip gauges on the cutout edge (channels 2065 and 2074 at Rib 3 and channels 2140 to 2149 at Rib 7) are also tabulated. Two five-element strip gauges of 1mm gauge length were installed at the mid thickness of SFB2a web edge. This distribution of stress at the cutout face for ribs 3 and 7 are shown in Figures174 and 175, respectively. FEA results obtained from SM3 are also included in the plot which shows general agreement with the static test results. The measured stress ranges on the cutout face, at the termination of the rib-to-SFB2a weld, were 18.8 ksi (130 MPa) at Rib 3 and 16.6 ksi (114 MPa) at Rib 7. Away from the weld termination, however, the stresses increased upto a maximum value before decreasing along the cutout face. The results showed that due to the stress concentration effect of the cutout geometry the maximum stress did not occur at the termination of the weld toe, but at about 0.6 in (15 mm) from the termination in the base metal condition.

7.5 Response of Bulkhead Plates at SFB2a

The maxima of stresses measured by the strain gauges on the bulkhead plates in ribs 3 and 7 at SFB2a are tabulated in Figures 157 and 158, respectively for the static test performed on November 1, 2010. The maxima of stresses observed to occur in LS-2. The stress ranges at these gauges are presented in Figures 161 and 162, respectively. The strain gauge CH 2099 on the south face of the bulkhead plate in Rib 7 malfunctioned and is denoted as “Bad”.

On each bulkhead plate the strain gauges along the diagonals that spanned between the cutout termination on the rib towards the mid span of the SFB2a and the opposite top corner of bulkhead plate, measured tensile stresses. Due to the presence of inherent micro-discontinuities along the fusion boundary at the weld toe, the stress normal to the weld toe is primarily responsible for the fatigue crack growth along the toe (mode I cracking). Adjacent to the subfloor beam cutout, the gauge normal to the bulkhead plate-to-rib weld toe was close to the diagonal tension/compression stress fields (discussed in Chapter 4). This pattern of stress distribution was consistent with the transfer of the simulated wheel loads from the deck plate to the SEs by shear in the SFB2a web. This shear introduced diagonal tension and compression stress fields in the bulkhead plate.

The maxima of the stresses adjacent to the cutout were 4.3 ksi (30 MPa) at CH 2014 in Rib 3 south face and 3.5 ksi (24 MPa) at CH 2076 in Rib 7 north face. Near the top edge of the bulkhead plate (opposite to the cutout on the diagonal tension band), large stress concentrations occurred at the weld toes due to the diagonal tension fields (Figures 159 and 160). The gauges at the top edge of the bulkhead plate were oriented along the

diagonal tension bands. Also the tensile stress was highest at the weld toe and it decreased away from the weld toe (Figures 157 and 158). The maximum stress observed at this location were 7.7 ksi (52 MPa) on CH 2024 (on north face) in Rib 3 and 6.4 ksi (44 MPa) on CH 2087 (on north face) Rib 7.

Two pairs of back-to-back rosette gauges of $^1/_4$ in. gauge length were also provided on the bulkhead plate - one pair located centrally and another pair towards the cutout adjacent to the middle uniaxial gauge. The central rosette gauge was located such that the middle arm was vertical. As a result, one of the perpendicular arms was aligned with the tension diagonal and the other arm was aligned with the compression diagonal. As seen in Figures 157 and 158, the gauges along the tensile diagonal (channels 2006, 2018, 2007, 2019 at Rib 3 and channels 2081, 2093, 2082, 2094 at Rib 7) experienced tensile stresses while the gauge normal to them (channels 2004, 2016, 2009, 2021 at rib 3 and CH 2079, 2091, 2084, 2096 at Rib 7) experienced compressive stresses. The vertical arm of the rosette gauge installed at the center measured stress close to 0 ksi (0 MPa). The estimated principal stresses at the rosette gauges on the bulkhead plates in ribs 3 and 7 are shown in Tables 24 to 27. The directions of principal stresses were close ($< 10^o$ except at Rib 7 south face gauge with channels 2094, 2095 and 2096 where it was 19.4^o) to the direction of the gauges normal to the weld toes.

7.6 Phase 2B Static Test

7.6.1 Phase 2A and Phase 2B Static Test Measurements for Critical Gauges

At the beginning of Phase 2B testing, a static test was performed on September 28, 2011 to establish the state of the structure compared to the virgin state before the

Phase 2A testing. As noted in section 5.6.4, no fatigue damage was visible in the prototype deck at the conclusion of the Phase 2A testing. The findings of this static test are presented in the following.

The distribution of the longitudinal stresses in the transverse cross section Y-Y at the strain gauges on the soffit of ribs is plotted in Figure 176. As it was in Phase 2A, these gauges recorded the maximum longitudinal stresses in LS-1, when actuators #3 and #5 were loaded to the maximum. These stresses for LS-1 were plotted along with the static test measurements from November 1, 2010 in Figure 177. This figure shows that the initial static test measurements were similar for Phase 2A and Phase 2B.

Responses of the rib-to-deck plate connections were measured in Rib 7 at section Y-Y, where uniaxial strain gauges were installed in back-to-back configuration on the deck plate and the rib walls (Figure 178). Except for channels 1362 and 1363 that were on the deck plate directly under the load pads, stresses in all the gauges were similar to initial Phase 2A static test results discussed in section 7.3. Channels 1362 and 1363 showed inconsistent measurements throughout Phase 2A testing as will be discussed with respect to intermittent static test results in chapter 8. Since these gauges were directly under the load pads, they were replaced prior to Phase 2B testing assuming they were damaged in Phase 2A testing under heavy pressure. These gauges measured lower stresses in Phase 2B compared to measurements in Phase 2A. These gauges were located at regions with high stress gradient as seen from crawl test results and FE analyses because of which even a small change in the location of these replaced gauges could potentially cause considerable difference in the measured stress values.

The maxima and the range of stresses measured for Phase 2B static test at all the strain gauges installed on SFB2a around the cutouts for ribs 3 and 7 are tabulated in Figures 179 and 180, along with the location of the strain gauges. These stresses at the critical gauges when compared to Phase 2A static test measurements on November 1, 2010, were found similar (Figures 147, 152, 157, 158 and 176 to 180). The comparisons confirmed that the prototype deck was essentially in the same condition as before the Phase 2A testing.

7.6.2 Response of End Subfloor Beam SFB1

For Phase 2B, the gauges on SFB1 at ribs 3 and 7 were reconnected to the data logger and their response was monitored. These gauges at ribs 3 and 7 are shown in Figures 92 and 93 respectively, reproduced from Alapati (2012). Strain gauge channels 1294, 1296 and 1298 on the south face of SFB1 to the east of Rib 7 (towards SE A) were not reconnected due to the lack of available data channels in the data logger. The maxima and range of stresses measured by the SFB1 gauges during the Phase 2B static test of September 28, 2011 are tabulated in Figures 181 to 184 for ribs 3 and 7, respectively. The figures also show the stresses measured by the strain gauges installed on the bulkhead plates in ribs 3 an 7, which will be discussed in a later section.

The stresses in SFB1 were considerably less than the stresses in SFB2a since SFB1 was supported by the relatively rigid floor beam and therefore experienced less deformation under load. The west side of Rib 3 and the east side of Rib 7 primarily experienced compressive stresses, whereas the east side of Rib 3 and the west side of Rib 7 primarily experienced tensile stresses. At the gauges adjacent to Rib 3, the maxima on the gauge normal to the weld toe were about -8.2 ksi (-57 MPa) and 7.4 ksi.(51 MPa). At

the gauges adjacent to Rib 7, the maxima of principal stresses were -7.4 ksi (-51 MPa) and 3.8 ksi (26 MPa). Although SFB1 was not directly loaded by an actuator, the distribution of load from the deck plate to the subfloor beam and to the stringer extension still followed similar path as in SFB2a. The stress distributions indicated that SFB1 was also subjected diagonal tension and compression stress fields around ribs 3 and 7 resulting from shear forces due to the simulated wheel loads since the SFB was made integral with the SEs and hence load bearing. Similar to SFB2a, a forked diagonal tensile stress field developed, distributed above and below the cutout in the shear span between the load and the SE. Stress concentrations developed at the edge of the cutouts in the web of the subfloor beam, and in the bulkhead plates where the tension fields were interrupted.

For quantitative comparison of stresses between Phase 1 and Phase 2, the maxima of stresses and the stress ranges measured by the gauges at SFB1 in Phase 1 are reproduced in Figures 185 to 188 from Alapati (2012). Unlike in Phase 1, the loading in Phase 2 was applied around SFB2a only, because of which SFB1 experienced less deformation under Phase 2 loading. Accordingly, the stresses in SFB1 during Phase 2 were significantly lower (from 40% to 75%) compared to the stresses observed in Phase 1. In Phase 1, the maxima of stress ranges at rib 3 and 7 were 15.3 ksi (105 MPa) and 13.7 ksi (94 MPa), respectively. In Phase 2, the maxima of stress ranges at these ribs were respectively 7.3 ksi (50 MPa) and 6.5 ksi (45 MPa).

7.6.3 Response of Bulkhead Plates at SFB1

The bulkhead plates in ribs 3 and 7 at SFB1 were instrumented as shown in Figures 92 and 93. Only the south face of the bulkhead plates at SFB1 was instrumented.

These gauges were oriented horizontally, at an angle of about 17° to the weld toe normal. The maxima of stresses and the stress ranges measured by the strain gauges on the bulkhead plates in ribs 3 and 7 at SFB1 are presented in Figures 181 to 184 for the static test performed on September 28, 2011, along with the measurements at other gauges on SFB1.

The response of these bulkhead plates were similar to what was observed in Phase 1 (Alapati 2012). On each bulkhead plate the strain gauges at the opposite diagonals that spanned between the cutout termination on the rib and the opposite top corner of bulkhead plate, measured tensile and compressive stresses similar to the bulkhead plates in SFB2a. Tensile stresses were measured at the gauges on the diagonal that passed through the cutout termination towards the mid span of the SFB. Compressive stresses were measured at the gauges on the diagonal that passed through the cutout termination towards the SEs. This pattern of stress distribution was consistent with the transfer of the simulated wheel loads from the deck to the SEs by shear in the SFB1 web, as was discussed earlier. The shear introduced diagonal tension and compression stress fields in the bulkhead plate.

SFB1 was supported by the floor beam and loading was concentrated mainly above SFB2a as such, SFB1 experienced less deformation Therefore, consistent with the response of subfloor beams discussed earlier, the stresses measured in the bulkhead plates at SFB1 were smaller than the stresses measured in the bulkhead plates at SFB2a. At SFB1 the maxima of stresses measured at the upper gauges was 3.2 ksi (22 MPa) in compression at CH 1015 and 2.9 ksi (20 MPa) in tension at CH 1014. The maxima of stresses measured at gauge channels 1015 and 1014 in Phase 1 were -7.0 ksi (48 MPa)

and 7.1 ksi (49 MPa), respectively. At the lower gauges adjacent to cutout terminations, the maxima of stresses measured was about 2.6 ksi (18 MPa) in compression at CH 1016 and 2.3 ksi (16 MPa) in tension at CH 1017. The maxima of stresses measured at gauge channels 1016 and 1017 in Phase 1 were -5.0 ksi (35 MPa) and 4.9 ksi (34 MPa), respectively.

8 RESULTS OF FATIGUE TEST

Fatigue testing was carried out in two phases – Phase 2A and Phase 2B. In each of these phases, 5 million loading cycles were applied on the refurbished prototype deck. Intermittent static tests were performed during the fatigue testing of the deck. These static tests permitted collection of larger data samples at a higher sampling rate that produced stable data with reduced noise and helped in accurate state determination of the specimen. Intermittent static tests were carried out weekly and after any significant event that interrupted the tests. Changes in the state of the deck were assessed by comparing the stresses at the critical gauges. The evaluation of these intermittent static tests and the performances of the various critical connections such as rib-to-SFB2a, rib-to-bulkhead plate and rib-to-deck plate are discussed in this chapter.

8.1 Phase 2A Fatigue Testing

Phase 2A fatigue testing was initiated on December 20, 2010. Initially, the fatigue test was conducted only during the day and was shutdown at night. From January 17, 2011 the fatigue testing of deck was continued day and night, except for interruptions due to static tests and routine maintenance. The fatigue test for Phase 2A was completed on April 18, 2011 after 5.14 million cycles. The deck specimen was thoroughly inspected for any fatigue cracks and a static test was performed to acquire information on any changes in behavior of the specimen compared to the baseline condition at the beginning of the test. No fatigue cracks were visible and the static test measurements at strain gauges did not indicate any significant change in the condition or the response of the deck specimen.

8.2 Evaluation of Intermittent Static Test Results for Phase 2A

The stress ranges obtained from the intermittent static tests performed during the fatigue test against the number of fatigue load cycles corresponding to the static tests are plotted Figures 189 to 192 for some of the critical gauges. These gauges are identified in the figures. The stress range is plotted as the ordinate or the Y-axis, and the number of fatigue load cycles corresponding to the static tests is plotted as the bottom abscissa or the bottom X-axis. The dates of the static tests are indicated on the top abscissa. Only 11 static test dates are shown in the figures to avoid clutter for static tests performed at close intervals.

Figure 189 shows the history of the maximum principal stress ranges measured at the 1 mm rosette gauges on the north and south faces of SFB2a web, adjacent to the cutout for ribs 3 and 7. Also shown on this figure are the stress ranges measured at the first gauge of the 1mm strip gauge at the edges of the cutout abutting the rib-to-SFB2a weld termination on the subfloor beam web (channels 2065 and 2140 at the cutouts for ribs 3 and 7 respectively). Stress ranges for all the channels on the SFB2a web were stable. A lower stress range was measured at rosette gauge with channels 2049, 2050 and 2051 as seen in the figure. It was due to the malfunctioning of the AD card. It was replaced after 390,000 cycles on January 13, 2011 (see section 7.1) and the measurements obtained thereafter were consistent.

Figures 190 and 191 show the stress ranges at the critical gauges on the bulkhead plates of ribs 3 and 7, respectively. Among Rib 3 gauges, CH 2014 experienced higher stress range for the static test on February 16, 2011, however, the stress values dropped down to normal on the subsequent static test performed on February 21, 2011 and

thereafter (Figure 190). The data shown in the figure suggests that it was a minor fault in the data which may have been caused due to some electrical noise in the channel. Similarly a drop in stress range was observed for 2002 during the static test of April 11, 2011. The stress range for this channel also moved back closer to the normal values on the subsequent static test conducted on April 18, 2011. Among Rib 7 gauges, all the channels except CH 2087 showed consistent stress range measurement throughout the testing (Figure 191). The stress range for CH 2087 fluctuated between 5.5 ksi (38 MPa) and 7 ksi (48 MPa) throughout the testing. Also, for the static tests conducted between November 1, 2010 and January 17, 2011, the measurements for this gauge were not quantifiable. In view of consistent measurements observed at CH 2098 (Figure 191), which was also located at the similar location but on the other face, it can be concluded that the gauge channel 2098 was malfunctioning. There was no way of investigating it or replacing it, as it was inaccessible inside the ribs.

Figure 192 shows the stress ranges at the deck plate top and bottom gauges under load pad at section Y-Y. The strain gauge on the bottom of the deck plate was adjacent to the rib-to-deck plate weld toe. The stress range values for all the gauges in Figure 192 except CH 1362 were generally stable. CH 1362 is the gauge located under the loading pad at section Y-Y retained from Phase 1. This gauge was damaged during fatigue testing, which affected the measurements. The plots of the stress range history at all these gauges located at fatigue critical locations of the deck confirmed that the deck essentially remained undamaged after 5 million cycles of fatigue testing.

As discussed in section 5.6.4, the loading protocol for the Phase 2A fatigue testing did not produce the desired stress range in the deck, particularly the details of interest in

SFB2a (shown in Figures 189to 192). Although the deck was subjected to the desired maximum stress, the minimum stress was significantly higher than the target, resulting in a significantly lower stress range. The example of the deck elements not experiencing the targeted stress range is depicted in Figure 105, where a typical measured stress history is shown for the strain gauge CH 2065 located at the edge of the cutout for Rib 3 in SFB2a. Also shown on this figure is the intended stress history that was achieved by the correct loading protocol in Phase 2B. Due to the incorrect loading protocol in Phase 2A, the fatigue critical details in SFB2a although subjected to the desired maximum stresses, experienced stress ranges that were far below the respective fatigue limit. This is evident in the S-N plot of the fatigue critical details shown in Figure 193, plotted against the AASHTO fatigue design curves. Thus, it was concluded that the deck specimen did not experience any fatigue damage during the Phase 2A fatigue testing.

8.3 Assessment of Phase 2A Fatigue Testing

As discussed above, the incorrect loading protocol in Phase 2 testing affected the stress range experienced by SFB2a and other elements that were influenced by both the load steps 1 and 2. The details located away from SFB2a that were primarily influenced by only one of the loading steps, closely experienced the target stress range. This is evident from the measurements at the deck plate gauges on section Y-Y presented in Figure 194 showing the comparison of a typical stress history at the deck plate strain gauge CH 1362 for Phase 2A (incorrect loading protocol) and Phase 2B (correct loading protocol) testing. This gauge was located on the deck plate directly under the east loading pad of actuator #3 and was therefore influenced by the local effects of the simulated wheel load in LS-1. As is seen, the measured stress range at this gauge in Phase 2A was

about 90% of the targeted stress range. Thus, unlike the details in SFB2a the rib-to-deck plate connections at section Y-Y experienced 5 million cycles of desired stress range in Phase 2A.

Similar to the case of SFB2a, SFB1 also did not experience complete stress cycle during Phase 2A testing. From Phase 2B static test data, it was observed that the difference between LS-1 and LS-0 produced maximum stress range at SFB1. The stress ranges produced by the loading case of LS-1 and LS-2 (used in Phase 2A) were considerably small (less than 50%) compared to the targeted stress ranges.

8.4 Phase 2B Fatigue Testing

The fatigue testing for Phase 2B was initiated on September 17, 2011. On September 27, 2011, SFB1 gauges retained from Phase 1 testing were reconnected. A static test was performed on September 28, 2011 to obtain the stress data from the gauges at SFB1 in the existing state. Subsequently, static tests were carried out weekly.

Beginning October 4, 2011, temperature of the deck specimen was also monitored using a laser thermometer to determine if there was any effect of temperature on the measured stresses. These measurements were taken at SFB2a web during every inspection (8am, 12pm, 4pm, 8pm and 12pm). The temperature variation of the deck from October 4, 2011 till November 24, 2011 is presented in Figure 195. A 15^{o}F (8^{o}C) variation in temperature was observed. An example of one day (October 8, 2011) temperature variation is shown in Figure 196. A temperature variation from 67^{o}F to 71^{o}F (19^{o}C to 22^{o}C) observed for that day. The fluctuation in gauge measurements caused by this variation in temperature found to be insignificant.

During the fatigue test, the measurements at the rosette gauge (channels 2121,

2122, 2123), on the south face of SFB2a and to the east of Rib 7 were observed to fluctuate. It was first assumed that the fluctuation was caused by variation in temperature. However, no significant changes in stress values were observed at other gauges and during the period of October 24, 2011 to October 25, 2011, significantly high fluctuation was noted at this rosette (Figure 197). As seen in Figure 197, channels 2122 and 2123 were measuring high compressive stresses. CH 2121 was measuring a small stress of about 0.5 ksi (3 MPa) and was not observed to fluctuate. However, channels 2122 and 2123 fluctuated by more than 2.5 ksi (17 MPa) over 1×10^5 cycles in a period of about 28 hours. Suspecting the rosette gauge to be malfunctioning, on October 27, 2011 the test was interrupted and this rosette gauge was replaced. The stresses measured by the replaced rosette gauge are shown in Figure 198. The measurements at this gauge became stable and remained consistent for the remainder of the experiment. The difference in stresses between the old gauge and the replacement gauge can be noted from Figures 197 and 198. No noticeable difference was observed for CH 2121 while a difference of about 0.5 ksi (3 MPa) and 3.5 ksi (24 MPa) were observed at channels 2122 and 2123, respectively. Due to the limited and difficult access in the congested space between Rib 7 and the stringer extension, the replacement rosette gauge may not have been installed exactly at the same location of the old gauge. As a result, the measurements by the replaced gauges did not exactly match the measurements by the previous gauge.

The fatigue testing in Phase 2B was terminated on November 24, 2011 after 5.02 million cycles. A static test was also performed at the end of the fatigue test to evaluate the state of deck. The prototype deck specimen was thoroughly inspected and no fatigue cracking was noted.

8.5 Evaluation of Intermittent Static Test Results for Phase 2B

Similar to Phase 2A above, the stress ranges at a few critical gauges obtained from intermittent static tests performed during the Phase 2B fatigue testing of the deck are plotted against number of fatigue cycles in Figures 199 to 202.

Figure 199 shows the history of the maximum principal stress ranges measured at the 1mm rosette gauges on both north and south faces of SFB2a web, adjacent to the cutout for ribs 3 and 7. Also shown on the figure are the stress ranges measured by the first element of the 1mm strip gauge at the edges of the cutout abutting the rib-to-SFB2a weld termination on the subfloor beam web (channels 2065 and 2140 at the cutouts for ribs 3 and 7 respectively). Figures 200 and 201 show the stress ranges at the critical gauges on the bulkhead plates of ribs 3 and 7, respectively. Figure 202 shows the stress ranges at the deck plate top and bottom gauges under the load pad at section Y-Y. No significant change was noted in the measured stress ranges at these gauges over the duration of the fatigue test, confirming that the deck specimen essentially remained undamaged after 5 million cycles of fatigue testing in Phase 2B.

The stresses at the bulkhead plate gauges on SFB1 were noted to be drifting during the fatigue testing. Since the state of bulkhead plate couldn't be assessed physically, the stress ranges at the gauges obtained from static test measurements were plotted in Figures 203 and 204 for ribs 3 and 7, respectively. During Phase 1 fatigue testing, the stresses at these gauges were observed to change prompting the speculation that the bulkhead plate had developed fatigue cracking (Roy et.al 2012). As seen in the figures, the stress ranges were below 3 ksi (21 MPa) and no significant changes were observed at the gauge values during Phase 2B testing. This suggests that no further

damage had been incurred at the SFB1 bulkhead plate-to-rib connection details during Phase 2 testing.

8.6 Assessment of Fatigue Performance

8.6.1 Performance of Rib-to-SFB Connection

The performance of the fatigue critical connection detail at SFB2a cutout termination is assessed on the S-N plot against the AASHTO fatigue design curves in Figure 205. The stress ranges measured by the strain gauges adjacent to Rib 3 are plotted since they measured the maximum stress values (see discussion in section 7.4). For better accuracy, the stress ranges obtained from the static test measurements were used for the S-N plots. Since the static test was essentially a fatigue test at a slow rate, it could be expected that the connection details would be subjected to the same stress range as the static test during fatigue testing. The stress ranges denoted as S_n in Figure 205 is the stress normal to the rib-to-SFB weld adjacent to the cutout termination to the east of Rib 3 and calculated from the measurements of 1 mm rosette gauge.

The stress range normal to the SFB2a-to-rib weld toe was 10.2 ksi, (70 MPa) at Rib 7 on the north face of the cutout termination (refer to section 7.4 and Table 15). This normal stress was slightly less than the CAFT of the AASHTO Category C′ detail which is 12.0 ksi (83 MPa).

The measured stress range at the edge of the cutout and the weld termination on SFB2a was 17.2 ksi (119 MPa). The maximum stress obtained from FEA results at this location was 14.0 ksi (97 MPa) and the hot spot stress was 13.9 ksi (96 MPa). The fatigue resistance of this detail against cracking from the ground smooth weld toe at the

edge of a plate is defined as AASHTO Category B. The CAFT of the AASHTO Category B detail is 16.0 ksi (110 MPa). The measured stress range was higher while FEA result was lower than the CAFT of AASHTO Category B detail (Figure 205). As per IIW, this connection detail should have developed fatigue cracking at the 1.6 million fatigue load cycles (Figure 206).

The fatigue performance of the rib-to-SFB was also assessed based on local stresses obtained from FEA (Chapter 5). The hot spot stresses at the SFB-to-rib weld toe were 10.9 ksi (75 MPa) and 6.7 ksi (46 MPa) obtained from linear and quadratic extrapolations, respectively. The fatigue resistance of a cruciform or a T-joint with full penetration weld is defined by IIW (Hobbacher 2005) as a fatigue class (FAT) of 100 with a slope of -3. This fatigue design curve coincides with the AASHTO fatigue design curve for category B′ details for the finite life regime. The knee corresponding to constant amplitude fatigue limit (CAFL), however, occurs at 10 million cycles for the FAT 100 while it occurs at 2.55 million cycles for Category B′. As presented in section 4.2.1, the hot spot stress obtained from quadratic extrapolation was less than the fatigue limit which suggest that the life of the detail to be greater than 5 million cycles. The hot spot stress obtained from linear extrapolation had predicted the life of the connection detail to be 5 million cycles. Coincidentally, the hot spot stress obtained from linear extrapolation was exactly on the FAT 100 S-N curve. Since no fatigue cracking was observed at this rib-to-SFB2a weld toe after testing for 5 million fatigue cycles and the recommended curves are conservative lower bound to limited fatigue test data, a definitive conclusion cannot be obtained from this result. As per the AASHTO fatigue classification, the welded detail considered in this study for toe cracking is generally a category C detail. When it is

considered a category C detail for the use of AASHTO design S-N curve, the stress value at the hot spot lies in the finite life region in which a fatigue crack should have developed by 5 million cycles.

The hot spot stress calculated as per AASHTO recommendations (also used by IIW) was 14.7 ksi (101 MPa). This hot spot stress value was plotted in AASHTO S-N curve and compared for CAT C detail with CAFT at 10 ksi (69 MPa) as suggested in the AASHTO commentary (Figure 207). The extrapolated local structural stress range was well above 10 ksi (69 MPa) as was discussed in section 4.2.1. So, the subfloor beam-to-rib welded connection should have developed fatigue cracking at the weld toe at a (finite) design life of about 1.4 million cycles. In view of the inherent variability in the fatigue test results associated with micro and macro discontinuities at the weld toe, the AASHTO Category C design curve in the finite life region exhibits a lower bound or 95% confidence on the 95% probability of survival life for the detail category. Thus, it was expected that a significant number of connections belonging to this population will develop fatigue cracking at this life. The rib-to-subfloor beam connection survived 5 million cycles without any evidence of fatigue cracking, which exceeded the upper bound or 95% confidence on the 95% probability of failure life for the Category C details. This implies that this connection was subjected to a stress range that was below its CAFT and therefore, demonstrated infinite life. Figure 55 also showed the variation of normal stress (S_{11}) profile along a path normal to the toe of the rib-to-subfloor beam weld, obtained from the SM2A submodel analysis using nominal mesh size of $t \times t$. The stresses did not converge in SM2A at the reference points, and a jagged stress variation was noted due to the relatively large mesh size. Hence, the local structural stress at the weld toe, as

recommended by AASHTO, was influenced by the stress concentration resulting from the cutout geometry because of which the applicability of the latest AASHTO provisions for assessing infinite life performance of orthotropic bridge decks may be questionable.

Infinite life fatigue performance of a critical welded connection against fatigue cracking at the weld toe was evaluated by a local notch-stress based approach. This approach have been successfully used for assessing CAFT of welded cover plate and stiffener details in bridge girders and tube-to-transverse plate connections in highway sign, signal and high level luminaire support structures. The notch stress approach predicted an infinite life fatigue resistance of 30.7 ksi (212 MPa) for the rib-to-SFB2a welded connection against fatigue crack growth from the weld toe. The notch stress at the weld toe obtained from FEA was 23.8 ksi (164 MPa). Thus the rib-to-SFB welded connection was expected to demonstrate infinite life which was validated by the experimental results (Figure 208).

The performance of the fatigue critical connection detail at SFB1 cutout termination is assessed on the S-N plot against the AASHTO fatigue design curves in Figure 205. The stress ranges measured by the rosette element of the strain gauge normal to the weld toe (CH 1056) on the west of Rib 3 (north face) is plotted since it measured the maximum tensile stress value (refer to section 7.4). The maximum stress measured at this channel was 6.5 ksi (45 MPa). This normal stress was less than the CAFT of the AASHTO Category C detail. Hence, for the fatigue loadings used in Phase 2, no fatigue cracking was expected at this location.

8.6.2 Performance of Rib-to-Bulkhead Plate Connections at Intermediate Subfloor Beams

As presented in Figure Figure 7, adjacent to the cutout, the subfloor beam was welded to the rib wall using a CJP weld (deposited from both side) and the bulkhead plate was welded to the rib using PJP welds (deposited from both sides). As discussed earlier in chapters 4, 6 and 7, diagonal tension and compression fields form under shear loading. The presence of cutouts creates stress concentrations by interrupting the uniform flow of stresses. The stress concentration regions are developed at the cutout terminations and at the rib-to-bulkhead plate connections along those diagonal tension fields. Thus, the bulkhead plate-to-rib-to-SFB welded connection formed a cruciform as shown in Figure 57 loaded by the discontinuous elements (the SFB and the bulkhead plate) in the direction normal to the continuous member (the rib), with the possibilities of fatigue cracking through the weld throat, and at the weld toe. In Phase 1, the rib-to-bulkhead plate was fillet welded and had developed fatigue cracking through the weld throats (Alapati 2012). Analyzing this connection as a cruciform per the AASHTO specifications, Alapati assessed the fatigue performance of the detail as Category C for finite life. The fatigue performance of the refurbished connection in the Phase 2 deck at the intermediate SFBs containing the thicker SFB and bulkhead plates, and the rib-to-bulkhead plate PJP welds, was evaluated following the similar methodology and is presented in the following.

The nominal fatigue resistance of this connection is given in the AASHTO LRFD Bridge Design Specification (2005) and is used with US Customary units (SI system) as:

$$(\Delta F)_n = (\Delta F)_n^c \left(\frac{1.107 - 1.013\frac{2a}{t_p} + 1.23\frac{H}{t_p}}{t_p^{1/6}} \right) \leq (\Delta F)_n^c \quad (8)$$

where $(\Delta F)_n^c$ is the nominal fatigue resistance of the AASHTO Category C detail. The geometric parameters in the equation are shown in Figure 57, where

2a = is the lack of fusion, LOF (in.);

H = is the leg size of weld fillet or reinforcement (in.); and

t_p = is the thickness of the loaded plate (in.)

In the above equation, the expression within the parenthesis is a reduction factor for fatigue strength that is limited to a maximum value of 1. With increasing LOF, this factor reduces the fatigue resistance of the cruciform connection below that of AASHTO Category C details (due to increased likelihood of crack growth through the weld throat). The fatigue resistance of the detail for fatigue cracking at the weld toe is defined as Category C with the reduction factor assuming a value of 1 i.e., $(\Delta F)_n = (\Delta F)_n^c$.

For the rib-to-bulkhead plate connection details in Phase 2 prototype deck, the nominal values of *2a*, *H* and t_p were $^1/_8$ in. (3mm), $^1/_4$ in. (6 mm) and $^5/_8$ in. (15 mm), respectively (Figure 57). Substituting these values into Equation (8), the nominal fatigue resistance of the connection was obtained as:

$$(\Delta F)_n = 0.9 \times (\Delta F)_n^c \quad (9)$$

with fatigue cracking from the weld root controlling. Since the CAFT for the Category C detail is 10 ksi (69 MPa), the nominal fatigue resistance for this connection for infinite life was 9.0 ksi (62 MPa). In the finite life regime, the nominal S-N resistance curve of the detail was scaled from the AASHTO Category C design S-N curve. The

bulkhead-to-rib weld cracking occurred in Phase 1 through the throat of the weld. In Phase 1, this connection was fillet welded while in Phase 2 it was PJP beveled groove welded.

As discussed earlier, the cutout in the subfloor beam gave rise to the diagonal tension field under shear loading and magnified the stresses in the bulkhead plate near the cutout. Due to this complex distribution of stresses and the high stress gradient in the subfloor beam and the bulkhead plate adjacent to the cutout, the nominal stress at the subject detail could not be easily computed. Thus, the fatigue performance of the bulkhead plate-to-rib cruciform connection cannot be assessed based on the measurements. The maximum stresses at the stress concentration location obtained by the strain gauge measurements were influenced by the stress concentration due to the cutout and the weld toe notch. Nominal stresses are not influenced by such discontinuities, and are lower than the measured stresses at the weld toe surfaces. Hence it is safe to use the mean stresses (σ_m) as a more conservative approach for fatigue assessment.

In section 4.1.4, the variation of normal stress (normal to weld toe) through thickness of the bulkhead plate at the weld toe was presented and discussed (Figure 48). The stress at the mid surface does not contain the effects of the weld toe notch. This also removes the effect of any through thickness bending of the bulkhead plate, which was negligible as demonstrated in Figure 48. Thus, the mid surface stress only captured the magnification effect of the cutout in the subfloor beam. This through thickness stress when integrated, the mean stress value was obtained as 5.3 ksi (37 MPa) which is shown in Figure 209. This averaged stress was below nominal fatigue resistance curve obtained from Equation (9) and the infinite life fatigue resistance limit (Figure 210), and therefore

finite fatigue life of the detail (or fatigue cracking) was not expected.

The strain gauges on the bulkhead plates at the weld toes were applied in the direction normal to the weld toe. A rosette gauge was also installed adjacent to these gauges such that one arm of the rosette was normal to the weld toe and in the direction of diagonal tension field. The gauges on Rib 3 south face measured higher stresses, and therefore plotted against the FEA results in Figure 211. The steep stress gradient close to the weld toe can be considered as the weld notch effect. As it can be seen in the figure, the increment of the measured stresses toward the weld toe is comparable to the slope of the stress distribution if the notch effect was removed. Hence, the stress obtained from extrapolation of the stresses measured at channels 2014 and 2018 can be considered as the structural stress at the weld toe. As shown in the figure, the extrapolated stress was 4.6 ksi (32 MPa). This stress is lower than the IIW (Hobbacher 2007) CAFL for FAT 100 detail which is 12 ksi (83 MPa). Therefore, no fatigue cracking was observed which is consistent with the prediction made during the assessment of the detail made using FEA results in section 4.2.1.

In SFB1, the bulkhead plate gauges were reused from the Phase 1 testing. These gauges were oriented horizontal i.e. making 17° angle with the weld toe normal. Since this SFB was not considered critical for the test, further submodel analyses were not performed. The mesh size of the global model was 1 in. (25 mm), which is too coarse for obtaining converged stress profile at the bulkhead plate location. Hence, the fatigue performance of SFB1 cannot be assessed.

8.6.3 Performance of Rib-to-Deck Plate Connections

The fatigue performance of the rib-to-deck plate connection is evaluated in

Figures 212 and 213, where the fatigue test results for the Phase 1 and Phase 2 testing are presented on the AASHTO fatigue design S-N plot. The measured stress ranges were obtained at section Y-Y coincident with actuator #3, where strain gauges were provided on the top and bottom faces of the deck plate, and the inside and outside faces of the rib wall abutting the rib-to-deck plate connection at Rib 7. The same gauges were used in both Phase 1 and Phase 2 fatigue testing. For better accuracy, the plotted stress ranges were computed from the results of initial static tests performed at the beginning of each phases.

The stress ranges were obtained from the gauge adjacent to the west rib-to-deck plate connection, under the east load pad, where the rib-to-deck plate connection was subjected to the maximum stresses. The stress recorded by this gauge was compressive and remained compressive for all the transverse positions analyzed in Phase 1 (Alapati 2012). However, the presence of high tensile residual stresses at the weld toe can result in local tensile stress range leading to fatigue cracking from the weld toe.

As was shown earlier in sections 8.3 and 8.5, the stress ranges at the gauges remained constant throughout the fatigue tests for both phases, indicating that this rib-to-deck plate weld detail essentially remained undamaged. The rib-to-deck plate connection to the east of Rib 7 was subjected to a stress range of about 7.3 ksi (50 MPa) for 5 million cycles in Phase 1, and a stress range of about 4.7 ksi (32 MPa) for a combined 10 million cycles in Phase 2A and Phase 2B. The fatigue resistance of this connection detail is defined by AASHTO Category C against fatigue crack growth from the weld toe, having a CAFT of 10 ksi (69 MPa). Since the stress ranges in both phases of testing were well

below the CAFT, the connection detail exhibited infinite life. As such these tests are plotted independently.

9 CONCLUSION AND RECOMMENDATIONS

9.1 Conclusions

The Phase 2 study of the replacement orthotropic deck for the upper level of the signature bridge investigated the fatigue performance of a refurbished deck that was developed based on the recommendations of the Phase 1 study (Alapati, 2012). The primary focus of this investigation was the fatigue performance of the subfloor beam-to-rib connection and the bulkhead plate-to-rib connection at the intermediate subfloor beams. To reduce the high stresses in the subfloor beams and the bulkhead plates, the cutout was enlarged at the rib termination. The stresses at the fatigue critical details were further reduced by increasing the thicknesses of the subfloor beam from $^{5}/_{8}$ in. (16 mm) to $^{7}/_{8}$ in. (22 mm) and the bulkhead plate from $^{5}/_{16}$ in (8 mm) to $^{5}/_{8}$ in (16 mm). In addition, the number of subfloor beams between the floor beams was also increased from four to five, which reduced the spacing between the subfloor beams from 12 ft. $4^{1}/_{2}$ in. (3.467 m) to 8 ft. 3 in. (2.515 m). The bulk-head plate-to-rib welded connection over the top 7 in (178 mm) long critically stressed region was fabricated using a partial joint penetration weld.

The fatigue performance of the refurbished deck was evaluated by full size prototype testing of the modified Phase 1 specimen, where the intermediate floor beam was replaced to incorporate the improved design. Similar to the Phase 1 testing, the test setup simulated the global boundary conditions including the supporting floor framing. The deck was fatigue tested simulating the passage of the tandem axle of an AASHTO fatigue truck using hydraulic actuators. In the transverse direction the actuators were

positioned centrally on the deck, same as in the Phase 1 study. The longitudinal disposition of the actuators was determined by rolling a test truck representing a tandem axle centrally across the deck at a slow speed. Based on the deck response, four stationary hydraulic actuators were positioned in concentric and eccentric configuration about the intermediate subfloor beam SFB2a, and were loaded in paired sequence to simulate the passage of the tandem axle of an AASHTO fatigue truck across the intermediate subfloor beam.

The deck was tested for 5 million cycles at a load level equivalent to 3.45×HS15 (=3×0.75×HS20 or the HL-93 fatigue truck) including impact, to assess its fatigue performance for achieving 75 years' service life under site specific loading. A static test was performed prior to initiating the fatigue test to evaluate the base state of the structure. Additional static tests were performed intermittently during the fatigue test to assess the change in state of the deck and the critical details.

A full scale FE analysis of the prototype deck was done using ABAQUS. Based on its results, the deck was instrumented adequately to evaluate the deck response. The presence of the cutout in the subfloor beam caused high stress concentration in the bulkhead plate. The connection details at the intermediate subfloor beam at the cutout regions around ribs 3 and 7 were recognized as the fatigue critical locations due to high stress concentrations. Therefore, majority of the instrumentation was concentrated around these details in SFB2a to closely monitor the status and behavior of fatigue critical connections throughout the testing. The FEA data was also used in understanding the behavior of the deck and assessing the fatigue strengths of the rib-to-SFB, rib-to-deck plate and rib-to-bulkhead plate connection details. The fatigue resistance of the most

critical detail of rib-to-SFB2a was also assessed using local stress based approaches (hot spot stress and notch stress approaches). No significant conclusion could be made from the hot spot stress approach. However, the notch stress approach provided better correlation with the experimental results.

The deck specimen was subjected to 5 million cycles each time in Phase 2A and Phase 2B fatigue testing. The Phase 2B testing was required due to the use of erroneous loading protocol in Phase 2A. A strict inspection regimen was followed to inspect the deck specimen during the fatigue testing in which all the fatigue critical location were visually inspected and the stresses were monitored for any indication of changes in the condition of the deck specimen. The entire deck was carefully inspected after both Phase 2A and 2B testing, and static test data were compared throughout the testing. However, no indication of fatigue cracking was observed anywhere on the Phase 2 prototype deck.

The Phase 2 study verified that the refurbished deck would provide a 75 years' service life under site specific loading. With the design improvements the stresses at the fatigue critical details reduced significantly. The measured stress ranges at all details except at the cutout edge were at or below the constant amplitude fatigue threshold (CAFT) of their respective detail categories.

9.1.1 Deck Response Characteristics

The study demonstrated that the response of the orthotropic deck was characterized by global longitudinal and transverse flexure of the entire deck, and significant local distortion under the wheel loads. The deformations and high stresses were concentrated under the load patches and decreased rapidly away from the load patches. The deck plate experienced one stress cycle due to each axle of a tandem,

whereas the other deck elements such as the subfloor beams, stringer extensions and bulkhead plates, experienced one stress cycle for each passage of the tandem axles with small or no effect due to individual axles.

The load bearing subfloor beams experienced significant stress concentrations at the rib-to-subfloor beam cutouts. High stress concentrations were also found in the bulkhead plates at the cutouts and at the diagonally opposite corners at the top. These stresses were mostly in plane and the out-of-plane component was negligible. Compared to the intermediate subfloor beam the end subfloor beam that was placed on the floor beam experienced less stress.

9.1.2 Performance of the Rib-to-Deck Connection

The ribs were welded to the deck using a specified minimum 80% partial joint penetration weld and were inspected by Phased Array Ultrasonic Testing (PAUT) during fabrication. Since the deck plate was the primary member of the deck experiencing loading, the rib-to-deck plate welded connections experienced stress cycles for individual axles during the passage of the crawl truck. During fatigue testing, this detail was subjected to a stress range of about 4.7 ksi (32 MPa). The maximum stresses measured by strain gauges were found to be below the CAFT for the detail category when plotted in AASHTO S-N curve. Due to the use of incorrect loading protocol in Phase 2A, this connection detail experienced a total of 10 million cycles which is incidentally equal to 5 million cycles of vehicular loading. The rib-to-deck plate connection that was studied in Phase 2 belonged to the portion of the deck retained from the Phase 1 testing in which it was subjected to higher stress range of about 7.3 ksi (50 MPa).

9.1.3 Performance of the Rib-to-Subfloor Beam Connection

The subfloor beams were welded to the ribs using complete joint penetration weld at the cutout for 4 in (102 mm), transitioning to a partial joint penetration weld above it. Unlike Phase 1, these connections were provided with beveled groove welds. High stresses were observed at the subfloor beam cutouts.

The performance of rib-to-SFB2a connections were also assessed using local stress based approaches for stresses obtained from FE analyses. The hot spot stress methods recommended by Radaj (2006) and IIW (Hobbacher 2007) showed that the hot spot stresses obtained by the quadratic extrapolations at the hot spot was below the CAFL while that obtained by linear extrapolation was on the finite life line FAT line recommended by IIW (Hobbacher 2007). Since no fatigue cracking was observed on the deck, no conclusion can be made of this observation.

The hot spot stress method used by ship classification societies was recommended by AASHTO for performing fatigue assessment. The extrapolated stress for the method recommended by AASHTO showed stress that was higher than the CAFT value for the AASHTO Category C detail. According to this result the detail should have cracked at 1.4 million cycles. Since no fatigue cracks were observed at the completion of the experiment, it can be said that this method of assessment may not be applicable for orthotropic decks.

The notch stress approach however had predicted an infinite life for the rib-to-SFB2a detail. The predicted infinite life fatigue resistance from notch stress approach was 30.7 ksi (192 MPa) for the rib-to-SFB2a welded connection and the calculated notch stress at the weld toe from FEA results was 23.8 ksi (164 MPa). Based on the survival of

the deck this approach may be considered as a suitable method of assessing infinite fatigue life of orthotropic bridge decks.

The stress range normal to the intermediate subfloor beam-to-rib weld toe was 10.2 ksi (70 MPa), slightly less than the CAFT of the AASHTO Category C′ details. The stress ranges at the bulkhead plate were significantly less than the CAFT of AASHTO Category C details. The measured stress range normal to the weld termination at the edge of the cutout was 17.2 ksi (119 MPa). The fatigue resistance of this detail against cracking from the ground smooth weld toe at the edge of a plate is defined as AASHTO Category B. The measured stress range was higher than the CAFT of the AASHTO Category B details. The performance of this connection, however, exceeded the lower bound or 95% confidence on the 95% probability of survival life for the Category A details (i.e. base metal condition), which is close to the upper bound or 95% confidence on the 95% probability of failure life of the Category B details. Recognizing that the recommended CAFT values are conservative lower bound to limited fatigue test data, it can be concluded that the ground smooth weld termination at the edge of the cutout demonstrated infinite life.

9.1.4 Performance of the Bulkhead Plate-to-Rib Connection

The cutout below the rib soffit in the subfloor beam caused high stress concentration in the bulkhead plates. Pertaining to modifications from Phase 1, the bulkhead plates were attached to the ribs by 7 in. (178 mm) back-to-back beveled groove welds from the top of the bulkhead plates. This PJP detail was seen to be vulnerable to root cracking as it was in Phase 1. The maximum stresses measured at the rib-to-bulkhead plate detail were compared against fatigue resistance S-N curve of AASHTO

Category C with the reduction factor calculated based on the LOF at the connection. The nominal stress of 5.3 ksi (37 MPa) was obtained by averaging the through thickness stress at the weld toe. The extrapolated stress using the strain gauge measurements was 4.6 ksi (32 MPa). The hot spot stress obtained using the FEA result was 5.9 ksi (41 MPa). All these stresses as well as the stresses measured by the gauges at this detail were below the nominal SN resistance curve obtained by applying the reduction factor.

The fatigue testing of the prototype orthotropic deck was useful in understanding the behavior of deck and the deck elements under various loading conditions. Complex stress state and high stress concentrations that occurred at the subfloor beam-to-rib and rib to bulkhead plate connections in the presence of cutouts, when the subfloor beam was made integral with the stringers. Full scale fatigue tests are essential for proof testing of orthotropic decks and for developing adequate database and robust specification. The prototype testing provided critical information on issues related to fabrication and deck installation, design improvement and optimization, expected response of the orthotropic deck in service, and the effectiveness of the replacement deck design in achieving more than 100 years service life.

9.2 Recommendations

The prototype testing provided critical information on issues related to fabrication and deck installation, design improvement and optimization, expected response of the orthotropic deck in service, and the effectiveness of the replacement deck design in achieving more than 75 years' service life. Also the recommendations used from Phase 1 testing for the enhancements in design and fabrication of the deck were successfully tested. Success of orthotropic decks in providing a maintenance free service life primarily

depends on the quality of fabrication. Stringent inspection, including destructive and advanced non-destructive testing, and quality control should be implemented for fabrication of the replacement deck. The lessons learnt from the prototype testing should provide useful information in developing a robust quality assurance plan.

The size and details of the end subfloor beams that are supported on the main floor beams were different than the intermediate subfloor beams. The maximum stresses in the intermediate subfloor beams and the bulkhead plates at the rib cutouts were about 10.2 ksi (70 MPa), close to the AASHTO CAFT of the Category C′ details. Significant cracking at the bulkhead plate-to-rib welds were noted at this subfloor beam, where a fillet welded connection was used. It is recommended that the details of the end subfloor beam be the same as the intermediate subfloor beams.

TABLES

Table 1 Details of FEA Models

Models	No. of elements	No. of nodes	No. of degrees of freedom	Desired length of element (in)
Global Model	768,576	4,970,631	14,911,899	1
Submodel 1	198,054	1,119,765	3,359,295	$^1/_2$
Submodel 2	155,105	701,585	2,104,755	$^1/_4$
Submodel 3	315,834	1,389,506	4,168,518	$^1/_8$
Submodel 4	269,222	1,175,596	3,526,788	$^1/_{16}$
Submodel 5	56,928	246,180	738,540	$^1/_{32}$
Submodel 6	269,222	302,267	906,801	$^1/_{64}$
Submodel 2A	1,796	10,532	34,596	$^7/_8$

Table 2 Aspect Ratio for Submodel Elements

	Aspect ratio > 5		Aspect ratio >10		Aspect ratio > 15		Average aspect ratio	Largest aspect ratio
Submodel	No. of elements	%Total	No. of elements	% Total	No. of elements	% Total		
SM1	7940	4.01	3120	1.58			2.8	15.8
SM2	288	0.19	2	0.00			1.6	10.2
SM3	55	0.02	0	0.00			1.5	8.5
SM4	7456	2.77	316	0.12			1.6	11.3
SM5	26370	17.12	26070	16.93	5746	3.73	3.6	17.2
SM6	0	0.00	0	0.00			1.6	3.4
SM2A	1197	28.12	236	5.54	75	1.76	4.2	26.0

Table 3 Maximum and Minimum Face Angles for Submodel Elements

	Minimum angle < 10^o		Minimum angle < 45^o		Average minimum angle (degrees)	Smallest minimum angle (degrees)	Maximum angle > 160^o		Average maximum angle (degrees)	largest maximum angle (degrees)
Submodel	No. of elements	% Total	No. of elements	% Total			No. of elements	% Total		
SM1	40	0.02	4149	2.13	78	6	40	0.02	102	172
SM2	43	0.03	8388	5.62	74	3	281	0.19	106	182
SM3	50	0.02	1716	0.54	81	2	65	0.02	100	191
SM4	1,186	0.44	16666	6.19	72	3	4152	1.54	108	178
SM5	0	0.00	7938	13.94	65	12	1465	2.57	12	172
SM6	0	0.00	3502	0.20	71	45	0	0.00	109	135
SM2A	9	0.50	361	20.10	64	3	12	0.67	116	172

Table 4 Submodel Element Lengths Compared to Desired Length

	Minimum edge length < 0.5 × l		Minimum edge length < 0.25 × l		Maximum edge length > 1.25 × l		Maximum edge length > 1.5 × l	
Submodel	No. of elements	% Total	No. of elements	% Total	No. of elements	% Total	No. of elements	% Total
SM1	143164	72.29	8060	4.07	52374	26.44	28	0.01
SM2	1346	0.87	280	0.18	5651	3.64	133	0.09
SM3	2046	0.65	46	0.01	20851	6.60	3267	1.03
SM4	12520	4.65	8272	3.07	81537	30.29	33338	12.38
SM5	26647	17.30	26172	17.00	64827	42.10	39319	25.53
SM6	118142	6.88	0	0.00	612744	35.68	423578	24.66
SM2A	3440	80.81	1411	33.15	347	8.15	90	2.11

Table 5 Weight Measurement of the Test Truck

Items	Weight measured by each scale (lbs)				Total Weight (lbs)
	Front Left	Front Right	Rear Left	Rear Right	
Truck	3700	3250	3250	3900	14100
Truck + 1 Billet	5400	6800	4900	7600	24700
Truck + 2 Billets	8950	8350	8500	9400	35200
Truck + 3 Billets	12050	9900	11450	10900	44300
Truck + 4 Billets	13000	13450	13200	14050	53700
Truck + 5 Billets	14700	16100	15850	16000	62650

Table 6 Loading Protocol for Phase 2A Testing and Static Tests

Load Step	Actuator						
	Load (kip)				Displacement (in)		
	Actuator 3	Actuator 4	Actuator 5	Actuator 6	Actuator 7	Actuator 8	Actuator 9
0	-3.00	-3.00	-3.00	-3.00	0.00	0.00	0.00
1	-44.40	-3.00	-44.40	-3.00	0.07	0.07	0.10
2	-3.00	-44.40	-3.00	-44.40	0.12	0.13	0.07

Table 7 Principal Stresses for 1mm Rosette Gauges at the Cutout Termination

		CH #			Principal stress (ksi)	
Location	Face	Gauge 1	Gauge 2	Gauge 3	Max	Min
Rib 3	North	2051	2050	2049	9.81	1.37
	South	2059	2058	2057	8.25	1.50
Rib 7	North	2126	2125	2124	7.61	0.98
	South	2134	2133	2132	7.39	1.05

Notes:
Gauge 1: Gauge tangent to cutout
Gauge 2: Diagonal gauge
Gauge 3: Gauge perpendicular to Gauge 1

Table 8 Principal Stresses for Rosette Gauges on West of Rib 3 and East of Rib 7 at Cutout Terminations

		CH #			Principal stress (ksi)	
Location	Face	Gauge 1	Gauge 2	Gauge 3	Max	Min
Rib 3	North	2034	2035	2036	-0.82	-6.13
	South	2046	2047	2048	-0.59	-6.21
Rib 7	North	2109	2110	2111	-0.33	-4.69
	South	2121	2122	2123	-0.77	-5.99

Notes:
Gauge 1: Gauge parallel to rib-to-SFB weld toe
Gauge 2: Diagonal gauge
Gauge 3: Gauge perpendicular to rib-to-SFB weld toe

Table 9 Principal Stresses for Rosette Gauges on East of Rib 3 and West of Rib 7

Location	Face	CH #			Principal stress (ksi)	
		Gauge 1	Gauge 2	Gauge 3	Max	Min
Rib 3 (5 in below Deck Plate)	North	2025	2026	2027	1.16	0.22
	South	2037	2038	2039	1.27	0.23
Rib 3 (6 in below Deck Plate)	North	2028	2029	2030	2.91	0.44
	South	2040	2041	2042	3.15	0.56
Rib 7 (5 in below Deck Plate)	North	2100	2101	2102	1.64	0.28
	South	2112	2113	2114	1.38	0.22
Rib 7 (6 in below Deck Plate)	North	2103	2104	2105	4.07	0.55
	South	2115	2116	2117	3.50	0.52

Notes:
Gauge 1: Gauge parallel to rib-to-SFB weld toe
Gauge 2: Diagonal gauge
Gauge 3: Gauge perpendicular to rib-to-SFB weld toe

Table 10 Maximum and Minimum Stresses for 1mm Strip Gauges Adjacent to 1mm Rosettes at Ribs 3 and 7 Cutout Termination

Rib	North Face			South Face		
	CH #	Max	Min	CH #	Max	Min
Rib 3	2052	9.06	1.32	2060	8.28	1.51
	2053	8.05	1.21	2061	7.84	1.44
	2054	7.64	1.12	2062	7.57	1.38
	2055	7.32	1.08	2063	6.95	1.21
	2056	7.80	1.16	2064	6.88	1.20
Rib 7	2127	7.86	1.05	2135	7.60	1.02
	2128	7.43	0.94	2136	8.58	1.14
	2129	7.30	0.99	2137	7.25	1.01
	2130	6.65	0.87	2138	6.75	0.89
	2131	6.86	0.88	2139	6.27	0.80

Table 11 Maximum and Minimum Stresses for 1mm Strip Gauges on the Cutouts (Mid Thickness) of Ribs 3 and 7

Rib 3 Cutout			Rib 7 Cutout		
CH #	Max	Min	CH #	Max	Min
2065	9.87	1.78	2140	9.09	1.36
2066	10.63	1.87	2141	8.38	1.22
2067	10.8	1.89	2142	10.07	1.48
2068	10.79	1.86	2143	10.74	1.55
2069	11.14	1.88	2144	10.61	1.44
2070	8.84	1.38	2145	10.40	1.41
2071	8.38	1.29	2146	9.76	1.34
2072	8.06	1.20	2147	10.04	1.30
2073	8.16	1.21	2148	9.54	1.24
2074	8.30	1.19	2149	9.77	1.14

Table 12 Maximum and Minimum stresses for uniaxial gauges on Ribs 3 and 7 Bulkhead Plates

Rib 3				Rib 7			
		Measurements (ksi)				Measurements (ksi)	
Face	CH #	Max	Min	Face	CH #	Max	Min
North	2001	1.66	-0.43	North	2076	2.82	0.67
South	2013	2.00	-0.20	South	2088	2.66	0.66
North	2002	1.87	-0.38	North	2077	Bad	Bad
South	2014	0.56	-1.57	South	2089	2.30	0.57
North	2003	0.68	-0.47	North	2078	2.41	1.25
South	2015	0.64	-0.36	South	2090	1.25	0.32
North	2010	2.79	0.35	North	2085	2.62	0.33
South	2022	2.83	0.41	South	2097	2.91	0.36
North	2011	3.22	0.43	North	2086	3.00	0.35
South	2023	3.25	0.47	South	2098	3.32	0.39
North	2012	4.22	0.28	North	2087	4.95	1.05
South	2024	3.62	0.18	South	2099	Bad	Bad

Table 13 Crawl Test Principal Stresses for Rosette Gauges on Ribs 3 and 7 Bulkhead Plates

		CH #			Principal Stress (ksi)	
Location	Face	Gauge 1	Gauge 2	Gauge 3	Max	Min
Rib 3	North	2004	2005	2006	2.14	-0.98
East	South	2016	2017	2018	1.89	-0.98
Rib 3	North	2007	2008	2009	1.64	-1.49
Central	South	2019	2020	2021	1.49	-1.57
Rib 7	North	2079	2080	2081	1.08	-1.57
West	South	2091	2092	2093	1.95	-0.88
Rib 7	North	2082	2083	2084	2.66	-0.39
Central	South	2094	2095	2096	1.63	-1.45

Notes:

For rosettes close to cutout
Gauge 1: Gauge parallel to rib-to-bulkhead weld toe
Gauge 2: Diagonal gauge
Gauge 3: Gauge perpendicular to rib-to-bulkhead weld toe

For rosettes at the center of bulkhead plates
Gauge 1: Gauge along compression diagonal
Gauge 2: Vertical gauge
Gauge 3: Gauge along tension diagonal

Table 14 Principal and Normal Stresses Measured from 1mm Rosette Gauges at Cutouts for Load Step 1

Location	Face	Channel ID	Computed from measurements[a] φ[c] (deg)	σ_p[d] (ksi[b])	σ_q[e] (ksi[b])	σ[f] (ksi[b])	Angles measured from images β[h] (deg)	α[i] (deg)	σ_n[g] (ksi[b]) for P_R[j] = 82.8 kips
Rib 3	North	2049	41.84	13.32	1.52	8.08	8.0	40.2	8.41
		2050				13.28			
		2051				6.76			
	South	2057	5.05	13.43	1.59	13.33	-36.0	41.1	8.32
		2058				6.43			
		2059				1.69			
Rib 7	North	2124	43.49	9.88	1.80	6.09	20.0	23.5	8.60
		2125				9.88			
		2125				5.6			
	South	2132	-5.58	11.95	0.95	11.84	-40.0	--45.6	6.34
		2133				5.36			
		2134				1.06			

Notes:

[a]Tensile stresses are positive.

[b]1 ksi = 6.91 MPa

Refer for definition of parameters

[c]ϕ : direction of maximum principal stress

[d]σ_p : maximum principal stress range

[e]σ_q : minimum principal stress range

[f]σ : stress range in rosette arms

[g]σ_n : stress range normal to weld toe

[h]β : angle between gauge 1 and normal to weld toe

[i]α : angle between the principal stress and the normal to weld toe

[j]P_R : load range applied on the deck specimen

Table 15 Principal and Normal Stresses Measured from 1mm Rosette Gauges at Cutout for Load Step 2 using Technique 2

Location	Face	Channel ID	Computed from measurements[a] φ^c (deg)	$\sigma_p{}^d$ (ksi)	$\sigma_q{}^e$ (ksi[b])	σ^f (ksi)	Angles measured from images β^h (deg)	α^i (deg)	$\sigma_n{}^g$ (ksi[b]) for $P_R{}^j$ = 82.8 kips
Rib 3	North	2049	42.29	15.8	1.83	9.47	8.0	40.2	10.10
		2050				15.77			
		2051				8.16			
	South	2057	3.22	14.47	1.8	14.44	-36.0	41.1	9.41
		2058				7.44			
		2059				1.84			
Rib 7	North	2124	44.85	11.92	2.22	7.09	20.0	23.5	10.21
		2125				11.92			
		2125				7.04			
	South	2132	-3.95	14.08	1.18	14.03	-40.0	-45.6	7.87
		2133				6.77			
		2134				1.24			

Notes:

[a]Tensile stresses are positive.

[b]1 ksi = 6.91 MPa

Refer for definition of parameters

[c]ϕ : direction of maximum principal stress

[d]σ_p : maximum principal stress range

[e]σ_q : minimum principal stress range

[f]σ : stress range in rosette arms

[g]σ_n : stress range normal to weld toe

[h]β : angle between gauge 1 and normal to weld toe

[i]α : angle between the principal stress and the normal to weld toe

[j]P_R : load range applied on the deck specimen

Table 16 Maximum Principal Stress in SFB2a to the Bottom West Cutout of Rib 3

	Measurements		Computed principal stresses and directions			
Face	Channel ID	Stress[a] (ksi[b])	Maximum σ_p (ksi[b])	Minimum σ_q (ksi[b])	Direction[c] φ (degrees)	Illustration[d]
North	2031	4.66	7.8	-0.1	38.9	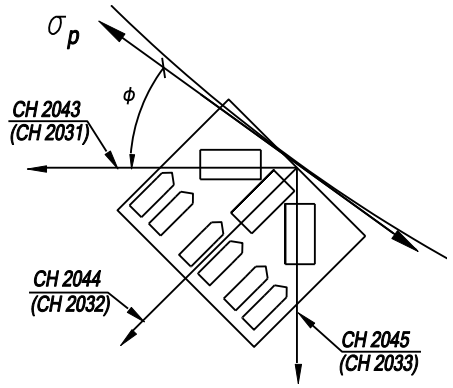
	2032	-0.05				
	2033	2.98				
South	2043	4.93	7.7	-0.2	36.5	
	2044	-0.04				
	2045	2.59				

Notes:
[a] Tensile stresses are positive.
[b] 1 ksi = 6.91 MPa.
[c] Orientation of the maximum principal stress as shown in the illustration measured from the weld toe normal as counterclockwise positive.
[d] Illustration drawn on the south face, looking north. The north face gauge channels are shown in parentheses

Table 17 Maximum Principal Stress in SFB2a to the Bottom East Cutout of Rib 7

	Measurements		Computed principal stresses and directions			
Face	Channel ID	Stress[a] (ksi[b])	Maximum σ_p (ksi[b])	Minimum σ_q (ksi[b])	Direction[c] φ (degrees)	Illustration[d]
North	2106	4.79	8.0	-0.1	-39.2	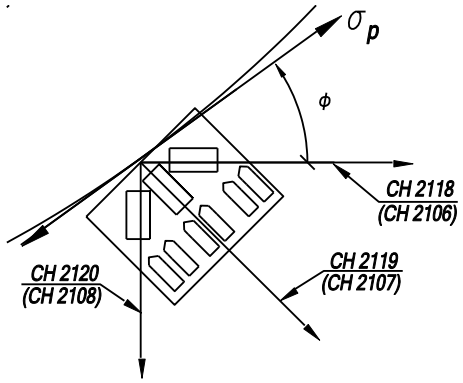
	2107	0.01				
	2108	3.15				
South	2118	5.79	8.2	0.4	34	
	2119	0.68				
	2120	2.85				

Notes:
[a] Tensile stresses are positive.
[b] 1 ksi = 6.91 MPa.
[c] Orientation of the maximum principal stress as shown in the illustration measured from the weld toe normal as counterclockwise positive.
[d] Illustration drawn on the south face, looking north. The north face gauge channels are shown in parentheses

Table 18 Measured Principal Stress in SFB2a to the East of Rib 3 – at 5 in from Deck Plate along Rib-to-SFB Weld Toe

	Measurements		Computed principal stresses and directions			
Face	Channel ID	Stress[a] (ksi[b])	Maximum σ_p (ksi[b])	Minimum σ_q (ksi[b])	Direction[c] φ (degrees)	Illustration[d]
North	2025	1.94	1.7	0.0	52.8	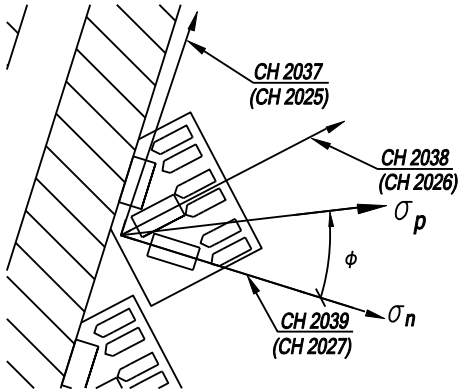
	2026	-0.84				
	2027	-3.25				
South	2037	1.33	2.2	0.0	42.4	
	2038	0.91				
	2039	-2.88				

Notes:
[a] Tensile stresses are positive.
[b] 1 ksi = 6.91 MPa.
[c] Orientation of the maximum principal stress as shown in the illustration measured from the weld toe normal as counterclockwise positive.
[d] Illustration drawn on the south face, looking north. The north face gauge channels are shown in parentheses

Table 19 Measured Principal Stress in SFB2a to the East of Rib 3 – at 6 in from Deck Plate along Rib-to-SFB Weld Toe

	Measurements		Computed principal stresses and directions			
Face	Channel ID	Stress[a] (ksi[b])	Maximum σ_p (ksi[b])	Minimum σ_q (ksi[b])	Direction[c] φ (degrees)	Illustration[d]
North	2028	2.70	4.4	2.1	31.4	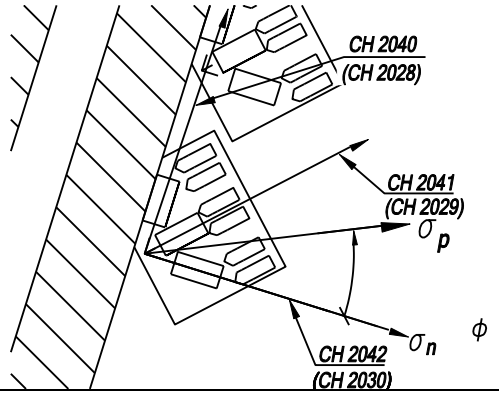
	2029	4.29				
	2030	3.78				
South	2040	3.12	5.4	2.2	32.5	
	2041	5.27				
	2042	4.49				

Notes:
[a] Tensile stresses are positive.
[b] 1 ksi = 6.91 MPa.
[c] Orientation of the maximum principal stress as shown in the illustration measured from the weld toe normal as counterclockwise positive.
[d] Illustration drawn on the south face, looking north. The north face gauge channels are shown in parentheses

Table 20 Measured Principal Stress in SFB2a to the West of Rib 3 Adjacent to Cutout Termination

	Measurements		Computed principal stresses and directions			
Face	Channel ID	Stress[a] (ksi[b])	Maximum σ_p (ksi[b])	Minimum σ_q (ksi[b])	Direction[c] φ (degrees)	Illustration[d]
North	2034	-4.34	-4.2	-13.0	-6.9	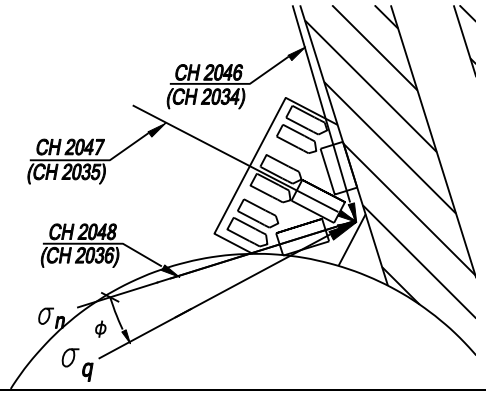
	2035	-9.65				
	2036	-12.86				
South	2046	-4.31	-4.3	-12.9	3.4	
	2047	-8.09				
	2048	-12.88				

Notes:
[a] Tensile stresses are positive.
[b] 1 ksi = 6.91 MPa.
[c] Orientation of the maximum principal stress as shown in the illustration measured from the weld toe normal as counterclockwise positive.
[d] Illustration drawn on the south face, looking north. The north face gauge channels are shown in parentheses

Table 21 Measured Principal Stress in SFB2a to the West of Rib 7 – at 5 in from Deck Plate along Rib-to-SFB Weld Toe

	Measurements		Computed principal stresses and directions			
Face	Channel ID	Stress[a] (ksi[b])	Maximum σ_p (ksi[b])	Minimum σ_q (ksi[b])	Direction[c] φ (degrees)	Illustration[d]
North	2100	1.40	2.4	0.7	39.4	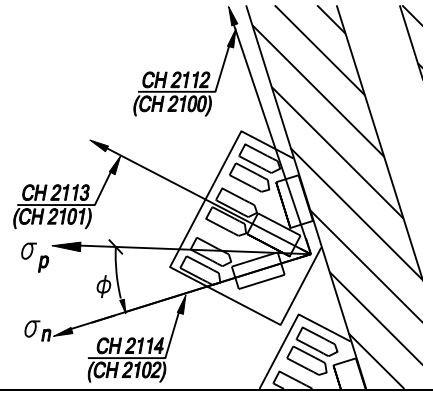
	2101	2.40				
	2102	1.73				
South	2112	0.91	1.8	-0.1	46.6	
	2113	1.79				
	2114	0.80				

Notes:
[a] Tensile stresses are positive.
[b] 1 ksi = 6.91 MPa.
[c] Orientation of the maximum principal stress as shown in the illustration measured from the weld toe normal as counterclockwise positive.
[d] Illustration drawn on the south face, looking north. The north face gauge channels are shown in parentheses

Table 22 Measured Principal Stress in SFB2a to the West of Rib 7 – at 6 in from Deck Plate along Rib-to-SFB Weld Toe

	Measurements		Computed principal stresses and directions			
Face	Channel ID	Stress[a] (ksi[b])	Maximum σ_p (ksi[b])	Minimum σ_q (ksi[b])	Direction[c] φ (degrees)	Illustration[d]
North	2103	3.19	6.4	3.0	14.7	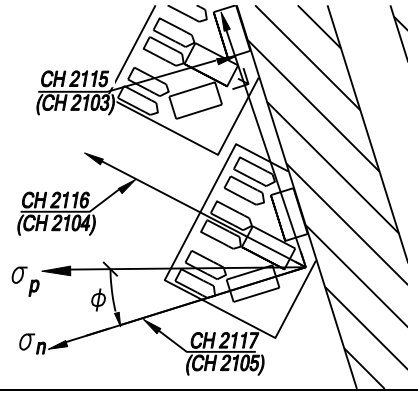
	2104	5.49				
	2105	6.13				
South	2115	2.99	5.6	2.4	25.0	
	2116	5.24				
	2117	5.05				

Notes:
[a] Tensile stresses are positive.
[b] 1 ksi = 6.91 MPa.
[c] Orientation of the maximum principal stress as shown in the illustration measured from the weld toe normal as counterclockwise positive.
[d] Illustration drawn on the south face, looking north. The north face gauge channels are shown in parentheses

Table 23 Measured Principal Stress in SFB2a to the East of Rib 7 Adjacent to Cutout Termination

	Measurements		Computed principal stresses and directions			
Face	Channel ID	Stress[a] (ksi[b])	Maximum σ_p (ksi[b])	Minimum σ_q (ksi[b])	Direction[c] φ (degrees)	Illustration[d]
North	2109	-3.64	-3.4	-9.8	11.4	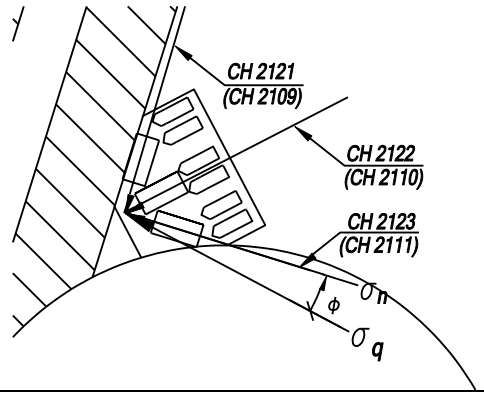
	2110	-5.34				
	2111	-9.52				
South	2121	-3.52	-3.4	-10.9	-7.2	
	2122	-8.07				
	2123	-10.76				

Notes:
[a] Tensile stresses are positive.
[b] 1 ksi = 6.91 MPa.
[c] Orientation of the maximum principal stress as shown in the illustration measured from the weld toe normal as counterclockwise positive.
[d] Illustration drawn on the south face, looking north. The north face gauge channels are shown in parentheses

Table 24 Maximum Principal Stress in SFB2a Bulkhead Plate towards East Cutout of Rib 3

	Measurements		Computed principal stresses and directions			
Face	Channel ID	Stress[a] (ksi[b])	Maximum σ_p (ksi[b])	Minimum σ_q (ksi[b])	Direction[c] φ (degrees)	Illustration[d]
North	2004	-1.59	3.2	-1.7	8.2	
	2005	1.44				
	2006	3.09				
South	2016	-1.52	3.1	-1.6	6.5	
	2017	1.30				
	2018	3.06				

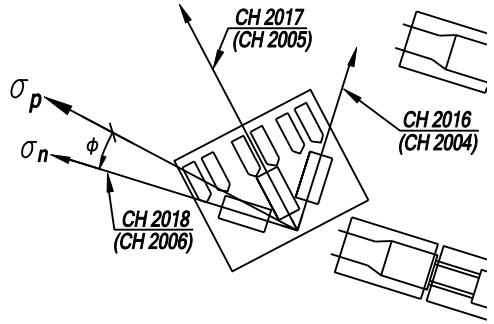

Notes:
[a] Tensile stresses are positive.
[b] 1 ksi = 6.91 MPa.
[c] Orientation of the maximum principal stress as shown in the illustration measured from the weld toe normal as counterclockwise positive.
[d] Illustration drawn on the south face, looking north. The north face gauge channels are shown in parentheses

Table 25 Maximum Principal Stress in SFB2a Bulkhead Plate central in Rib 3

	Measurements		Computed principal stresses and directions			
Face	Channel ID	Stress[a] (ksi[b])	Maximum σ_p (ksi[b])	Minimum σ_q (ksi[b])	Direction[c] φ (degrees)	Illustration[d]
North	2007	2.57	2.6	-3.1	0.4	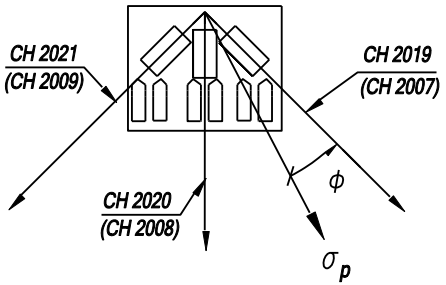
	2008	-0.22				
	2009	-3.09				
South	2019	2.22	2.2	-3.3	0.2	
	2020	-0.51				
	2021	-3.28				

Notes:
[a] Tensile stresses are positive.
[b] 1 ksi = 6.91 MPa.
[c] Orientation of the maximum principal stress as shown in the illustration measured from the weld toe normal as counterclockwise positive.
[d] Illustration drawn on the south face, looking north. The north face gauge channels are shown in parentheses

Table 26 Maximum Principal Stress in SFB2a Bulkhead Plate towards West Cutout of Rib 7

	Measurements		Computed principal stresses and directions			
Face	Channel ID	Stress[a] (ksi[b])	Maximum σ_p (ksi[b])	Minimum σ_q (ksi[b])	Direction[c] φ (degrees)	Illustration[d]
North	2079	-1.38	2.7	-1.5	-7.9	
	2080	0.07				
	2081	2.67				
South	2091	-1.54	2.7	-1.6	8.6	
	2092	1.18				
	2093	2.61				

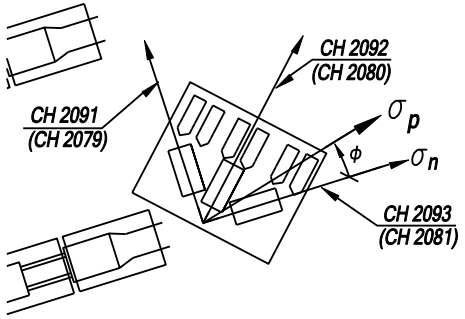

Notes:
[a] Tensile stresses are positive.
[b] 1 ksi = 6.91 MPa.
[c] Orientation of the maximum principal stress as shown in the illustration measured from the weld toe normal as counterclockwise positive.
[d] Illustration drawn on the south face, looking north. The north face gauge channels are shown in parentheses

Table 27 Maximum Principal Stress in SFB2a Bulkhead Plate central in Rib 7

	Measurements		Computed principal stresses and directions			
Face	Channel ID	Stress[a] (ksi[b])	Maximum σ_p (ksi[b])	Minimum σ_q (ksi[b])	Direction[c] φ (degrees)	Illustration[d]
North	2082	1.94	1.9	-3.3	-2	
	2083	-0.84				
	2084	-3.25				
South	2094	1.33	1.9	-3.5	19.4	
	2095	0.91				
	2096	-2.88				

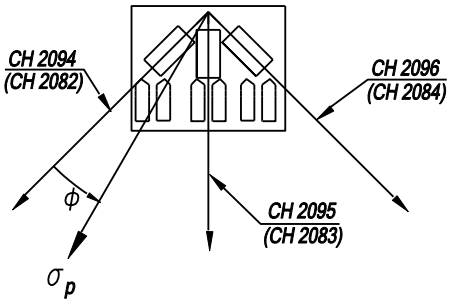

Notes:
[a] Tensile stresses are positive.
[b] 1 ksi = 6.91 MPa.
[c] Orientation of the maximum principal stress as shown in the illustration measured from the weld toe normal as counterclockwise positive.
[d] Illustration drawn on the south face, looking north. The north face gauge channels are shown in parentheses

FIGURES

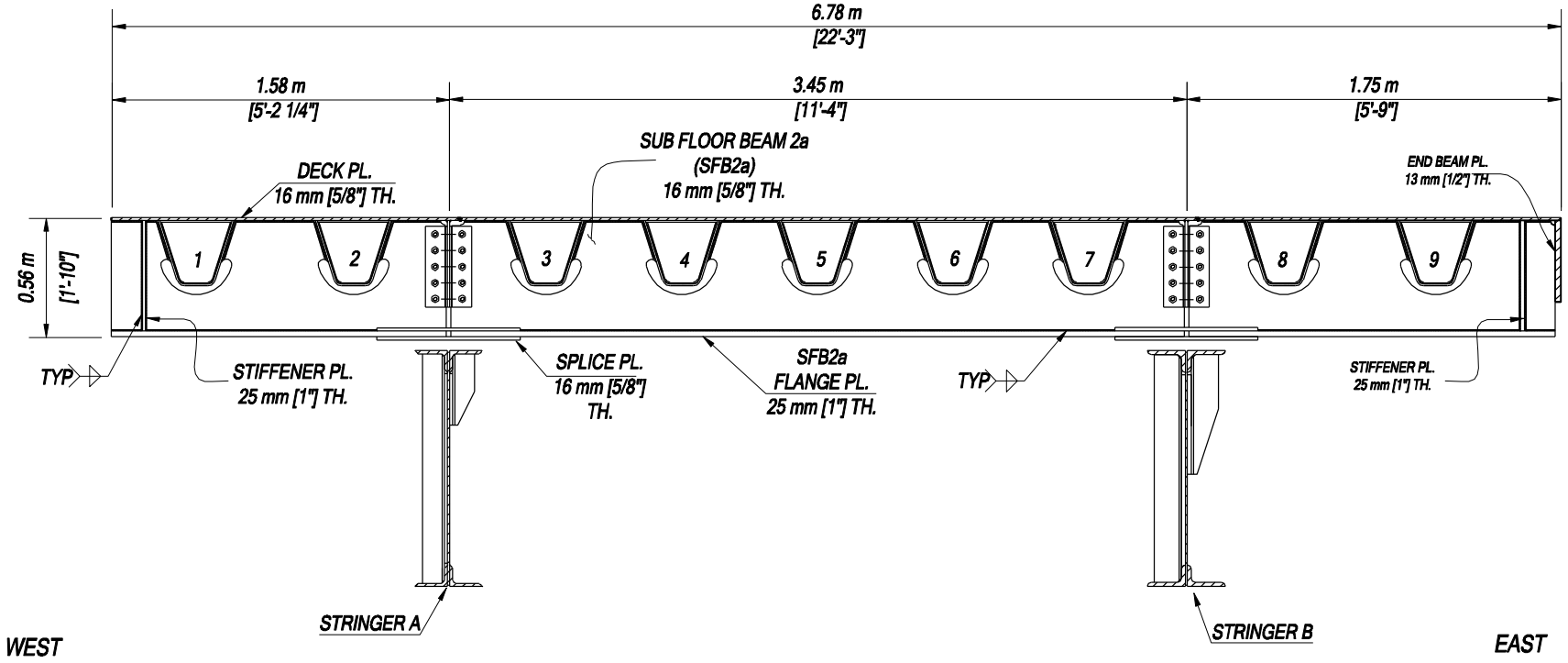

Figure 1 A typical section of the Phase 1 deck at intermediate subfloor beam (prepared by R. S. Deo Alapati)

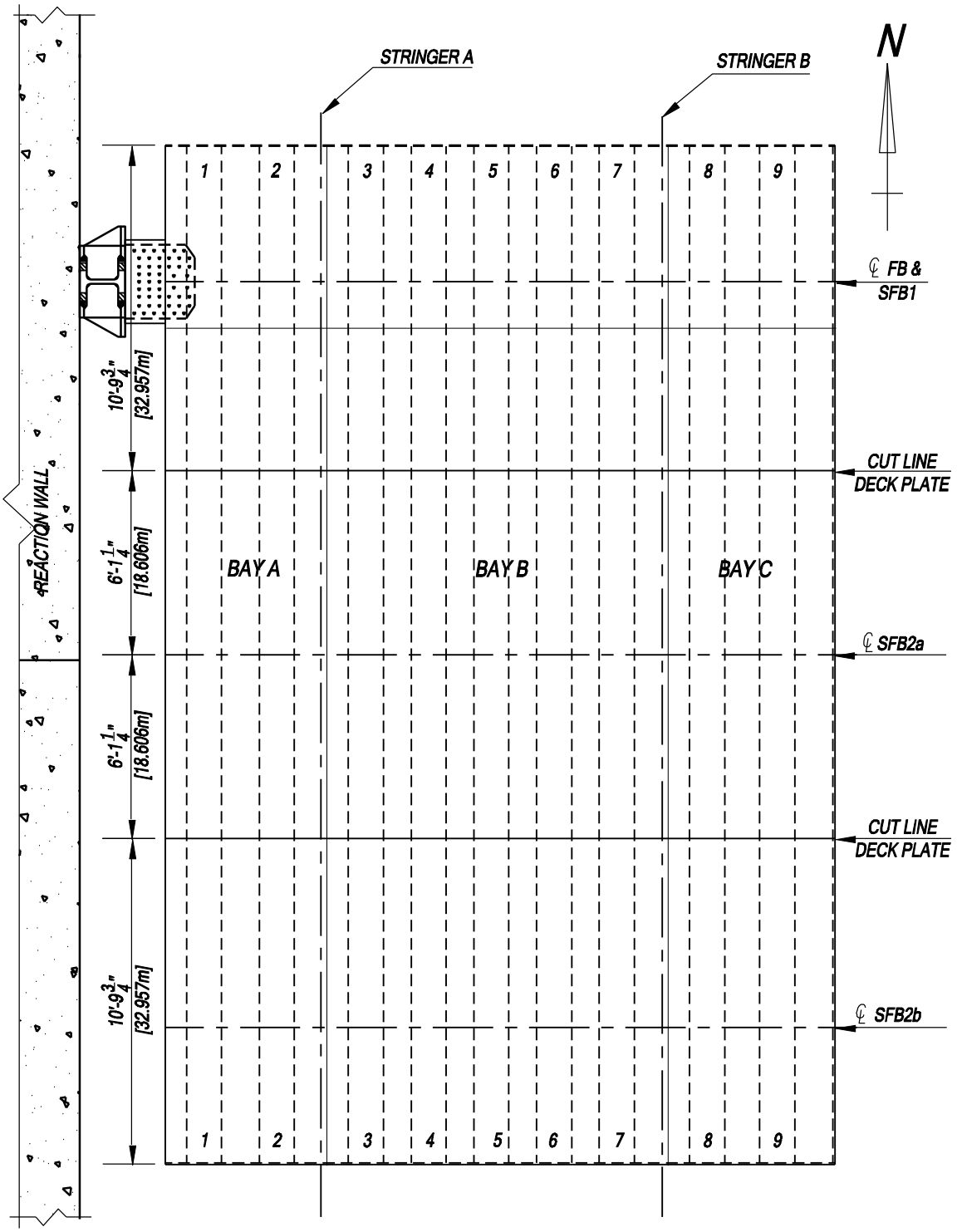

Figure 2 Plan view of the Phase 1 deck with cut lines marked (prepred by R.S. Deo Alapati)

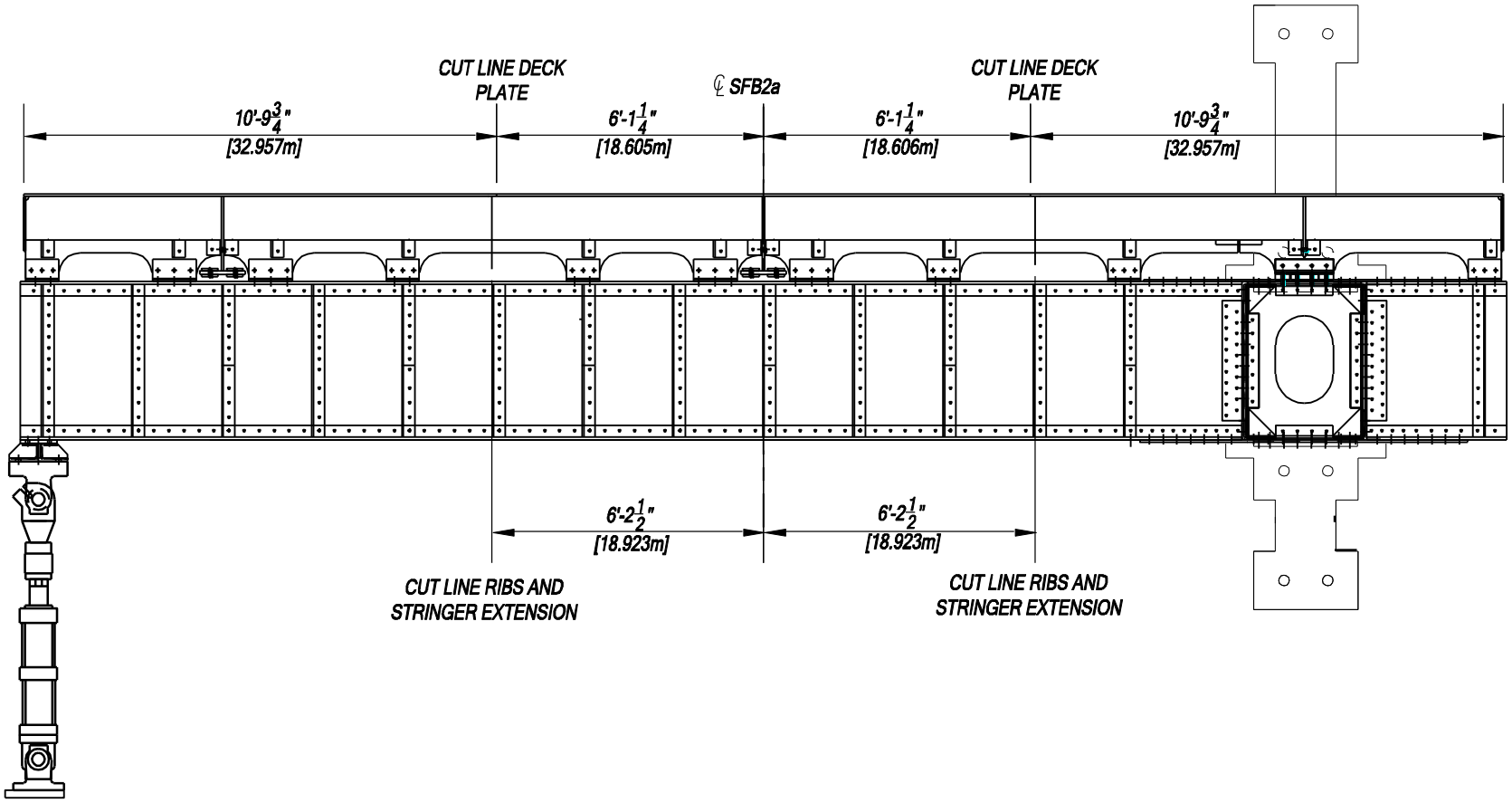

Figure 3 Side elevation of the Phase 1 deck with cut lines identified (prepared by R.S. Deo Alapati)

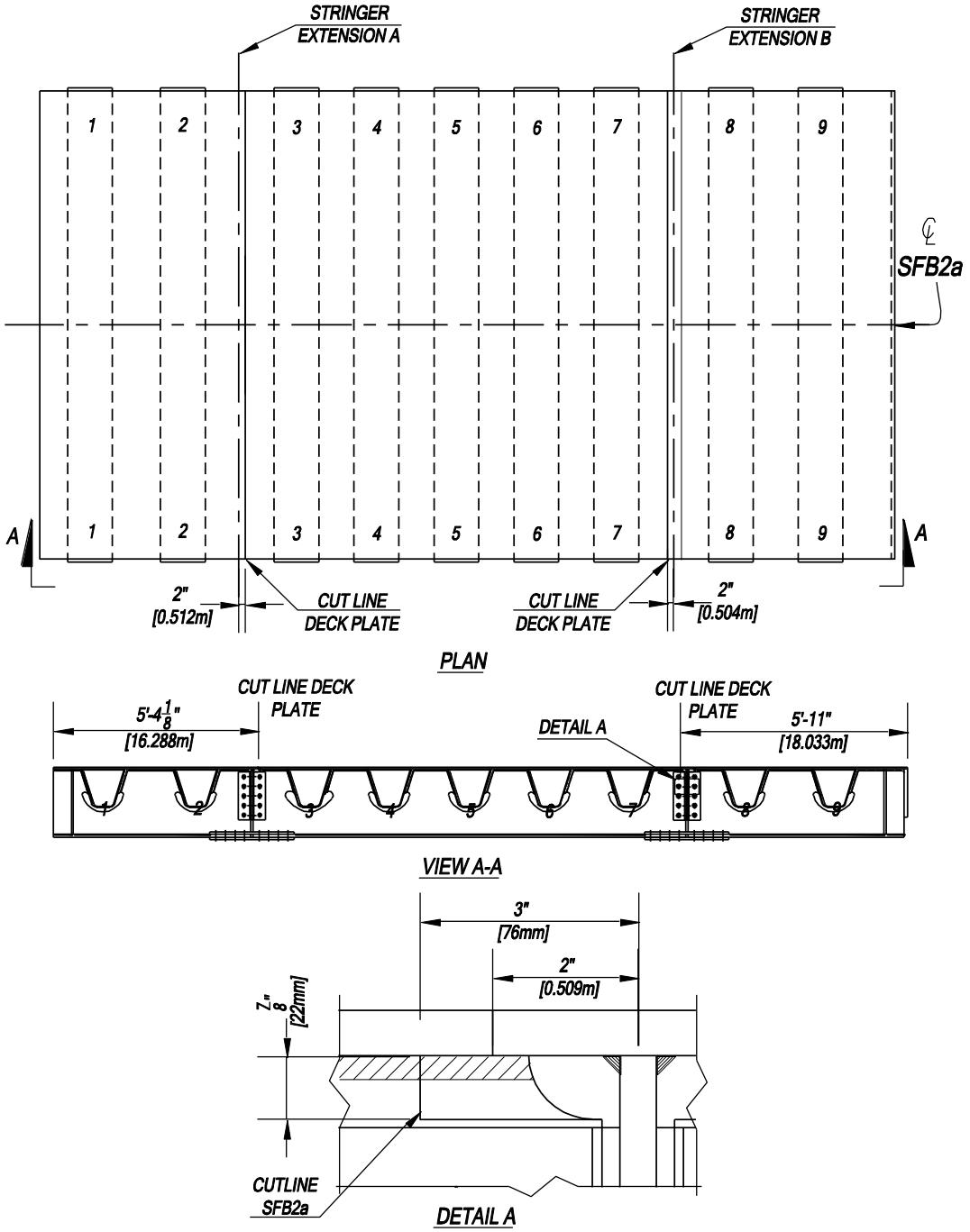

Figure 4 Longitudinal cut-lines on removed section of Phase 1 deck section (prepared by R.S. Deo Alapati)

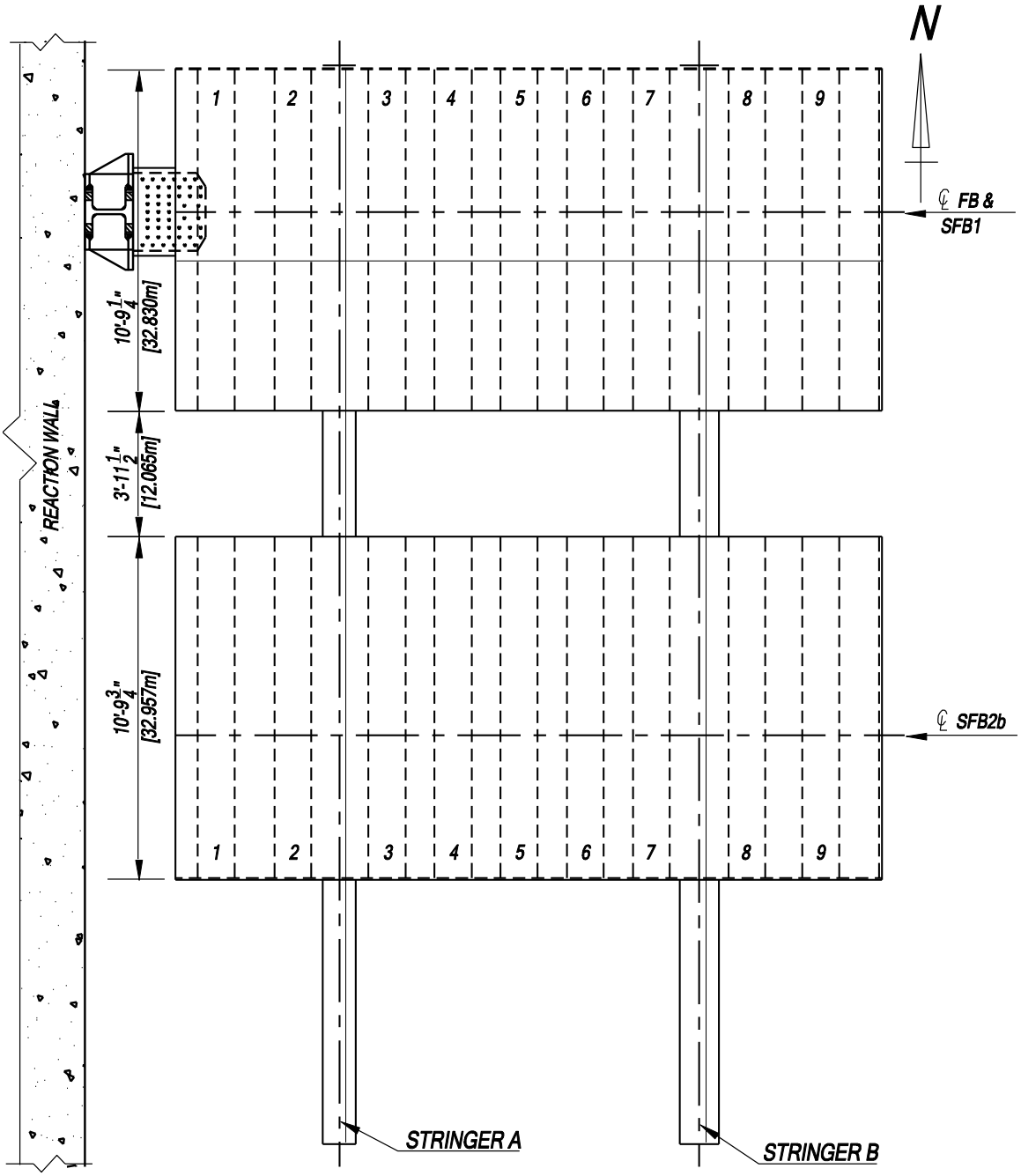

Figure 5 Deck modification for Phase 2 after removing the middle portion and moving the south section towards north (prepared by R.S. Deo Alapati)

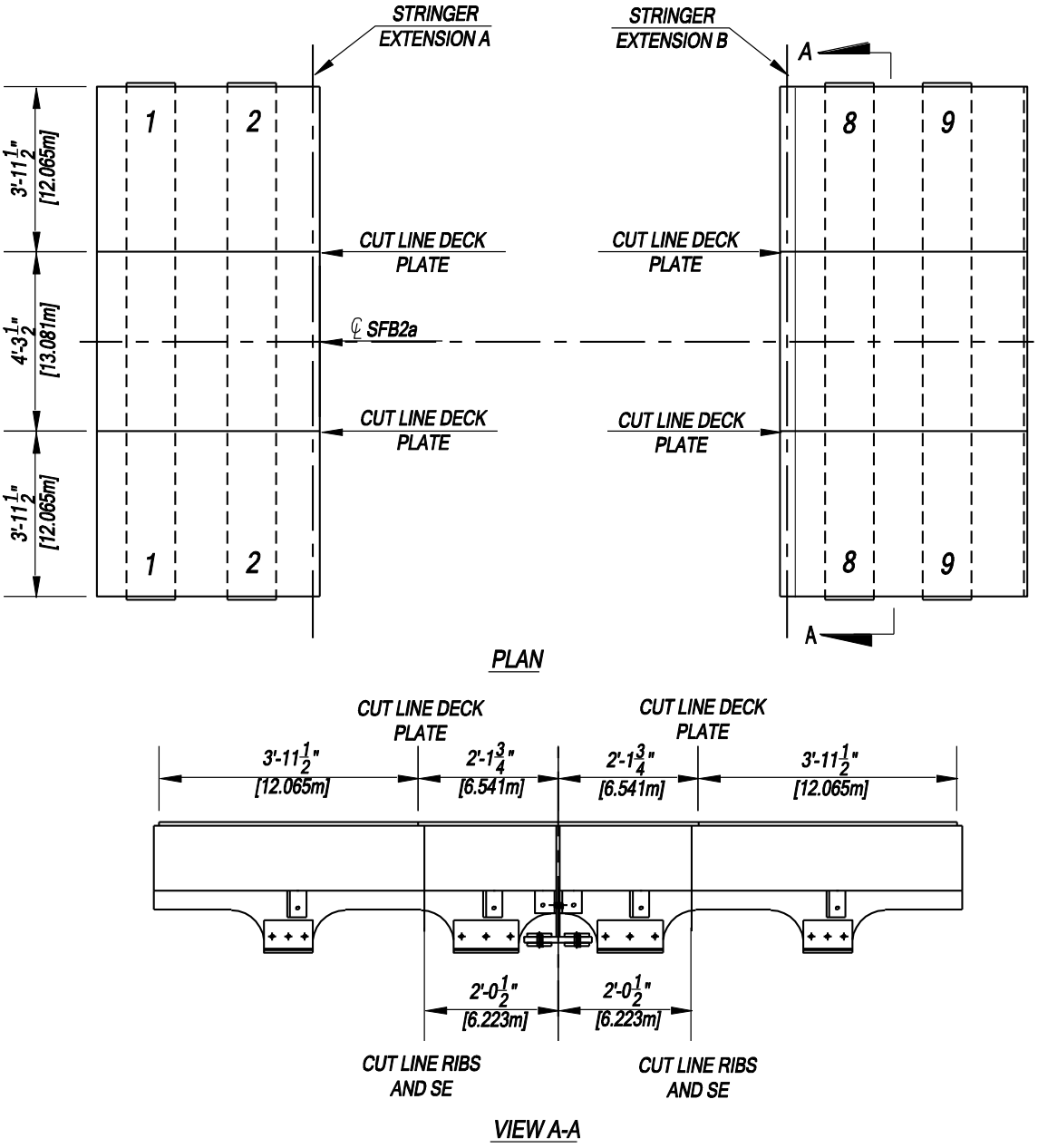

Figure 6 Cut plan for the exterior panels of the removed Phase 1 deck (prepared by R.S Deo Alapati)

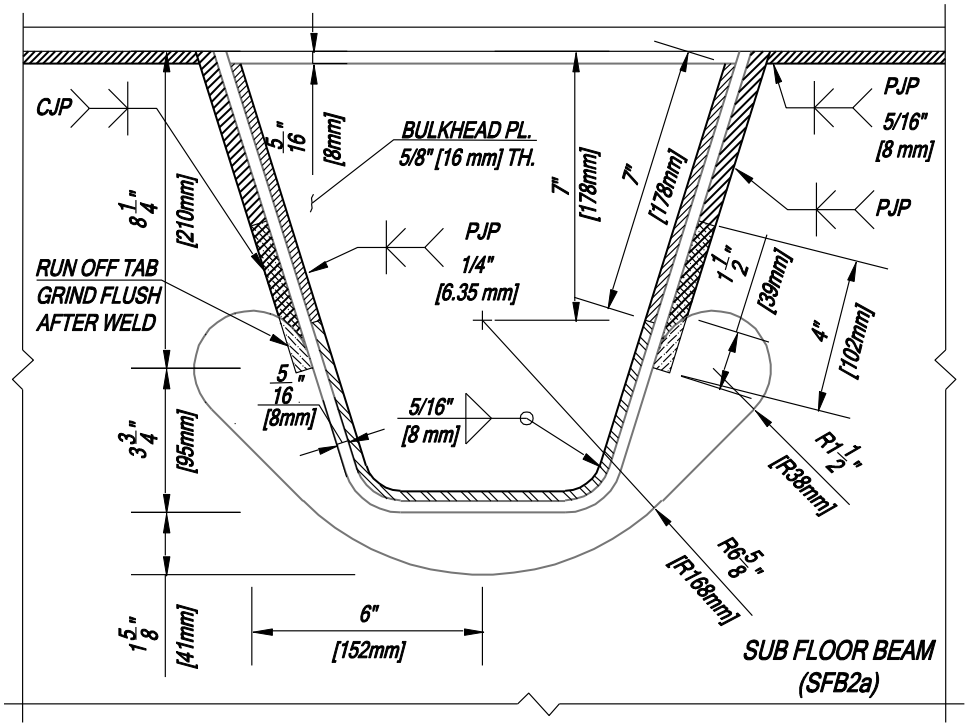

Figure 7 Details of the modified rib-to-subfloor beam connection

Figure 8 Splicing of deck plates by SAW

Figure 9 Inspection of deck plate welds by UT Level II inspectors using both conventional and Phased Array Ultrasonic testing devices

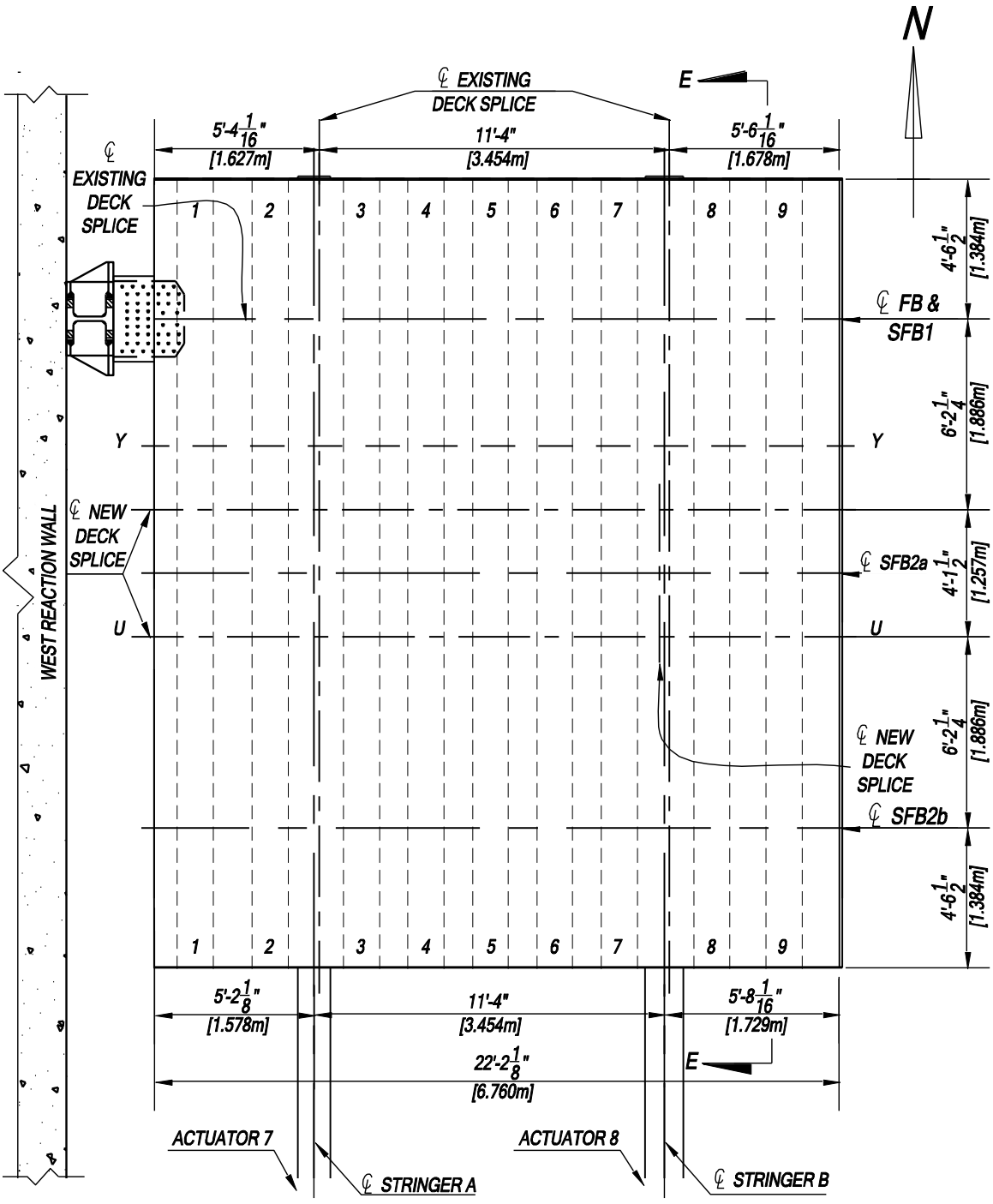

Figure 10 Plan view of the refurbished specimen for Phase 2 testing (prepared by R.S. Deo Alapati)

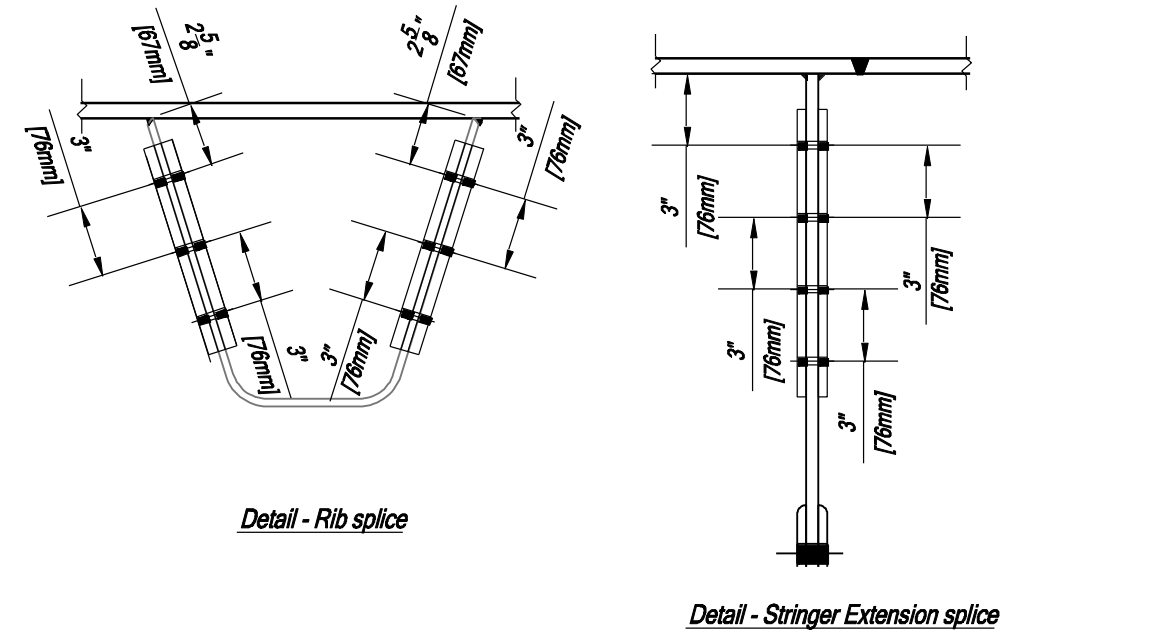

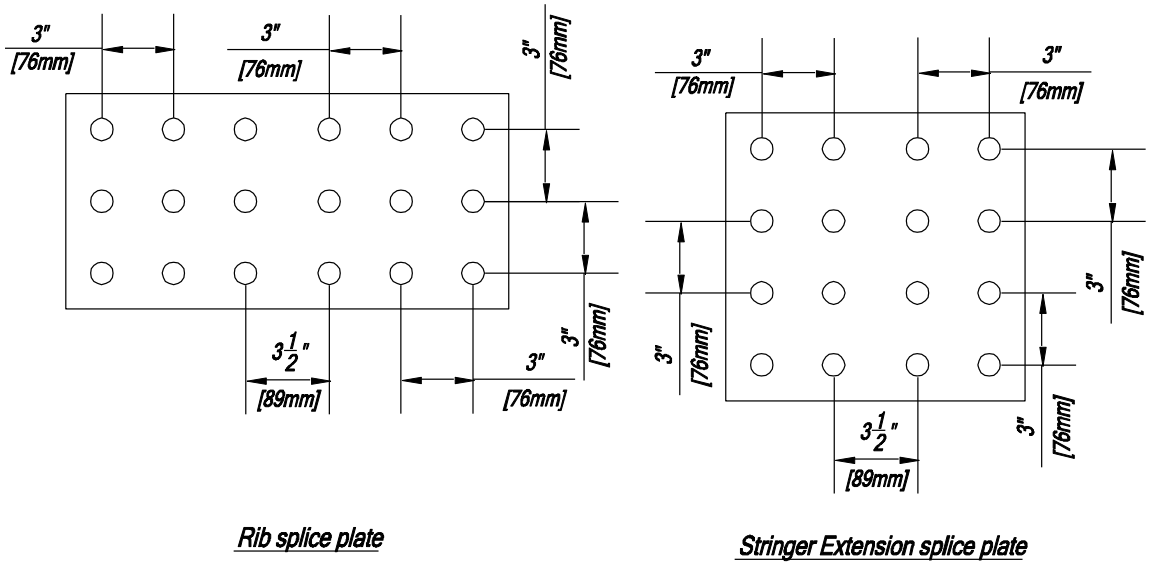

Figure 11 Details of splice plate for ribs and stringer extensions

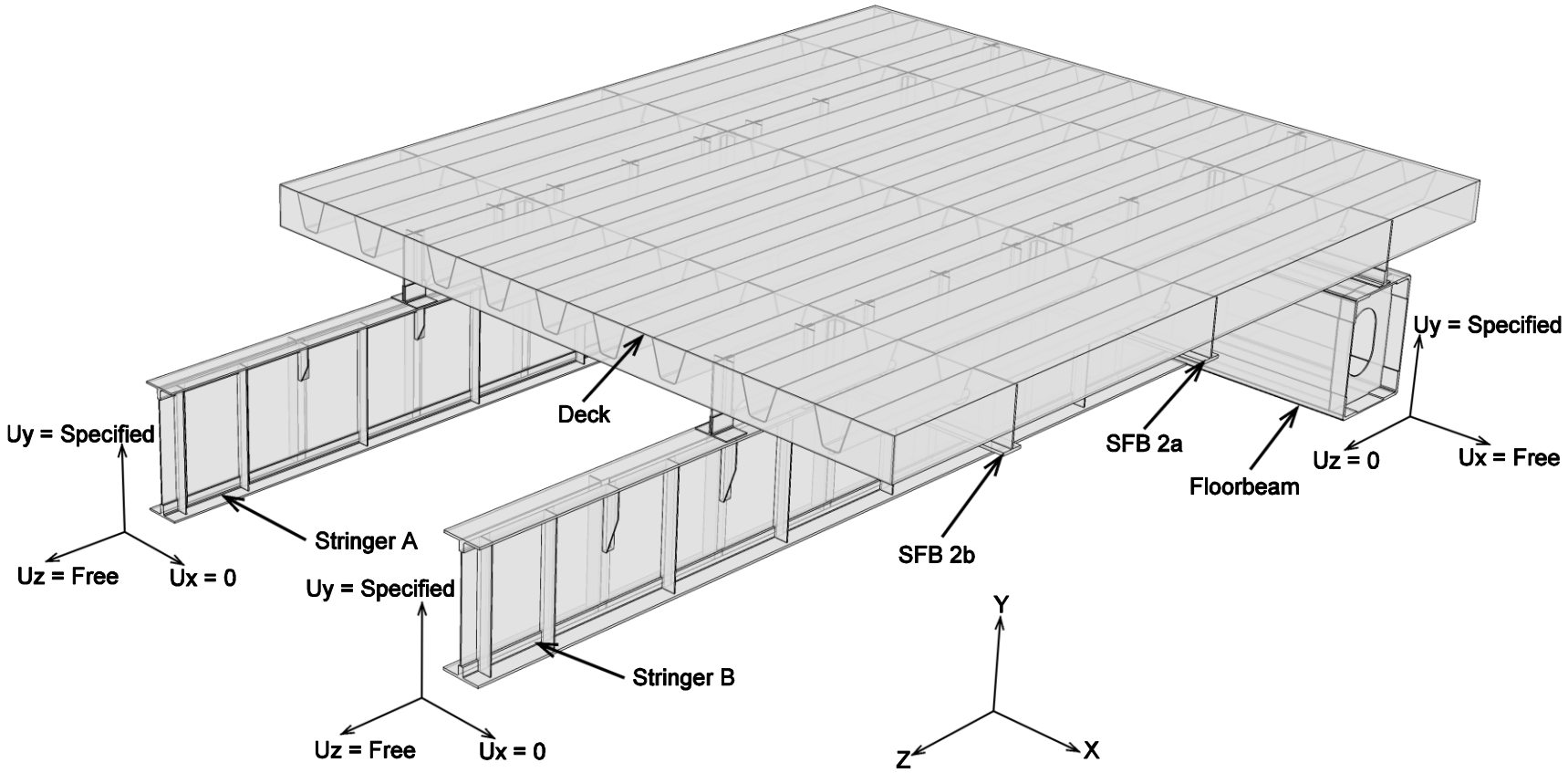

Figure 12 Global model of the deck specimen – above deck view

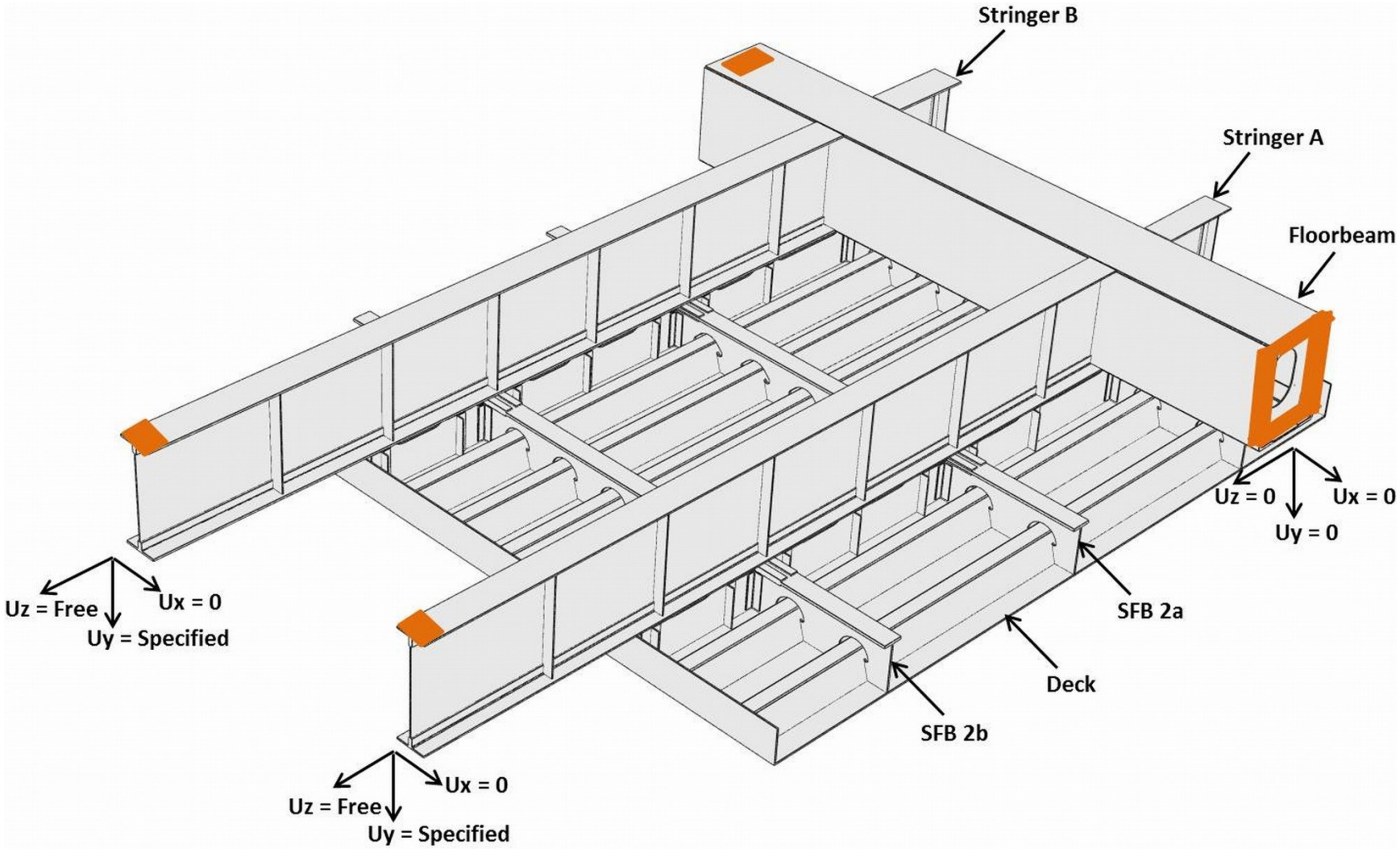

Figure 13 Underside view of global model

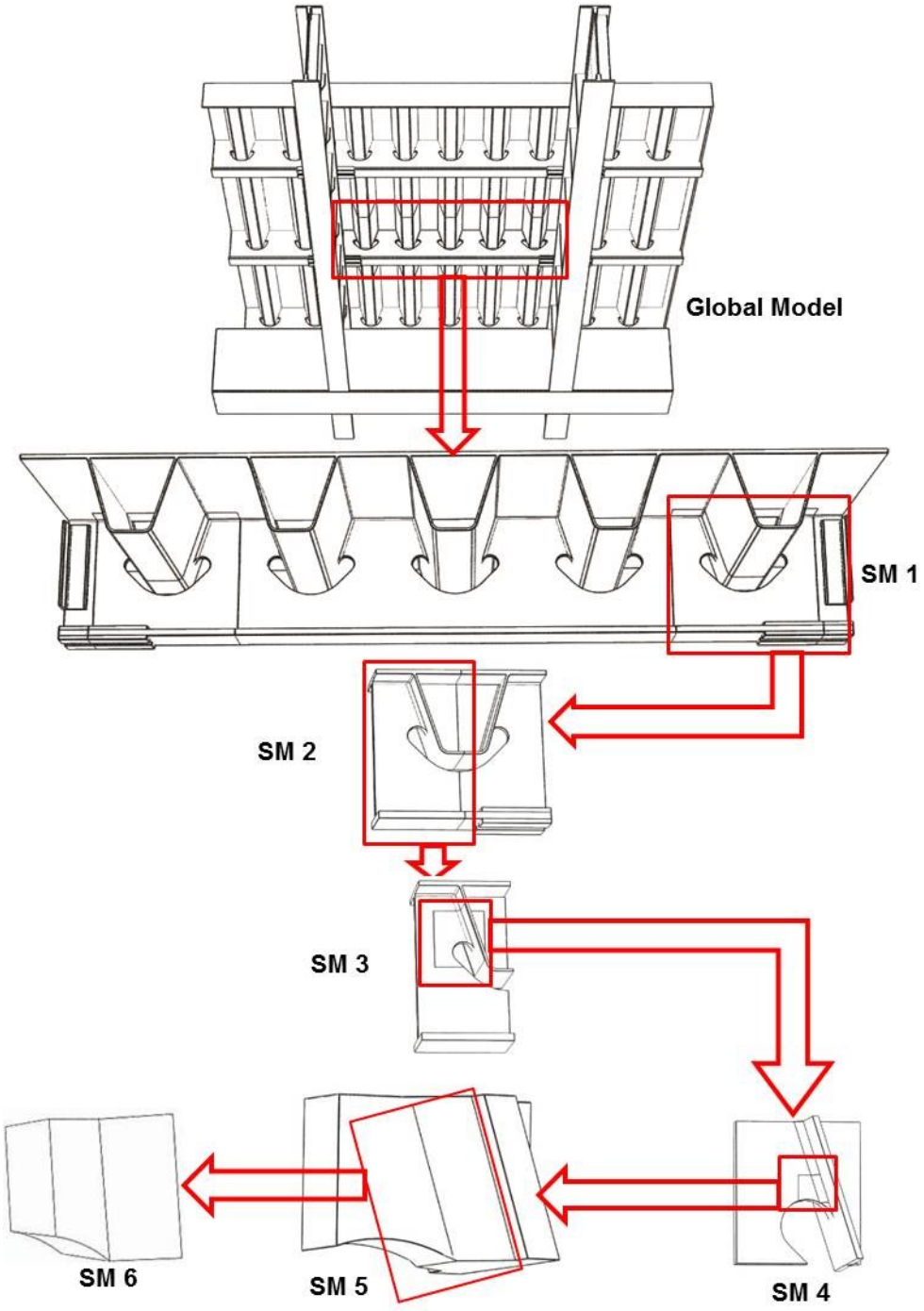

Figure 14 Progression of submodel analyses performed for Rib 7 (submodel progression for Rib 3 was similar but handed)

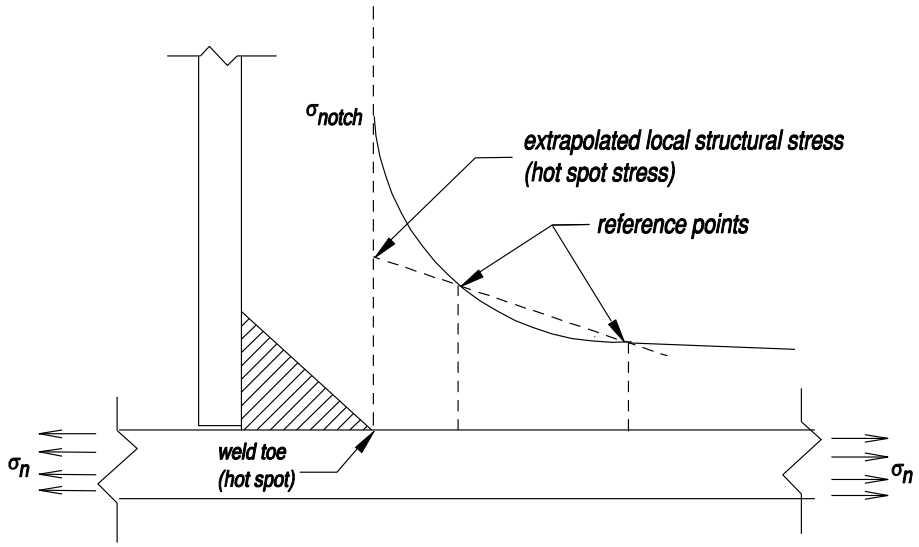

Figure 15 Typical variation of normal stress at weld toe

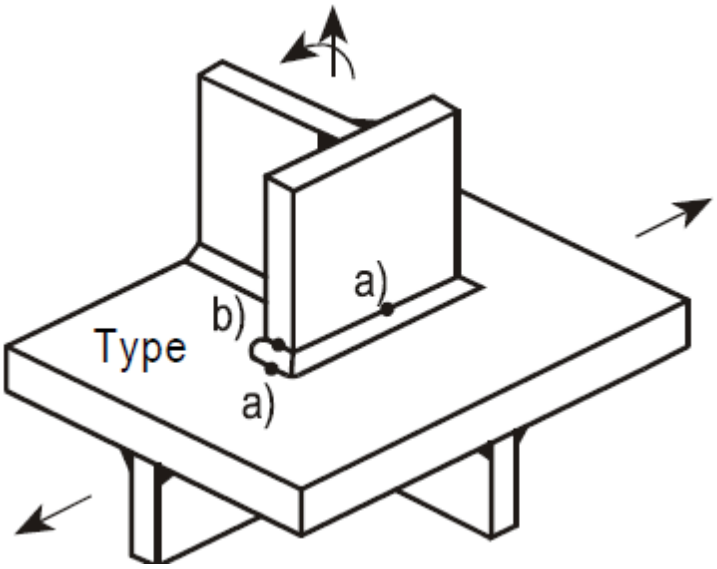

Figure 16 Applicable IIW hot spots types (taken from Hobbacher, 2007)

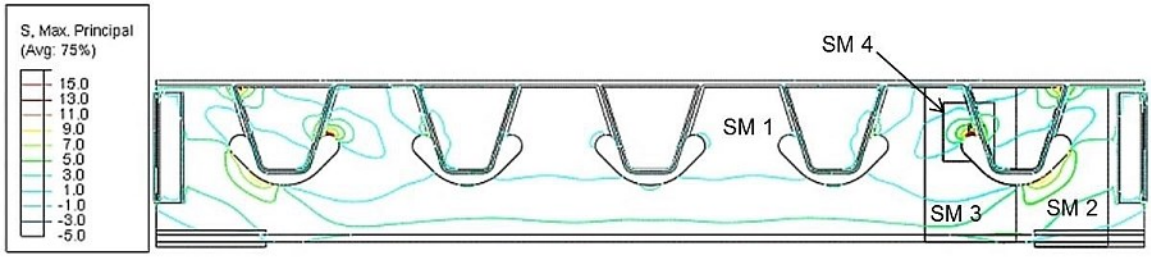

Figure 17 Overlaid contour plots of maximum principal stress for submodels SM1 to SM5 at Rib 7

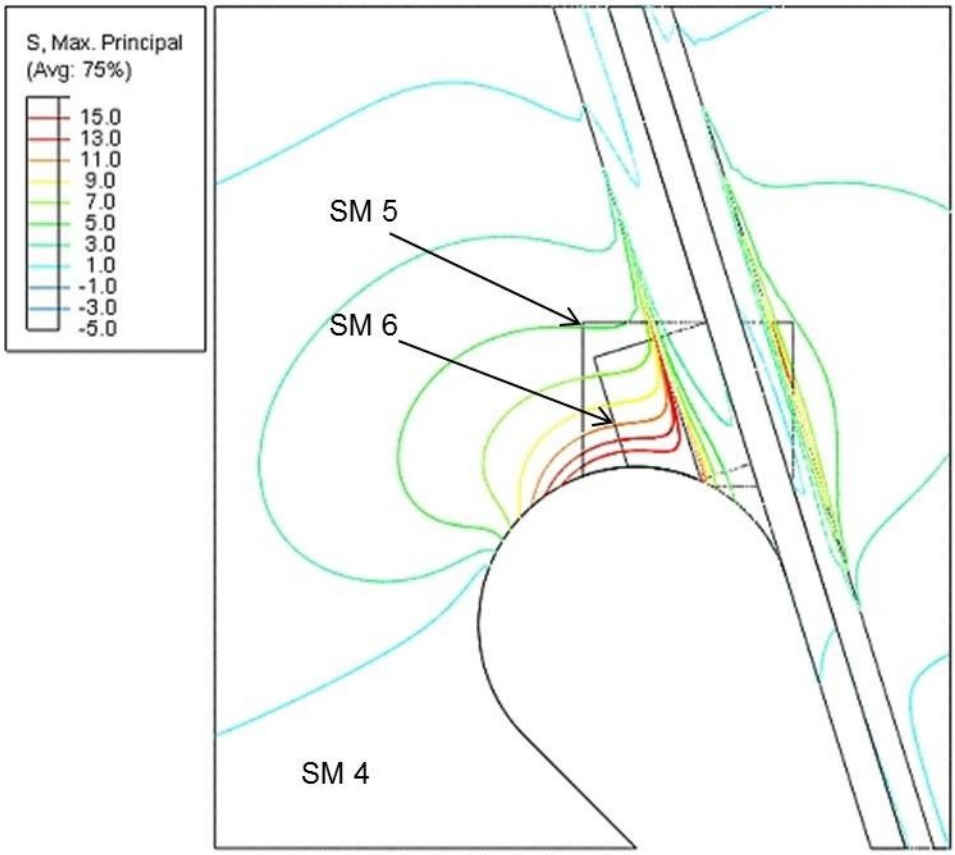

Figure 18 Overlaid contour plots of maximum principal stress for submodels SM4 to SM6 at Rib 7

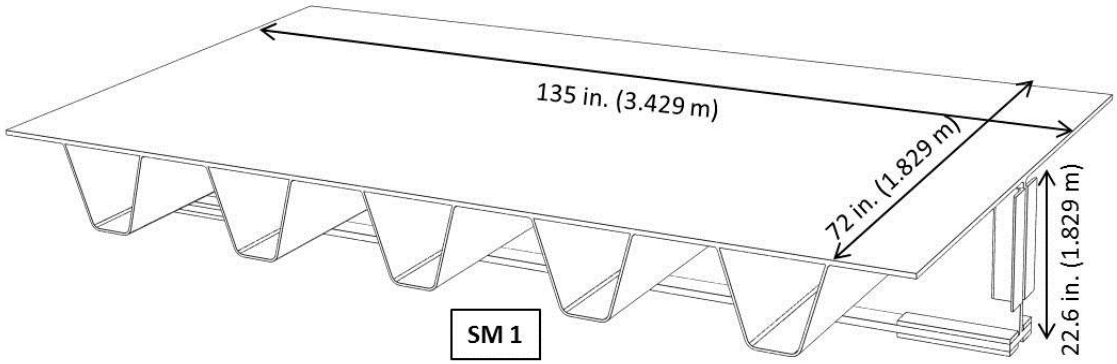

Figure 19 Dimensions of submodel SM1

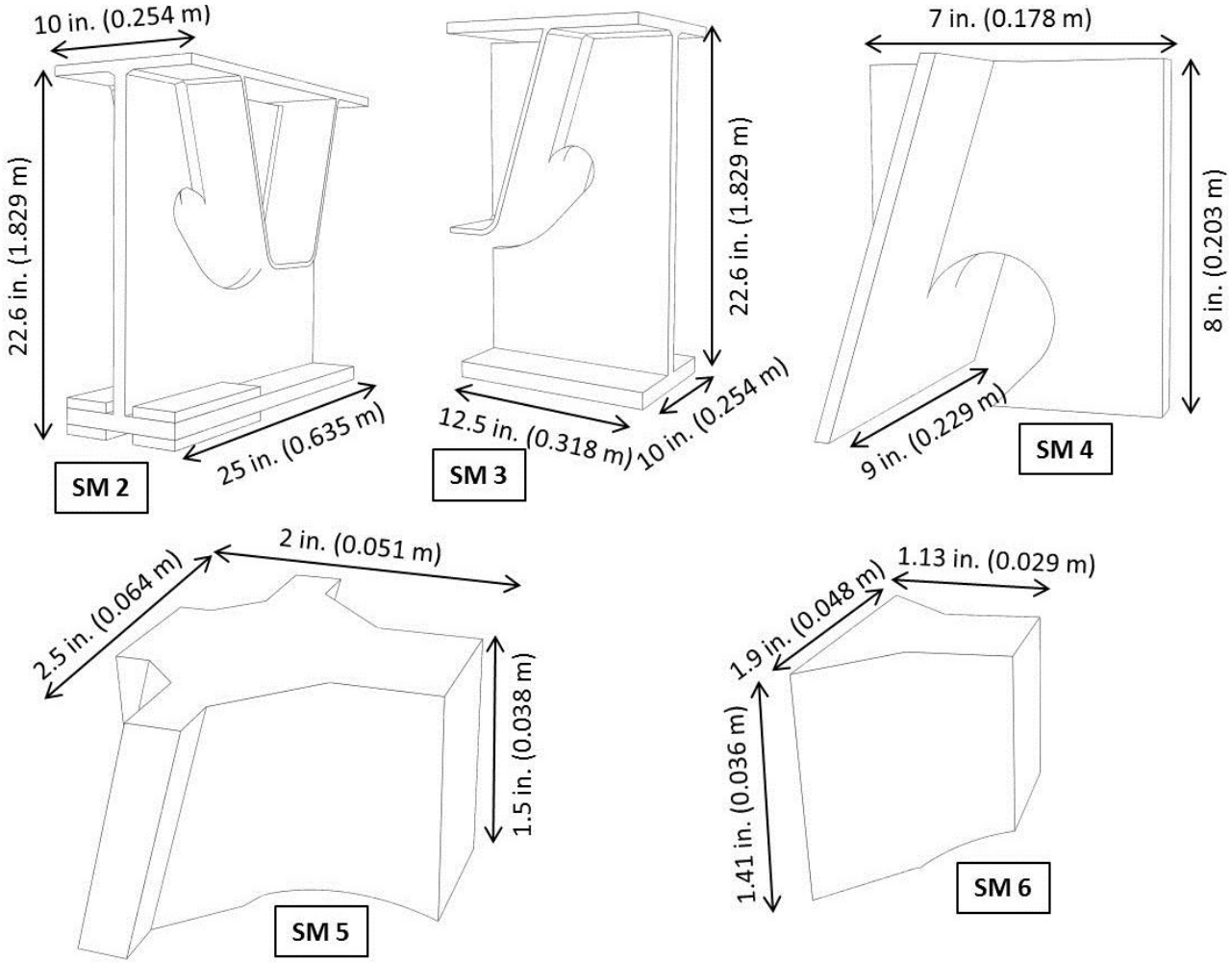

Figure 20 Dimensions of submodels SM2 to SM6

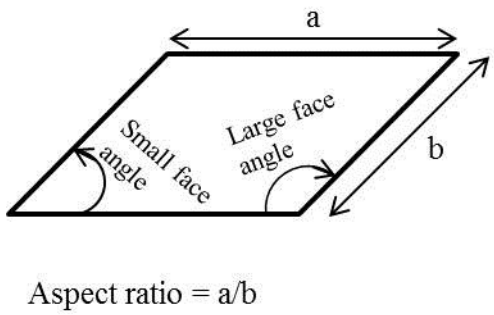

Figure 21 Definition of face (corner) angles and aspect ratio for a finite element

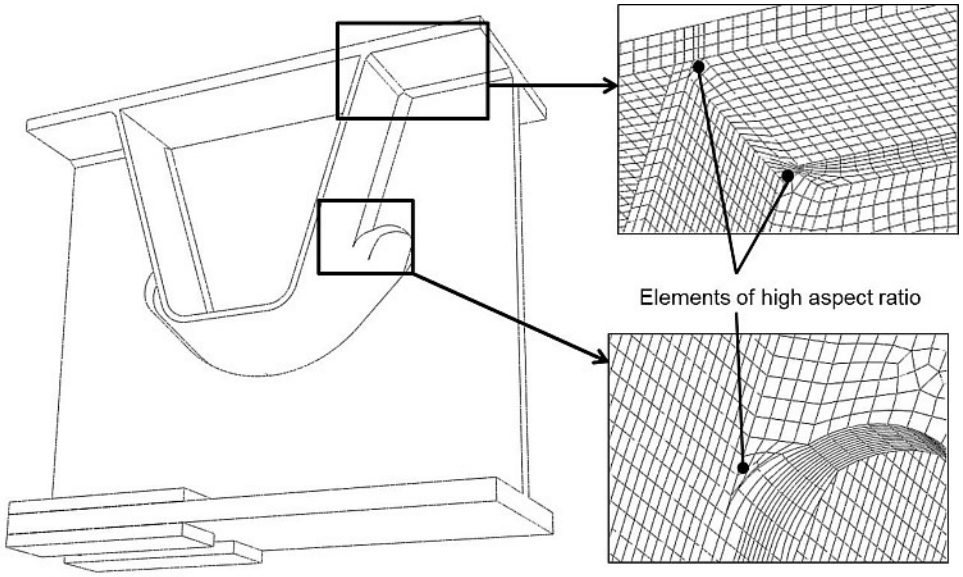

Figure 22 Locations of elements with aspect ratio >10

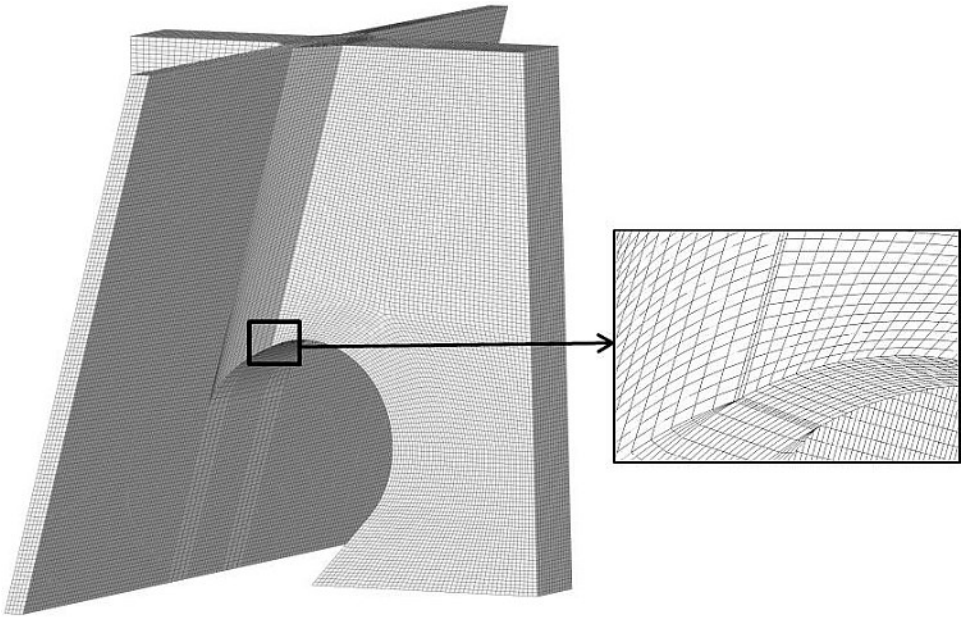

Figure 23 Example of high aspect ratio at the notch rounding and the cutout termination

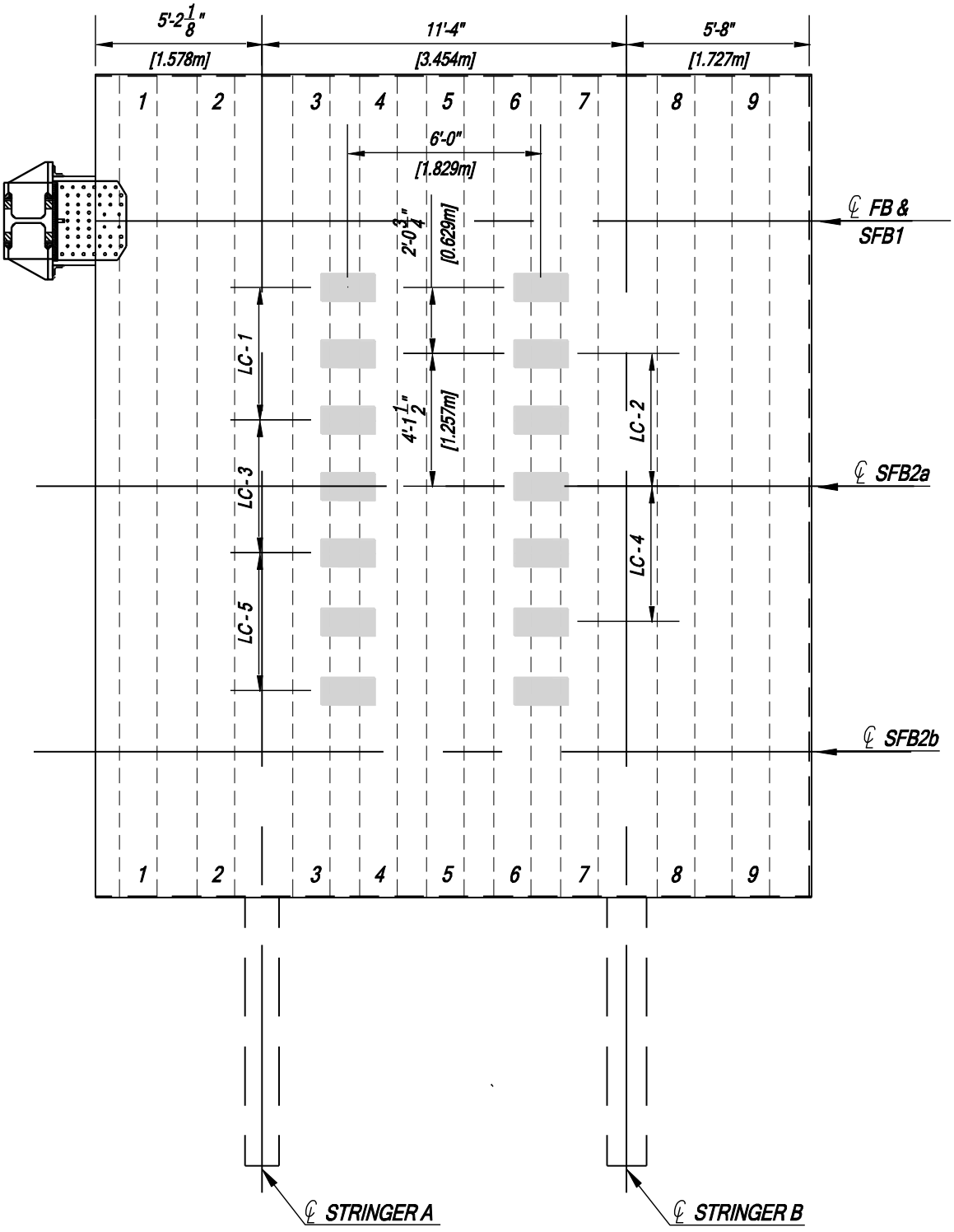

Figure 24 Locations of load patches in crawl test simulations

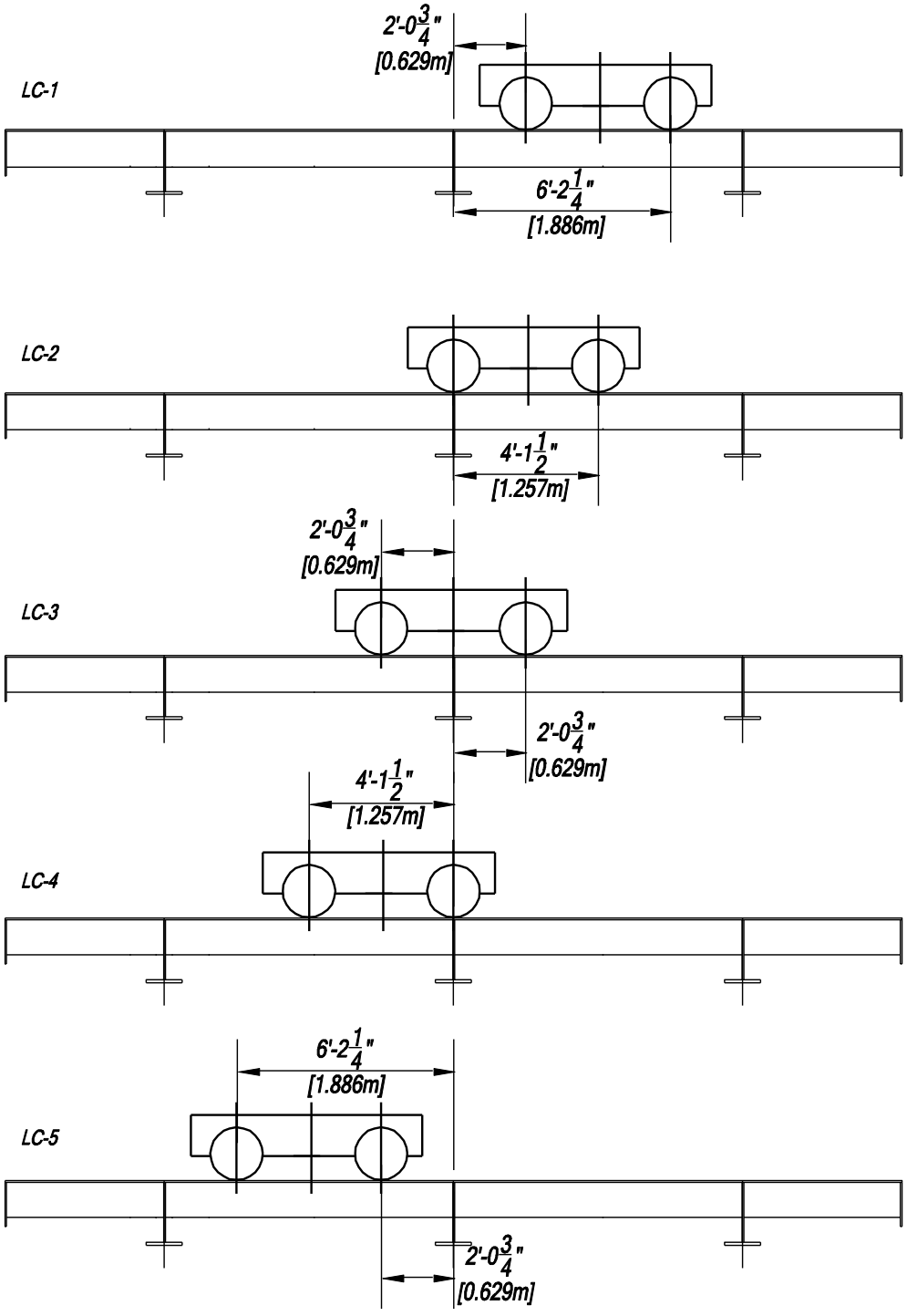

Figure 25 Longitudinal load positions for crawl test simulations

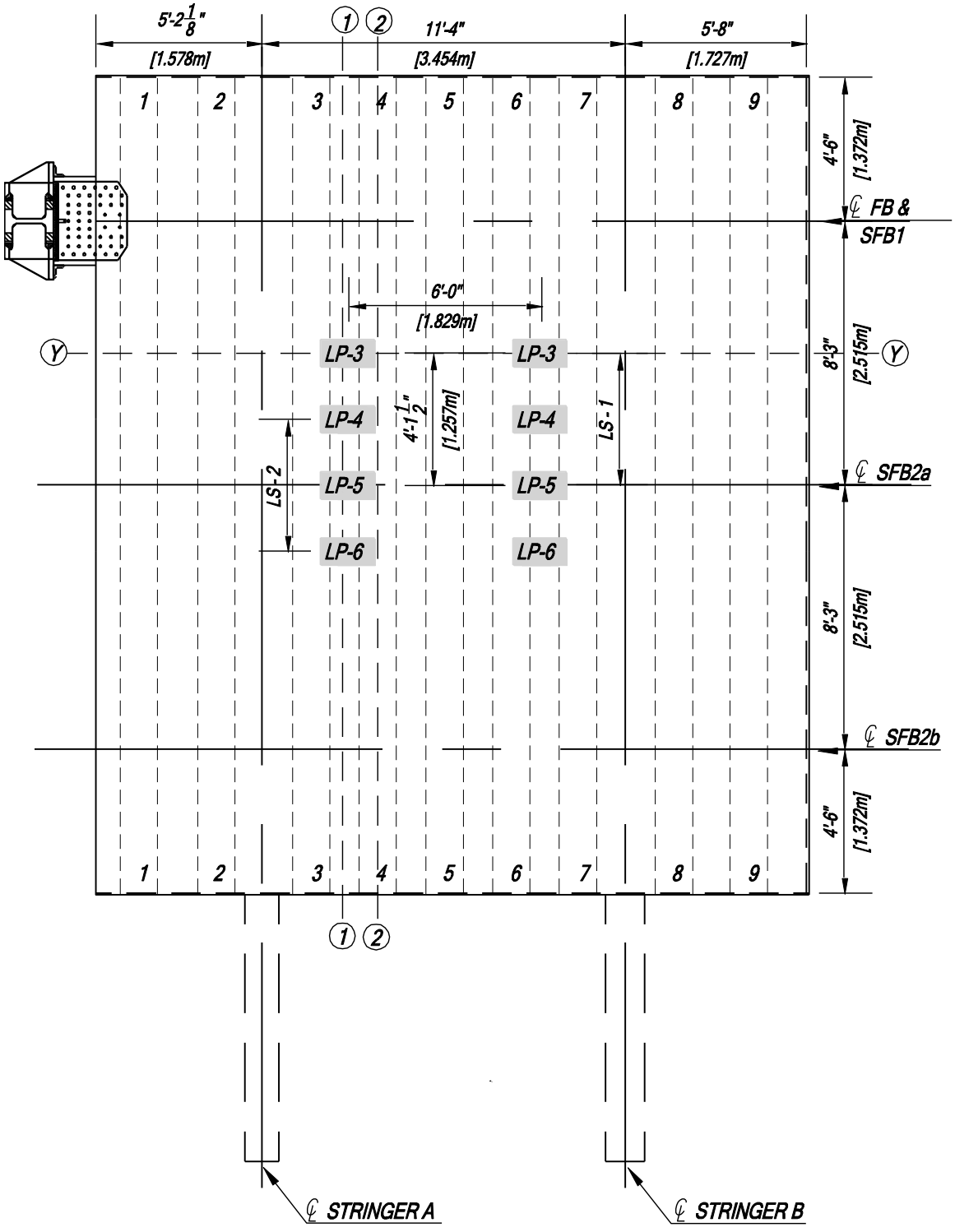

Figure 26 Configuration of the load patches on the global model simulating static test

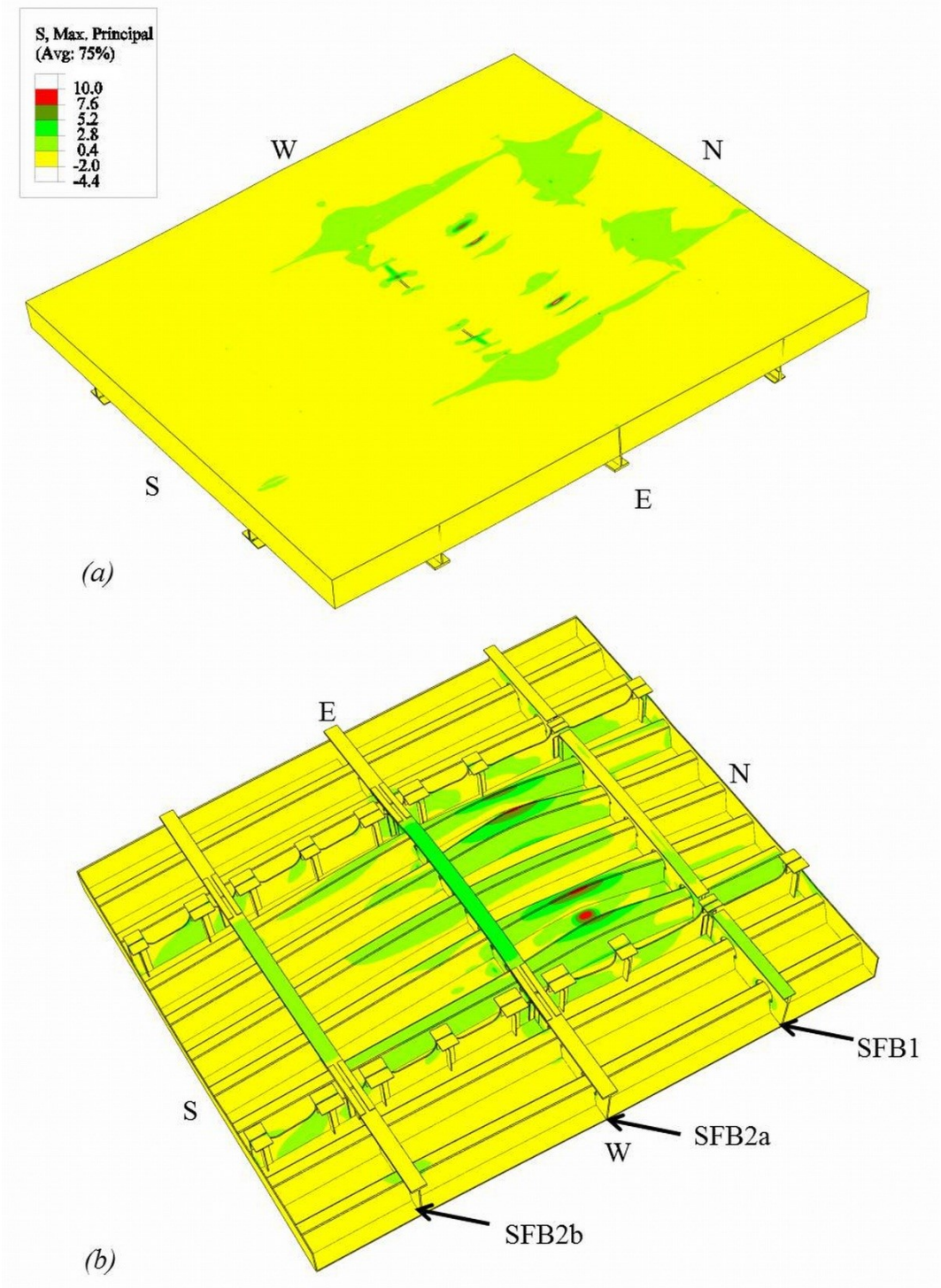

Figure 27 Contour of maximum principal stresses on the deformed configuration of the deck for static test simulation in LS 1: (a) top view; (b) underside view

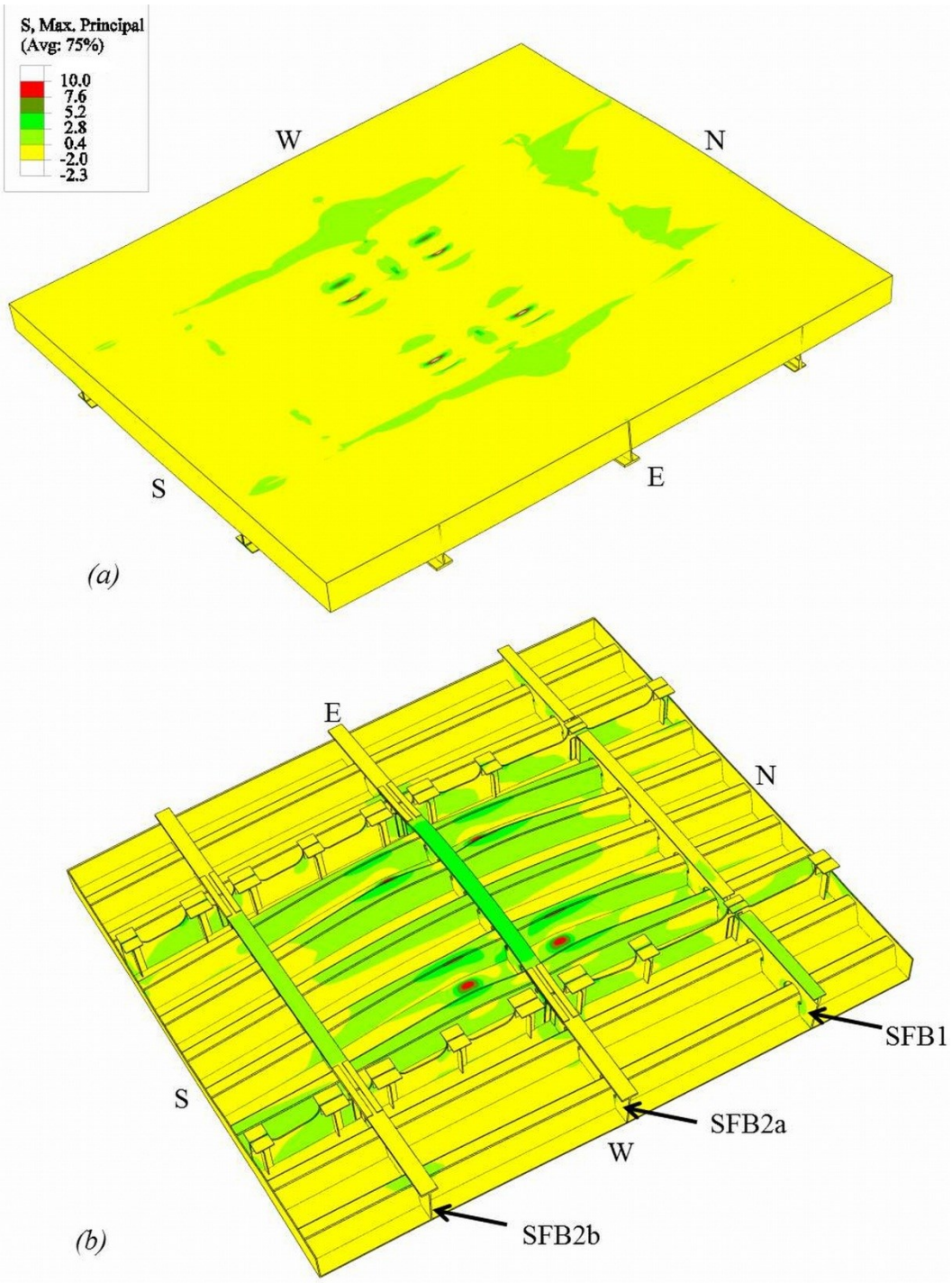

Figure 28 Contour of maximum principal stresses on the deformed configuration of the deck for static test simulation in LS 2: (a) top view; (b) underside view

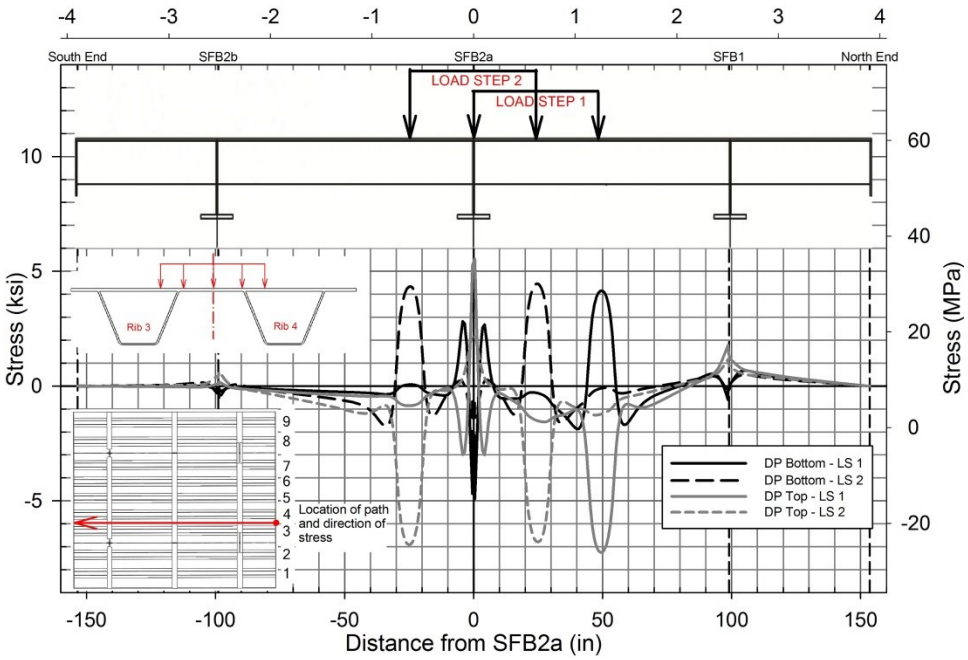

Figure 29 Longitudinal stress on the top and bottom face of the deck plate at a section through the load patch in static test simulation

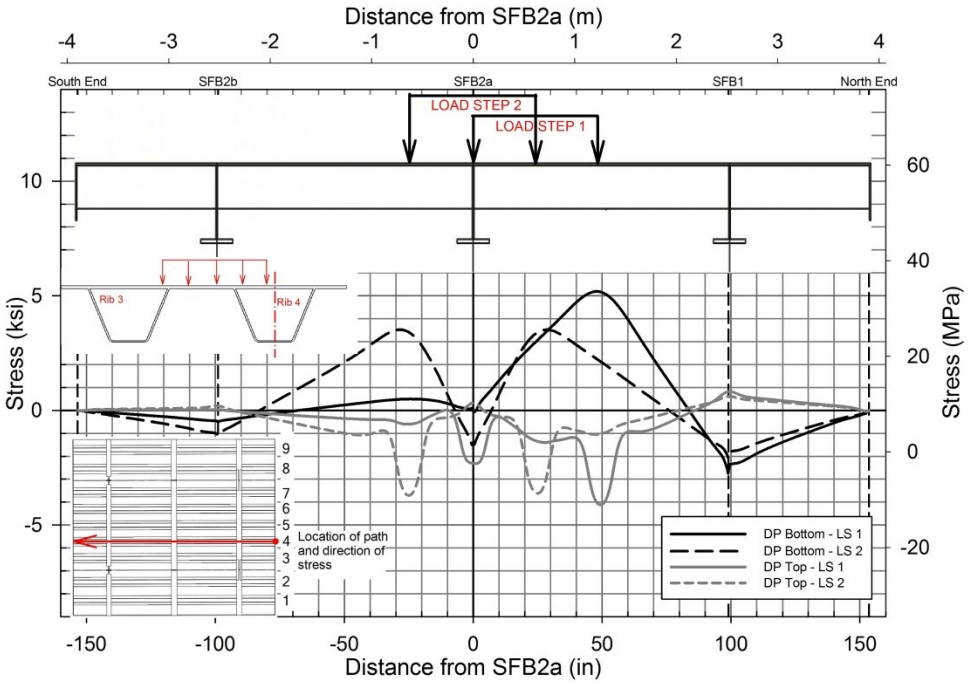

Figure 30 Longitudinal stress on the top of the deck plate and the soffit of Rib 4 at the centerline of Rib 4 in static test simulation

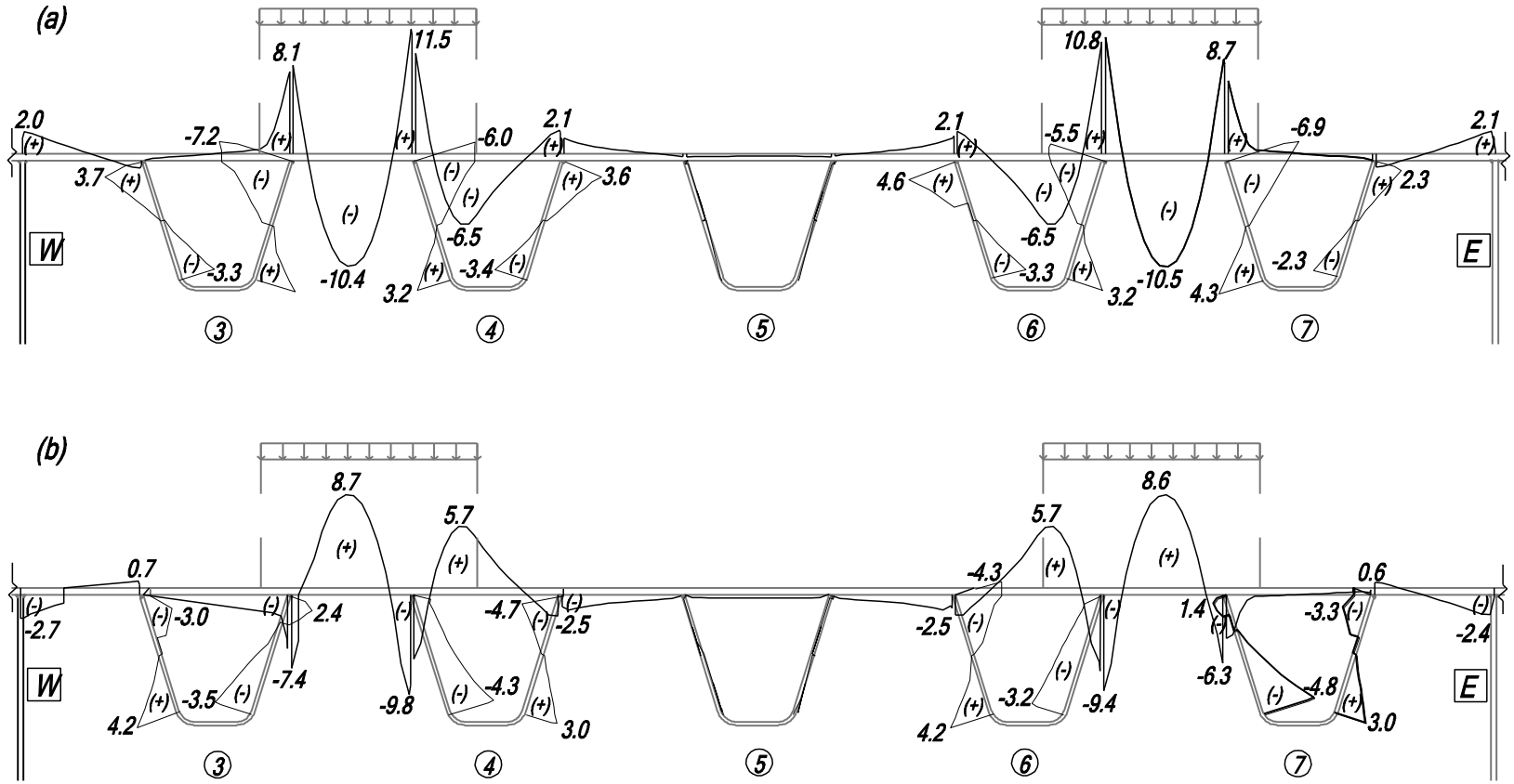

Figure 31 Transverse stresses in LS-1 of static test simulation: (a) on the top face of deck plate and the external faces of rib wall, (b) on the bottom face of deck plate and the internal faces of rib wall

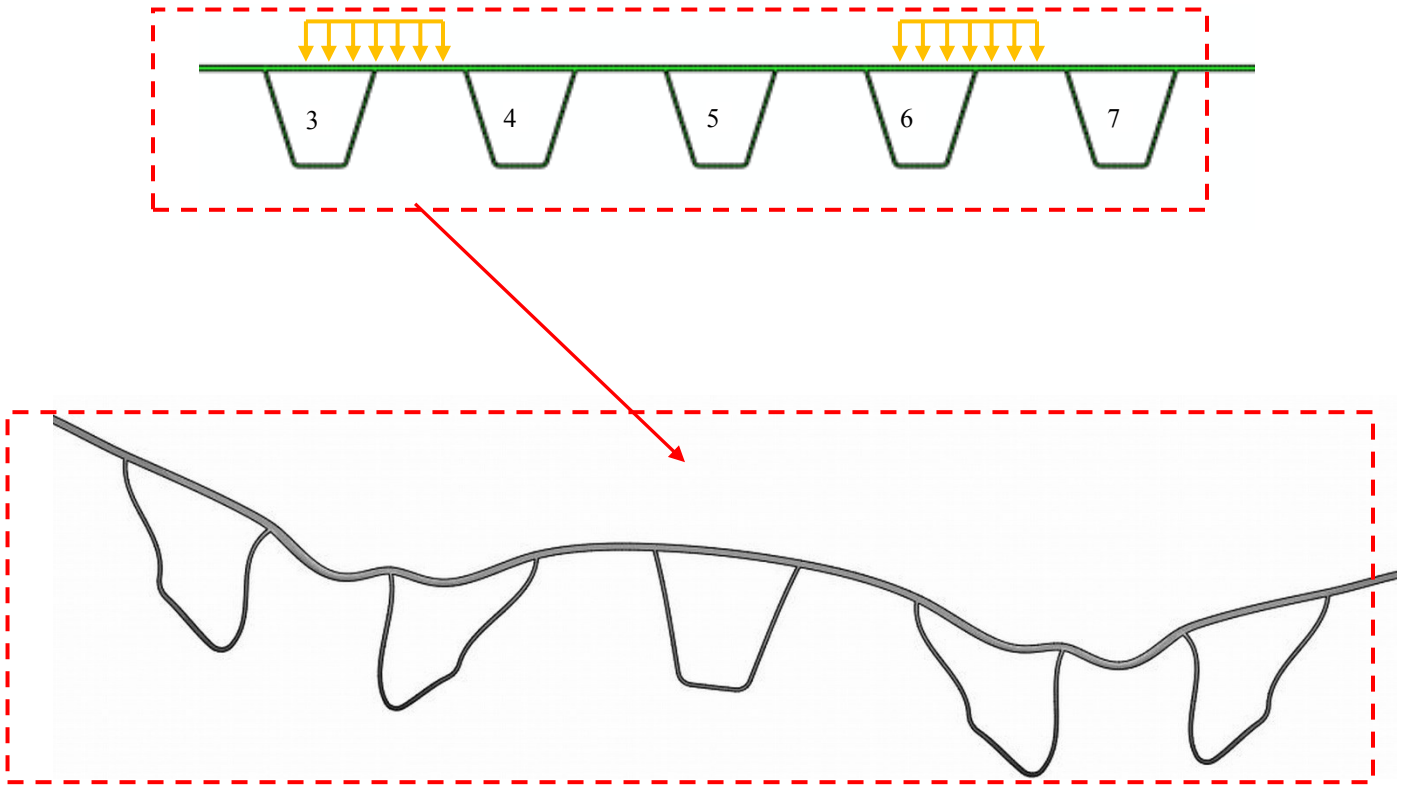

Figure 32 Deformation of the deck at section Y-Y in LS-1 of the static test simulation (magnification: 100×)

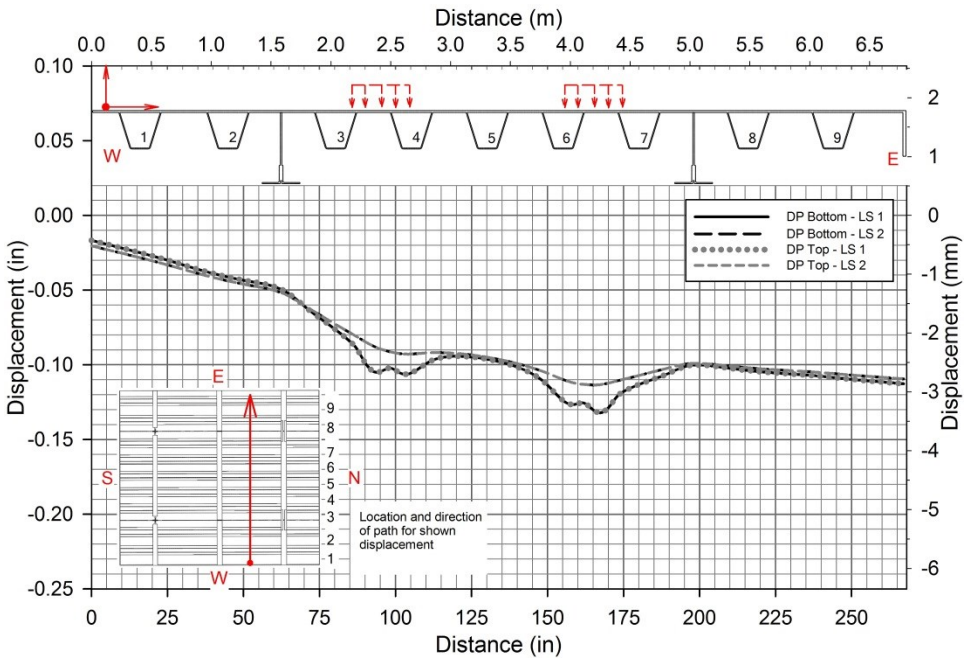

Figure 33 Vertical displacement of deck plate at transverse section Y-Y

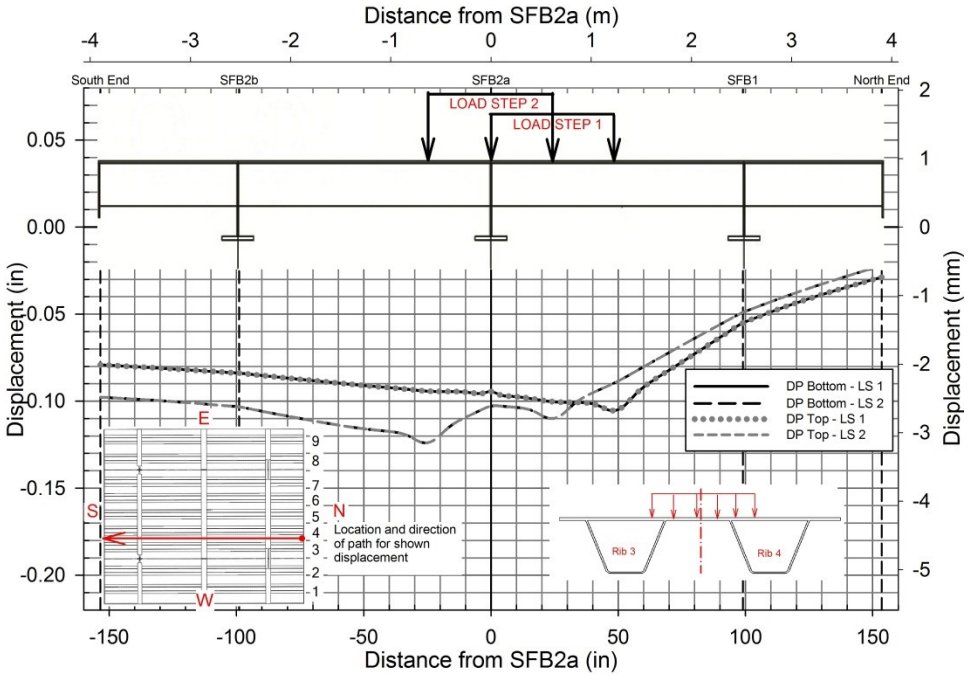

Figure 34 Vertical displacement of the deck plate at section 1-1

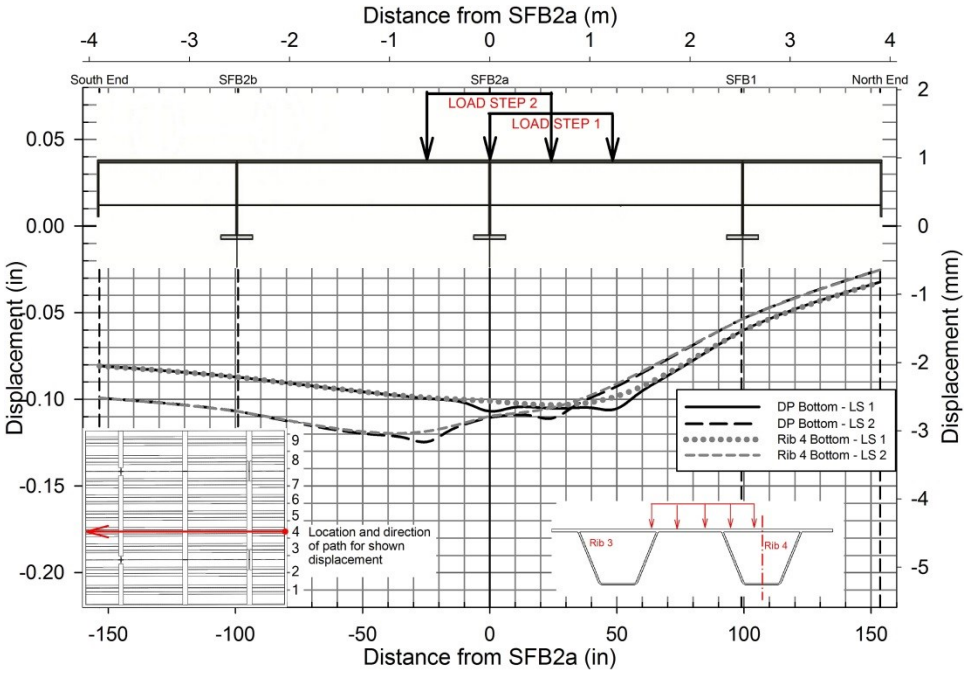

Figure 35 Vertical displacement of deck plate and rib at section 2-2

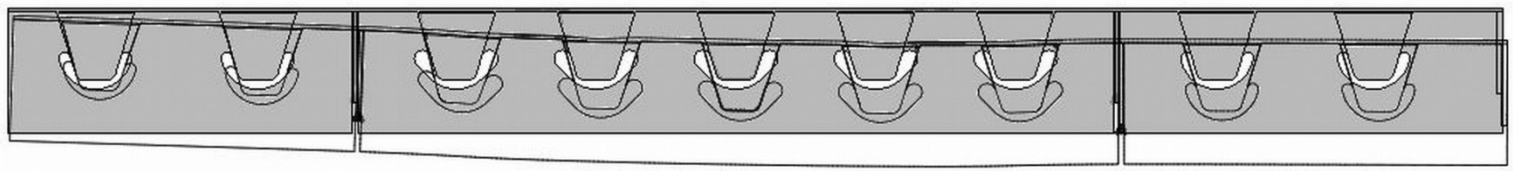

Figure 36 Maximum deformations of SFB2a in LS-1 of static test simulation (magnification: 100×)

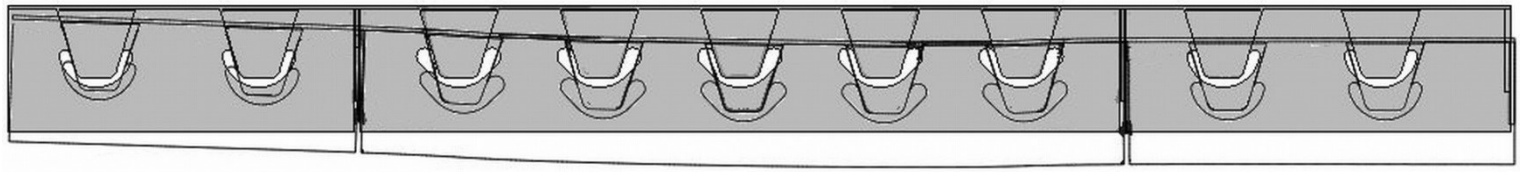

Figure 37 Maximum deformations of SFB2a in LS-2 of static test simulation (magnification: 100×)

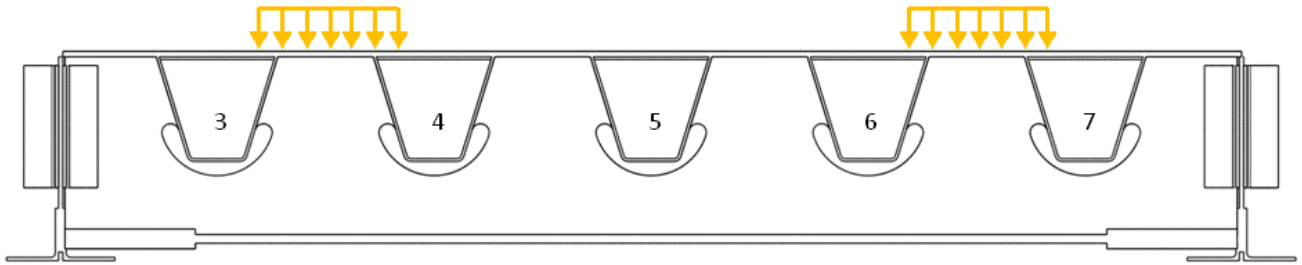

Shear force diagram

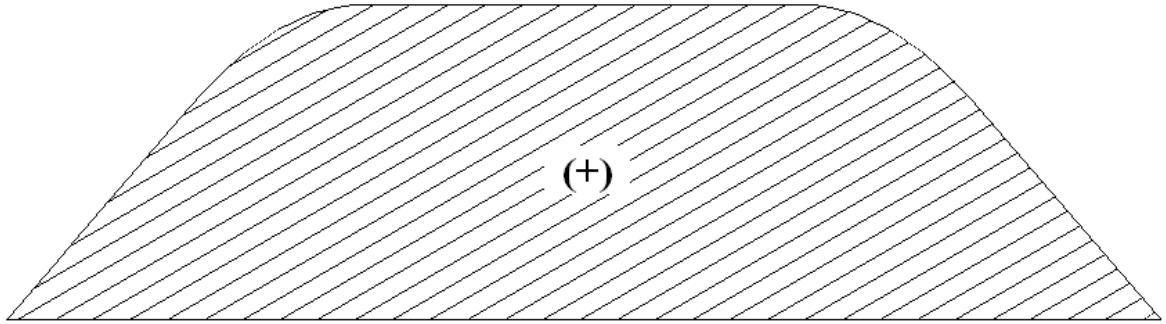

Bending moment diagram

Figure 38 Shear force and bending moment diagram of SFB2a in LS-1 (adapted from Alapati, 2012)

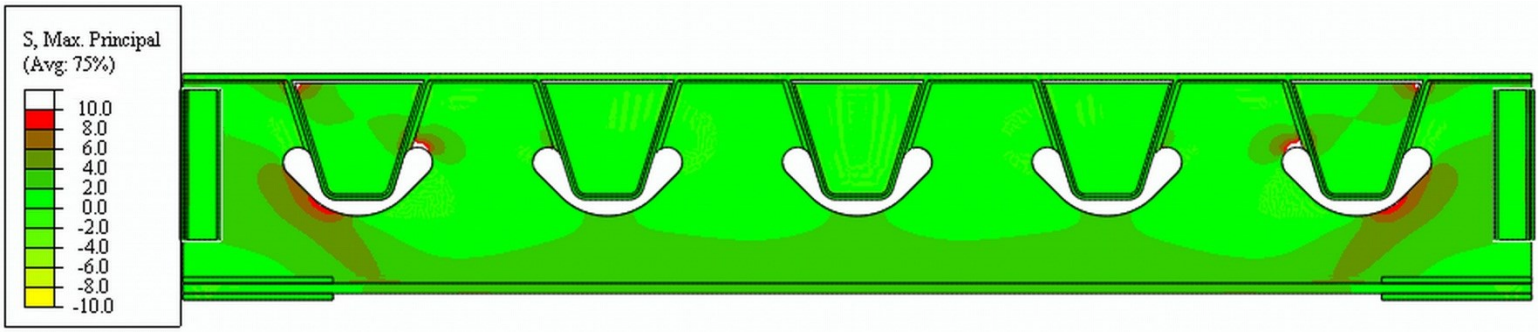

Figure 39 Maximum principal stresses in SFB2a in LS 1 in static test simulation

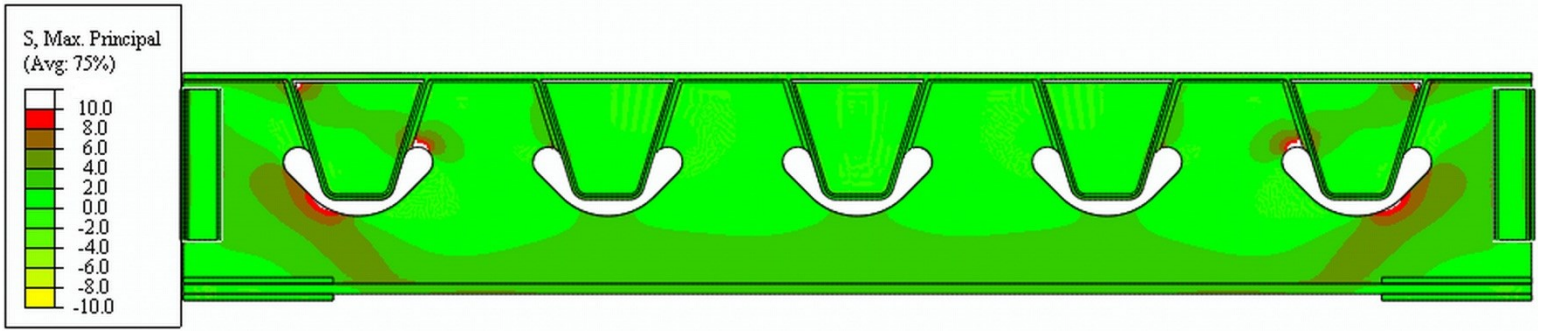

Figure 40 Maximum principal stresses in SFB2a in LS 2 in static test simulation

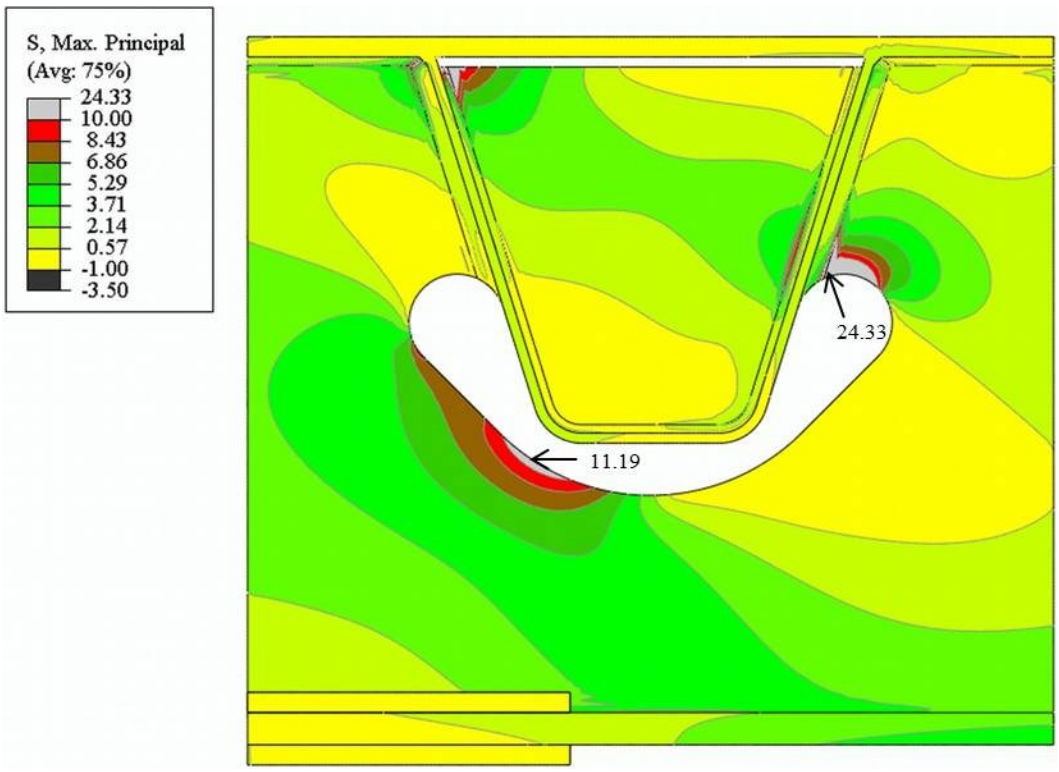

Figure 41 Stress contour plot around rib 7 at SFB2a cutout and bulkhead plate

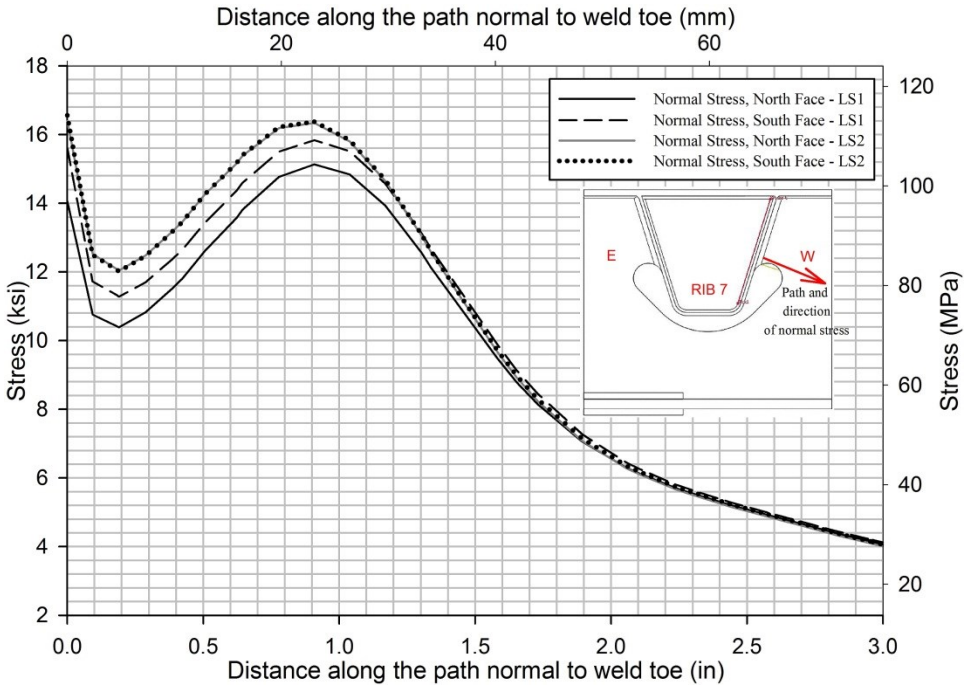

Figure 42 Comparative plots of stresses normal to weld toe at cutout termination on north and south faces

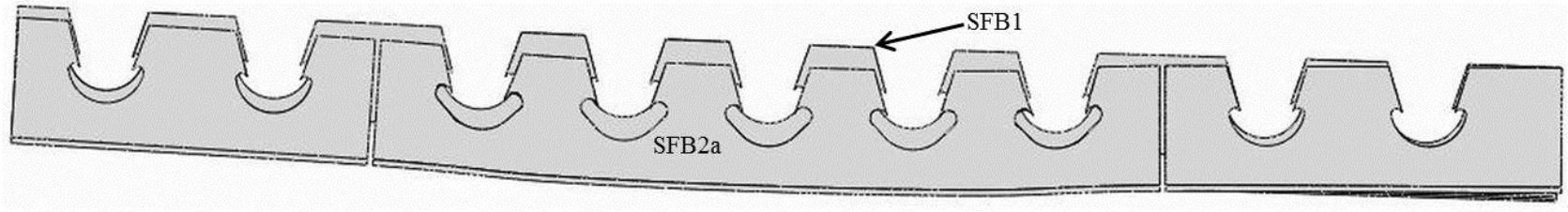

Figure 43 Comparison of deformation of SFB1 and SFB2a in static test simulation for LS-1 (magnification: 100×)

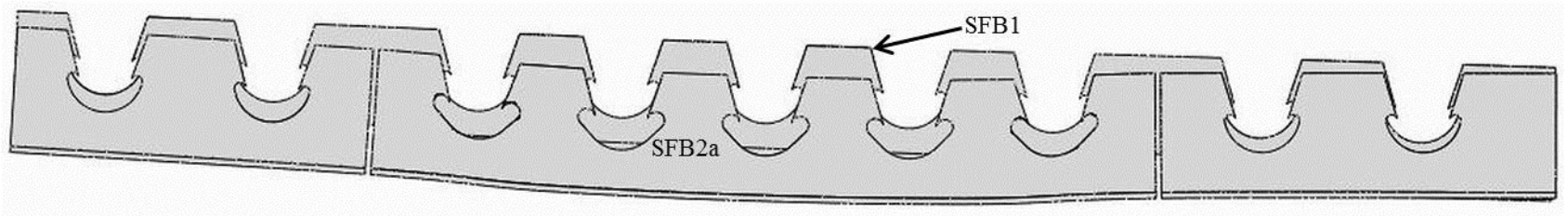

Figure 44 Comparison of deformation of SFB1 and SFB2a in static test simulation for LS-2 (magnification: 100×)

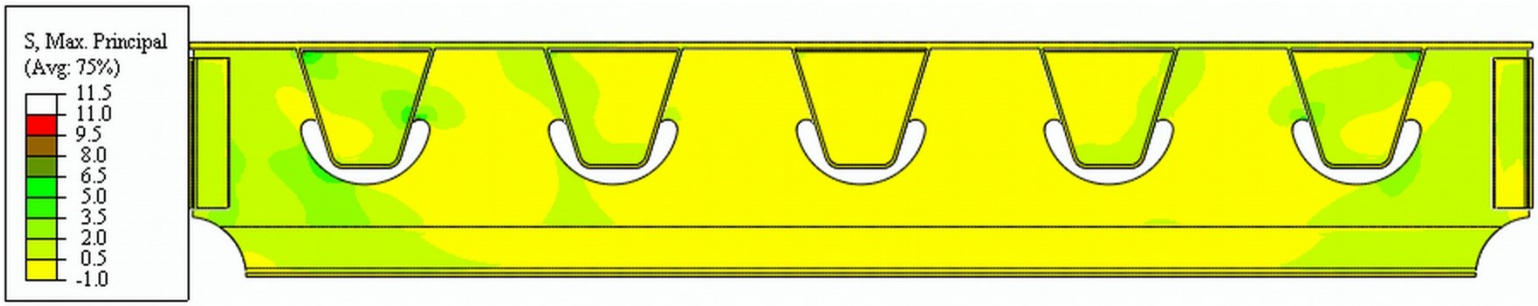

Figure 45 Maximum principal stresses in SFB1 in LS 1 in static test simulation

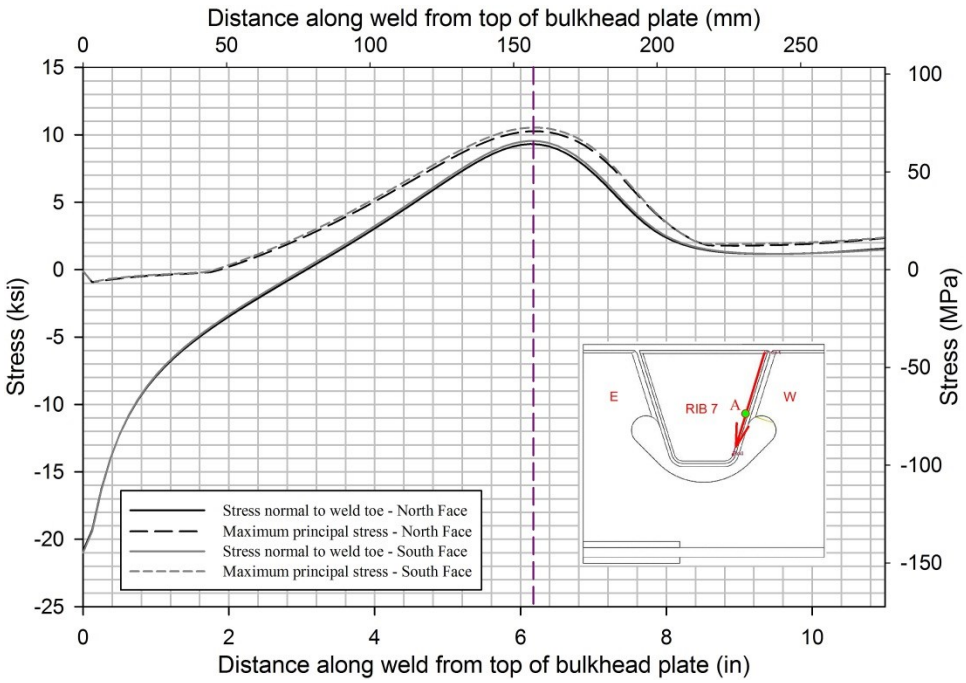

Figure 46 Maximum principal and normal stress at rib-to-bulkhead plate weld toe

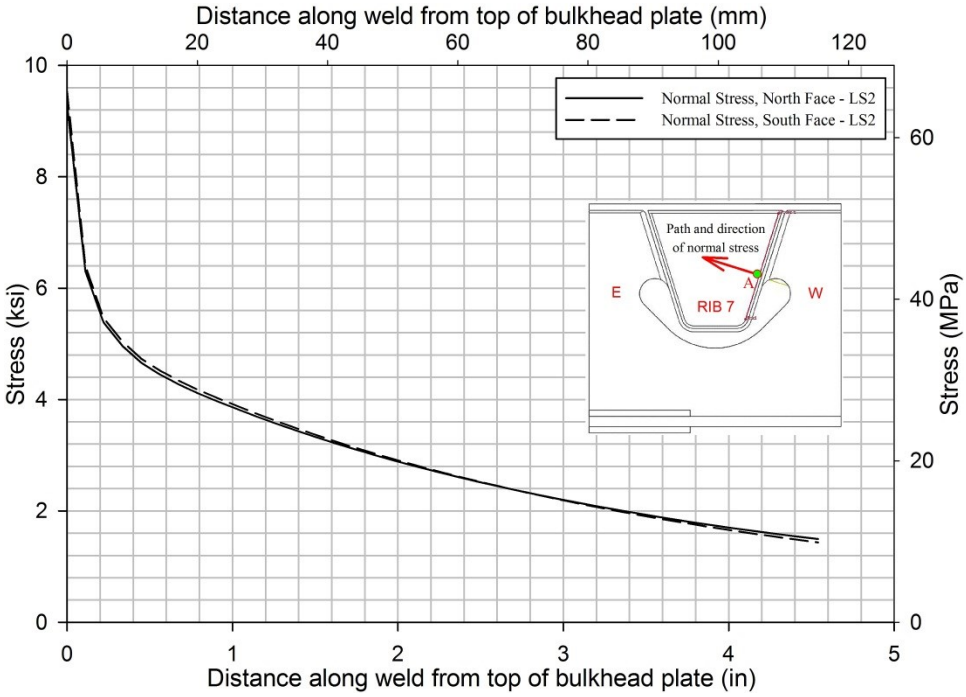

Figure 47 Variation of normal stress on bulkhead plate along the path perpendicular to weld toe

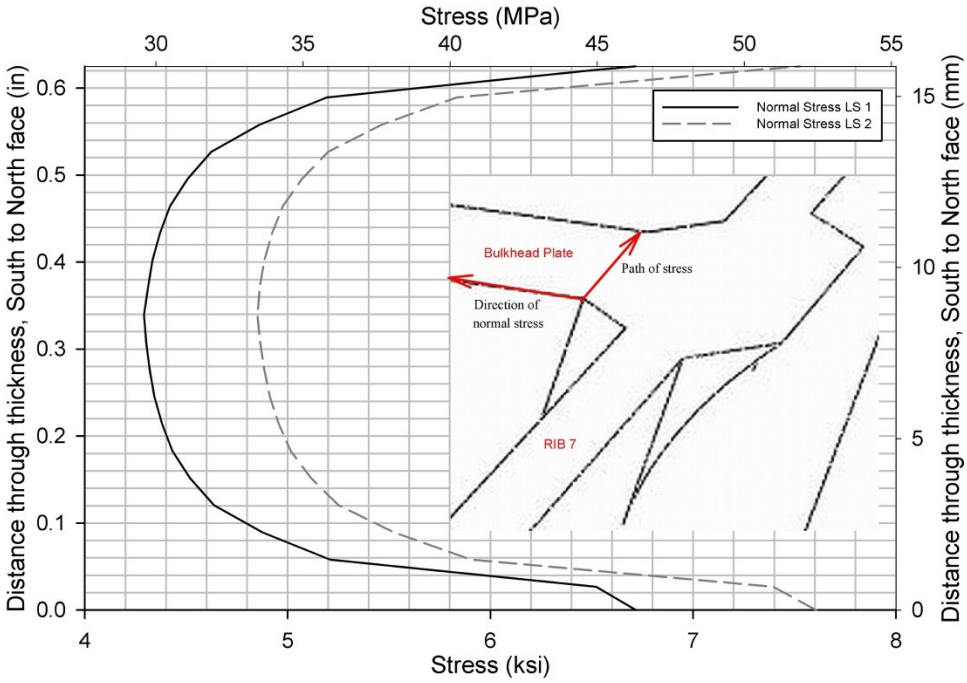

Figure 48 Through thickness normal stress variation at the rib-to-bulkhead plate weld toe

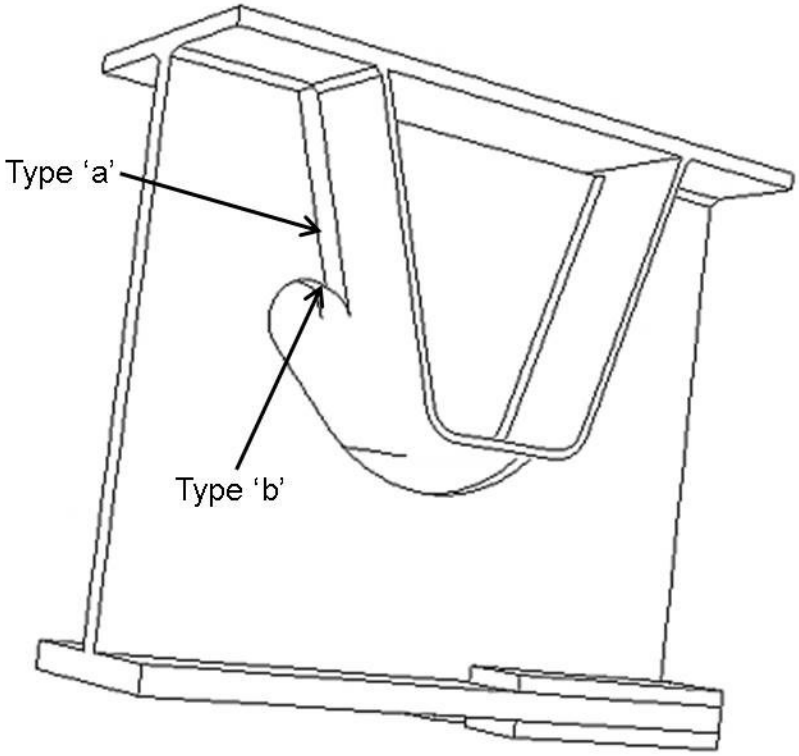

Figure 49 Hot spots types 'a' and 'b' at rib-to-SFB connection details

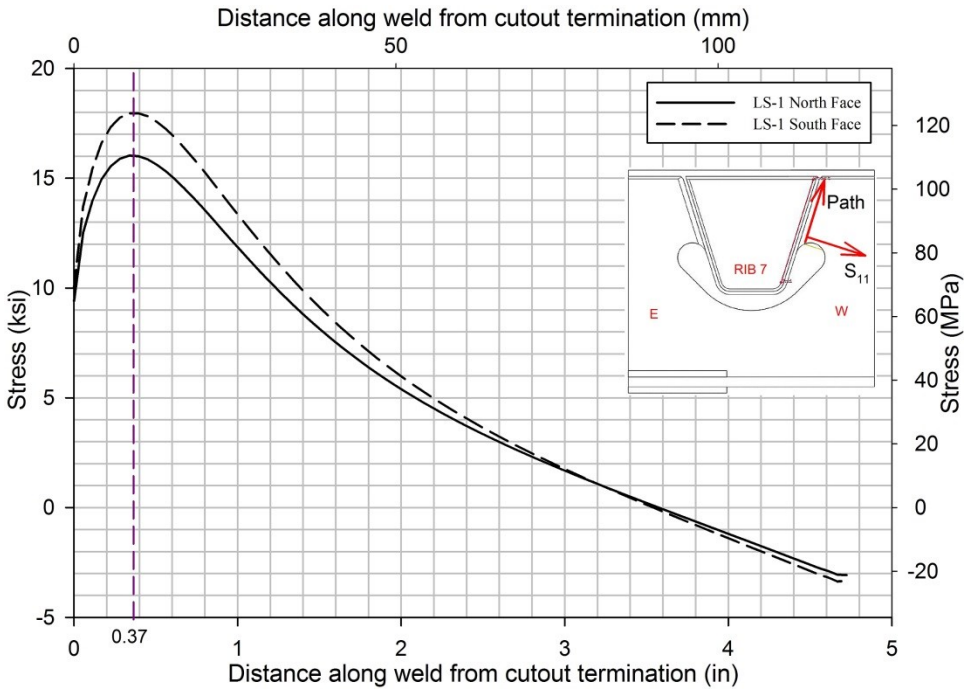

Figure 50 Normal stress along the SFB2a-to-rib weld toe

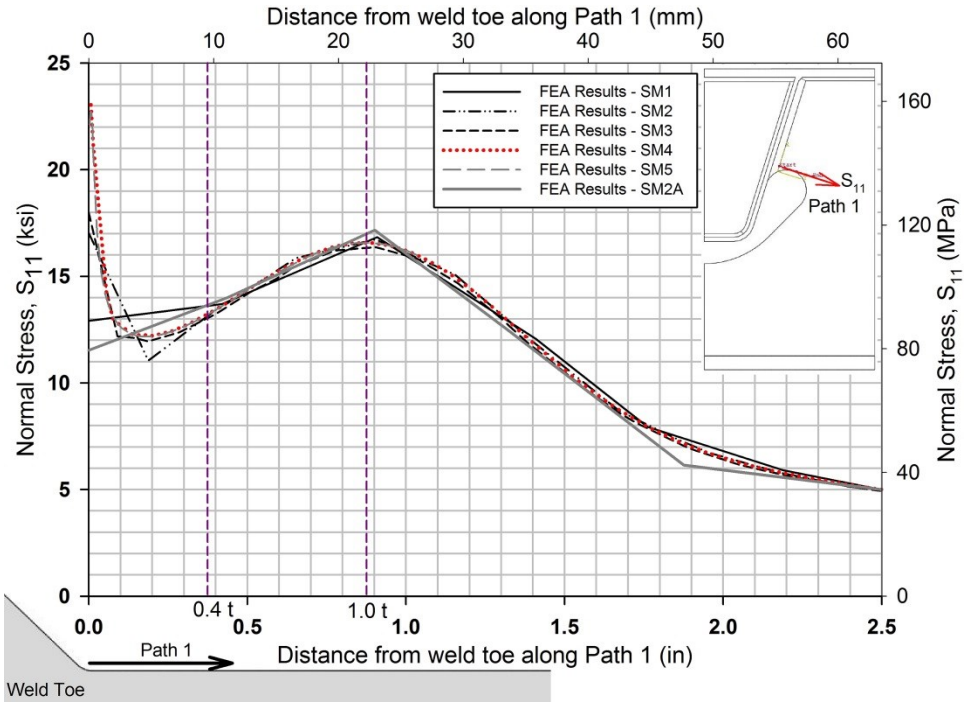

Figure 51 Variation of maximum stress S_{11} on the Rib 7 north face rib-to-SFB2a weld toe

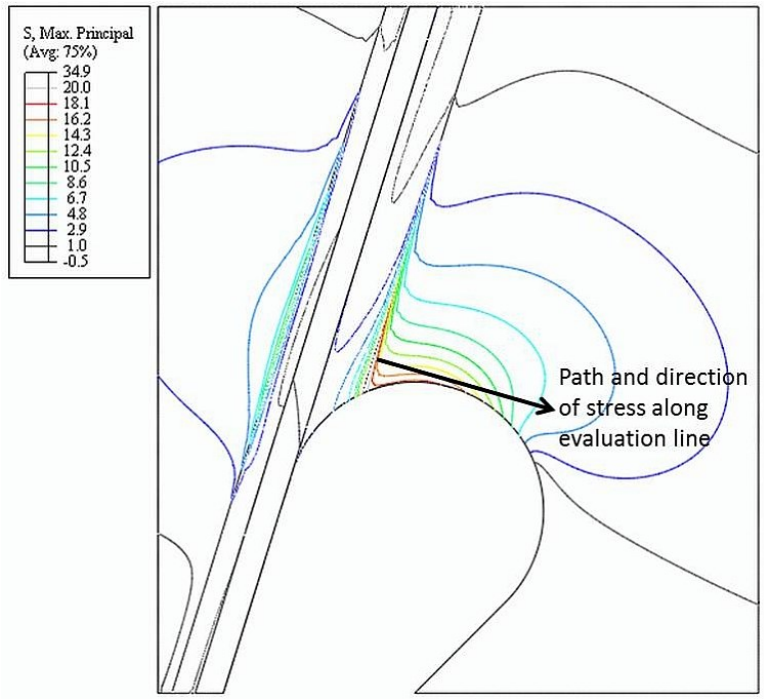

Figure 52 Contour plot at the cutout termination along with evaluation line and direction

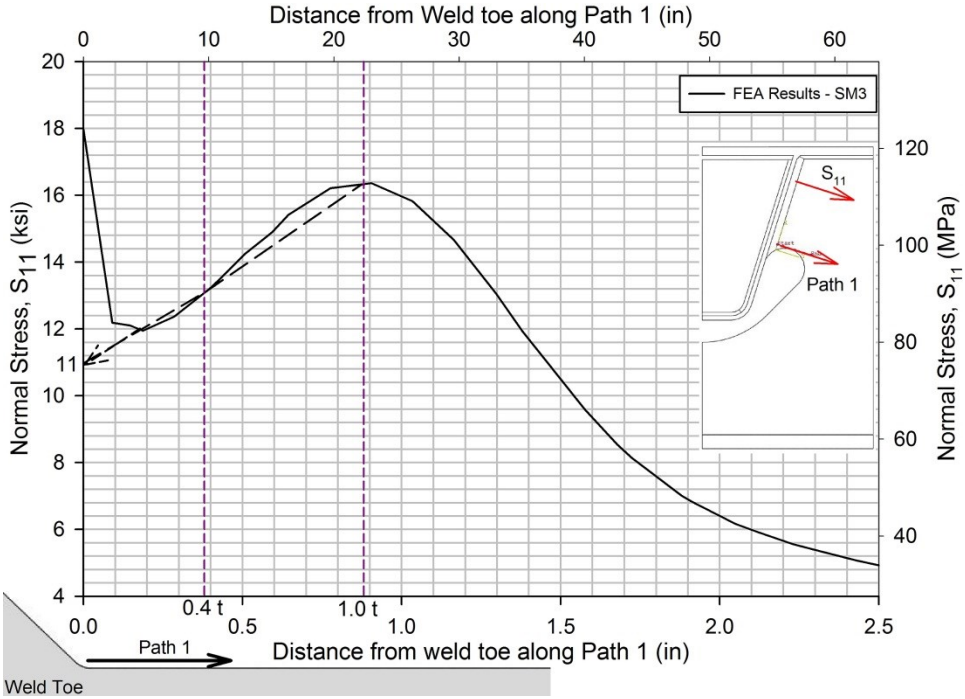

Figure 53 Hot spot stress calculated at rib-to-SFB2a weld toe from linear extrapolation

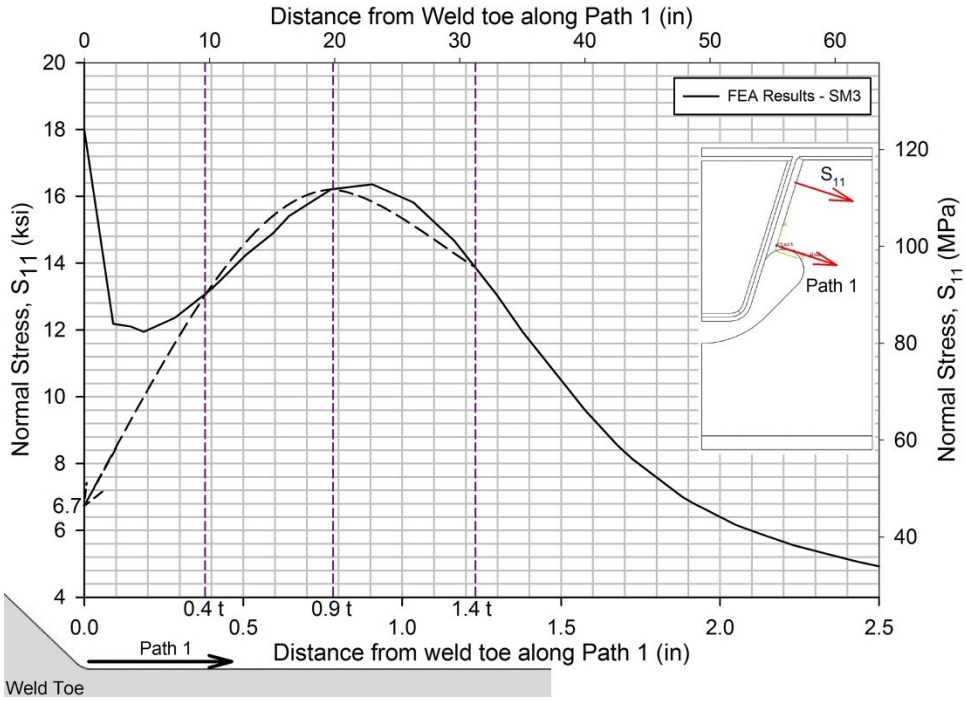

Figure 54 Hot spot stress at rib-to-SFB2a weld toe calculated from quadratic extrapolation

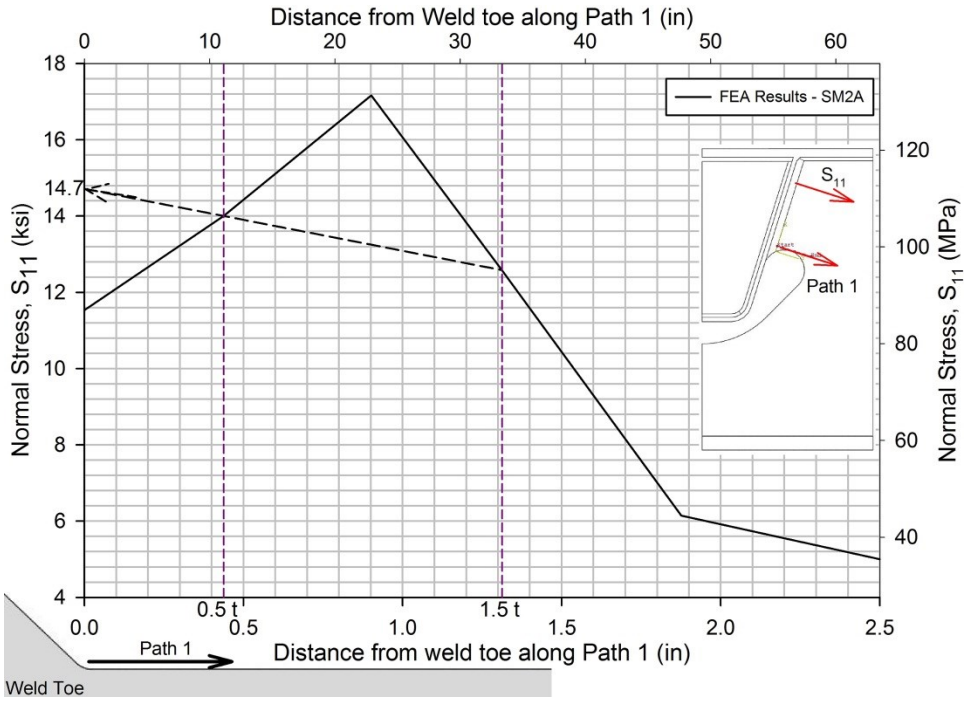

Figure 55 Local structural stress at rib-to-SFB2a weld toe as per AASHTO recommendations

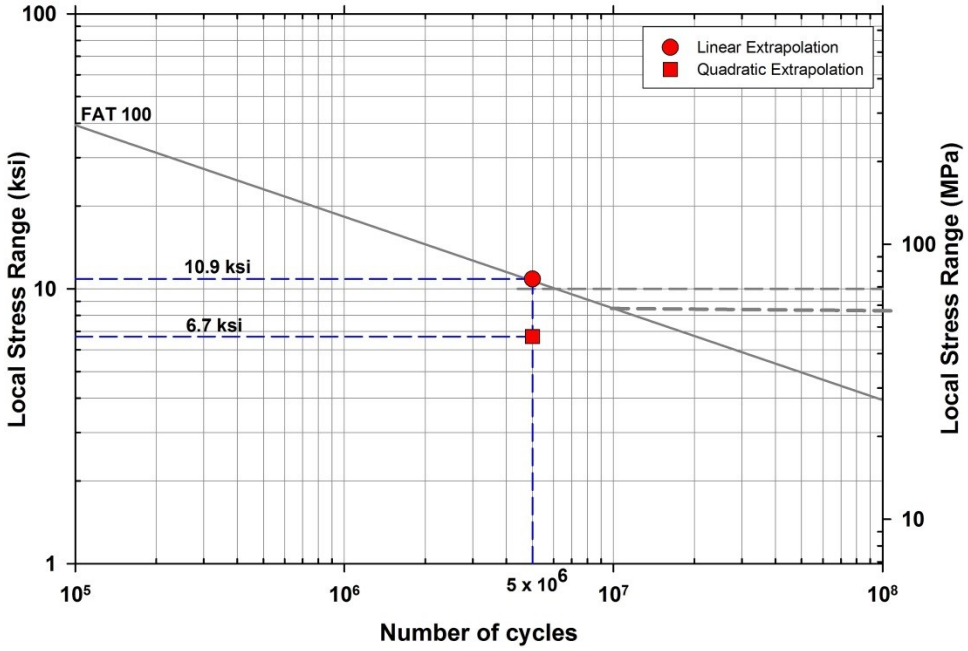

Figure 56 Evaluation of fatigue performance of rib-to-SFB2a weld connection using hot-spot stress

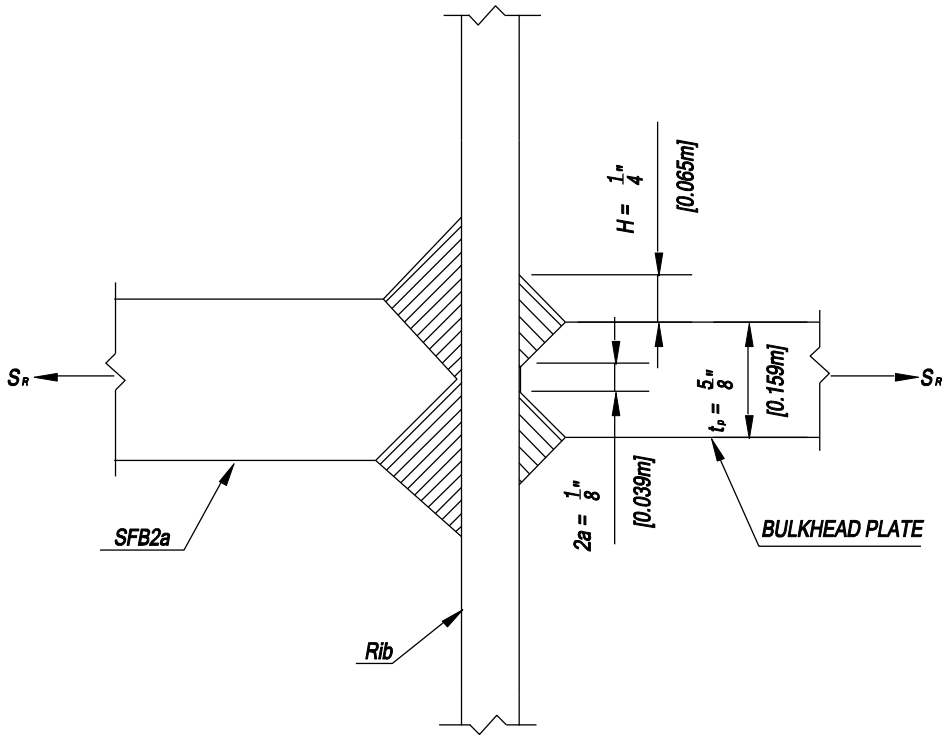

Figure 57 Cruciform connection at bulkhead plate-to-rib-to-SFB welded connection at intermediate subfloor beam

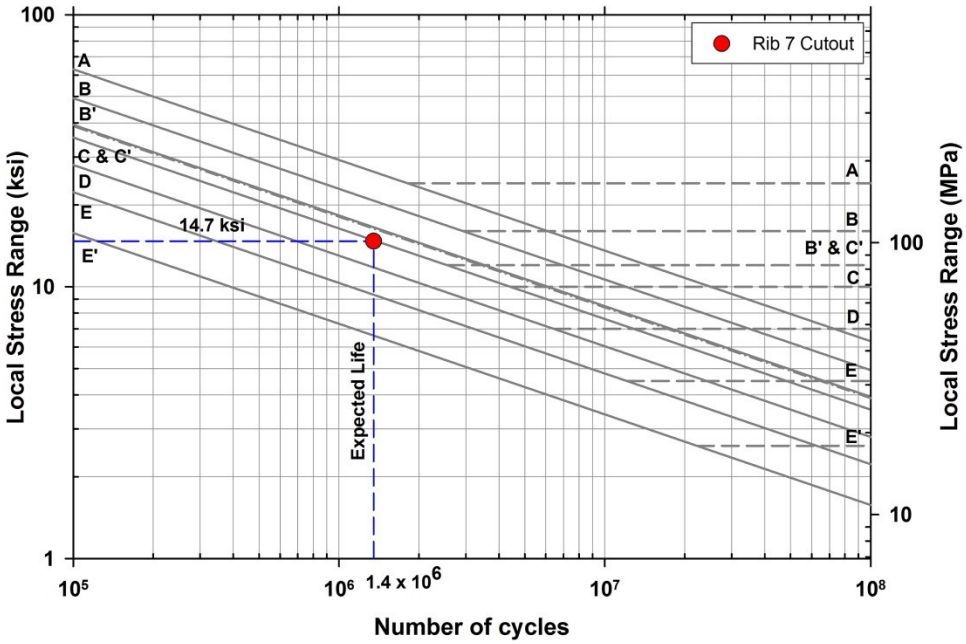

Figure 58 Evaluation of fatigue performance of rib-to-SFB2a weld connection as per AASHTO recommendations

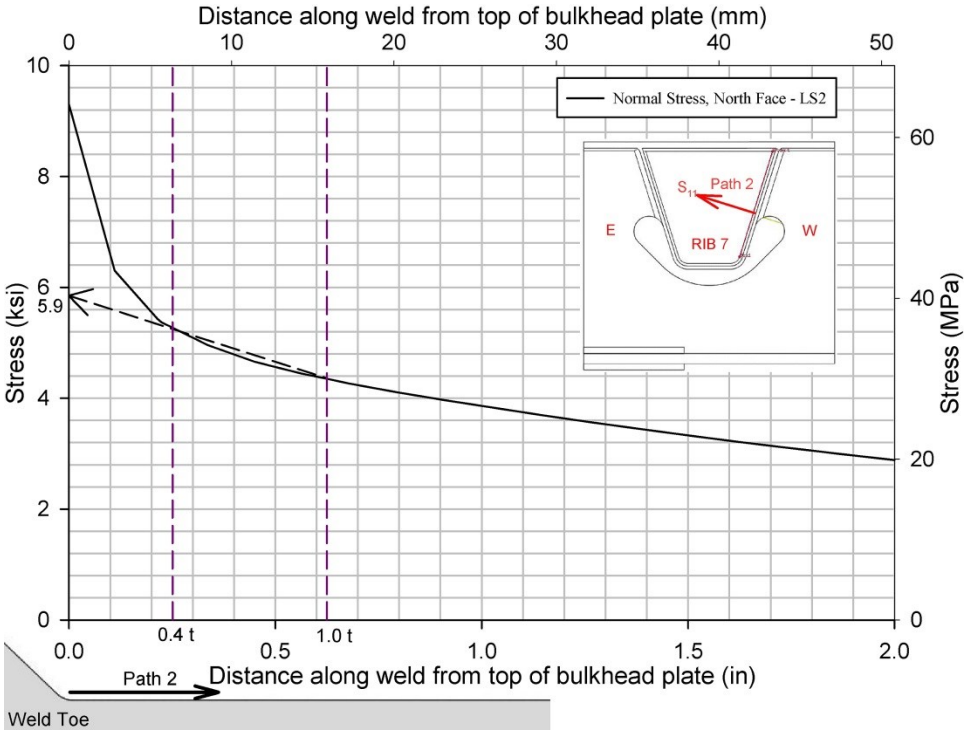

Figure 59 Hot spot stress calculated from quadratic extrapolation at rib-to-bulkhead plate weld toe

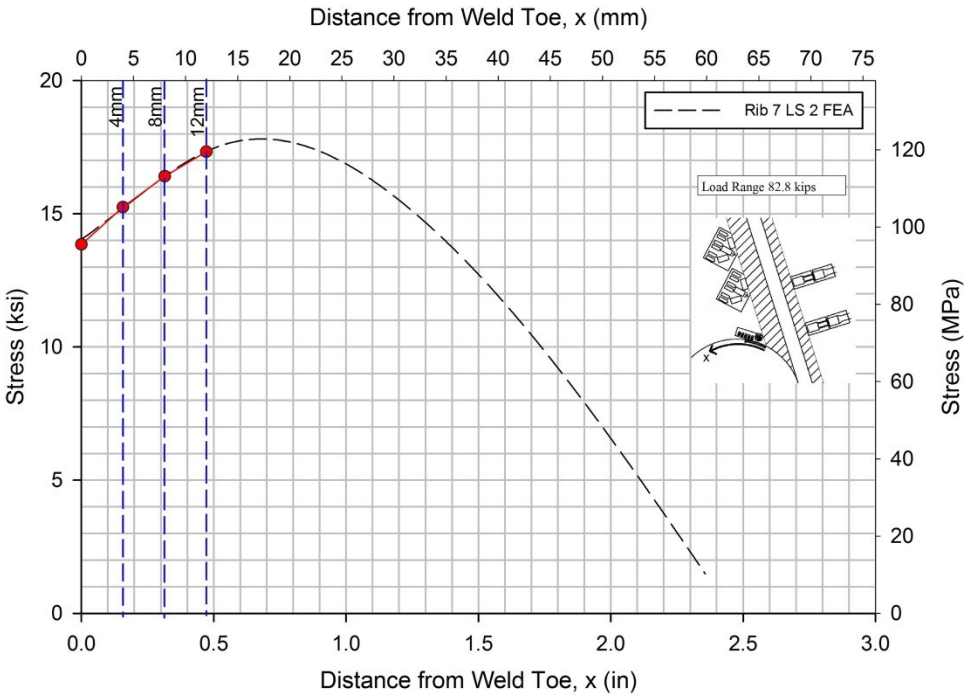

Figure 60 Hot spot stress extrapolated for cutout edge

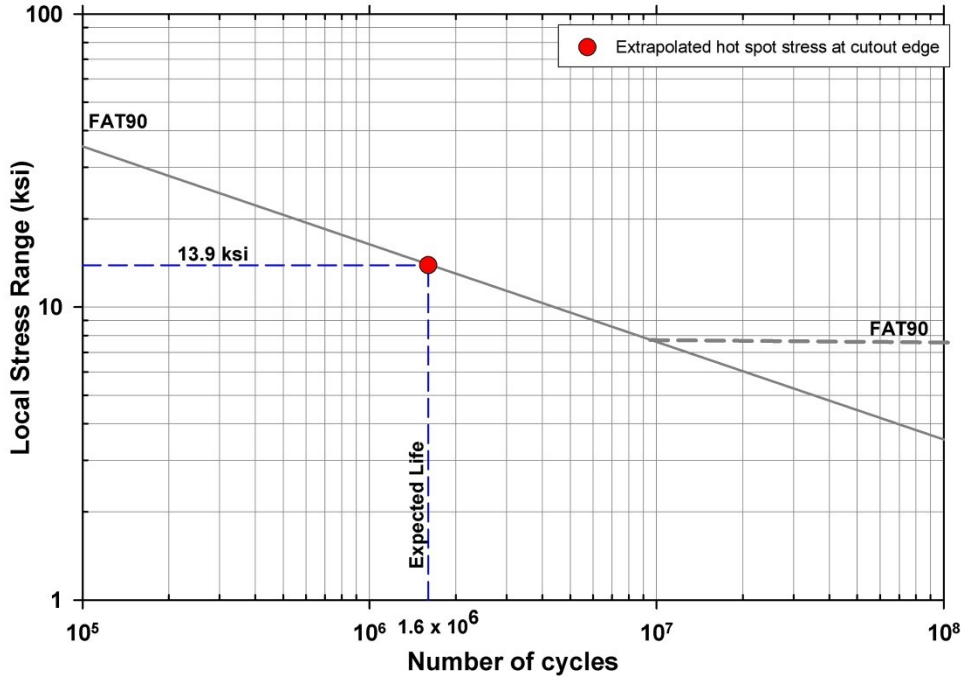

Figure 61 Evaluation of the fatigue performance of SFB2a cutout edge connection

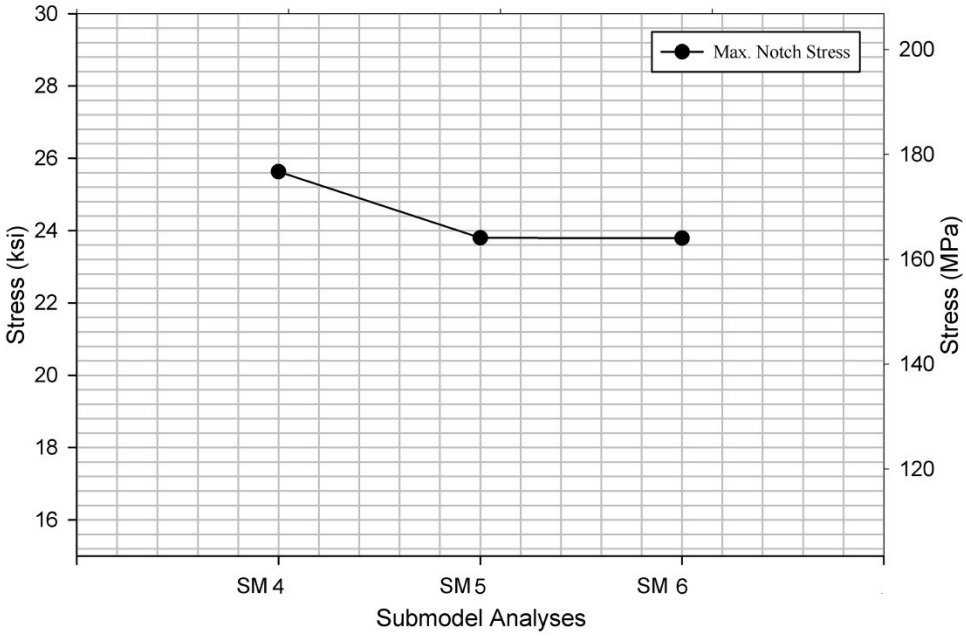

Figure 62 Convergence of notch stress at rib-to-SFB2a weld toe

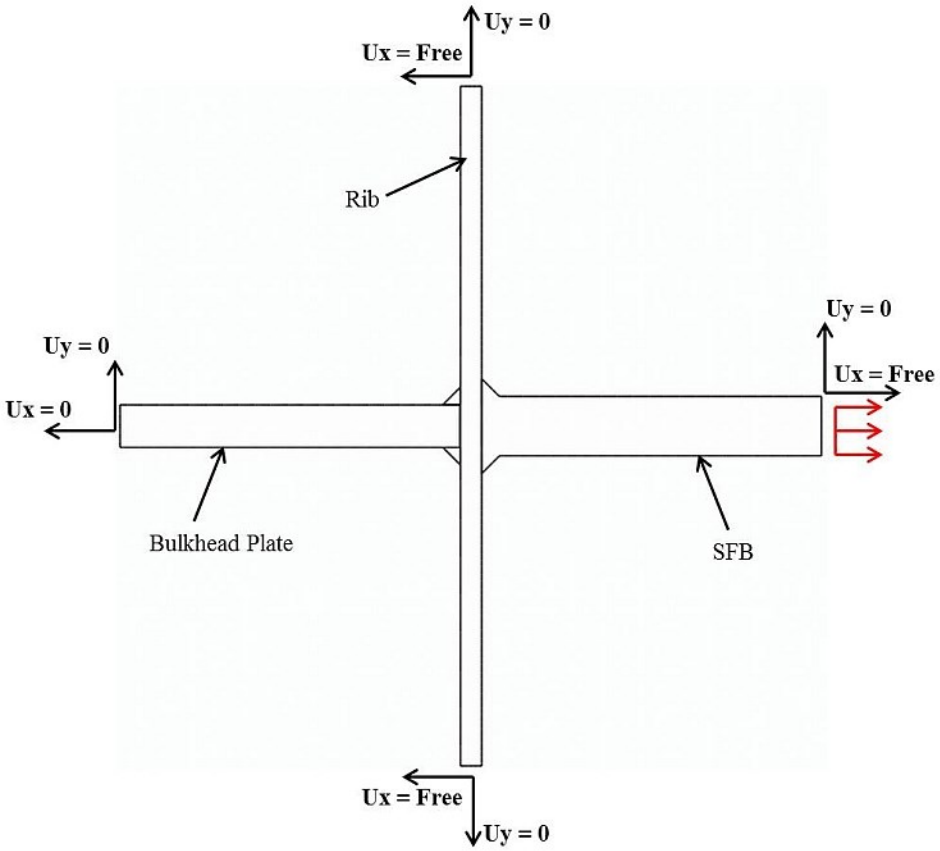

Figure 63 Model 1- a 2D model of the cruciform connection of the rib with SFB and bulkhead plate

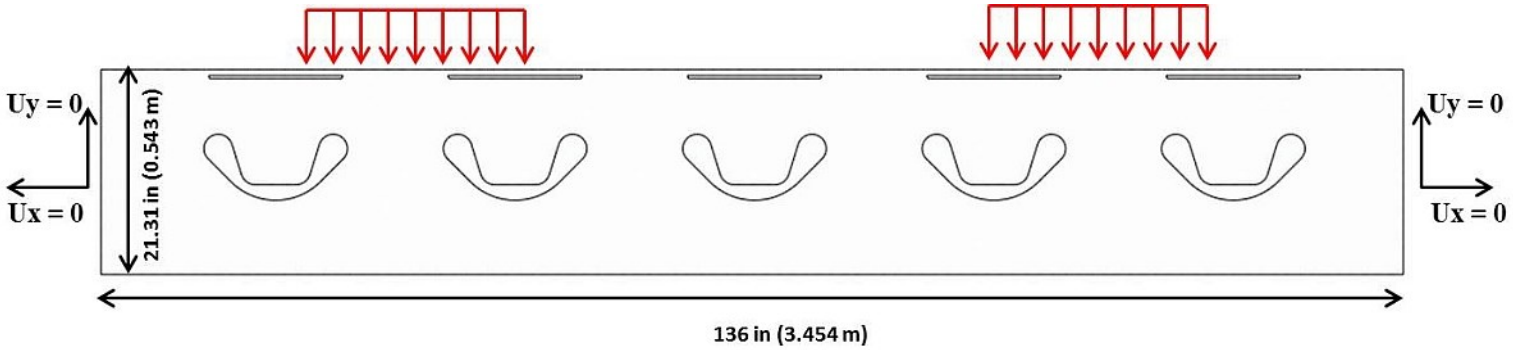

Figure 64 Model 2: A 2D model of the SFB (with cutouts under ribs) with boundary conditions and loading

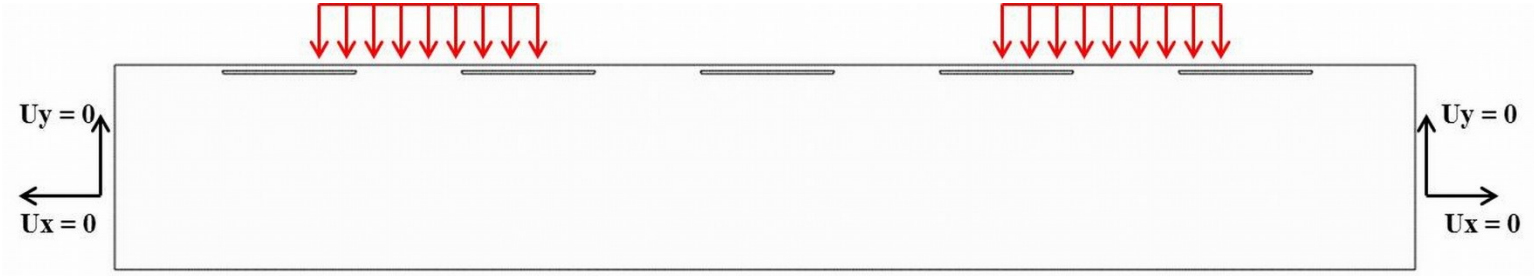

Figure 65 Model 2: A 2D model of the SFB (without cutouts under ribs) with boundary conditions and loading

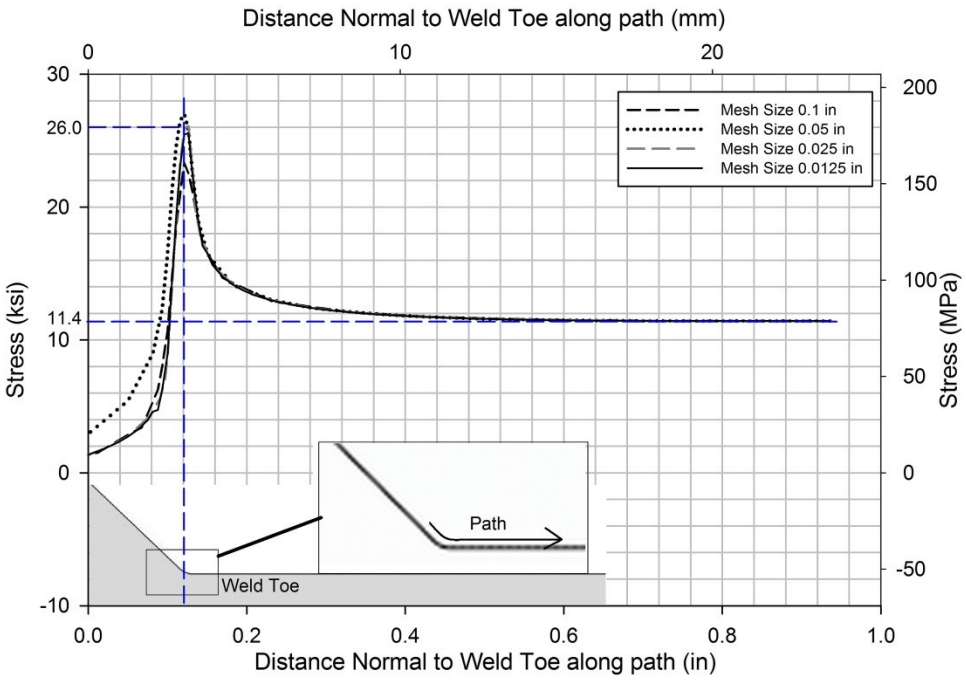

Figure 66 Convergence of normal stresses perpendicular to the weld toe for different mesh sizes in Model 1

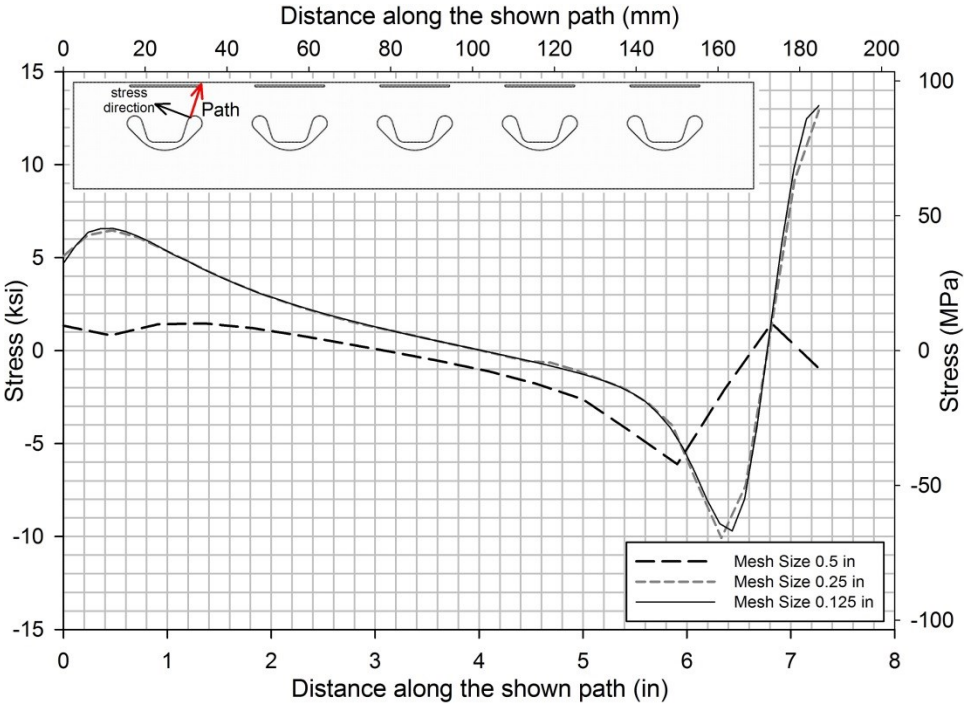

Figure 67Convergence of normal stresses along the weld toe for different mesh sizes in Model 2

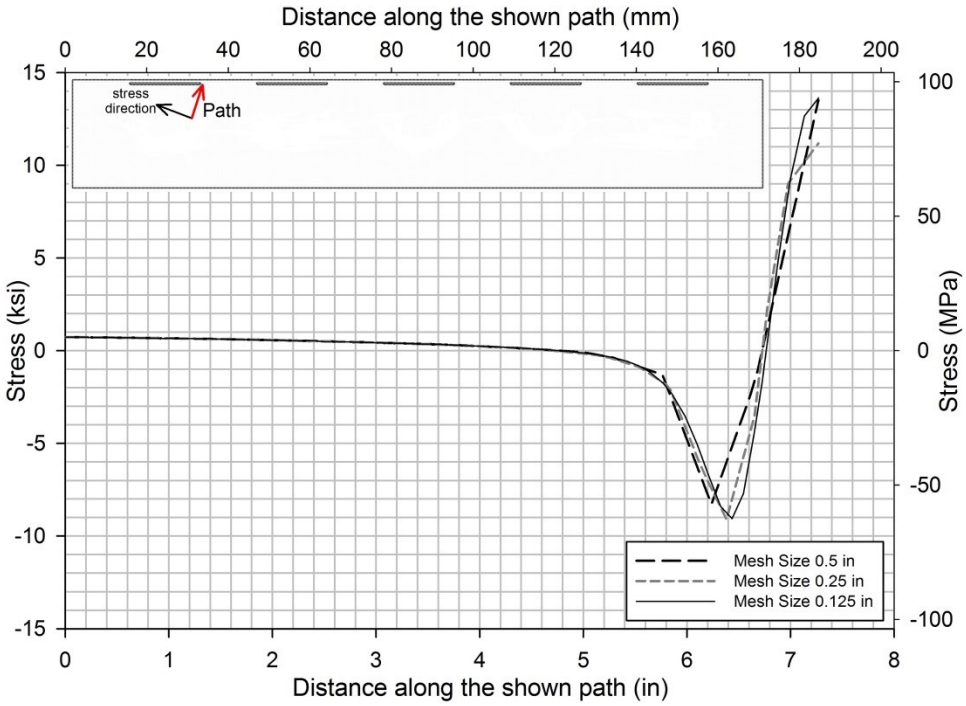

Figure 68Convergence of normal stresses along the weld toe path for different mesh sizes in Model 3

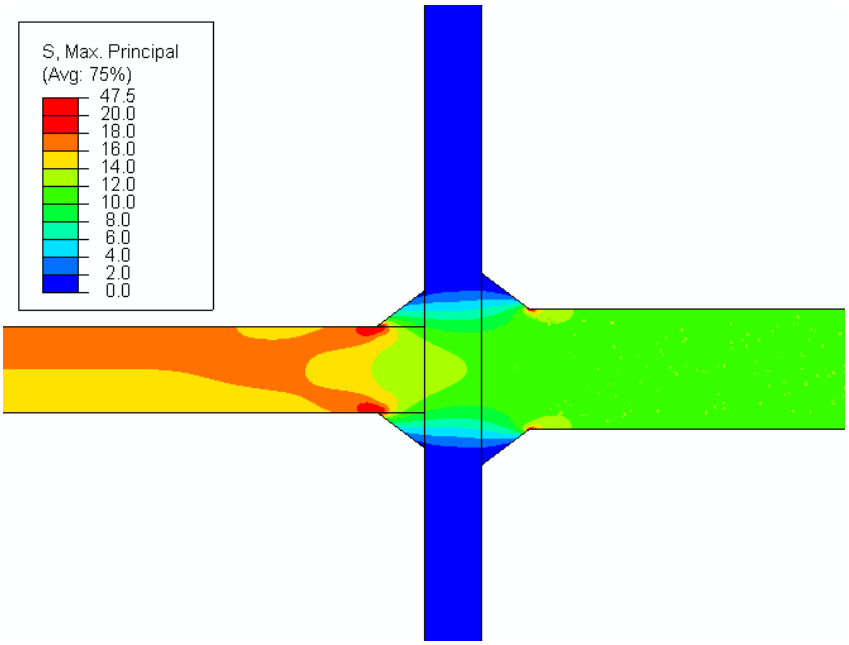

Figure 69 Maximum principal stress plot for Model 1

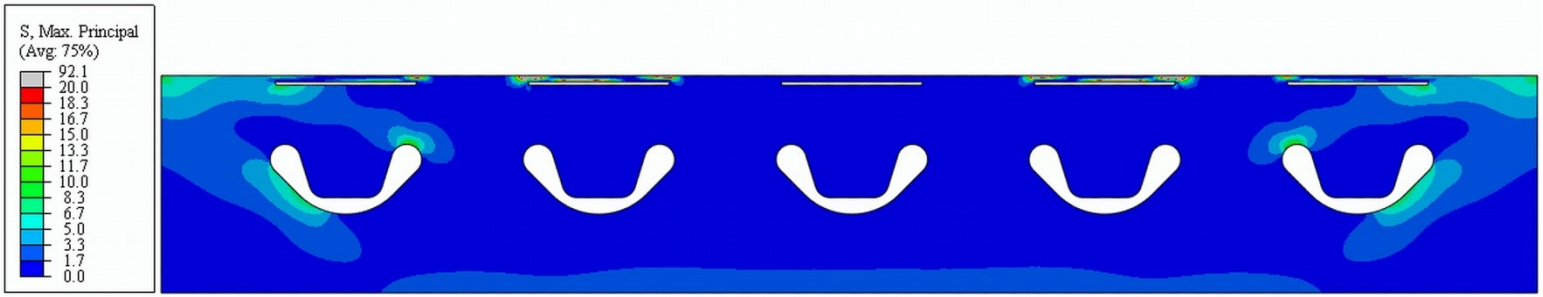

Figure 70 Maximum principal stress plot for Model 2

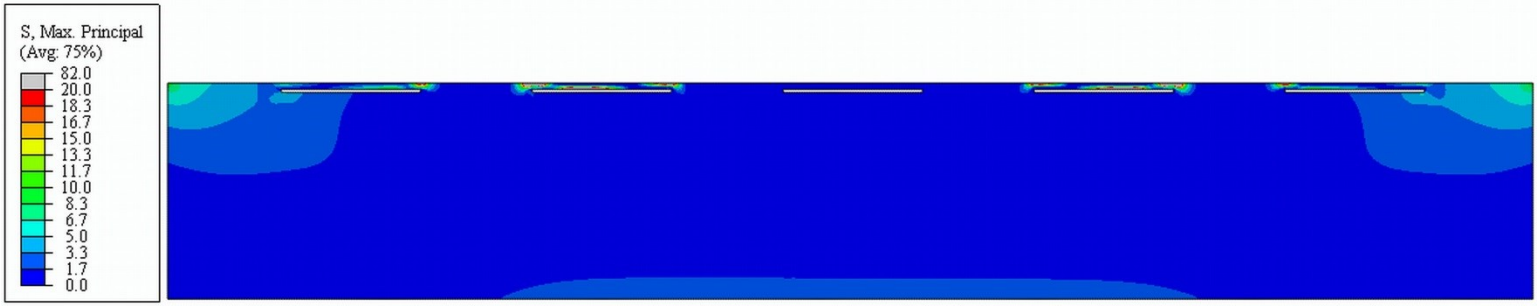

Figure 71 Maximum principal stress plot for Model 3

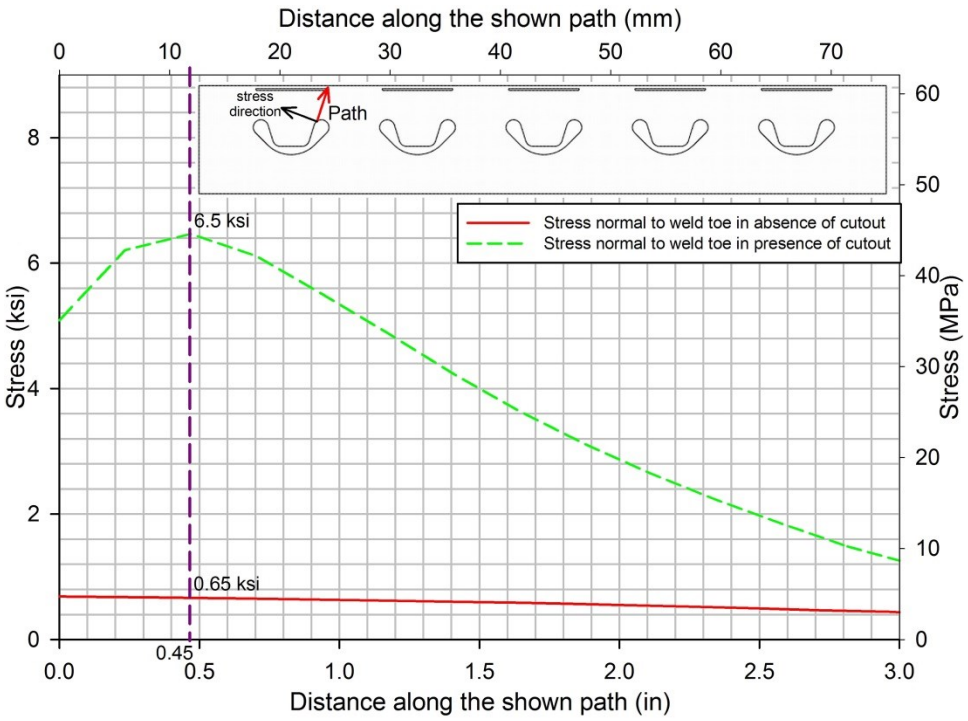

Figure 72 Stresses normal to weld toe along the weld toe path for Model 1 and Model 2

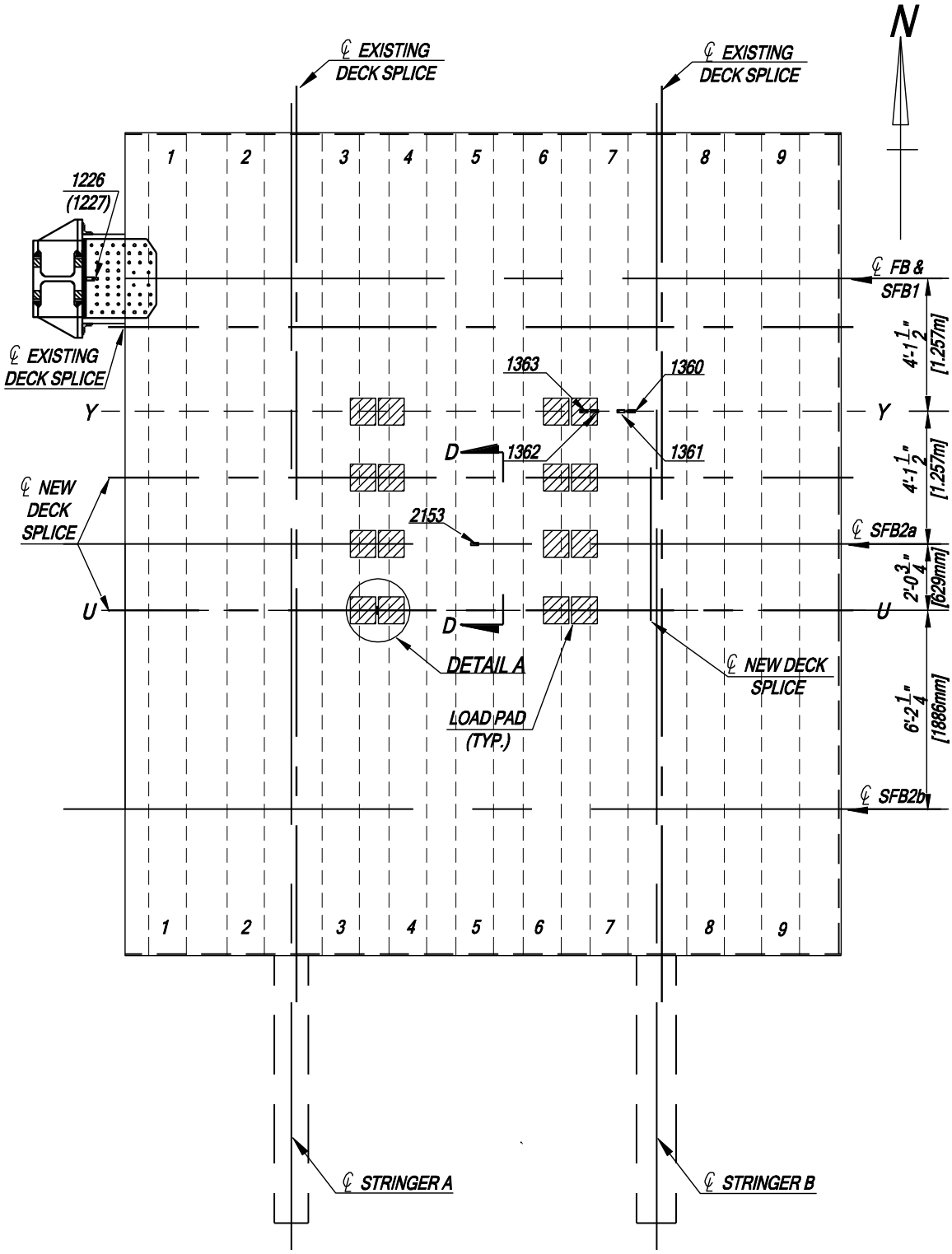

Figure 73 Plan view of Deck specimen with instrumentation on deck plate and floor beam (drawn by Alapati)

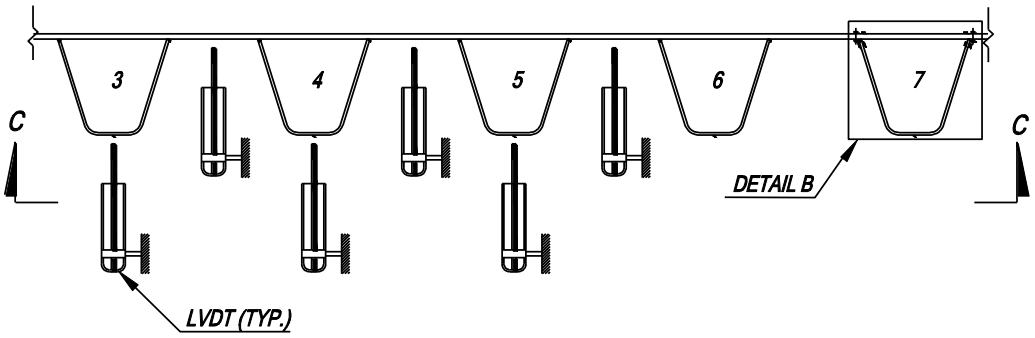

Figure 74 Locations of LVDTs at section Y-Y in Figure 73 (drawn by Alapati)

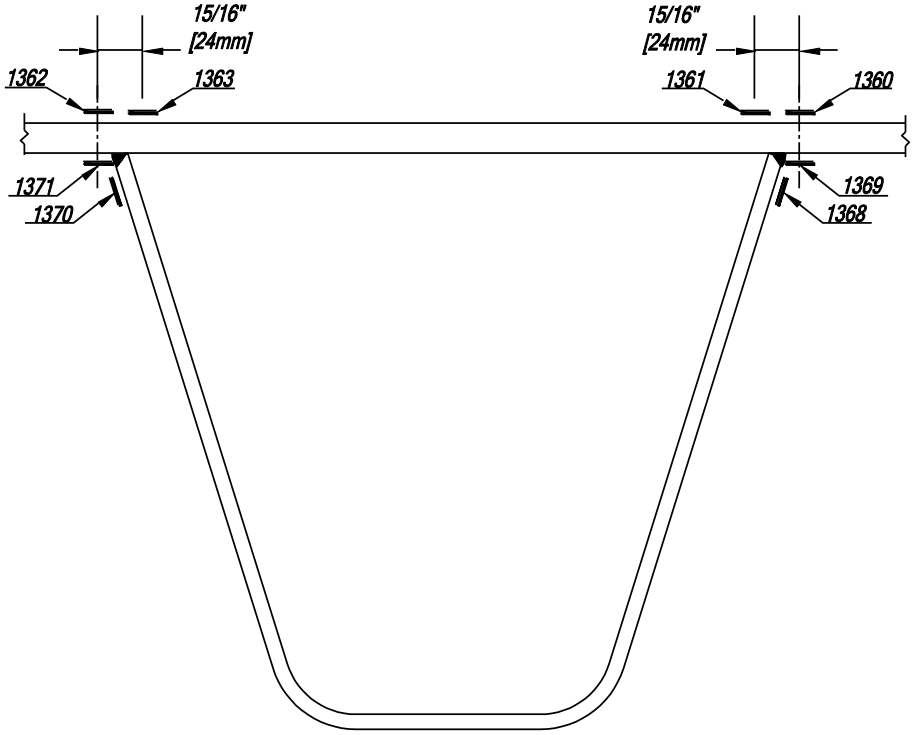

Figure 75 Detail B from Figure 74 (drawn by Alapati)

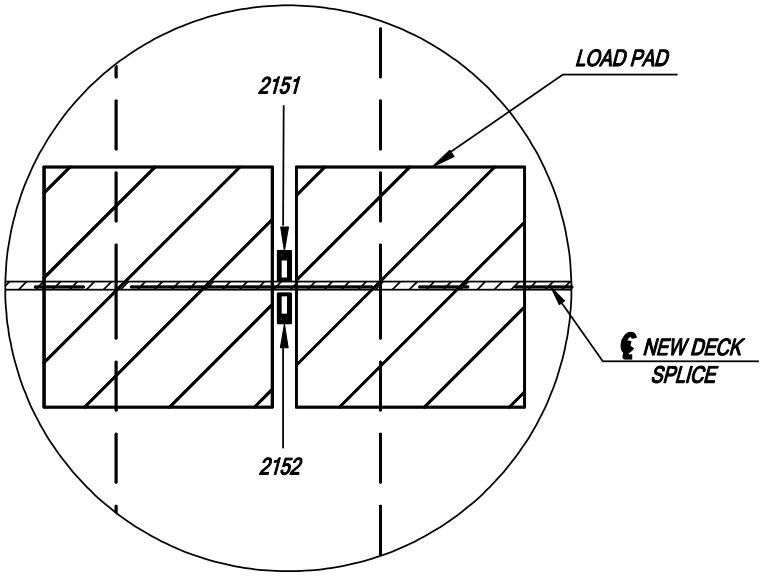

Figure 76 Detail A from Figure 73 showing gauges at section U-U (drawn by Alapati)

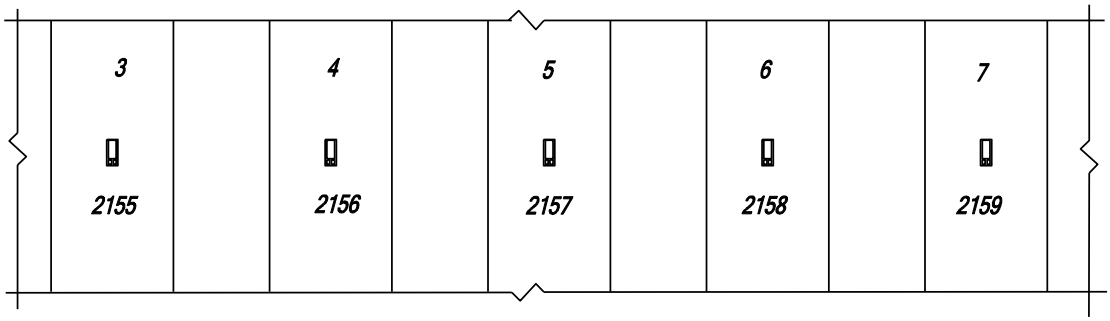

Figure 77 Part underside view showing gauges at rib soffits (Refer section C-C in Figure 74) (drawn by Alapati)

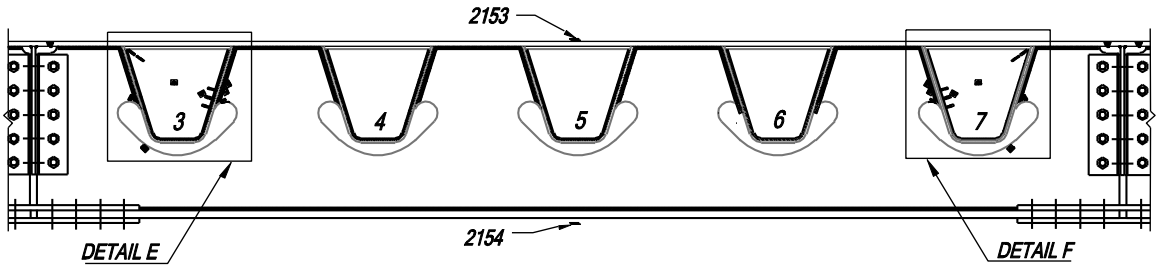

Figure 78 Elevation view of SFB2a in between stringer extensions (drawn by Alapati)

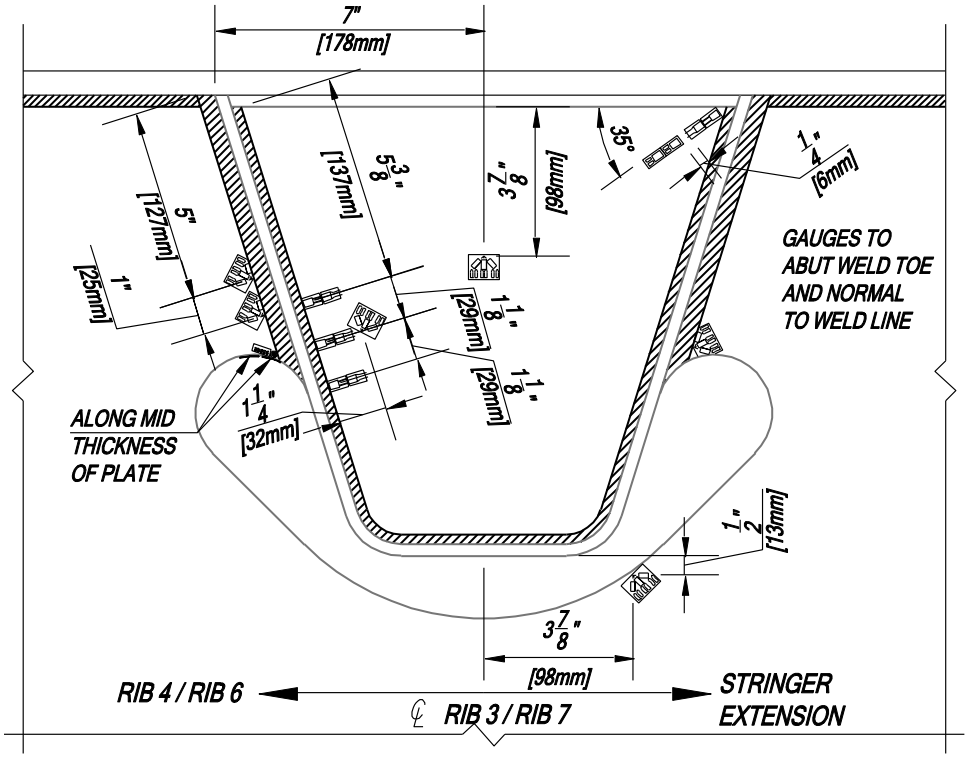

Figure 79 Details of gauge placements in SFB2a at ribs 3 and 7 (Details E and F in Figure 78 are similar but mirrored) (drawn by Alapati)

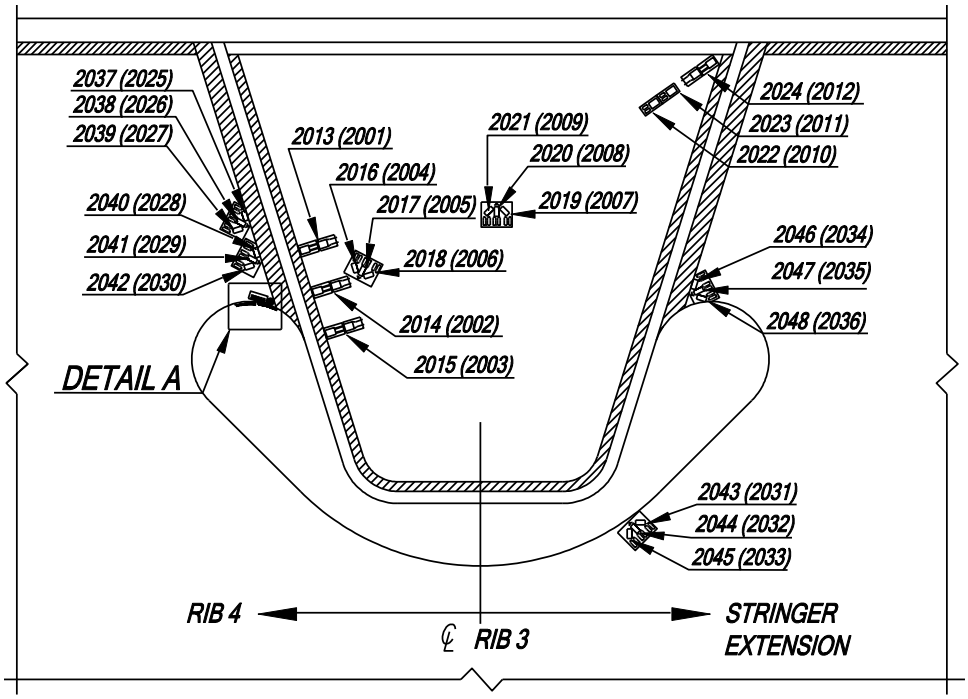

Figure 80 Detail instrumentation plan at Rib 3 – Detail E in Figure 78 (drawn by Alapati)

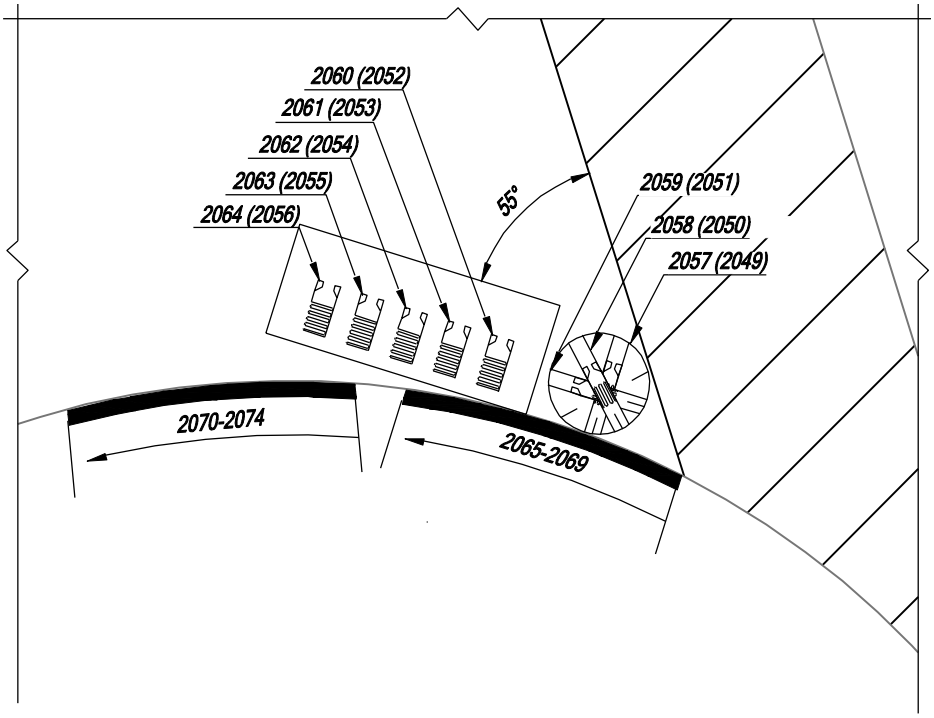

Figure 81 Enlarged view of Detail A in Figure 80 (drawn by Alapati)

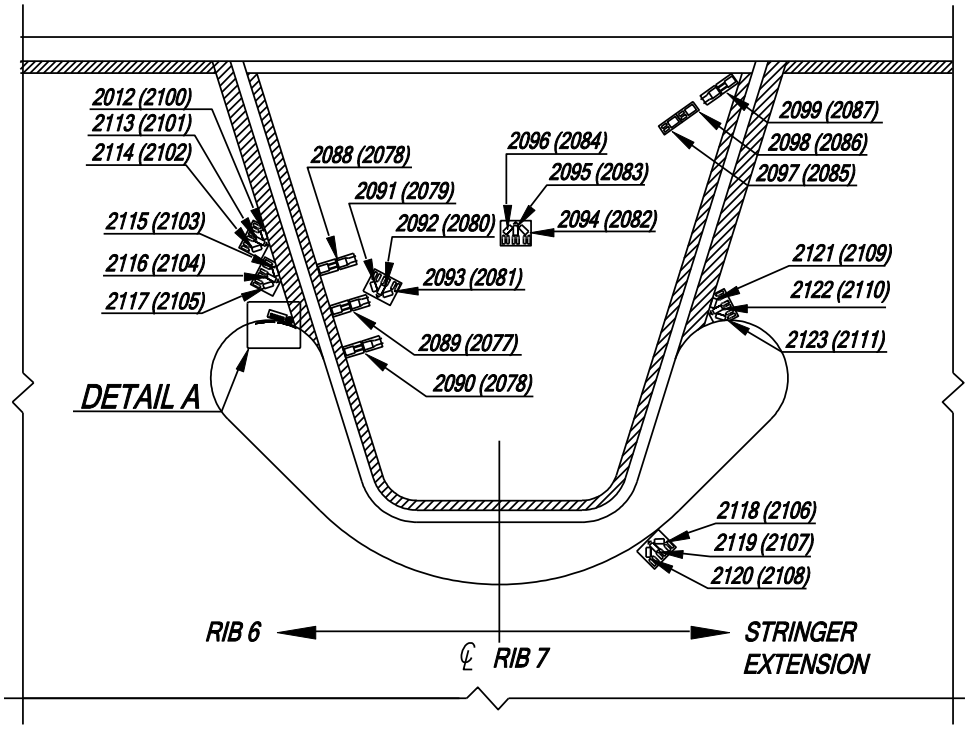

Figure 82 Detail instrumentation plan at Rib 7 – Detail F in Figure 78 (drawn by Alapati)

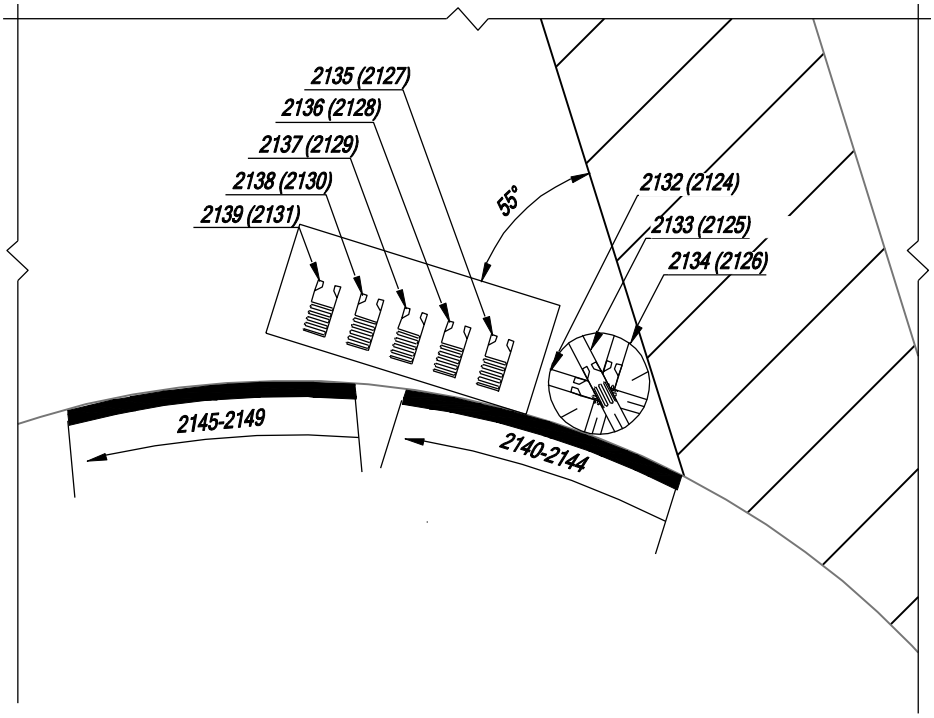

Figure 83 Enlarged view of Detail A in Figure 82 (drawn by Alapati)

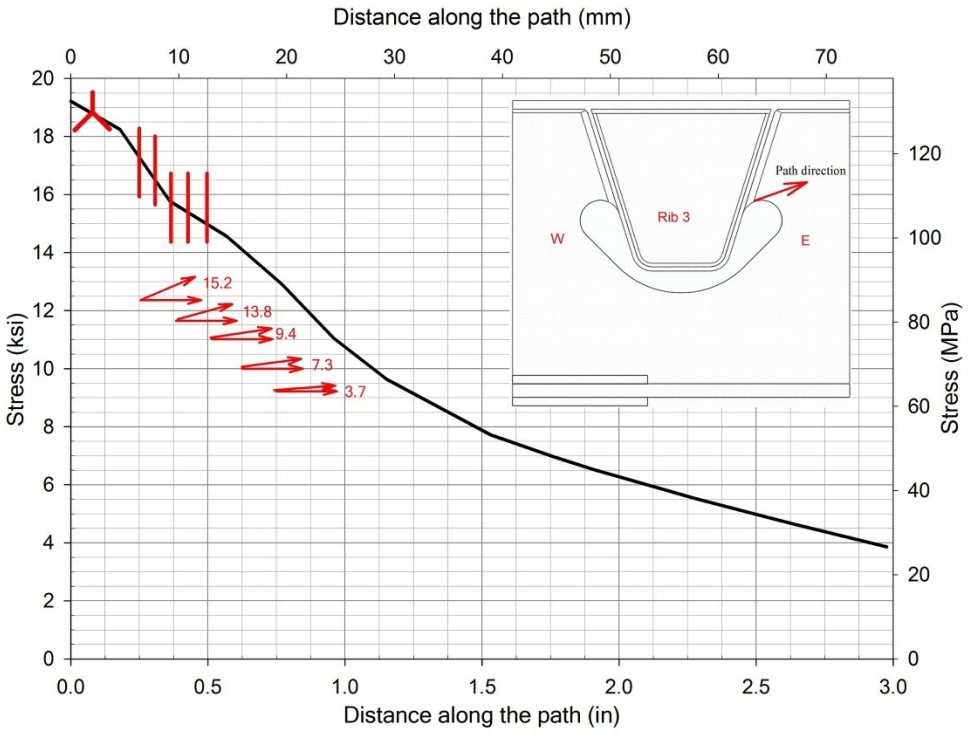

Figure 84 Stress on Rib 3 cutout and gauge placement plan

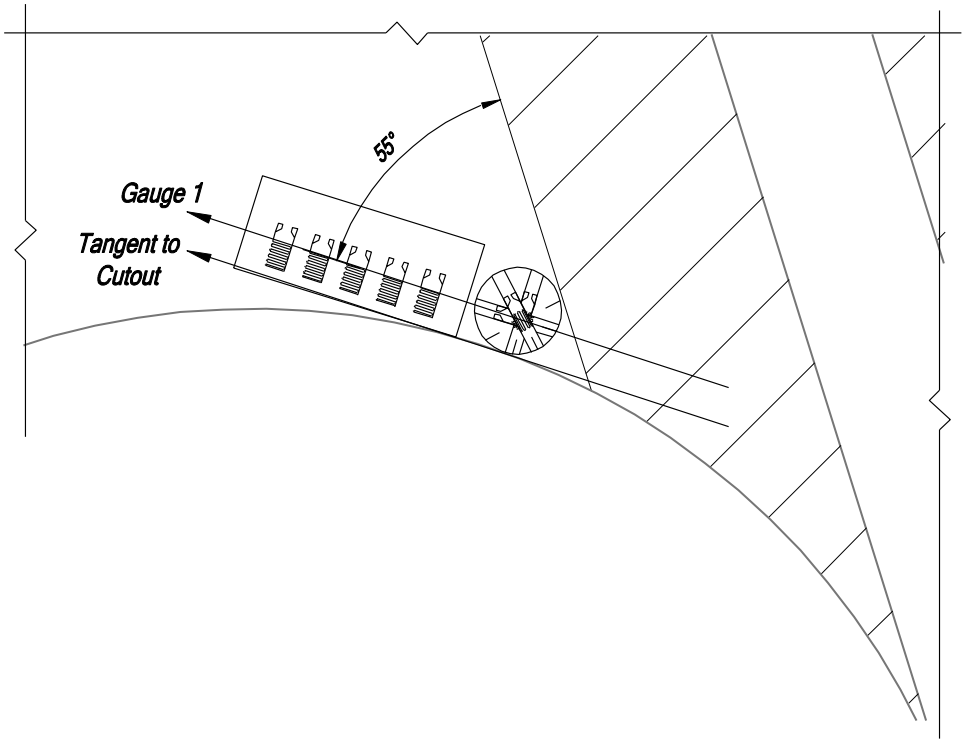

Figure 85 Proposed orientation of rosette and strip gauges at ribs 3 and 7 cutouts (drawn by Alapati)

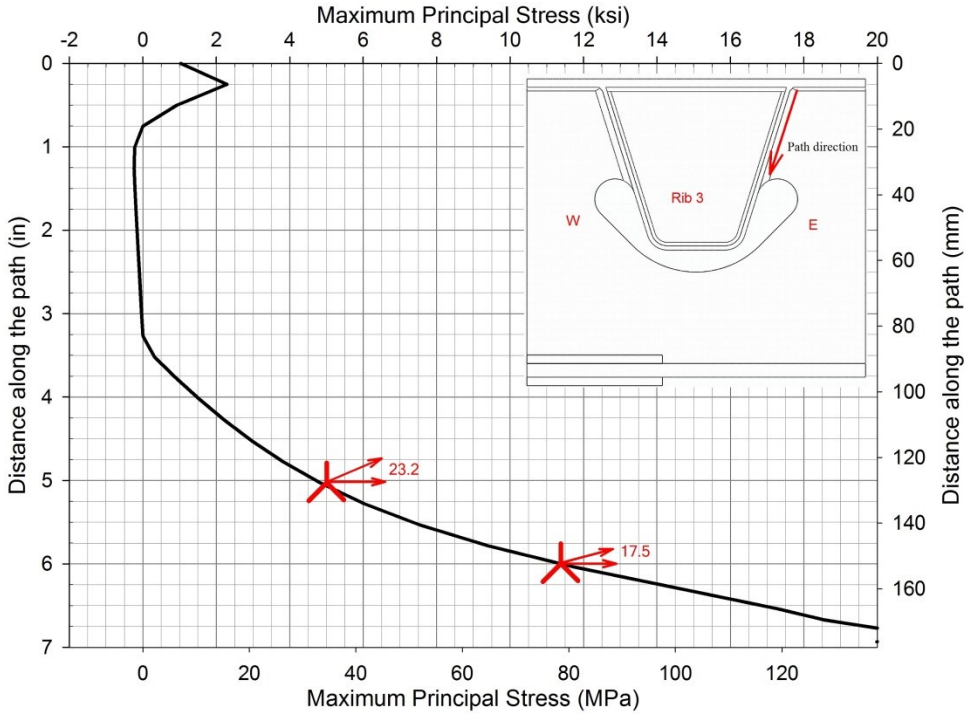

Figure 86 Stress along the rib-to-SFB2a weld toe at Rib 3 and gauge placement plan

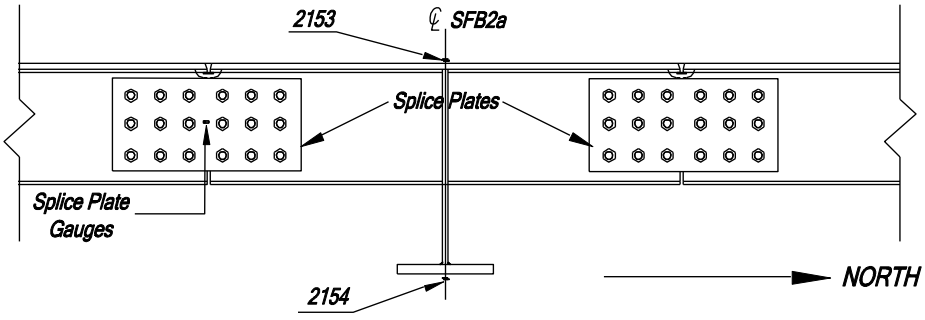

Figure 87 Section D-D from Figure 73 showing bolted connections at the splices and gauges on SFB2a at the section along Rib 5

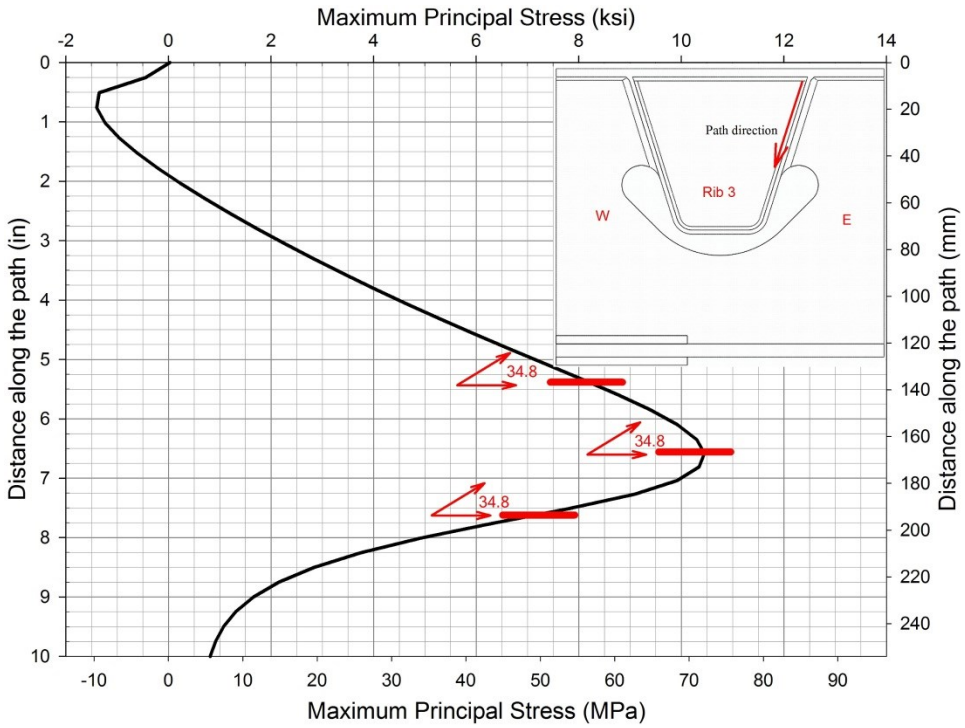

Figure 88 Stress along the rib-to-bulkhead plate weld toe at Rib 3 and gauge placement plan

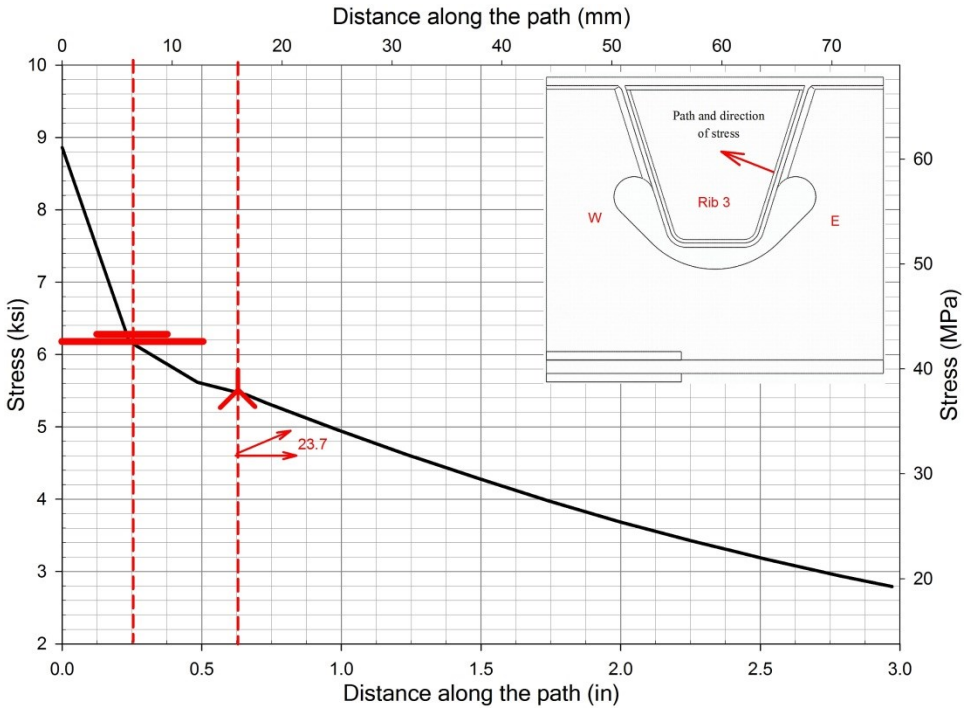

Figure 89 Stress along the shown path normal to rib-to-bulkhead weld toe on Rib 3 bulkhead plate and gauge placement plan

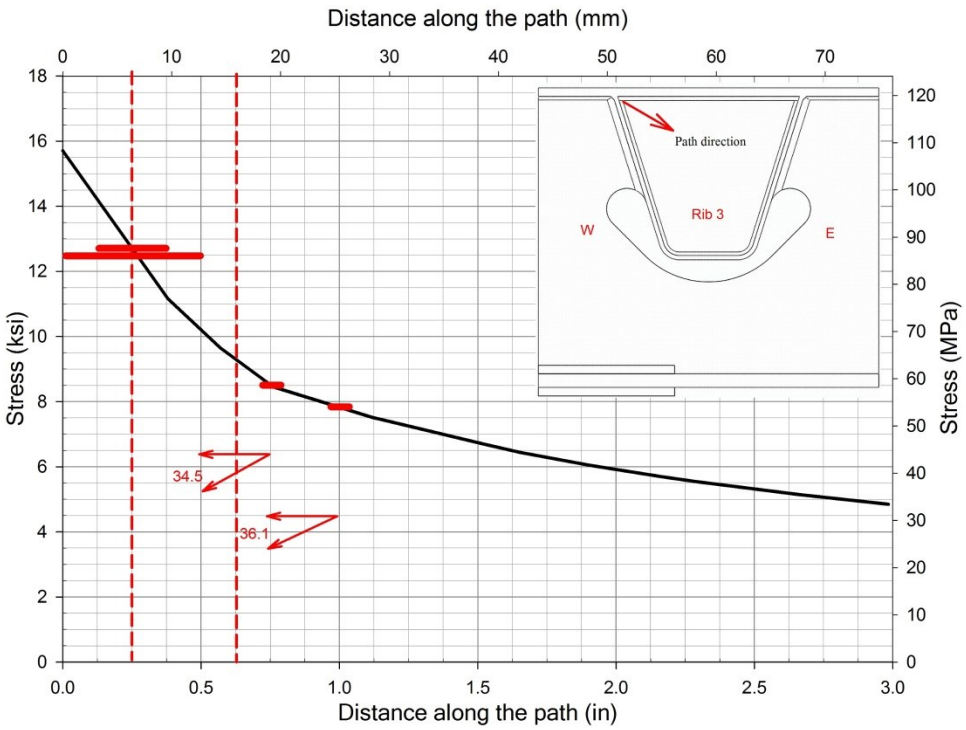

Figure 90 Stress along the shown path in Rib 3 bulkhead plate and gauge placement plan

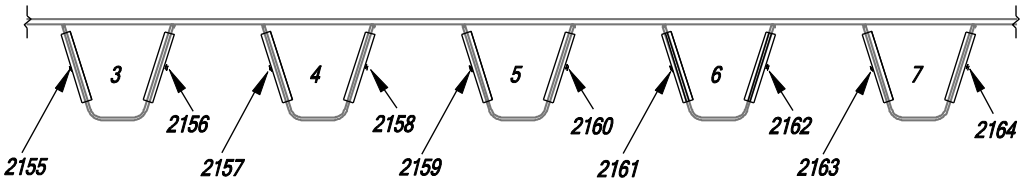

Figure 91 Section U-U (Figure 73) between stringers A and B showing gauges on splice plates

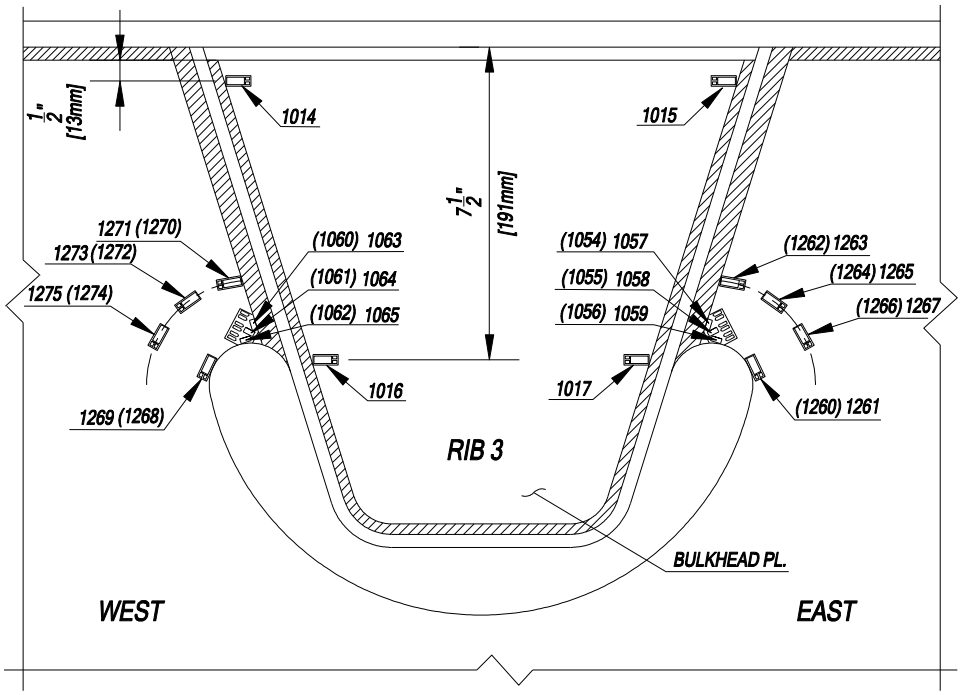

Figure 92 Instrumentation on south face of SFB1 at Rib 3 with north face strain gauges are shown in parentheses (Alapati, 2012)

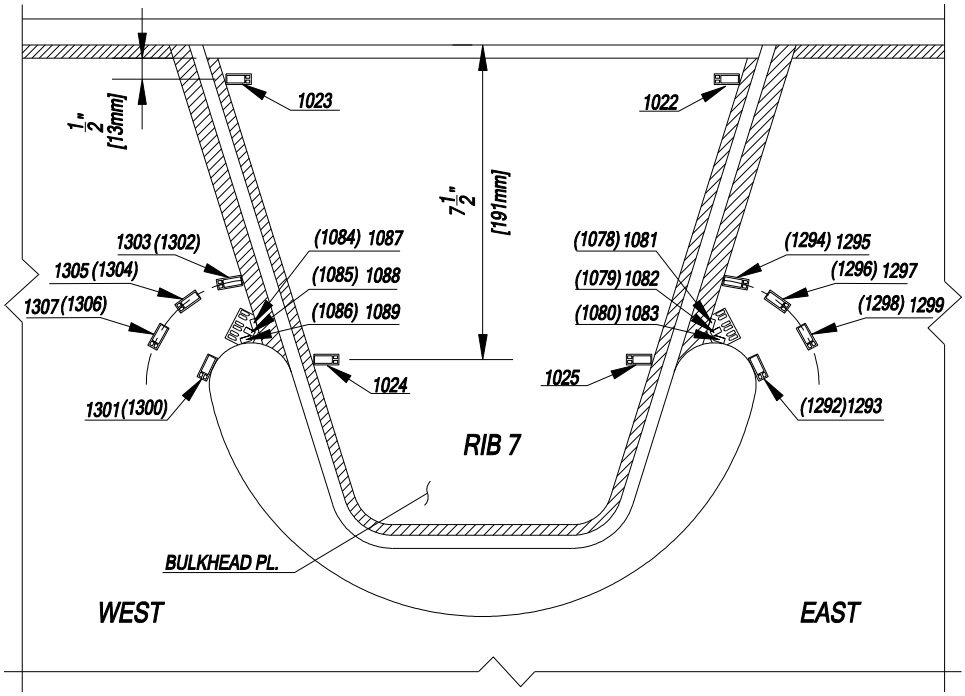

Figure 93 Instrumentation on south face of SFB1 at Rib 7 with north face strain gauges are shown in parentheses (Alapati, 2012)

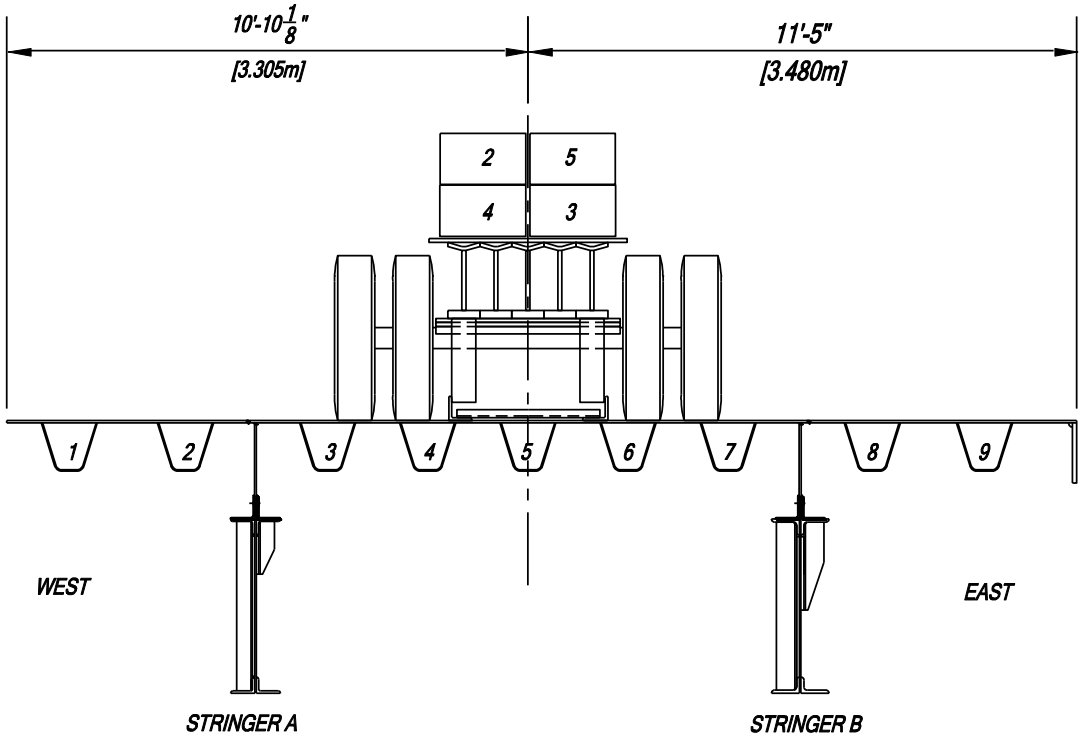

Figure 94 Crawl Test transverse position of truck (adapted from Alapati, 2012)

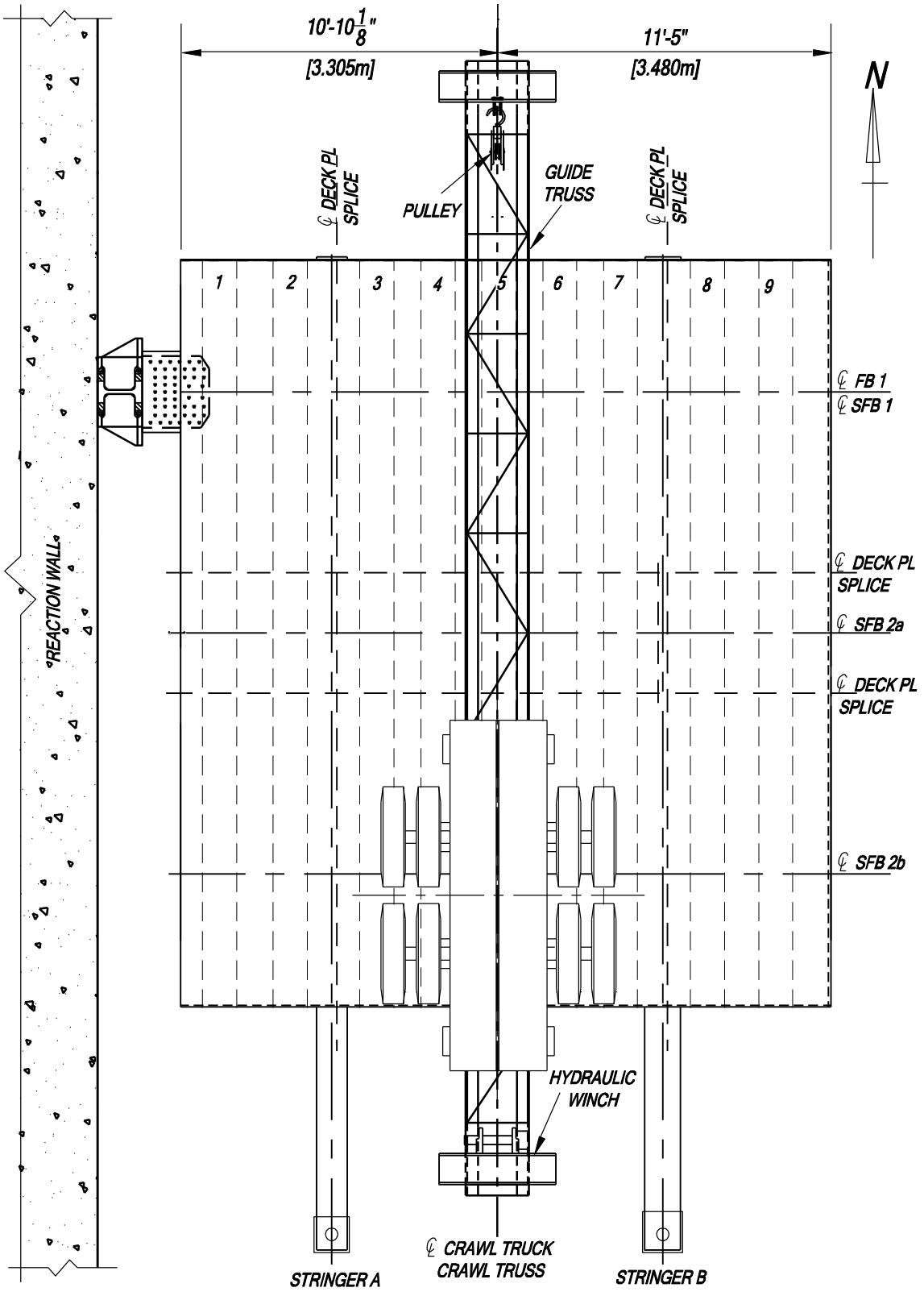

Figure 95 Crawl Test arrangement with guide truss and crawl truck in position (adapted from Alapati, 2012)

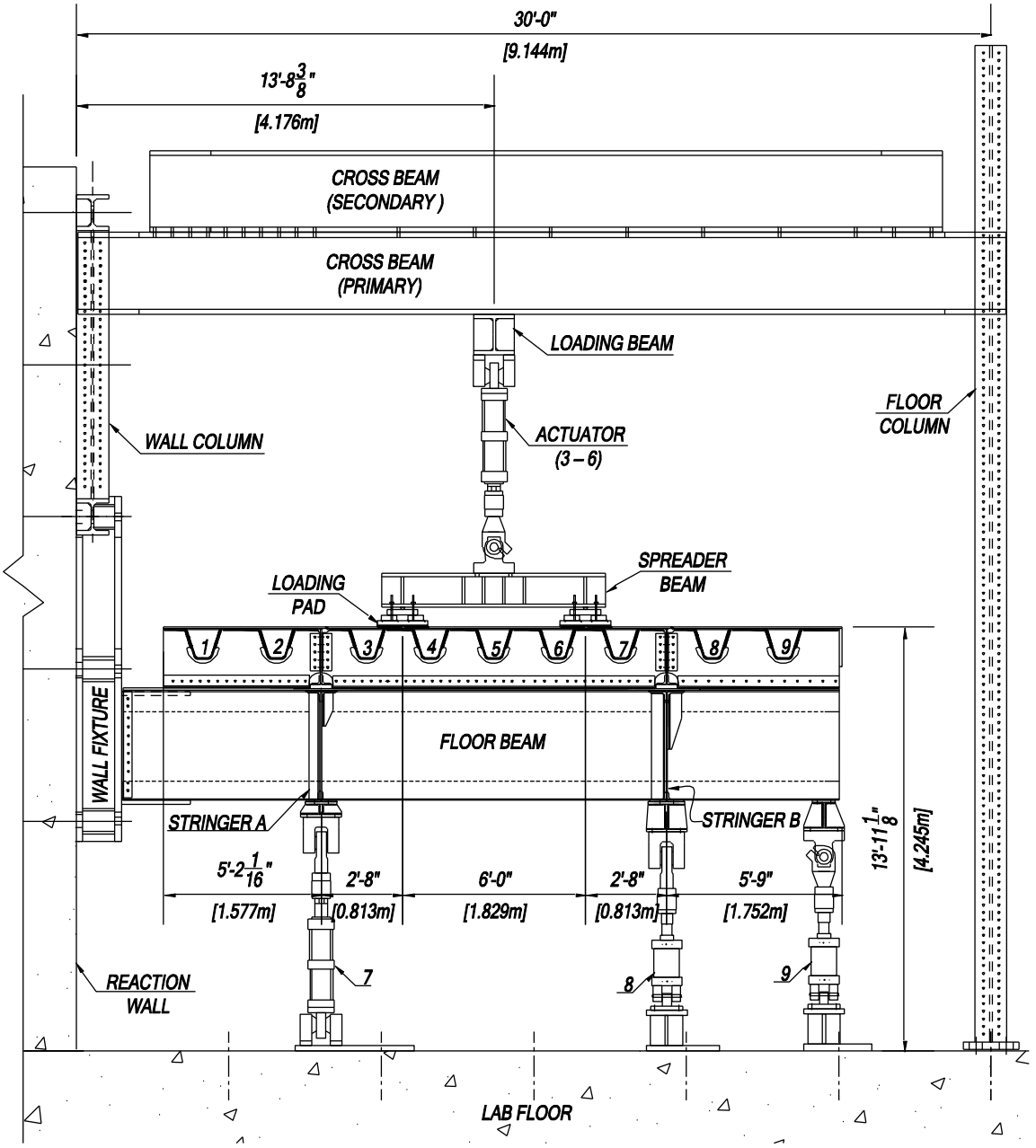

Figure 96 Front elevation of the test setup – looking north (adapted from Alapati, 2012)

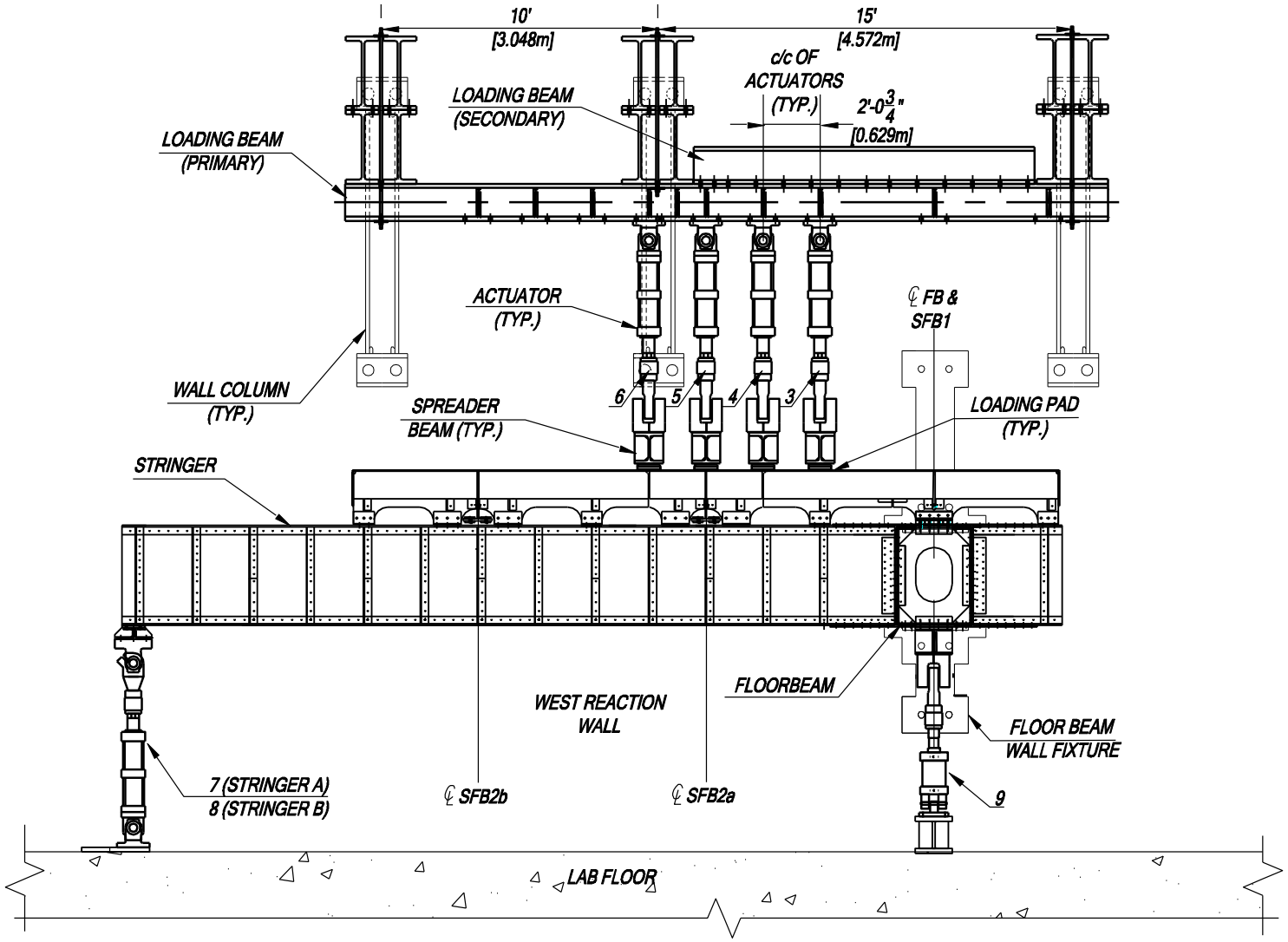

Figure 97 Side elevation of Phase 2 test setup – looking west (drawn by R. S. Deo Alapati)

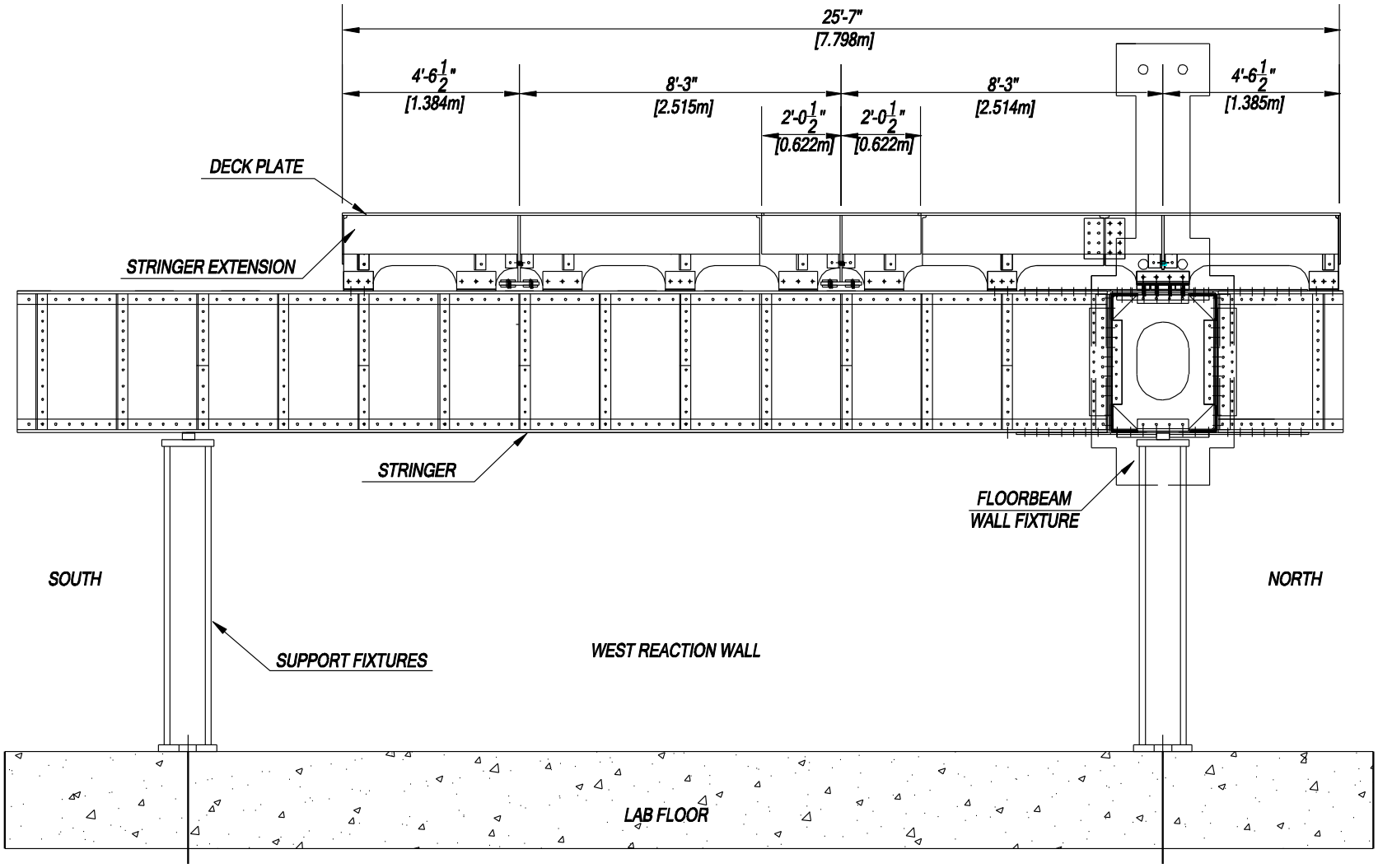

Figure 98 Section E-E in Figure 10 (drawn by R. S. Deo Alapati)

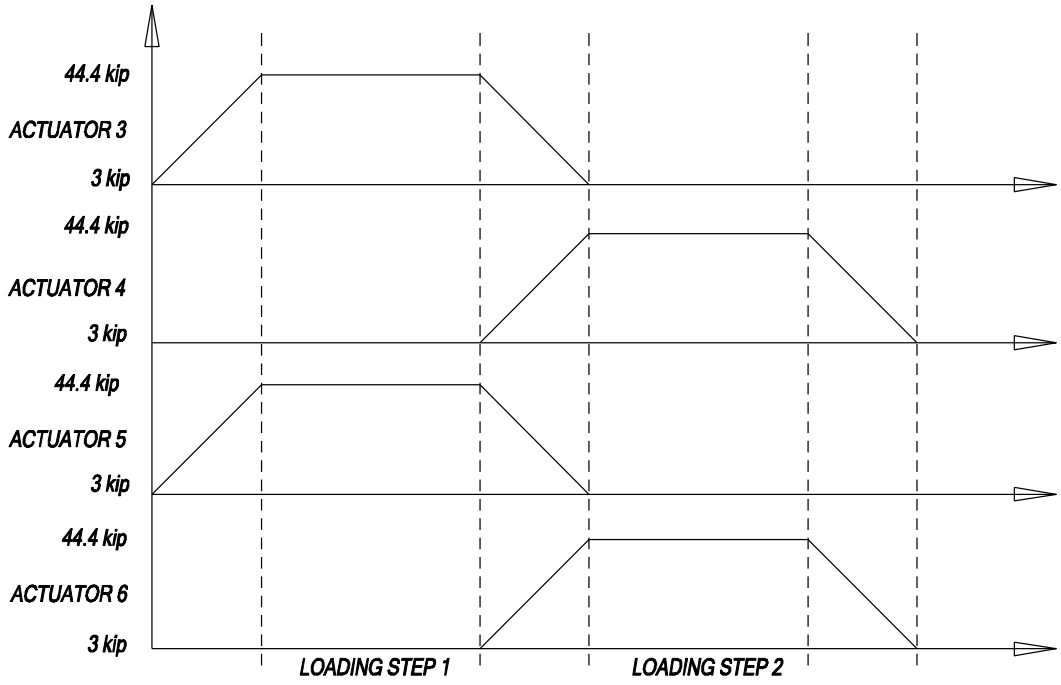

Figure 99 Loading protocol for static and fatigue testing

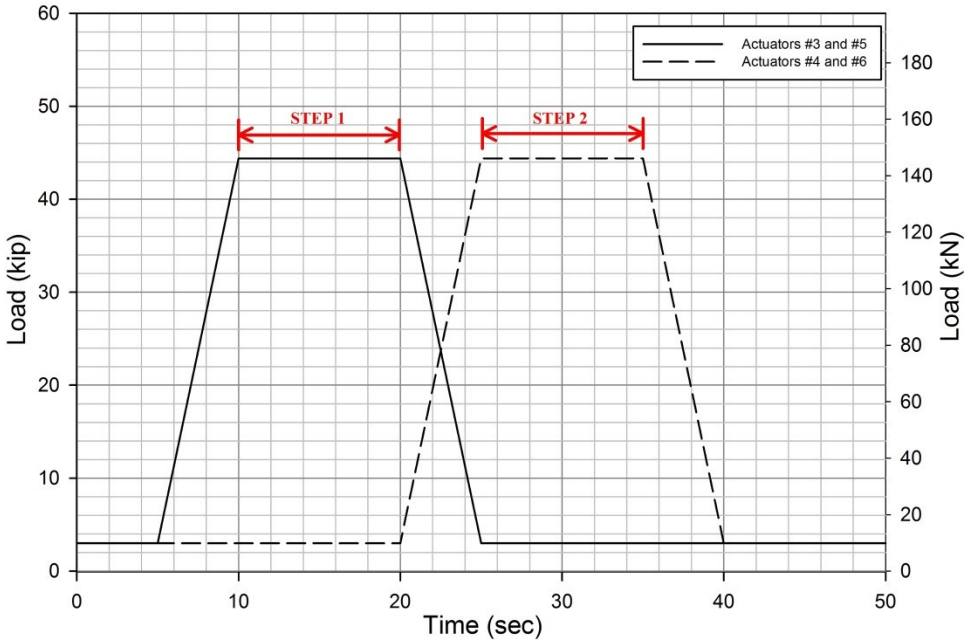

Figure 100 Programmed loading sequence for static test

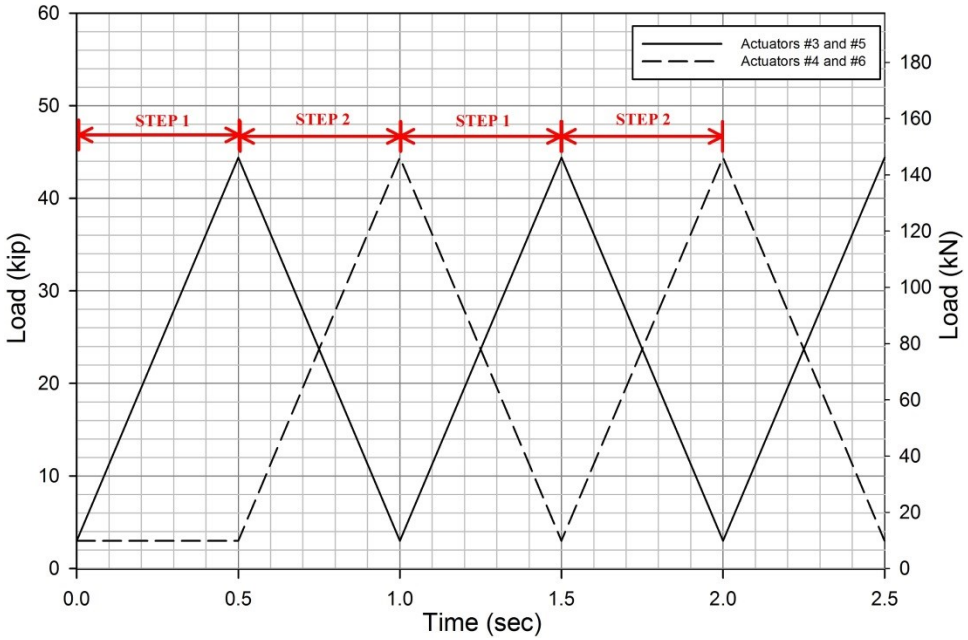

Figure 101 Programmed loading sequence for Phase 2A fatigue test

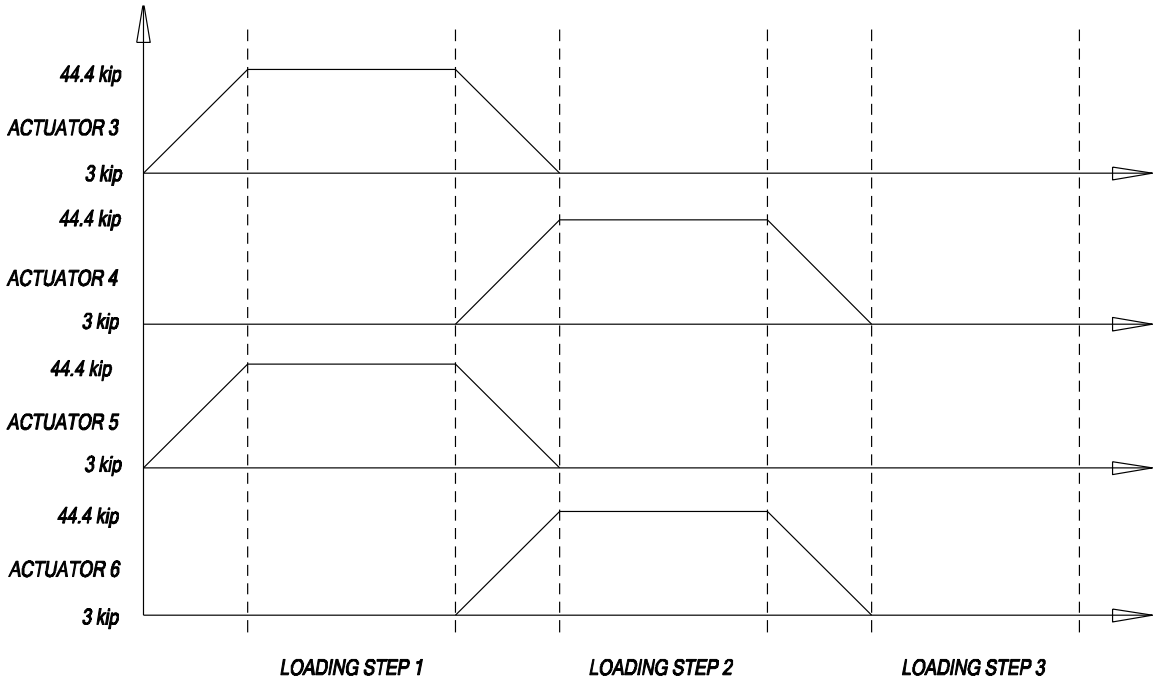

Figure 102 Loading protocol for static and fatigue testing for Phase 2

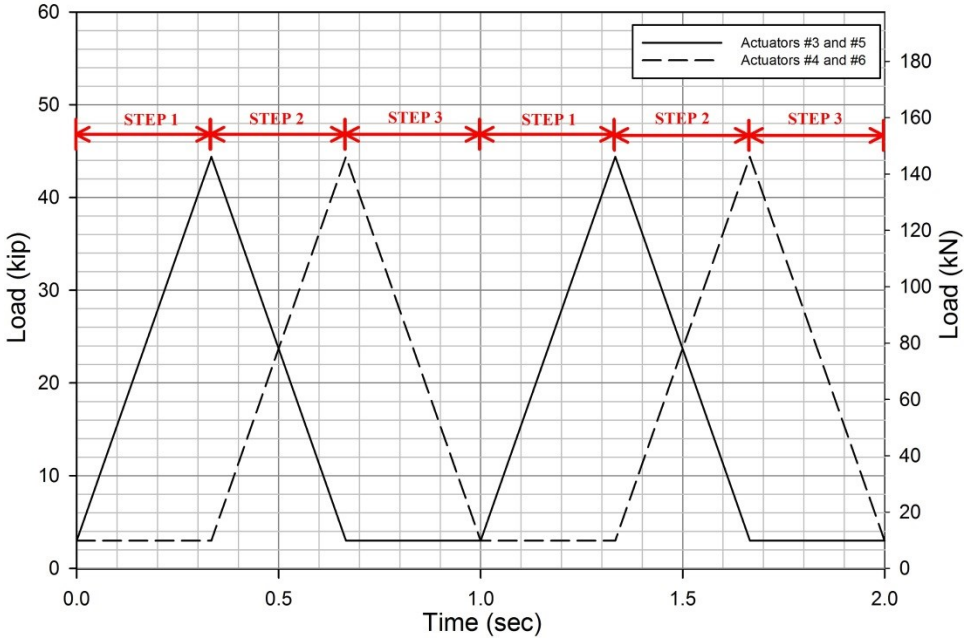

Figure 103 Programmed loading sequence for Phase 2B fatigue test

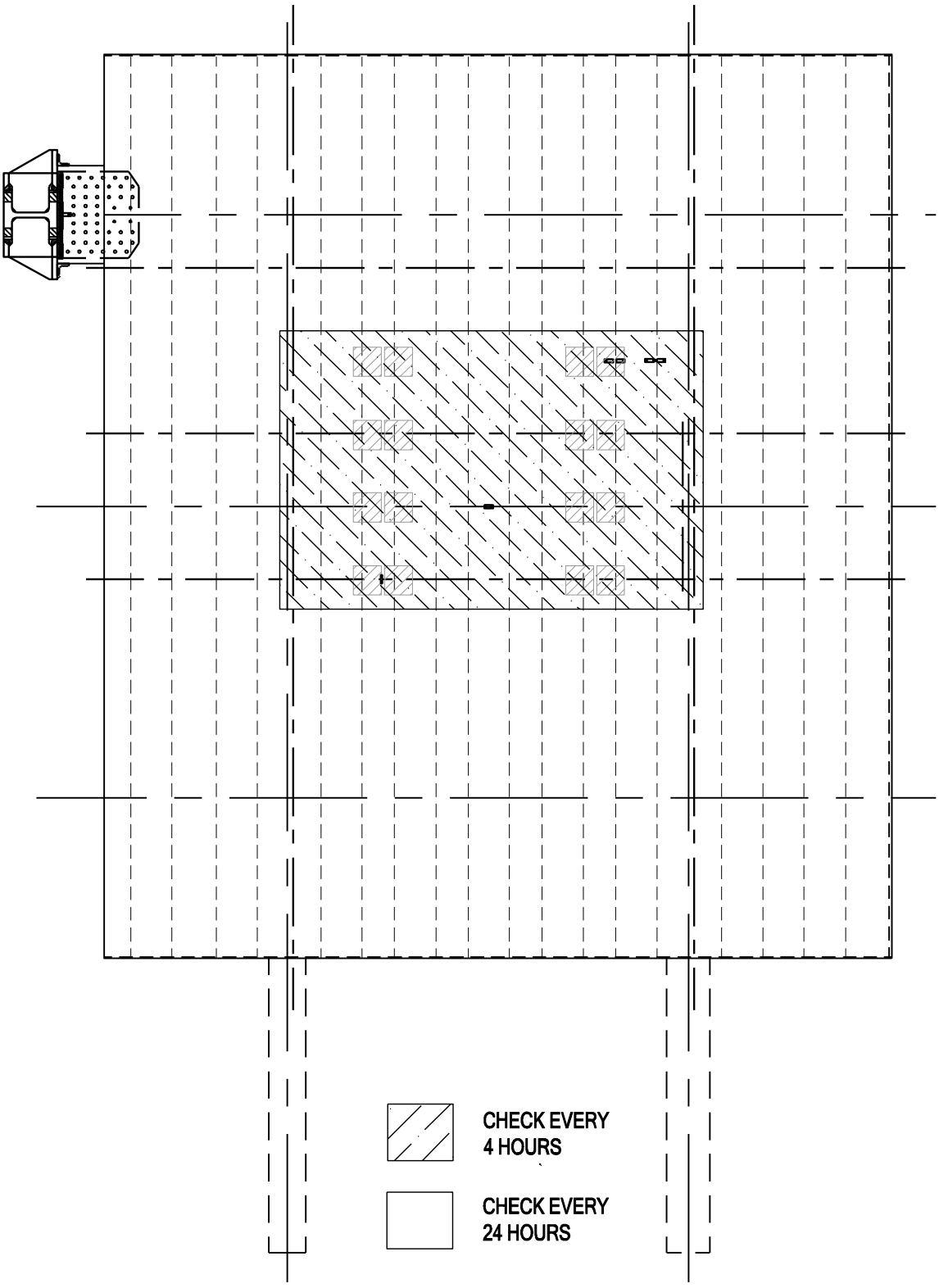

Figure 104 Inspection plan for fatigue testing (adapted from Alapati, 2012)

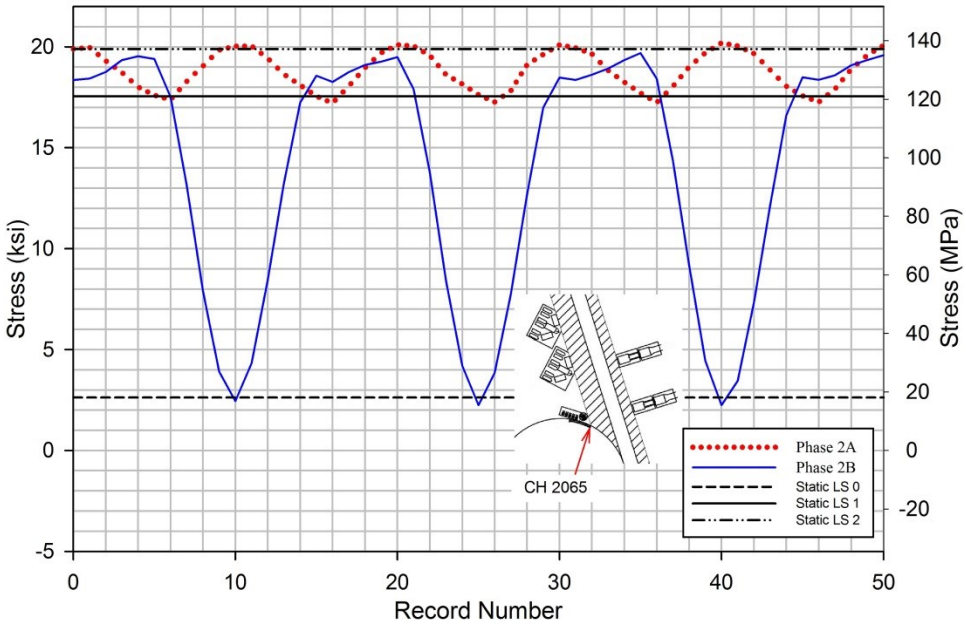

Figure 105 Stress profile comparison between Phase 2A and Phase 2B for CH 2065

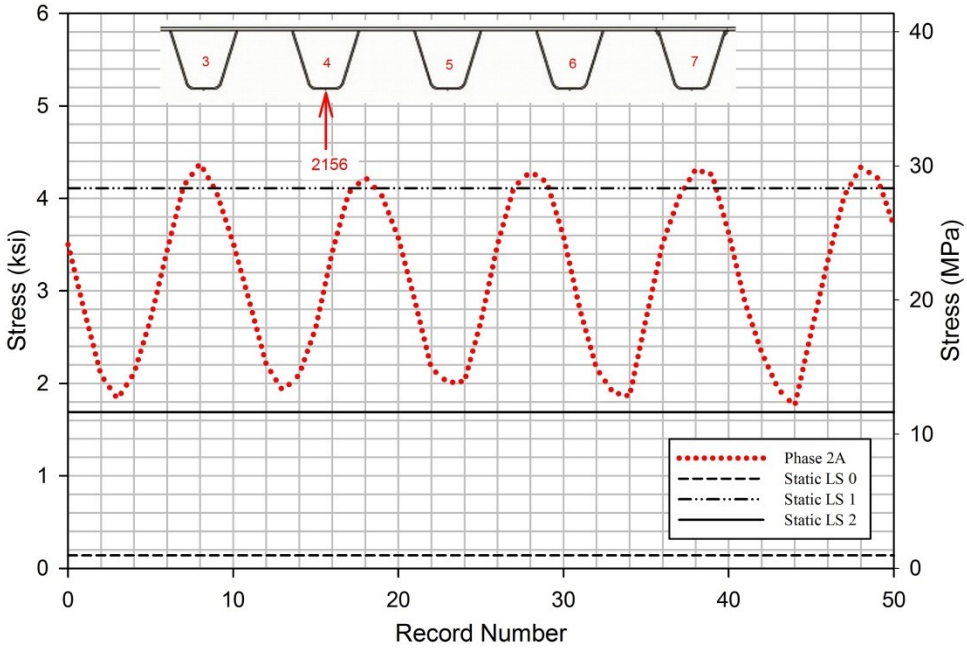

Figure 106 Stress profile of CH 2156 in Phase 2A

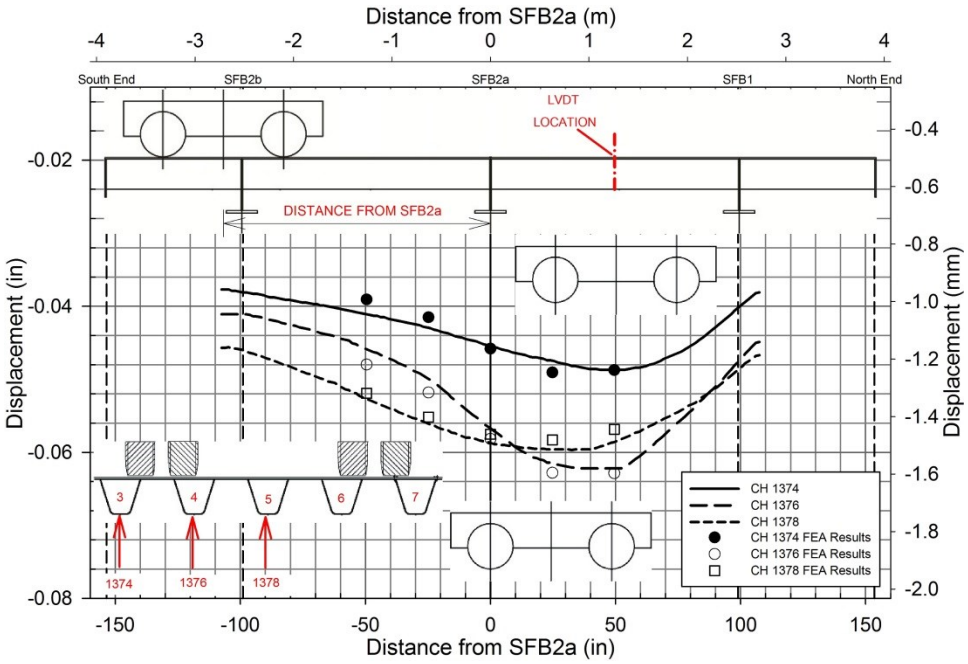

Figure 107 Displacements of rib soffits at section Y-Y

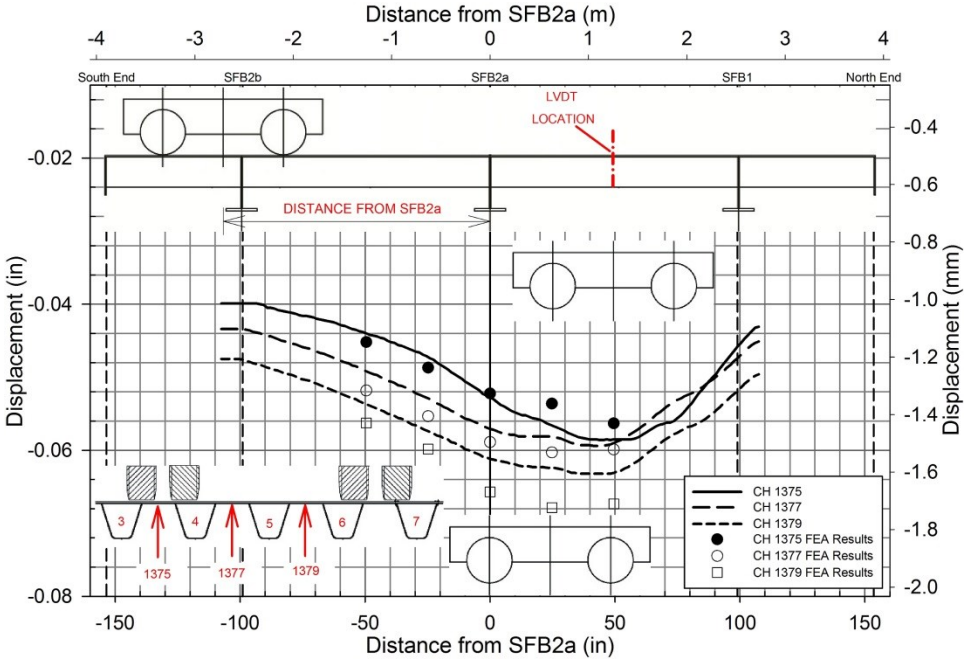

Figure 108 Displacements of deck plate soffits at section Y-Y

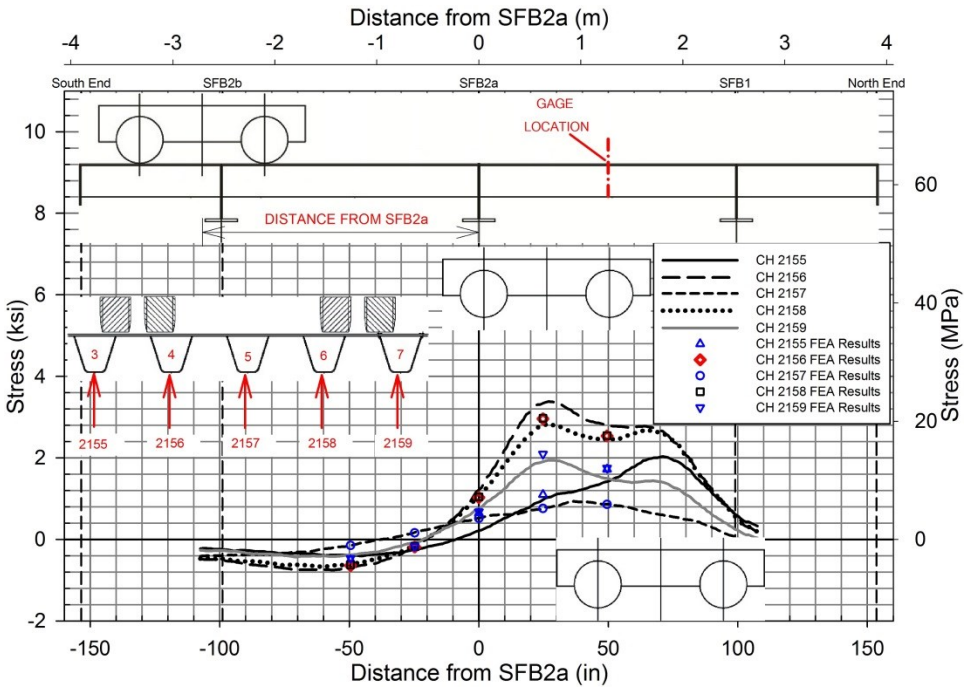

Figure 109 Longitudinal stresses measured at rib soffits at section Y-Y by channels 2155 to 2159

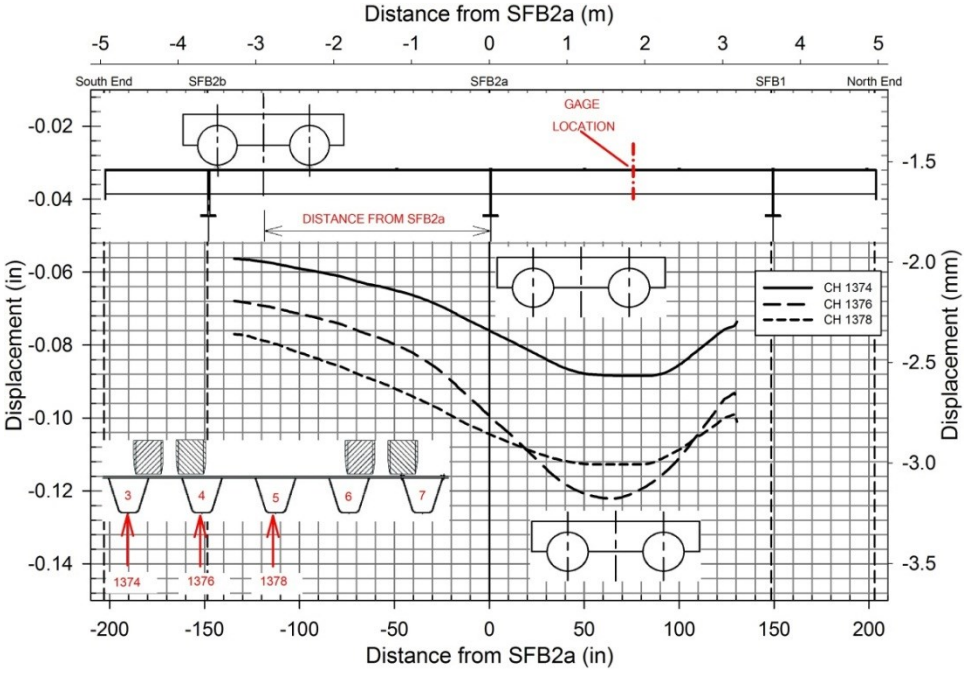

Figure 110 Displacements of rib soffits at section Z-Z in Phase 1

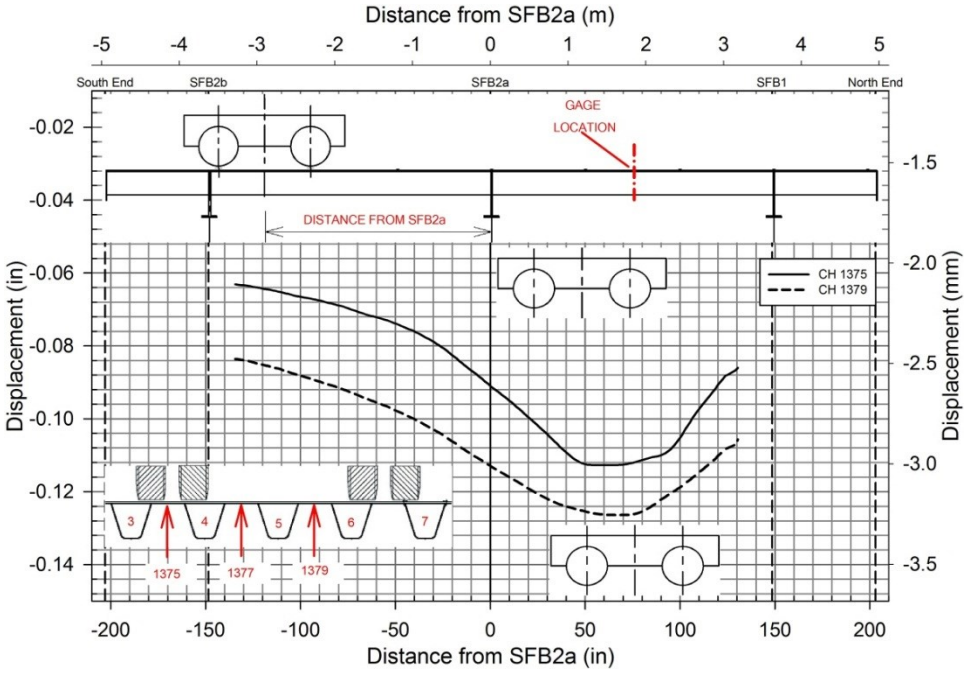

Figure 111 Displacements of deck plate at section Z-Z in Phase 1

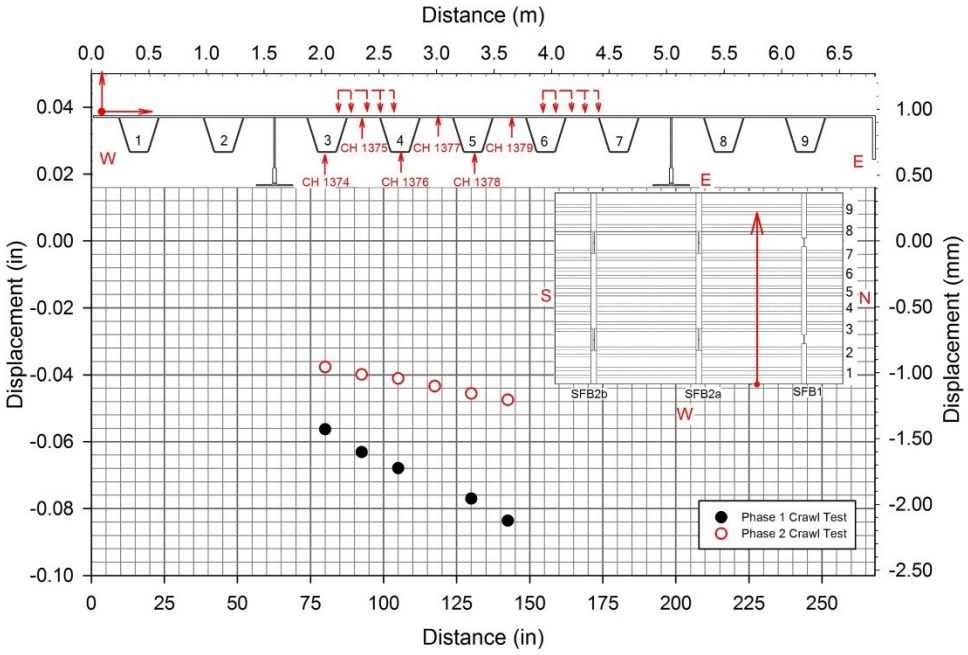

Figure 112 Comparison of LVDT displacements between Phase 1 section Z-Z and Phase 2 section Y-Y

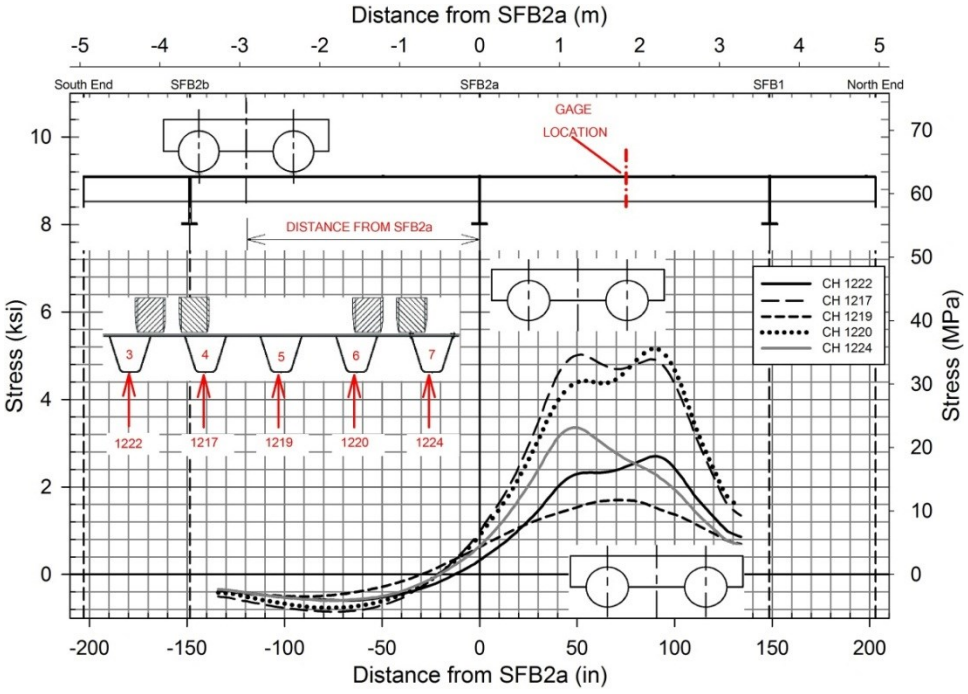

Figure 113 Comparison of longitudinal stresses measured at rib soffits by CH 1217 to 1224 for Phase 1

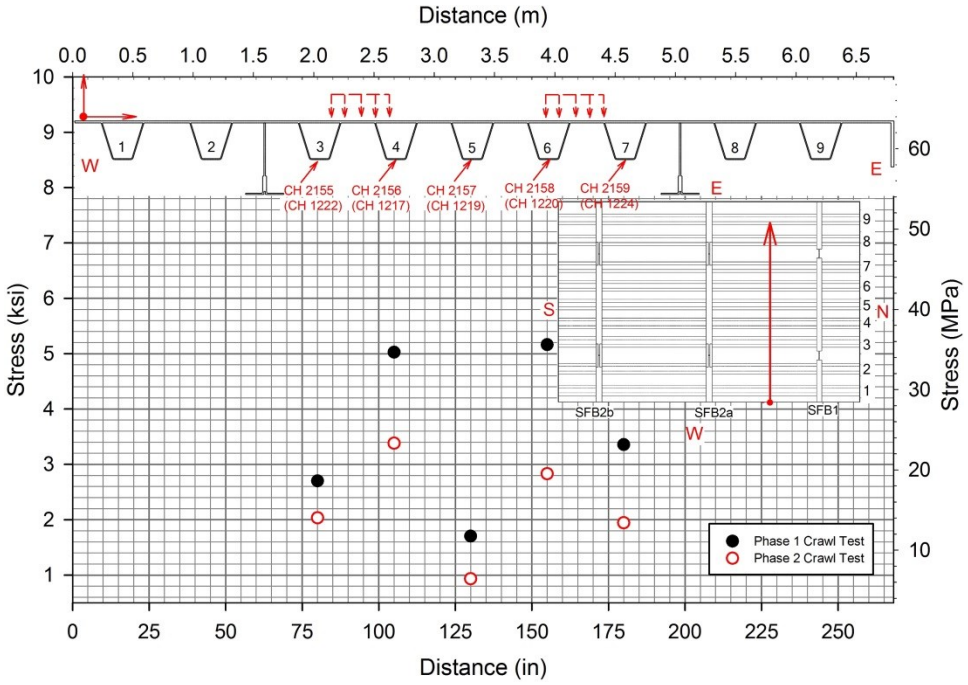

Figure 114 Comparison of maximum stresses at rib soffit gauges between Phase 1 section Z-Z and Phase 2 section Y-Y

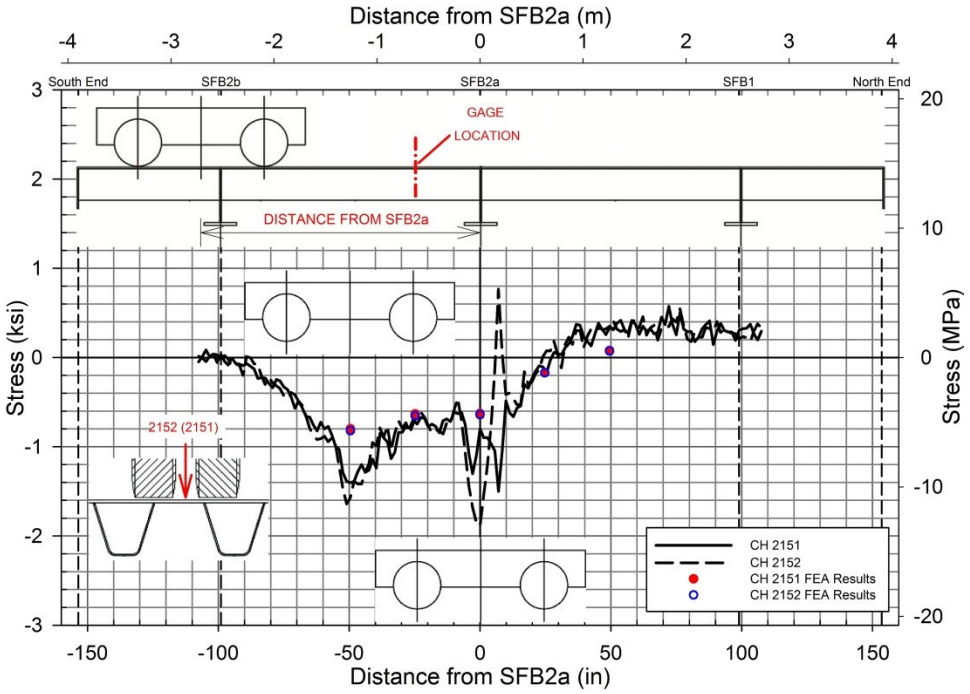

Figure 115 Crawl test plot for CH 2151 and CH 2152 located at section U-U

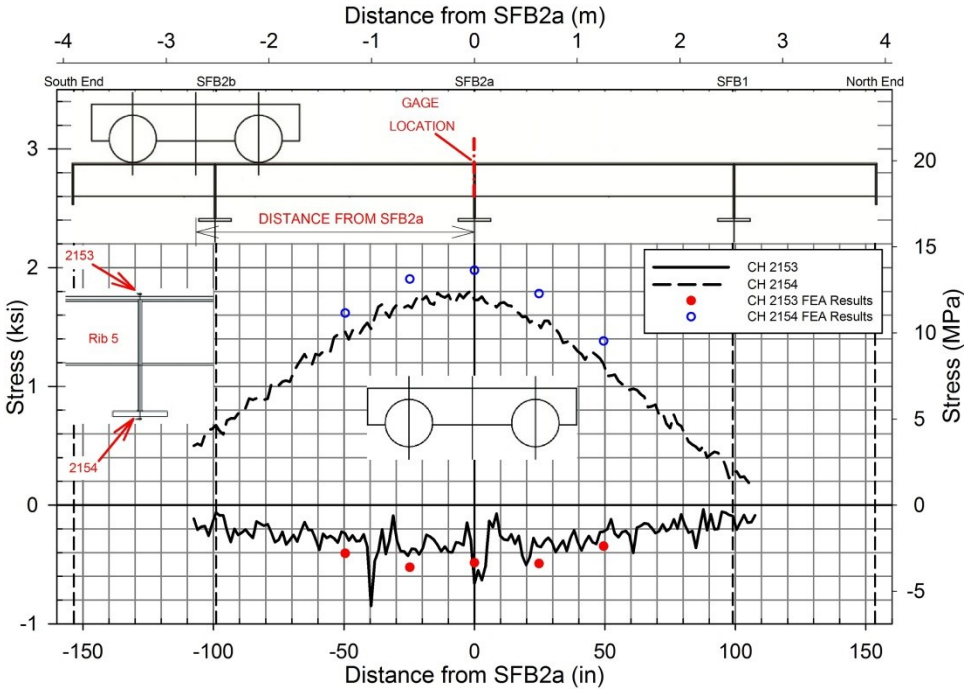

Figure 116 Crawl test plot for CH 2153 and CH 2154 at SFB2a

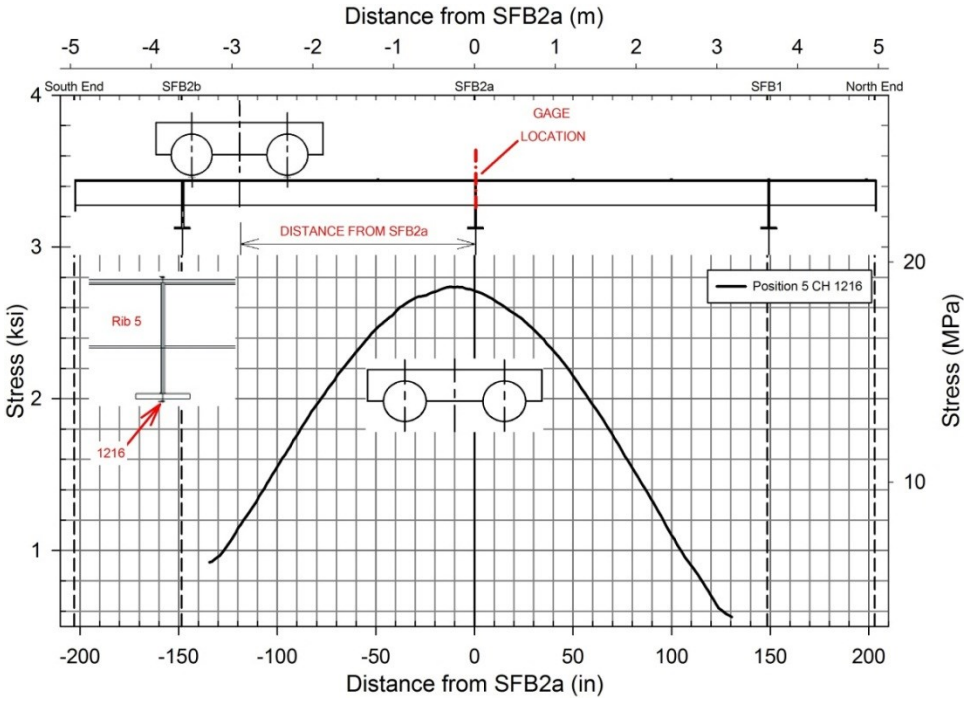

Figure 117 Crawl test plot for CH 1216 at SFB2a in Phase 1

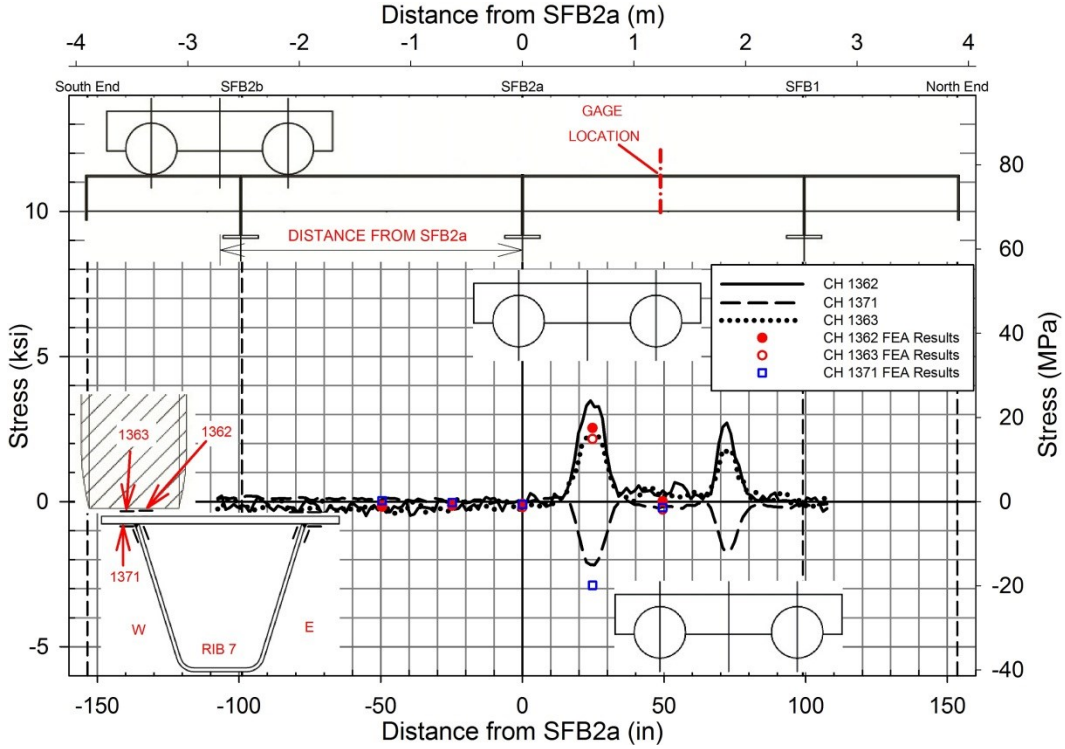

Figure 118 Crawl test stress plots at section Y-Y for channels shown in the figure

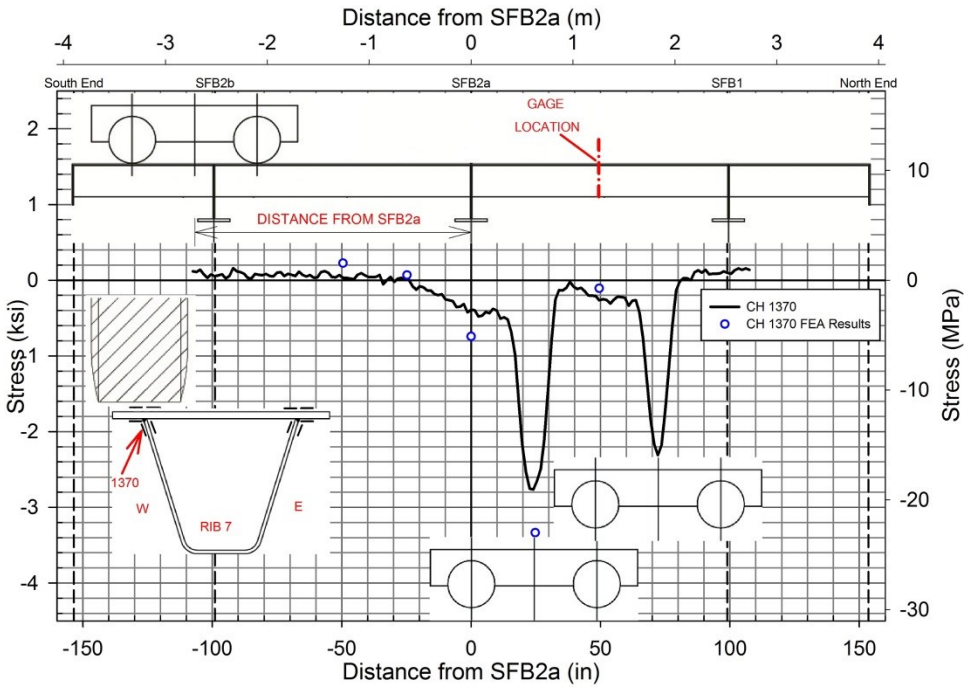

Figure 119 Crawl test stress plots at section Y-Y for gauge on west external face of Rib 7

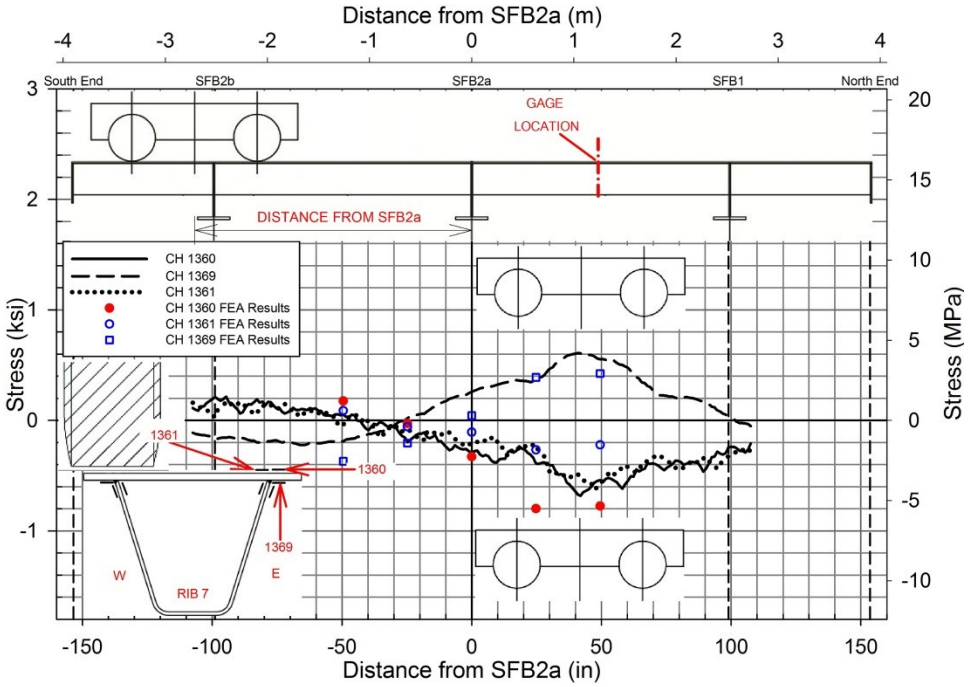

Figure 120 Crawl test stress plots at section Y-Y for channels shown in the figure

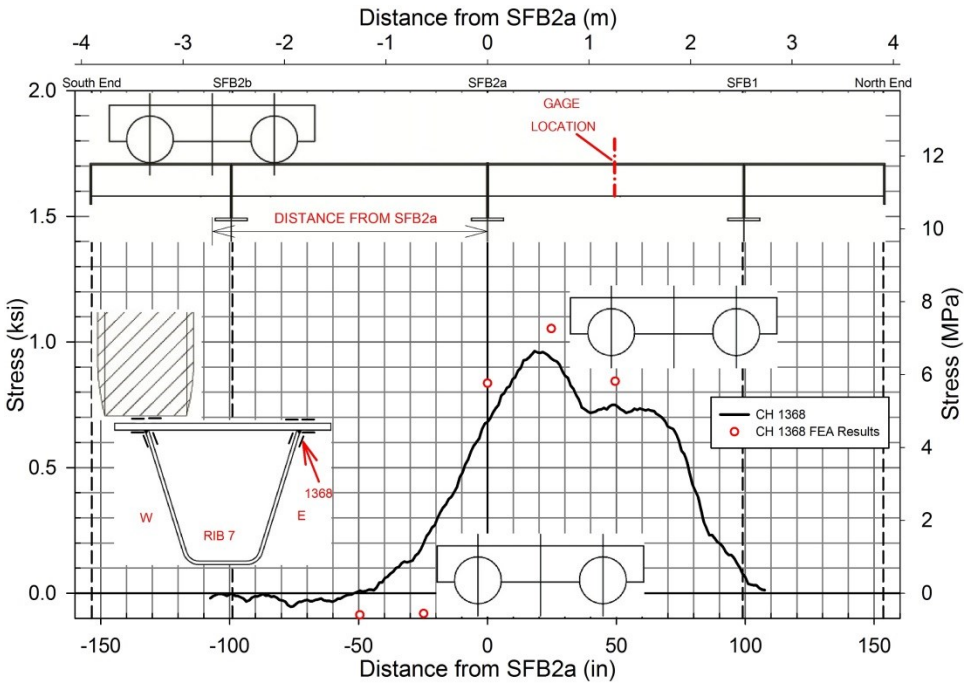

Figure 121 Crawl test stress plots at section Y-Y for gauge on east external face of Rib 7

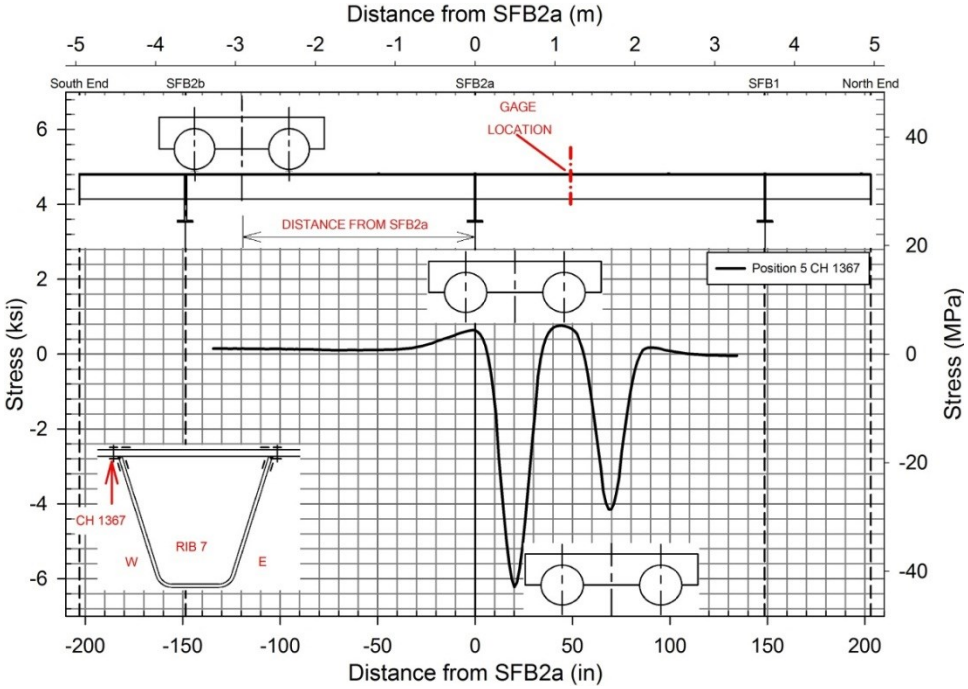

Figure 122 Crawl test stress plots for CH 1367 in Phase 1

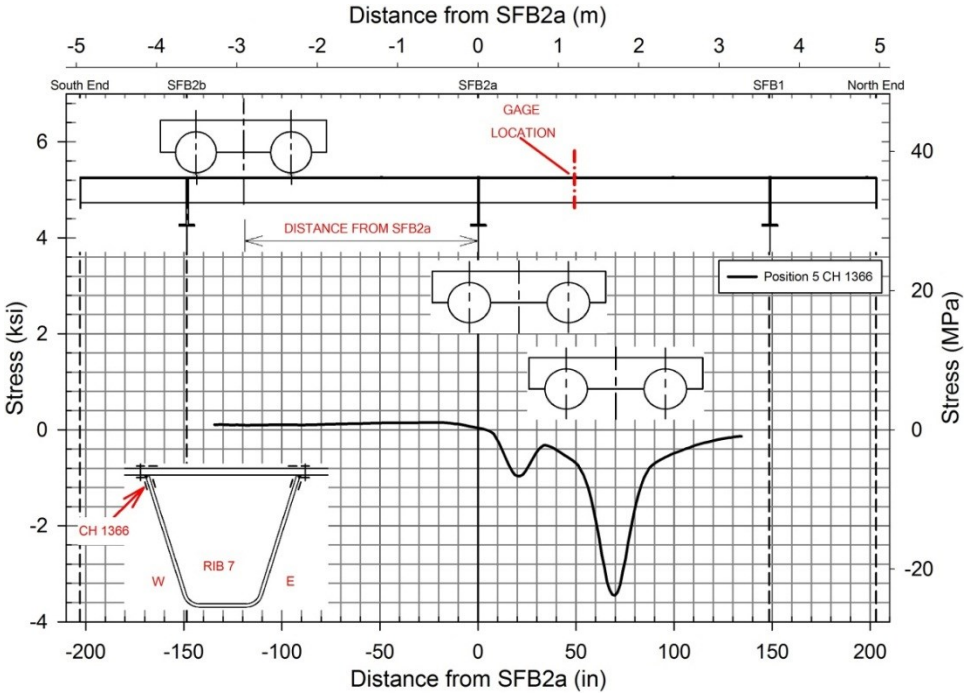

Figure 123 Crawl test stress plots for CH 1366 in Phase 1

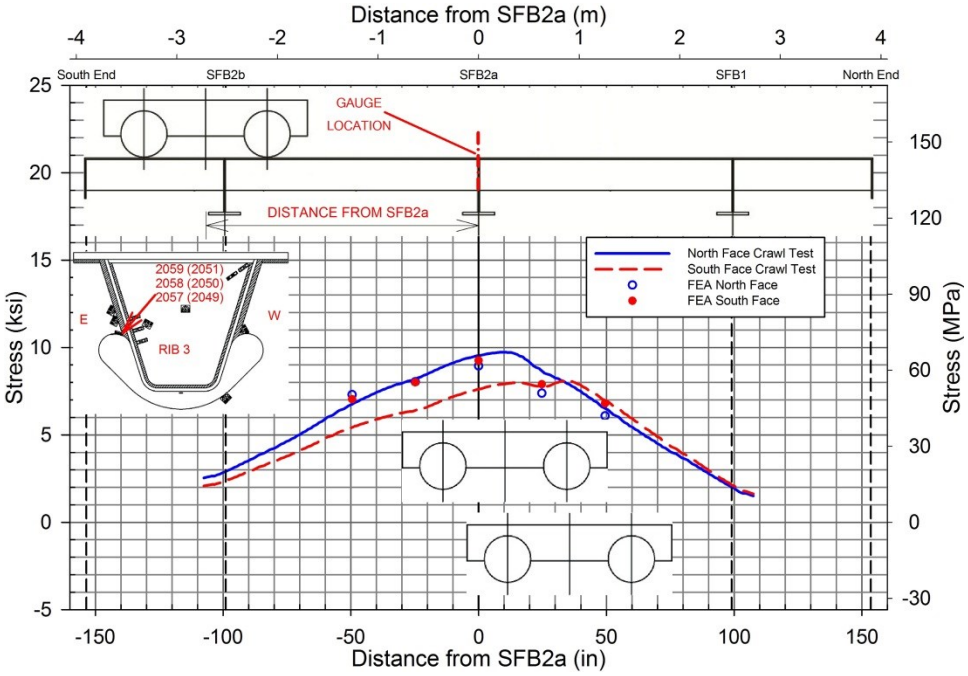

Figure 124 Principal stress plots for 1mm rosette gauges at Rib 3 east cutout

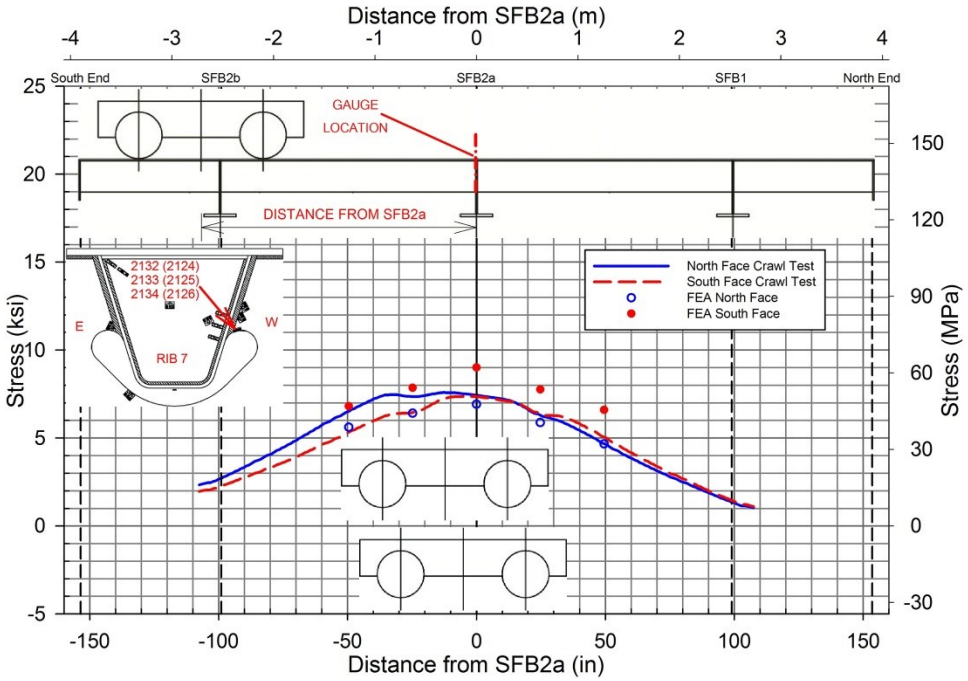

Figure 125 Principal stress plots for 1mm rosette gauges at Rib 7 west cutout

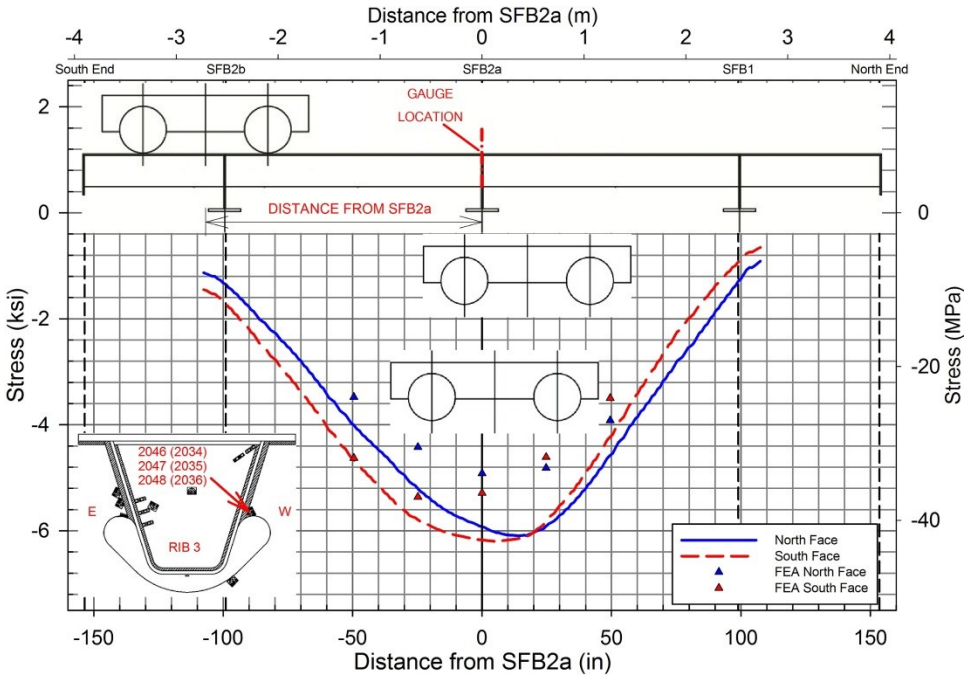

Figure 126 Principal stress plots for rosette gauges at Rib 3 west cutout

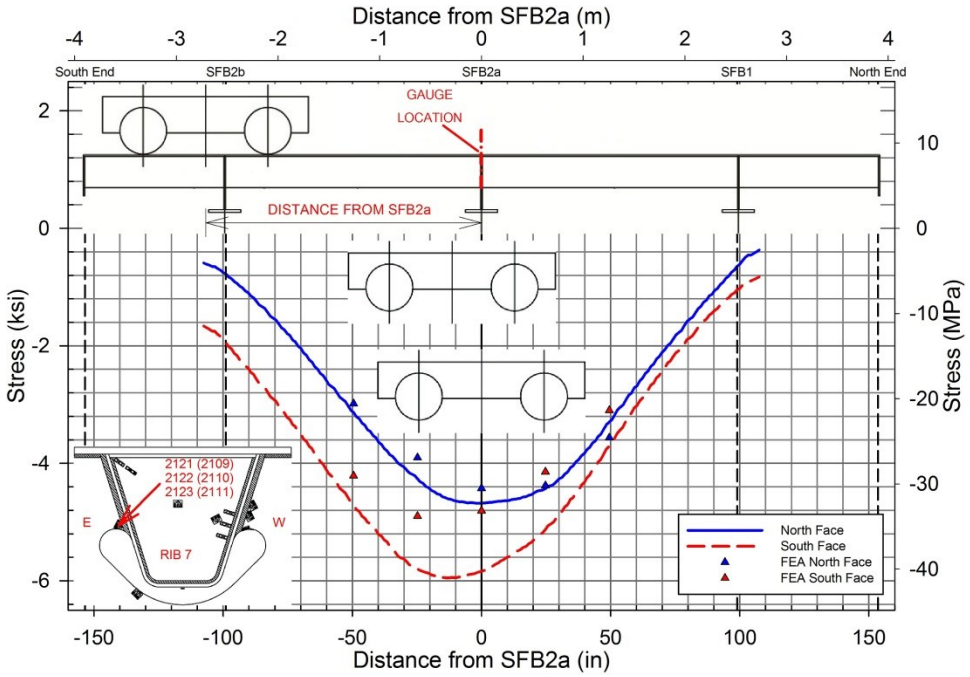

Figure 127 Principal stress plots for rosette gauges at Rib 7 east cutout

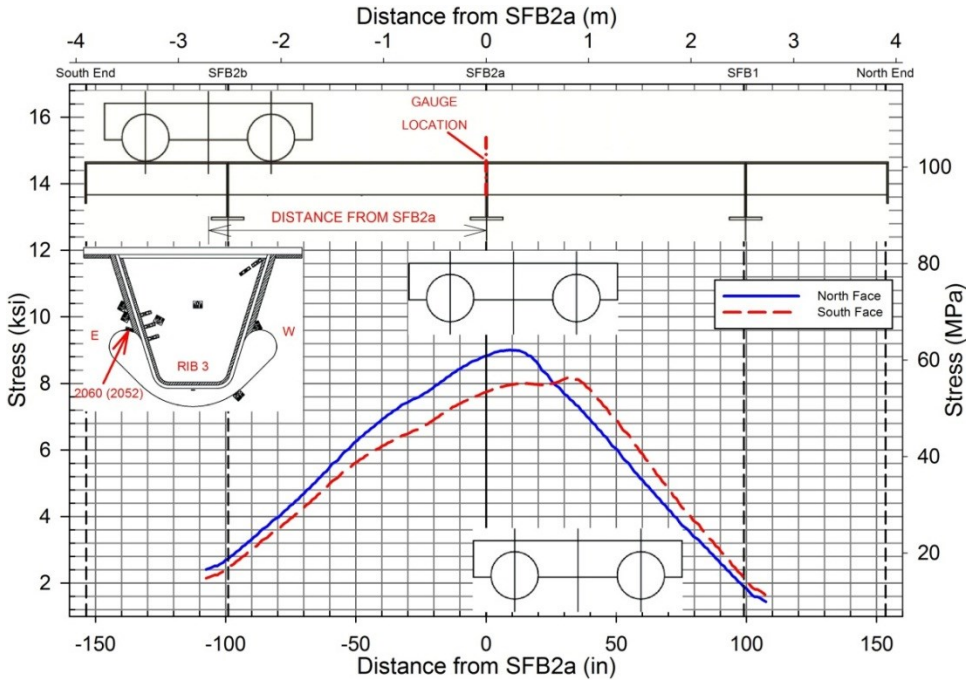

Figure 128 Stress plot for single gauge among 1mm strip gauge at Rib 3 cutout

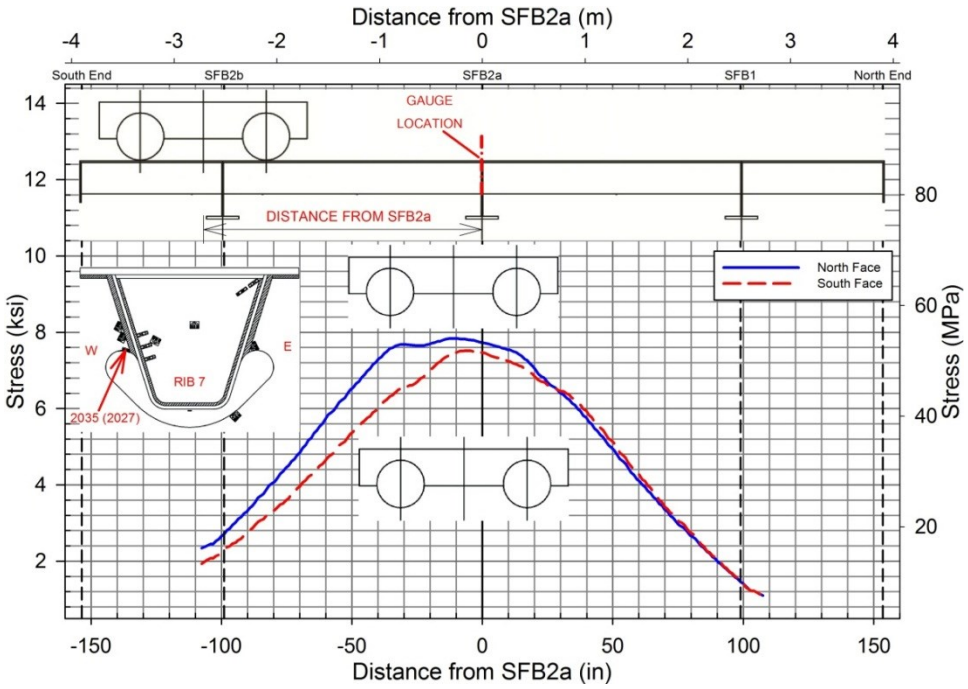

Figure 129 Stress plot for single gauge among 1mm strip gauge at Rib 7 cutout

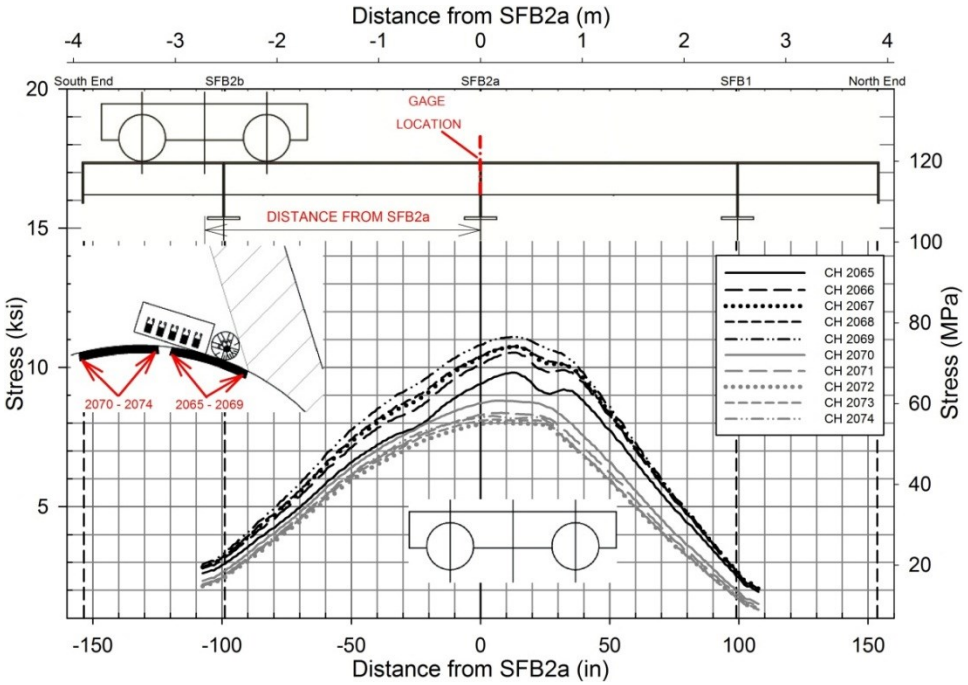

Figure 130 Crawl test stress plots for CH 2065 to CH 2074 at Rib 3 east cutout edge

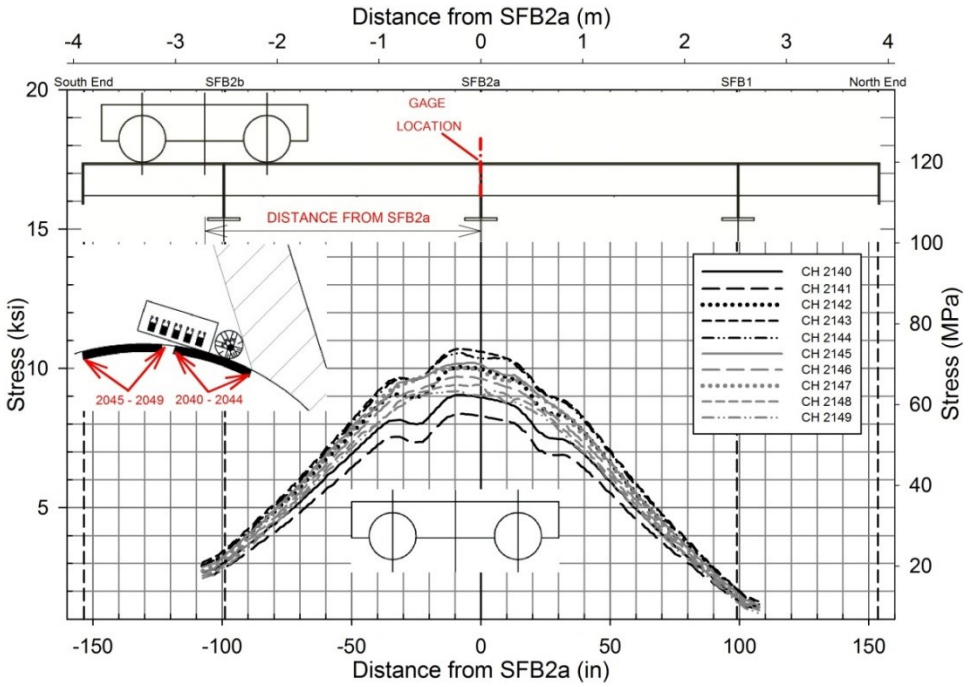

Figure 131 Crawl test stress plots for CH 2140 to CH 2149 at Rib 7 west cutout edge

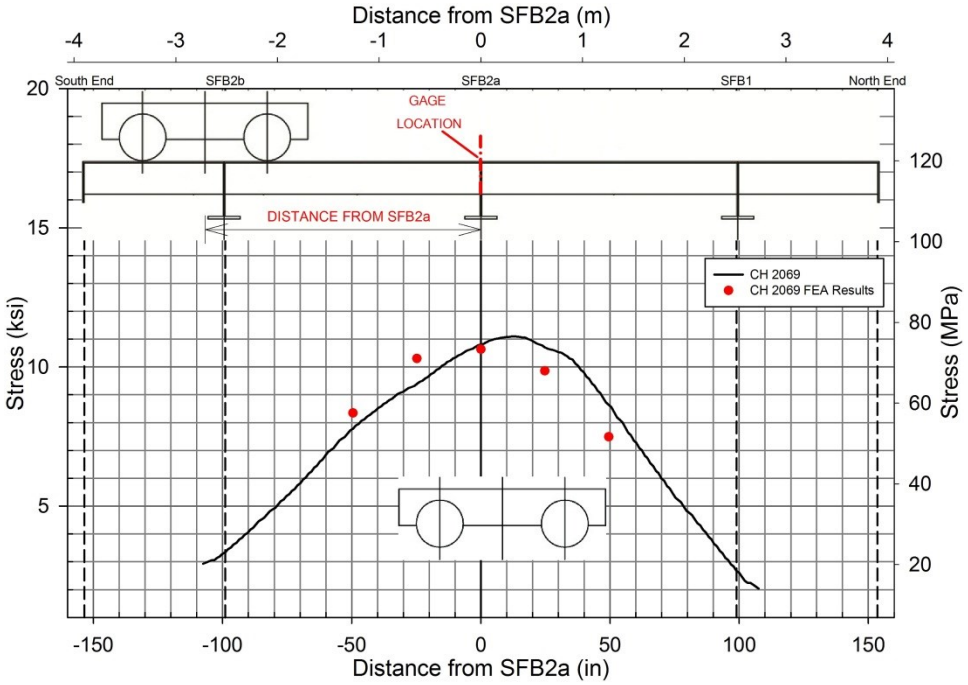

Figure 132 Crawl test stress plots for CH 2069, maximum at Rib 3 east cutout edge

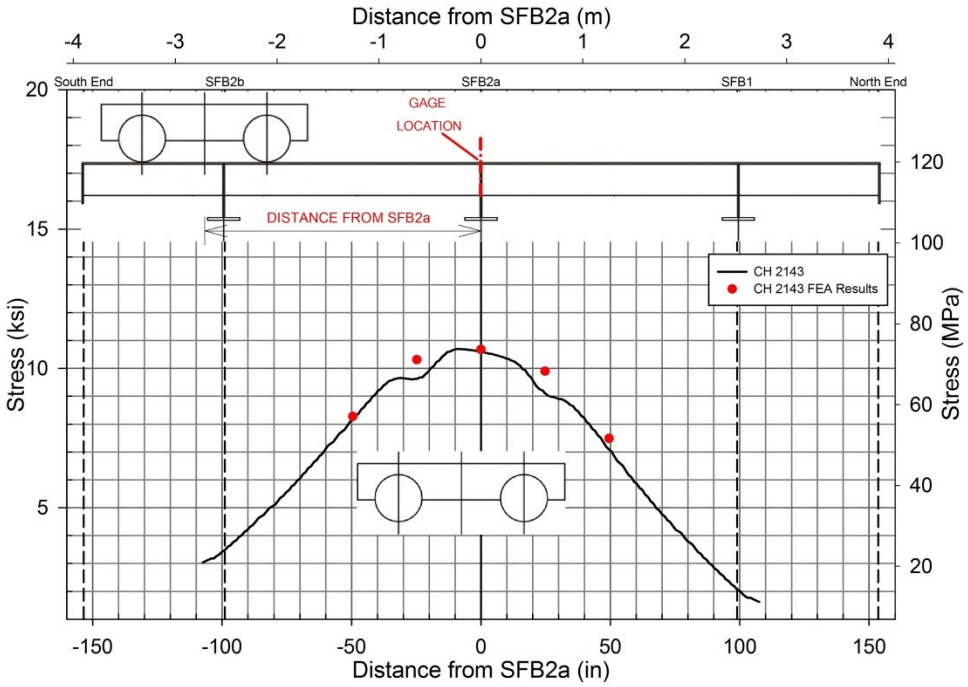

Figure 133 Crawl test stress plots for CH 2143, maximum at Rib 7 west cutout edge

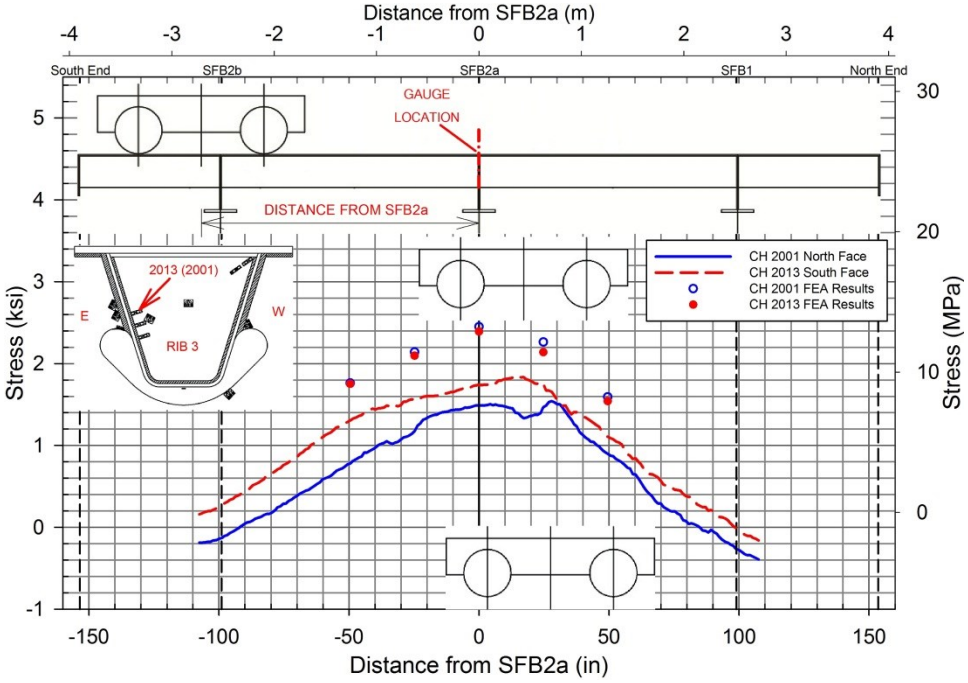

Figure 134 Stress profile for crawl test measured by CH 2013 and 2001 in Rib 3 bulkhead plate

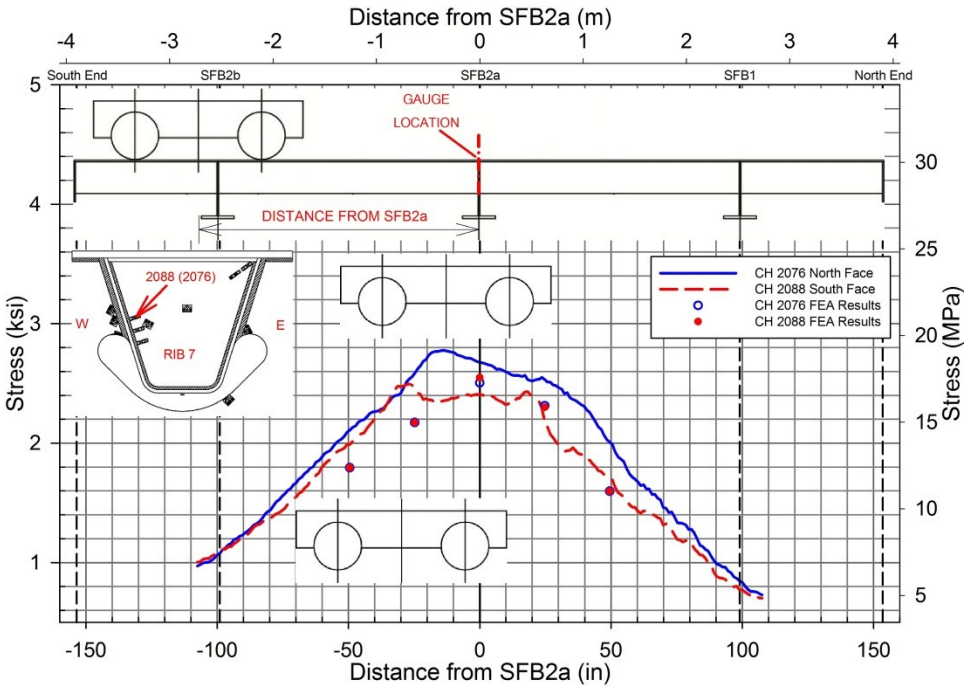

Figure 135 Stress profile for crawl test measured by CH 2088 and 2076 in Rib 7 bulkhead plate

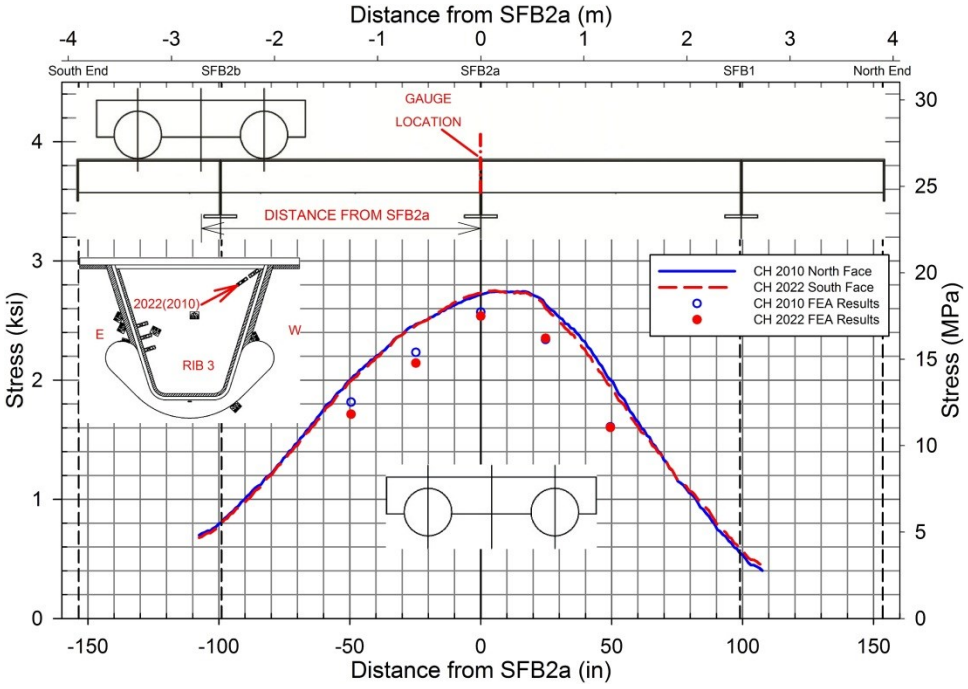

Figure 136 Stress profile for crawl test measured by CH 2022 and 2010 in rib 3

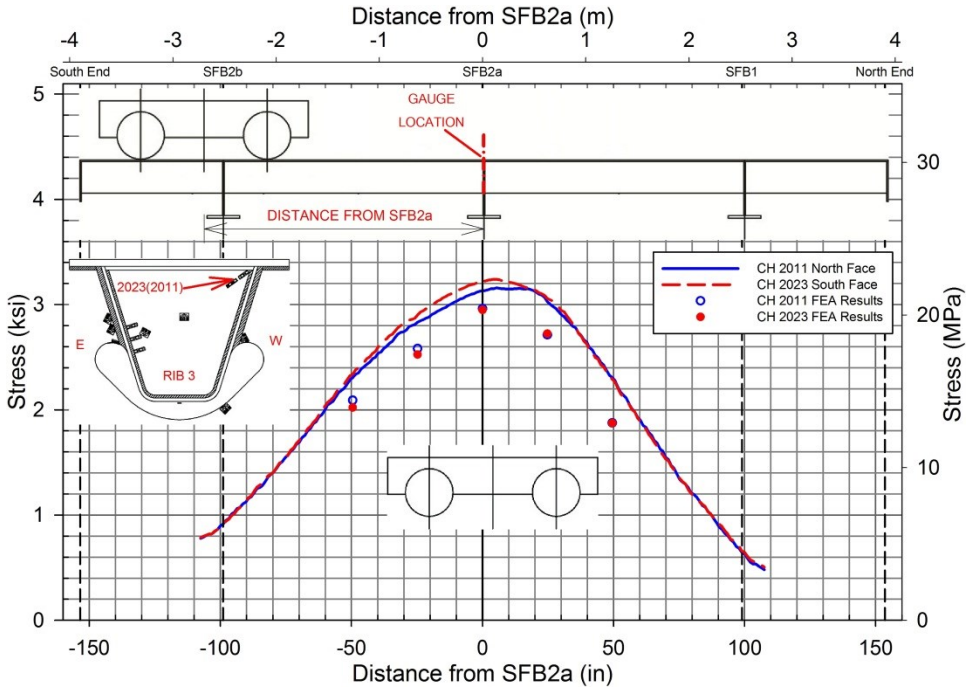

Figure 137 Stress profile for crawl test measured by CH 2023 and 2011 in Rib 3 bulkhead plate

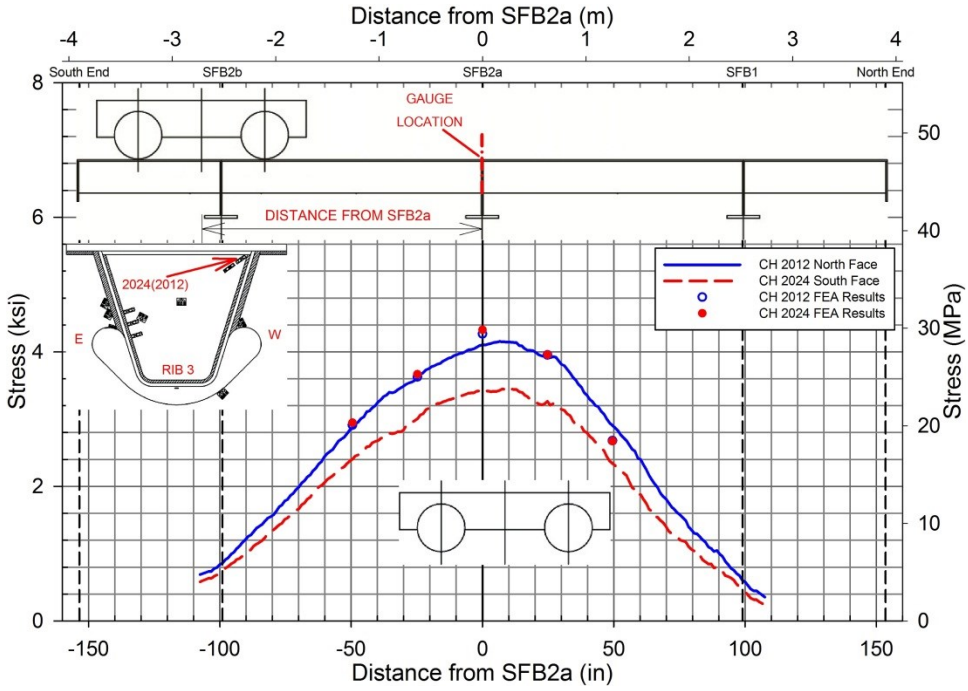

Figure 138 Stress profile for crawl test measured by CH 2024 and 2012 in Rib 3 bulkhead plate

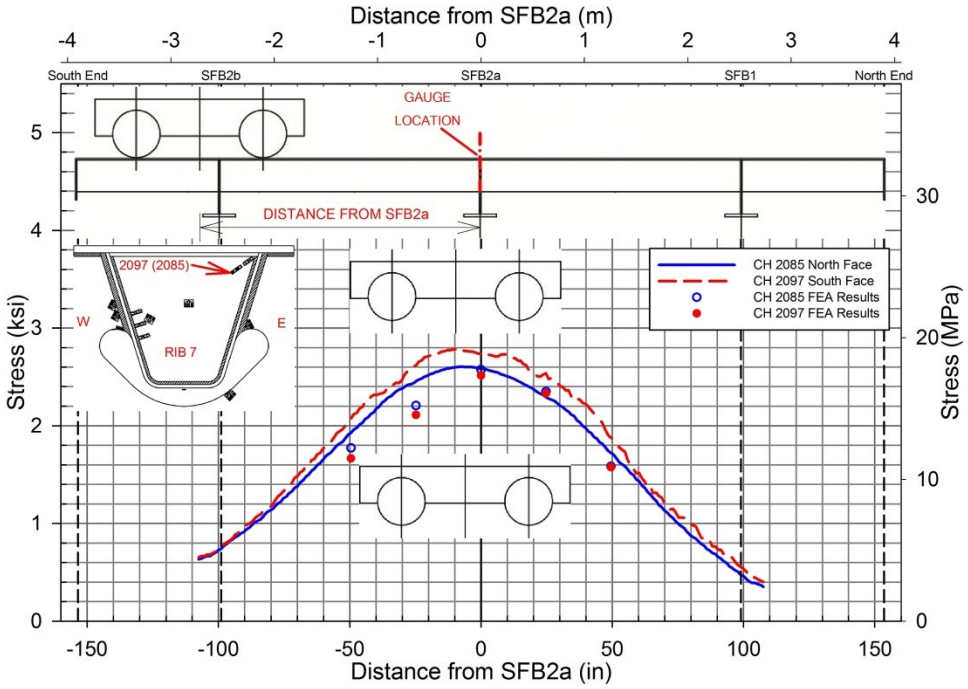

Figure 139 Stress profile for crawl test measured by CH 2097 and 2085 in Rib 7 bulkhead plate

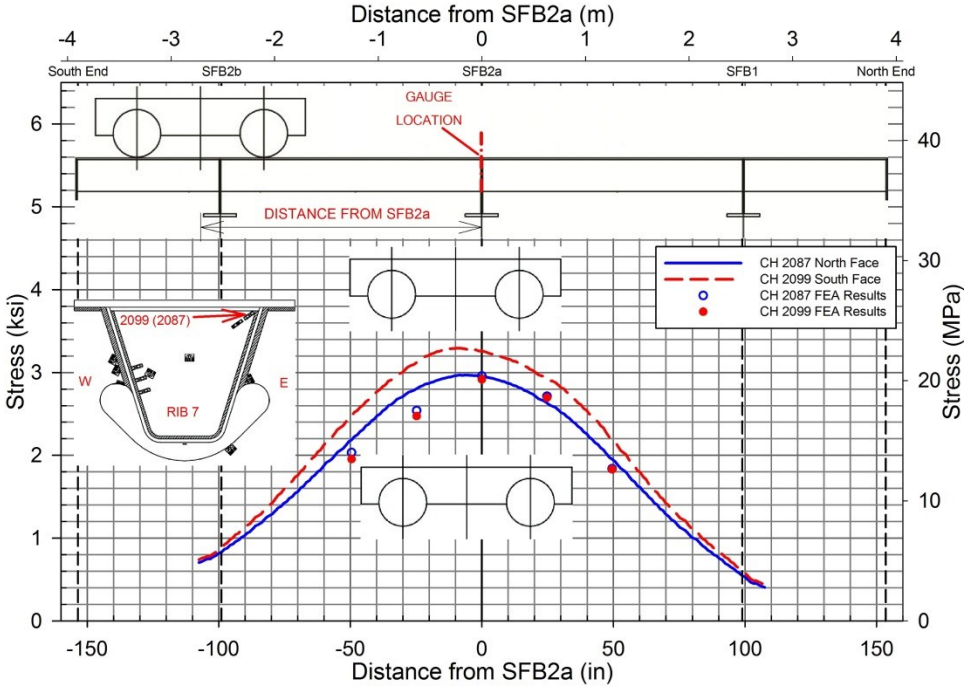

Figure 140 Stress profile for crawl test measured by CH 2099 and 2087 in Rib 7 bulkhead plate

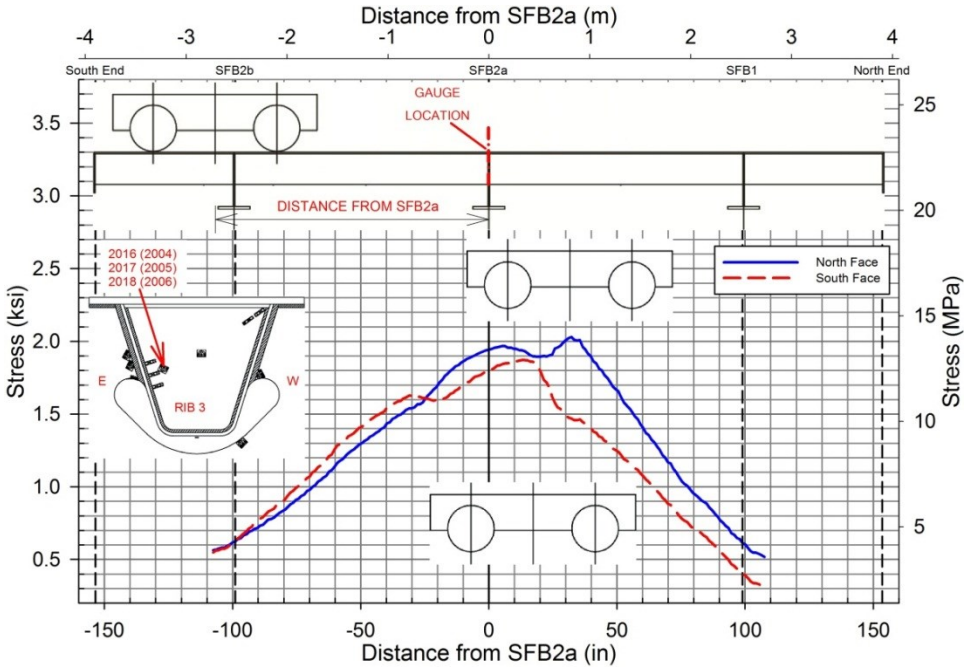

Figure 141 Crawl test principal stress profile for rosette close to cutout in Rib 3 bulkhead plate

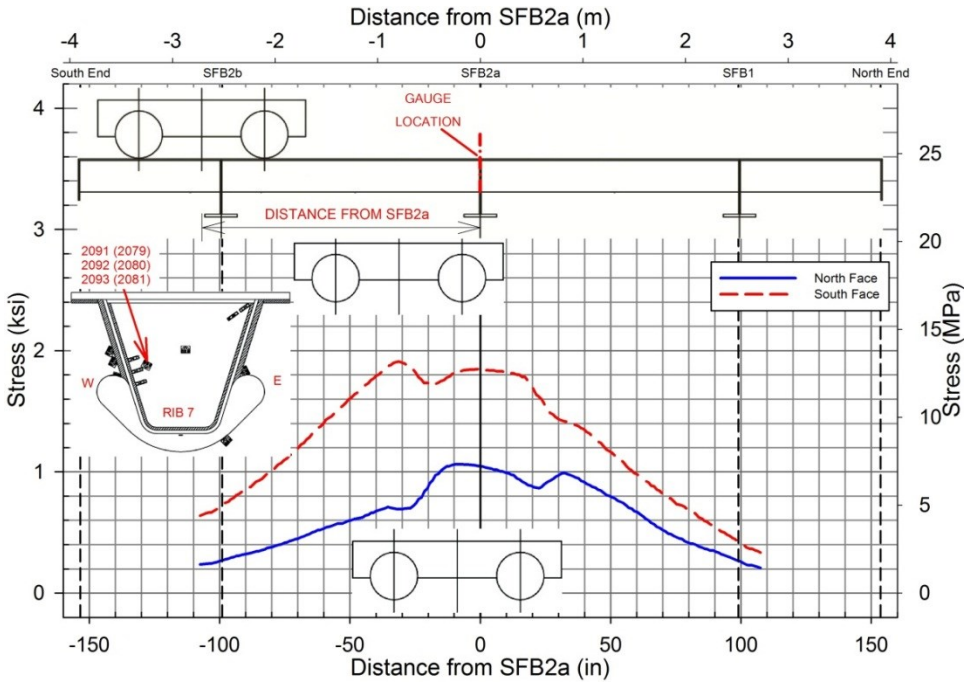

Figure 142 Crawl test principal stress profile for rosette close to cutout in Rib 7 bulkhead plate

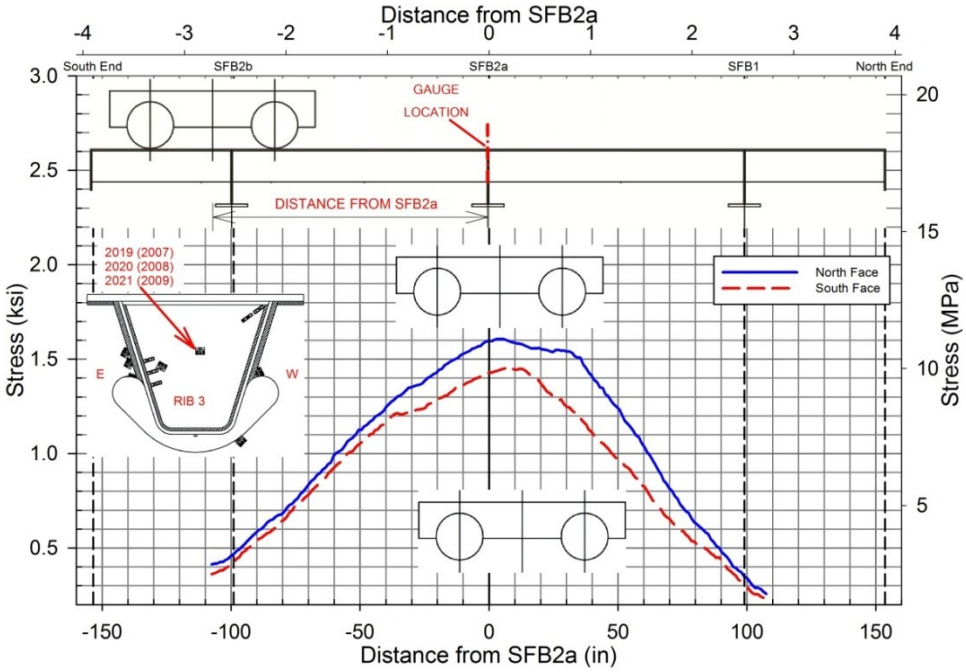

Figure 143 Crawl test principal stress profile for rosette placed centrally in Rib 3 bulkhead plate

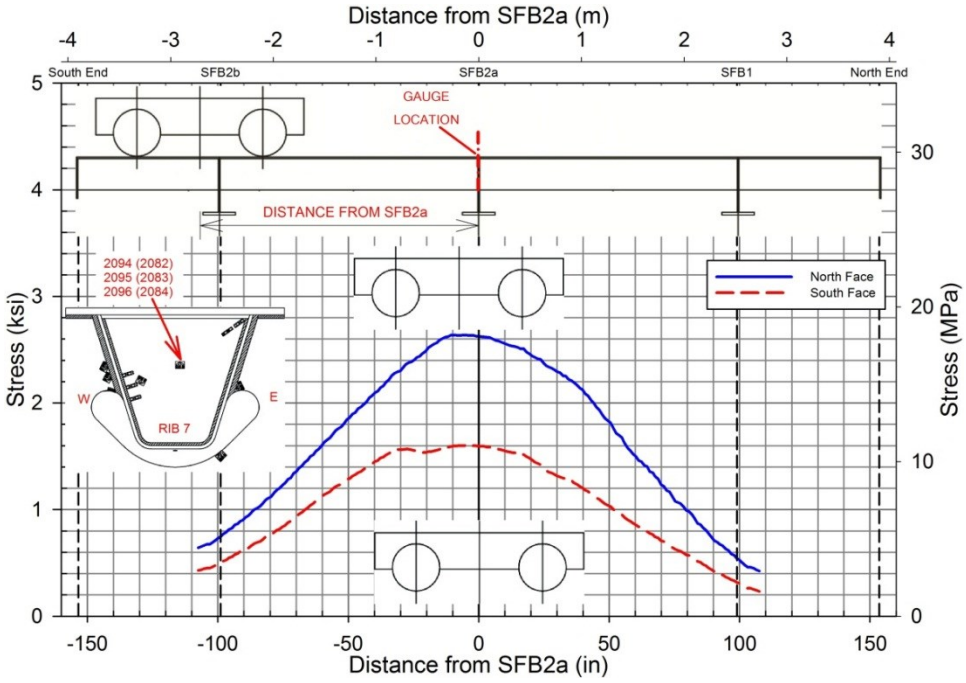

Figure 144 Crawl test principal stress profile for rosette placed centrally in Rib 7 bulkhead plate

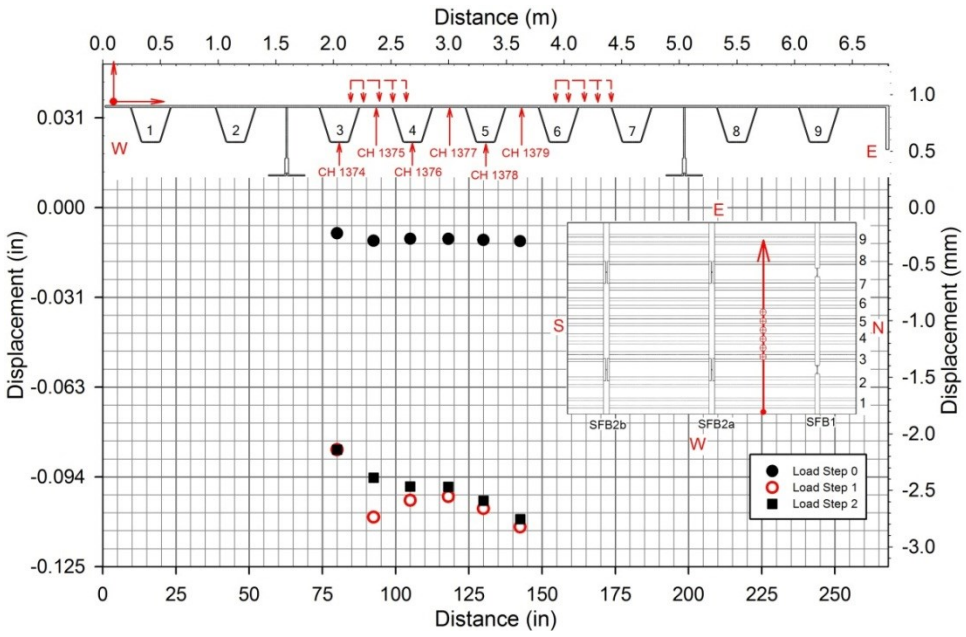

Figure 145 Measured vertical displacements at section Y-Y for each load step during the static test of November 1, 2010

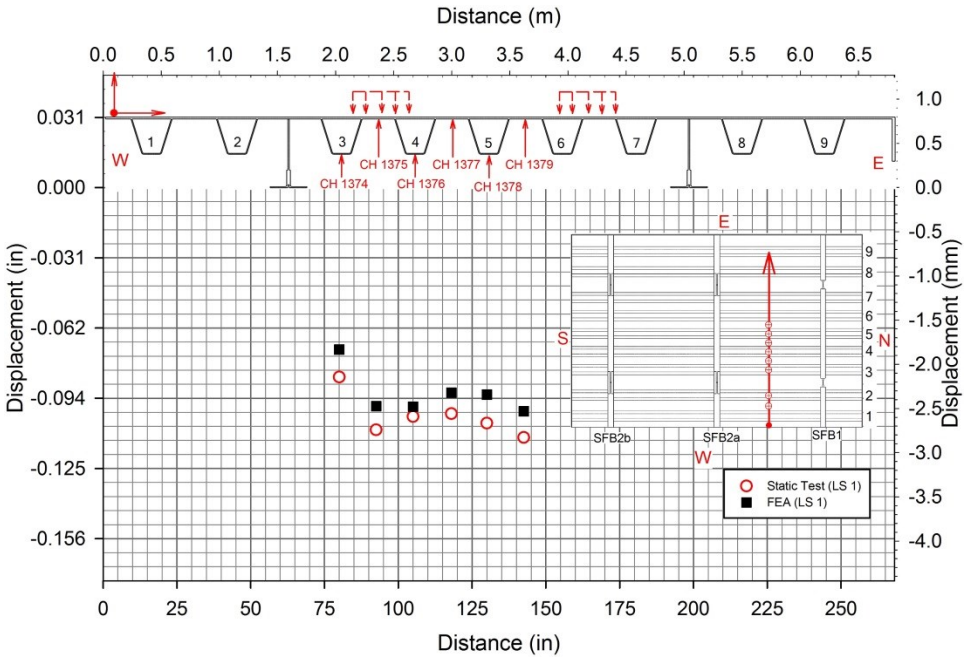

Figure 146 Comparison of the measured vertical displacements at section Y-Y in LS-1 with the FEA results

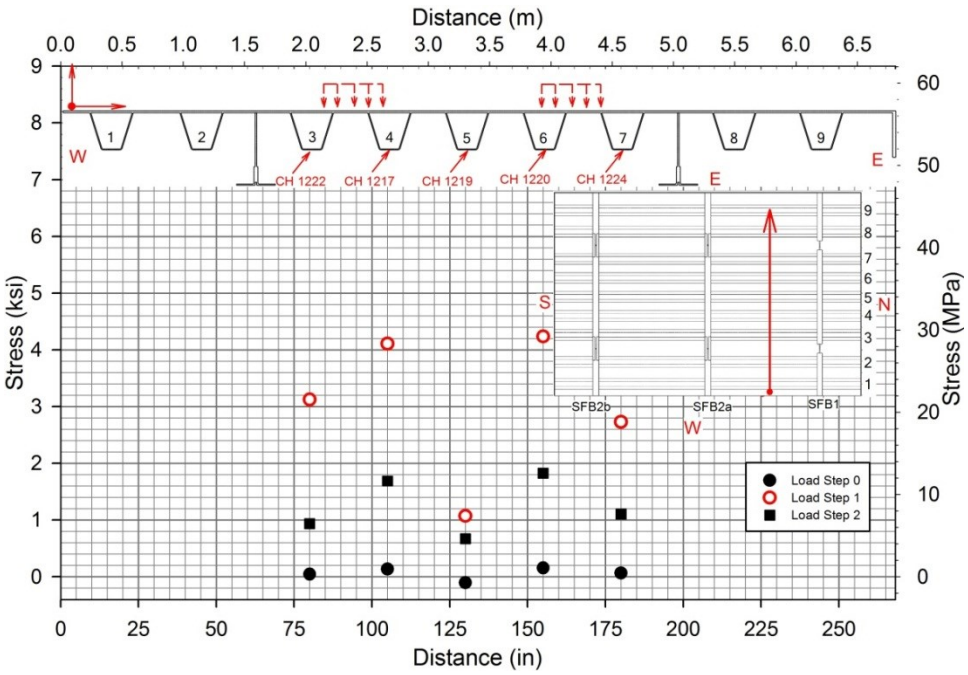

Figure 147 Measured longitudinal stress at the rib soffits on section Y-Y for each load step during the static test November 1, 2010

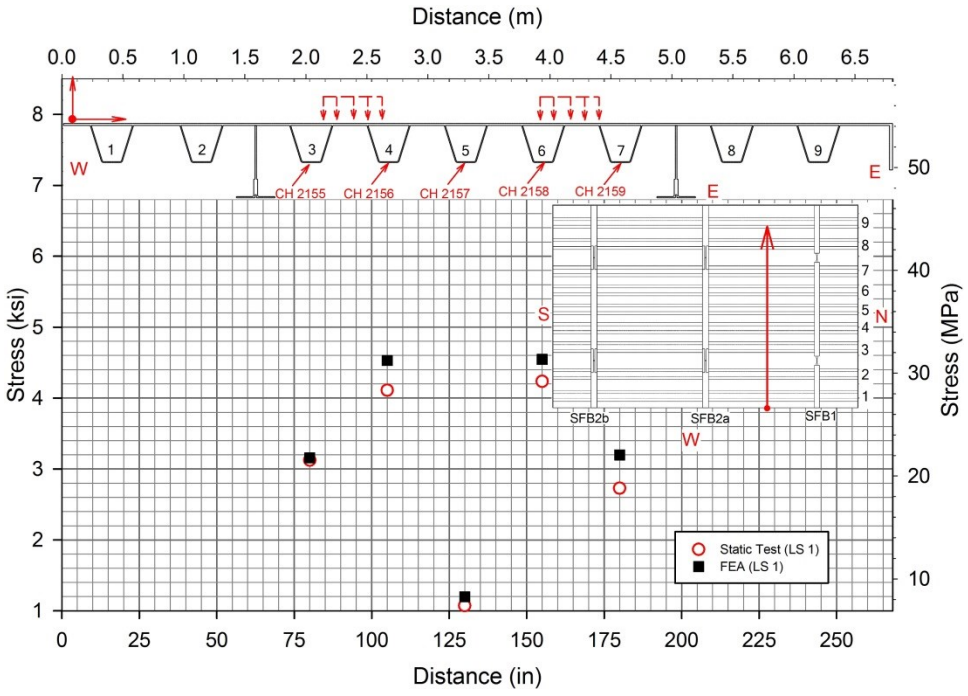

Figure 148 Comparison of the measured longitudinal stress at rib soffits on section Y-Y in LS-1 with FEA results

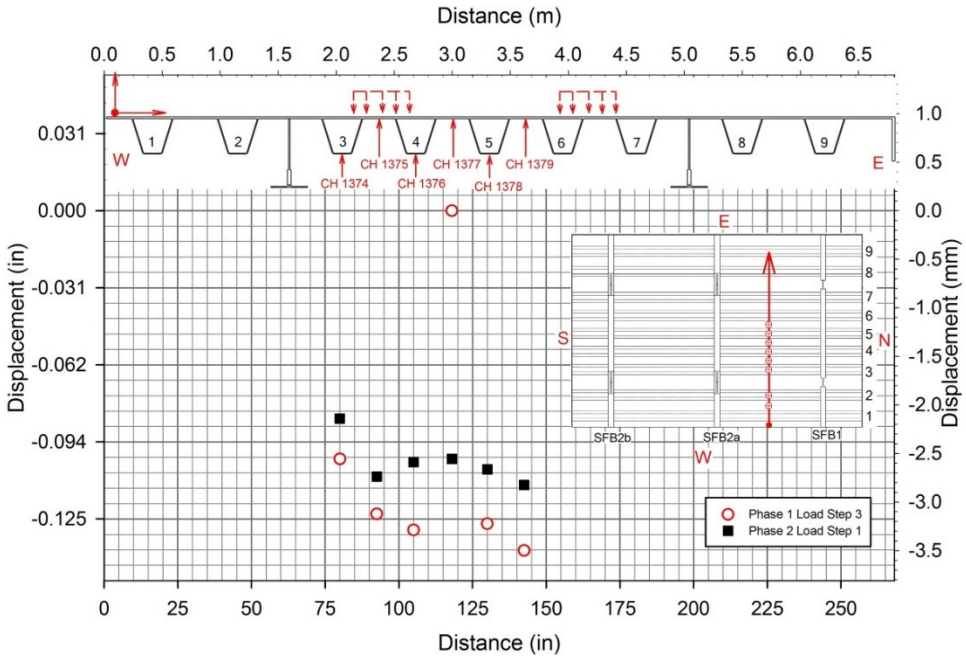

Figure 149 Comparison of the maximum measured displacements between the initial static tests of Phase 1 and Phase 2

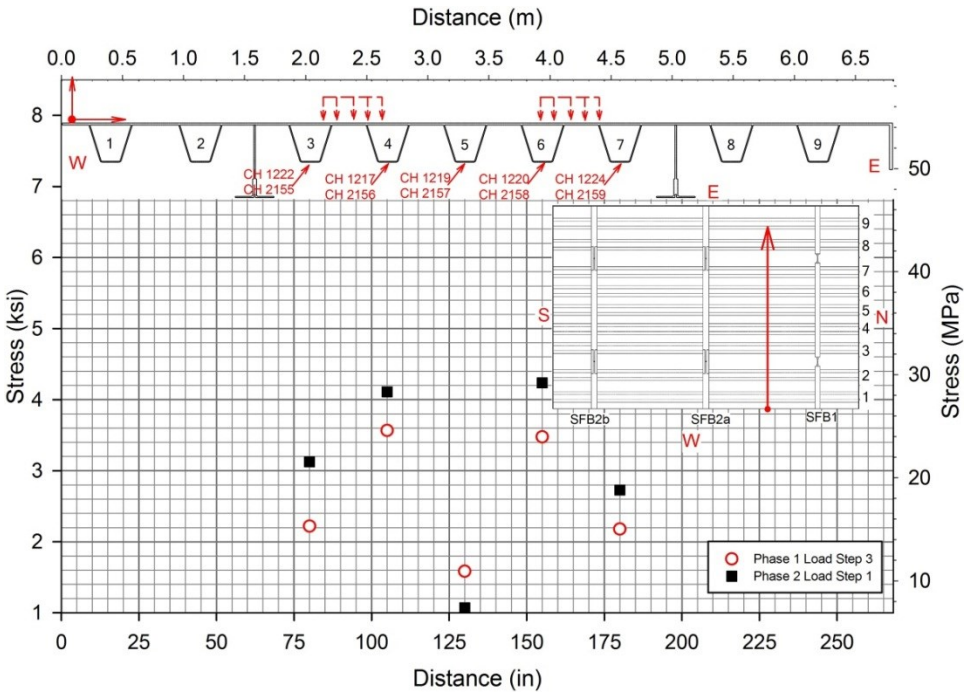

Figure 150 Comparison of the maximum measured longitudinal stress at the rib soffits measured between static tests of Phase 1 and Phase 2

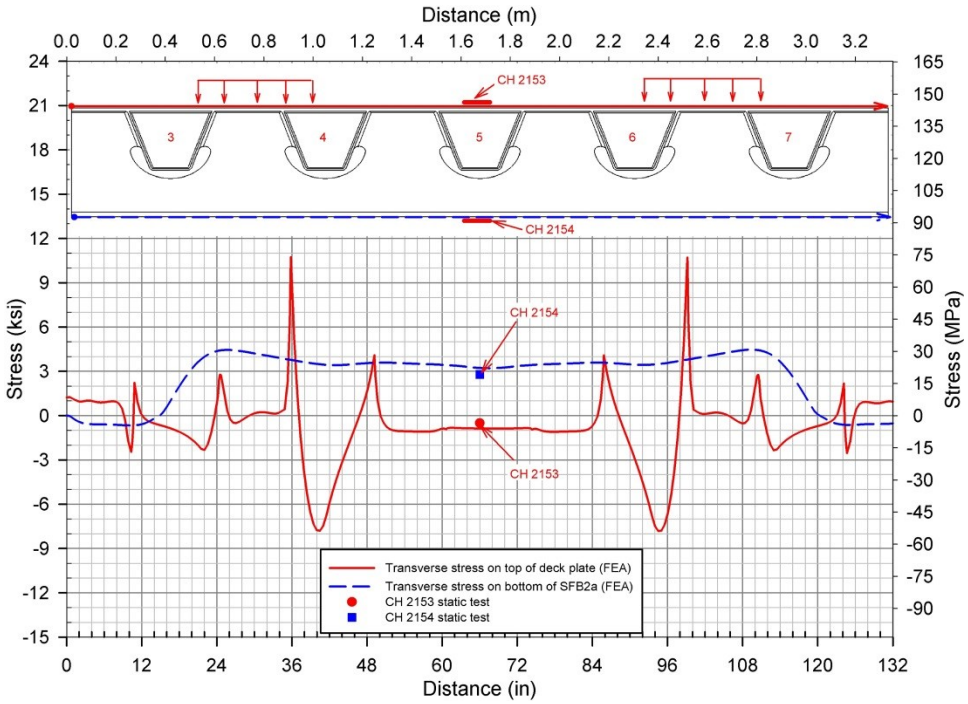

Figure 151 Transverse stresses on the top of deck plate and bottom of SFB2a

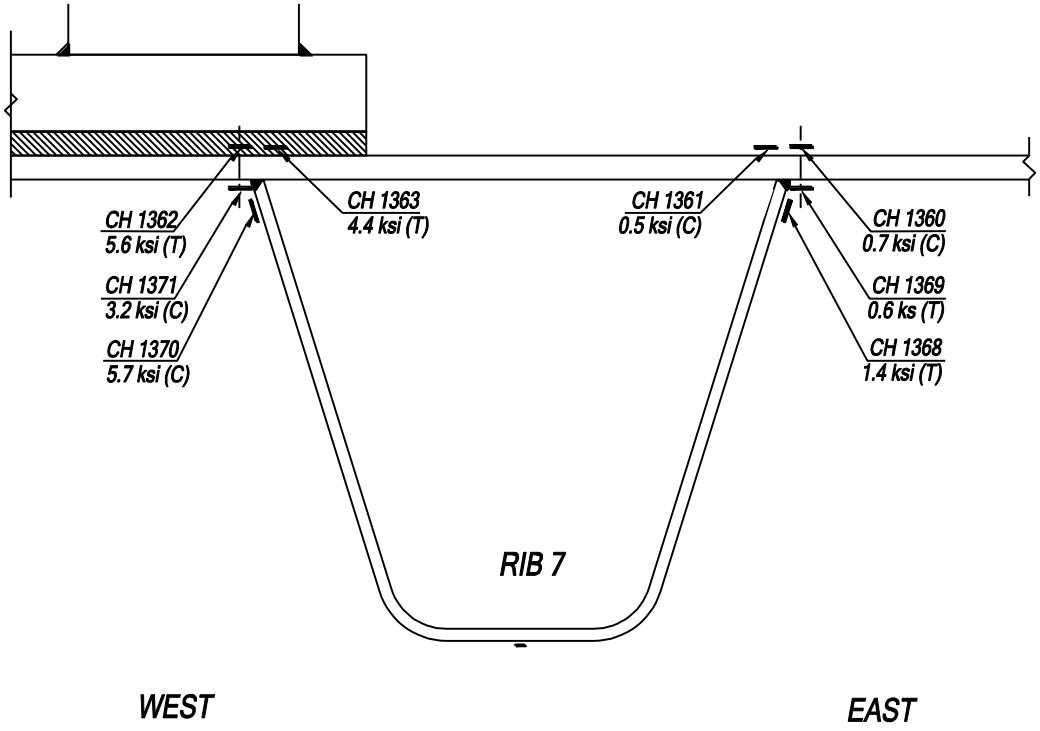

Figure 152 Maximum stresses in the deck plate and rib wall of Rib 7 at section Y-Y for static test of November 1, 2010

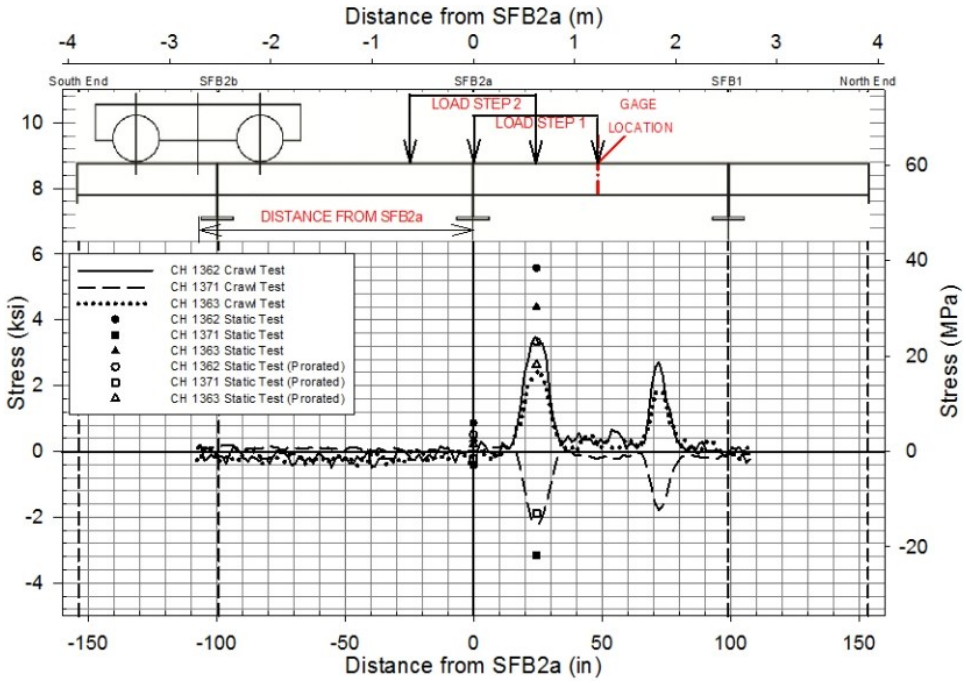

Figure 153 Comparison of static test results with crawl test for deck plate or Rib 7 at section Y-Y

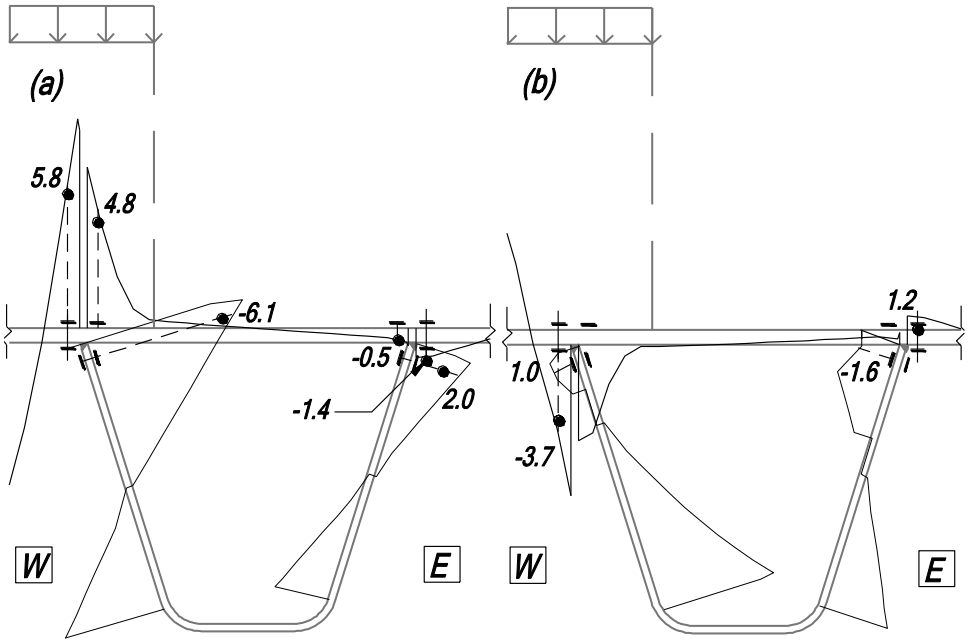

Figure 154 Transverse stresses from FEA with LS-1 static test results plotted as dots at Rib 7 gauged locations: (a) on the top face of deck and external faces of ribs, (b) on the bottom face of deck and internal faces of ribs

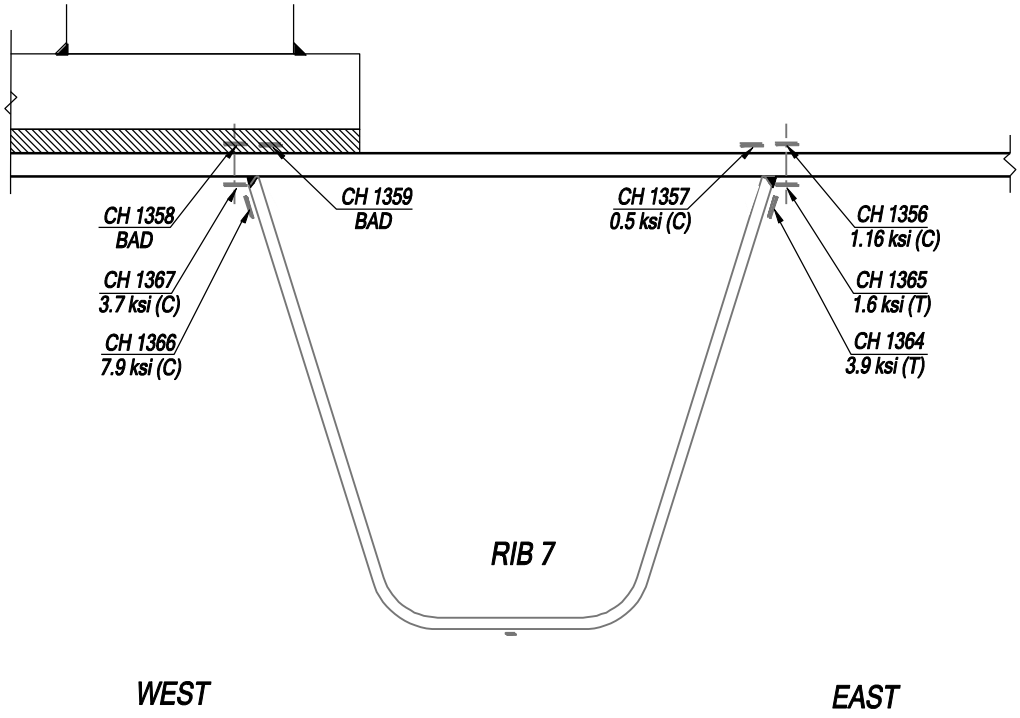

Figure 155 Maximum stresses in the deck plate and rib wall of Rib 7 at section X-X for Phase 1 static test of January 29, 2009

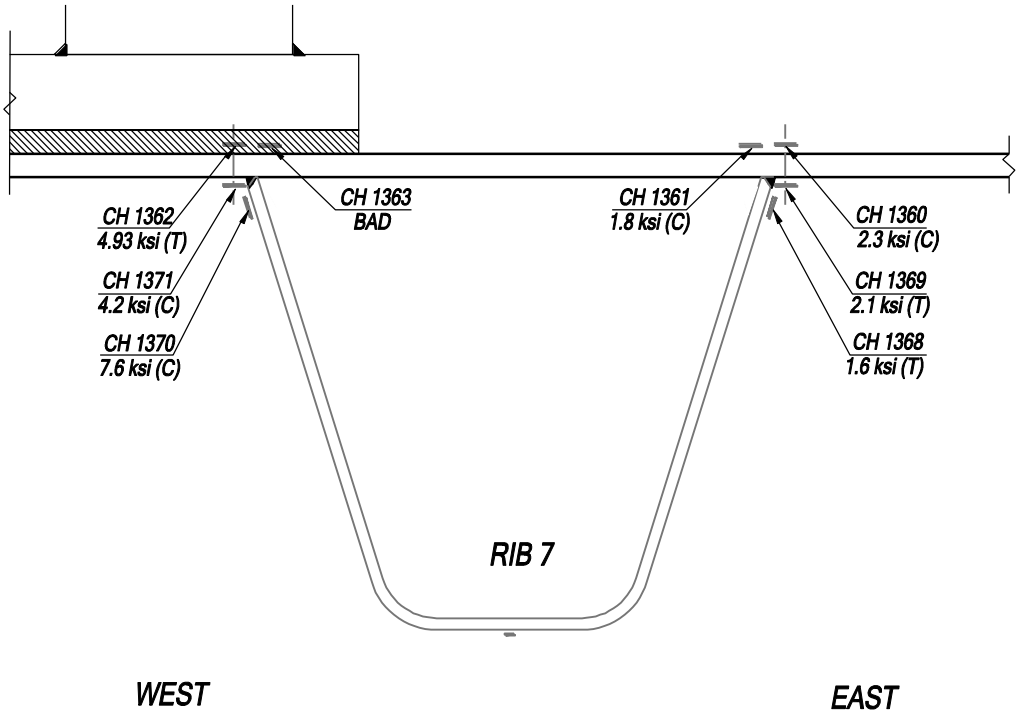

Figure 156 Maximum stresses in the deck plate and rib wall of Rib 7 at section Y-Y for Phase 1 static test of January 29, 2009

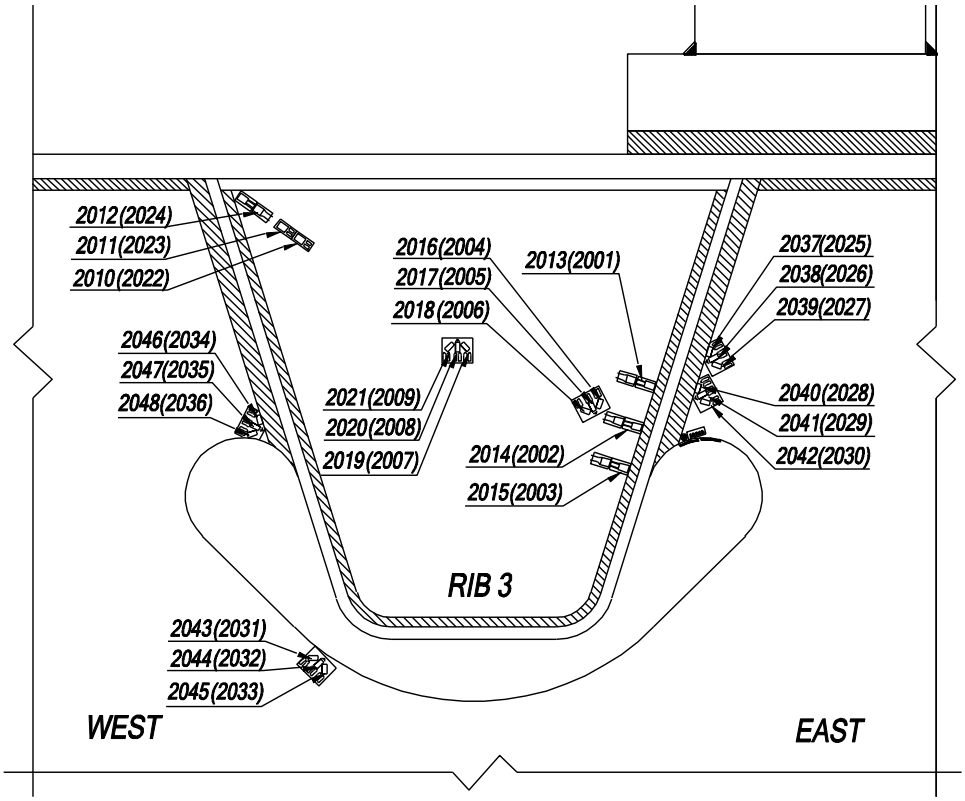

View looking north (showing south face); Gauges on the north face are identified in parentheses

West of Rib 3			
North face		South face	
CH	Measured Value (ksi)	CH	Measured Value (ksi)
2031	4.7	2043	4.9
2032	-0.4	2044	-0.4
2033	3.0	2045	2.6
2034	-4.3	2046	-4.3
2035	-9.7	2047	-8.1
2036	-12.9	2048	-12.9

East of Rib 3			
North face		South face	
CH	Measured Value (ksi)	CH	Measured Value (ksi)
2025	1.1	2037	1.0
2026	1.7	2038	2.2
2027	0.6	2039	1.4
2028	2.7	2040	3.1
2029	4.3	2041	5.3
2030	3.8	2042	4.8

Bulkhead Plate			
North face		South face	
CH	Measured Value (ksi)	CH	Measured Value (ksi)
2001	3.5	2013	3.9
2002	3.4	2014	4.3
2003	1.2	2015	0.8
2004	-1.9	2016	-1.6
2005	1.4	2017	1.3
2006	3.1	2018	3.1
2007	2.6	2019	2.2
2008	-0.4	2020	-0.5
2009	-3.1	2021	-3.3
2010	4.6	2022	4.6
2011	5.3	2023	5.5
2012	7.7	2024	6.4

Figure 157 Measured maxima of stresses on SFB2a around Rib 3 cutout and on the bulkhead plate in Rib 3 during the initial static test of November 1, 2010

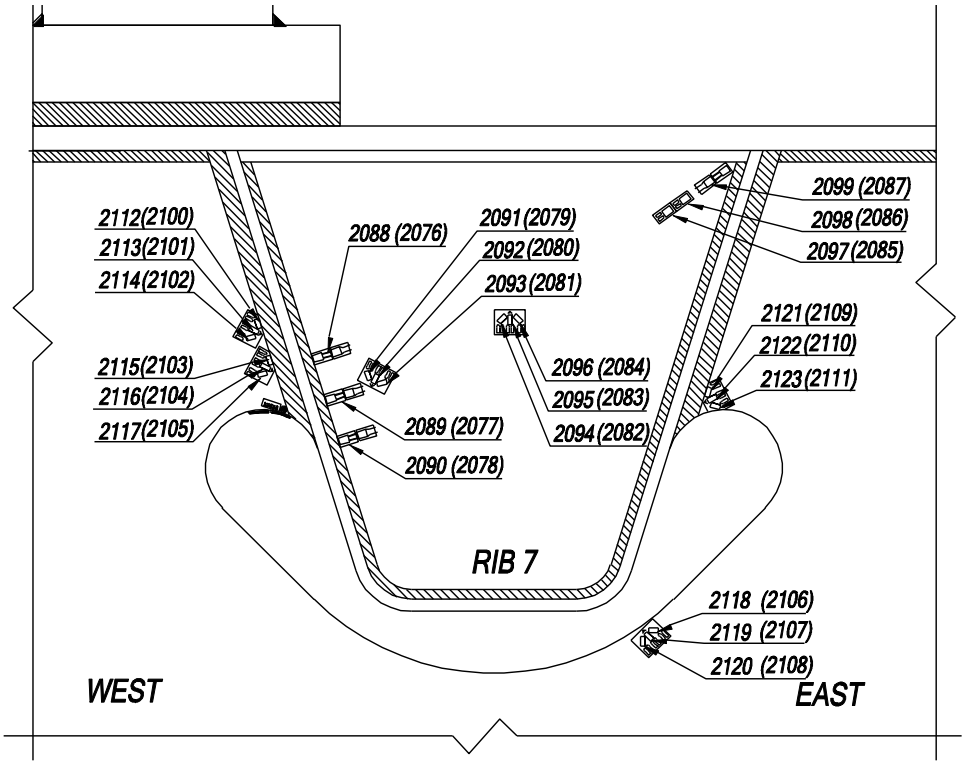

View looking north (showing south face); Gauges on the north face are identified in parentheses

West of Rib 7			
North face		South face	
CH	Measured Value (ksi)	CH	Measured Value (ksi)
2100	1.4	2112	0.9
2101	2.4	2113	1.8
2102	1.7	2114	0.8
2103	3.2	2115	3.0
2104	5.5	2116	5.2
2105	6.1	2117	5.1

East of Rib 7			
North face		South face	
CH	Measured Value (ksi)	CH	Measured Value (ksi)
2106	4.8	2118	5.8
2107	-0.5	2119	0.7
2108	3.2	2120	2.9
2109	-3.6	2121	-3.5
2110	-5.3	2122	-8.1
2111	-9.5	2123	-10.8

Bulkhead Plate			
North face		South face	
CH	Measured Value (ksi)	CH	Measured Value (ksi)
2076	3.7	2088	3.1
2077	3.1	2089	2.7
2078	0.9	2090	0.7
2079	-1.5	2091	-1.8
2080	-0.4	2092	1.2
2081	2.7	2093	2.6
2082	1.9	2094	1.3
2083	-0.8	2095	0.9
2084	-3.3	2096	-2.9
2085	4.1	2097	4.4
2086	4.7	2098	5.3
2087	7.1	2099	Bad

Figure 158 Measured maxima of stresses on SFB2a around Rib 7 cutout and on the bulkhead plate in Rib 7 during the initial static test of November 1, 2012

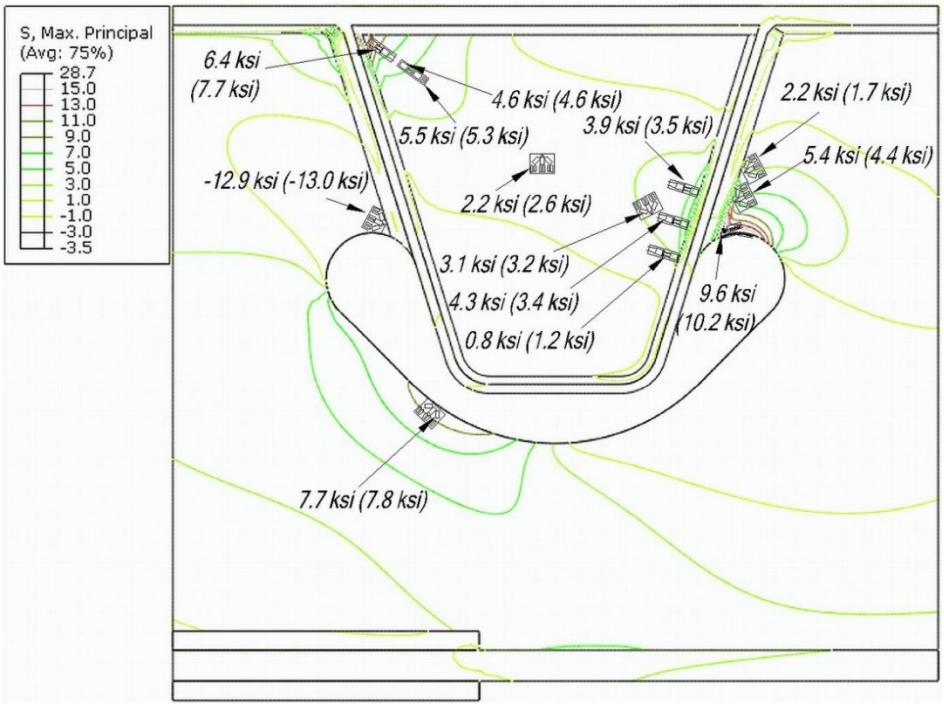

Figure 159 Measured stresses on SFB2a around Rib 3 cutout for LS-2 (north face in parentheses) overlaid on the FEA contour of maximum principal stresses

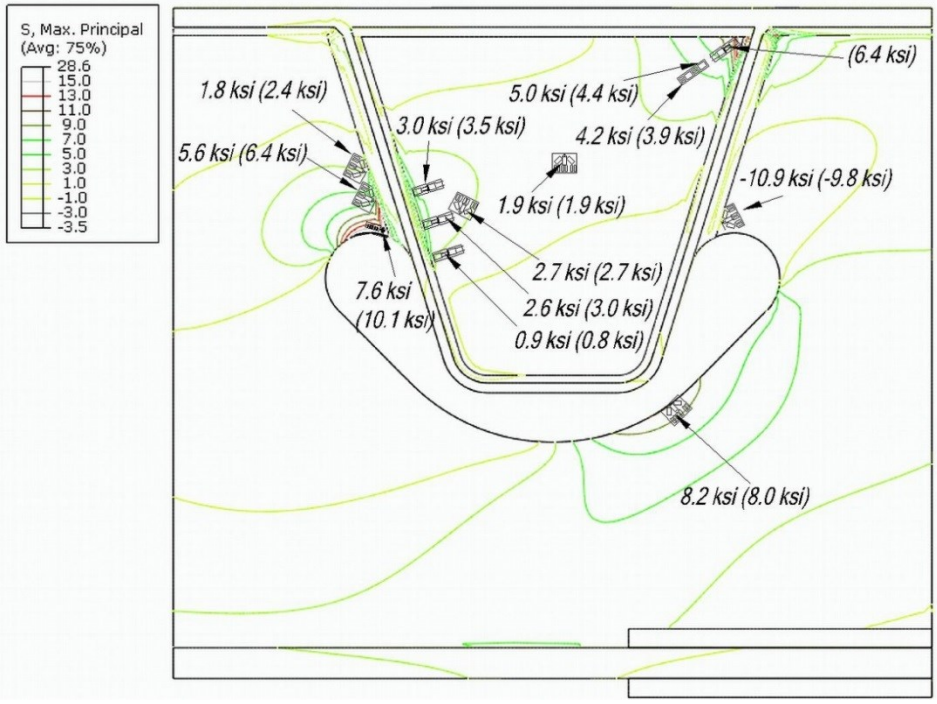

Figure 160 Measured stresses on SFB2a around Rib 7 cutout for LS-2 (north face in parentheses) overlaid on the FEA contour of maximum principal stresses

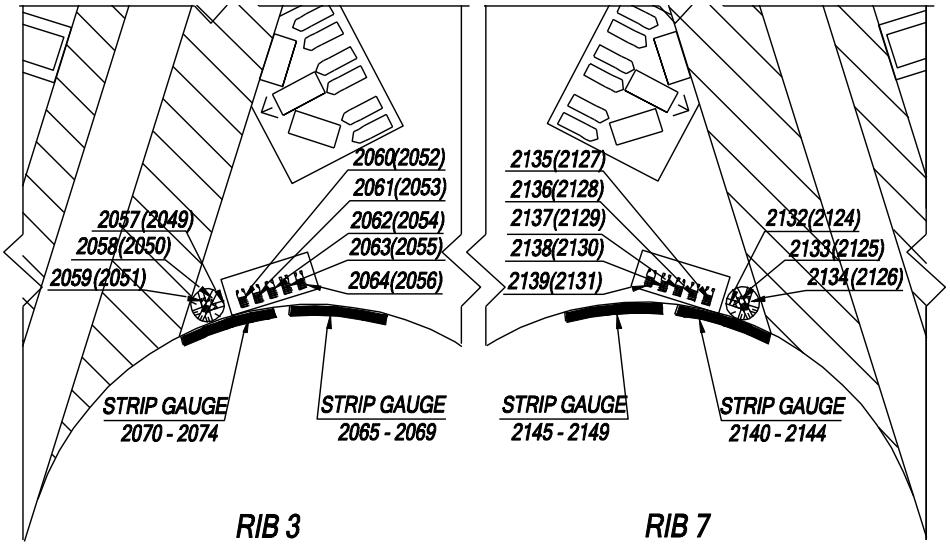

View looking north (showing south face); Gauges on the north face are identified in parentheses

Rib 3 Cutout			
North face		South face	
CH	Measured Value (ksi)	CH	Measured Value (ksi)
2049	9.9	2057	15.6
2050	17.0	2058	7.6
2051	8.3	2059	1.1
2052	15.7	2060	15.6
2053	13.9	2061	15.2
2054	13.0	2062	14.3
2055	12.3	2063	13.3
2056	13.3	2064	13.2

Rib 7 Cutout			
North face		South face	
CH	Measured Value (ksi)	CH	Measured Value (ksi)
2124	8.1	2132	16.1
2125	13.6	2133	7.7
2126	8.0	2134	1.4
2127	13.9	2135	13.0
2128	13.1	2136	14.8
2129	12.9	2137	12.4
2130	11.7	2138	11.6
2131	12.1	2139	10.8

Rib 3 Cutout Face	
CH	Measured Value (ksi)
2065	19.5
2066	20.7
2067	20.9
2068	20.8
2069	21.3
2070	16.3
2071	15.3
2072	14.5
2073	14.5
2074	14.6

Rib 7 Cutout Face	
CH	Measured Value (ksi)
2140	14.9
2141	16.1
2142	17.8
2143	18.9
2144	18.7
2145	17.9
2146	17.0
2147	17.5
2148	16.5
2149	16.2

Figure 161 Measured maxima of stresses on SFB2a around Rib 3 and Rib 7 cutout during the initial static test (looking north) of November 1, 2010

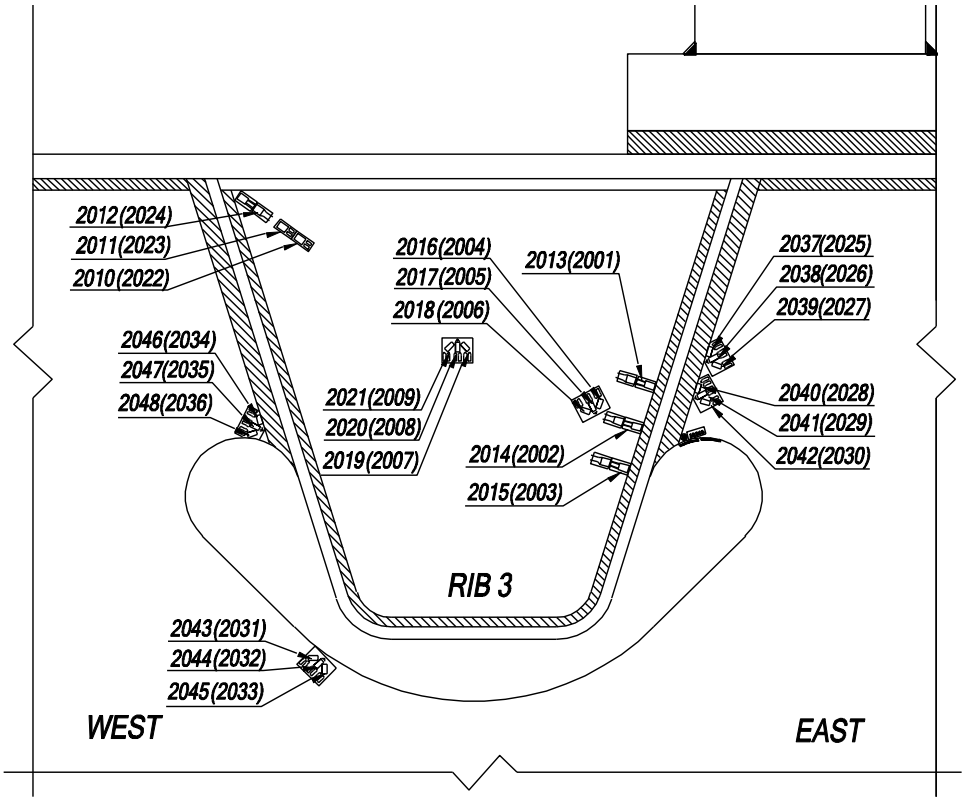

View looking north (showing south face); Gauges on the north face are identified in parentheses

West of Rib 3			
North face		South face	
CH	Measured Value (ksi)	CH	Measured Value (ksi)
2031	4.5	2043	4.8
2032	0.4	2044	0.4
2033	3.1	2045	2.7
2034	3.4	2046	3.4
2035	8.0	2047	6.7
2036	10.8	2048	11.0

East of Rib 3			
North face		South face	
CH	Measured Value (ksi)	CH	Measured Value (ksi)
2025	1.3	2037	1.3
2026	1.9	2038	2.4
2027	1.0	2039	1.7
2028	2.8	2040	3.2
2029	4.2	2041	5.1
2030	3.7	2042	4.6

Bulkhead Plate			
North face		South face	
CH	Measured Value (ksi)	CH	Measured Value (ksi)
2001	3.5	2013	3.7
2002	3.5	2014	3.43
2003	1.5	2015	1.0
2004	1.3	2016	1.1
2005	1.7	2017	1.5
2006	3.2	2018	3.1
2007	2.7	2019	2.3
2008	0.2	2020	0.1
2009	2.3	2021	2.5
2010	4.4	2022	4.3
2011	5.0	2023	5.1
2012	7.1	2024	5.9

Figure 162 Measured stress ranges on SFB2a around Rib 3 cutout and on the bulkhead plate in Rib 3 during the initial static test (looking north) of November 1, 2010

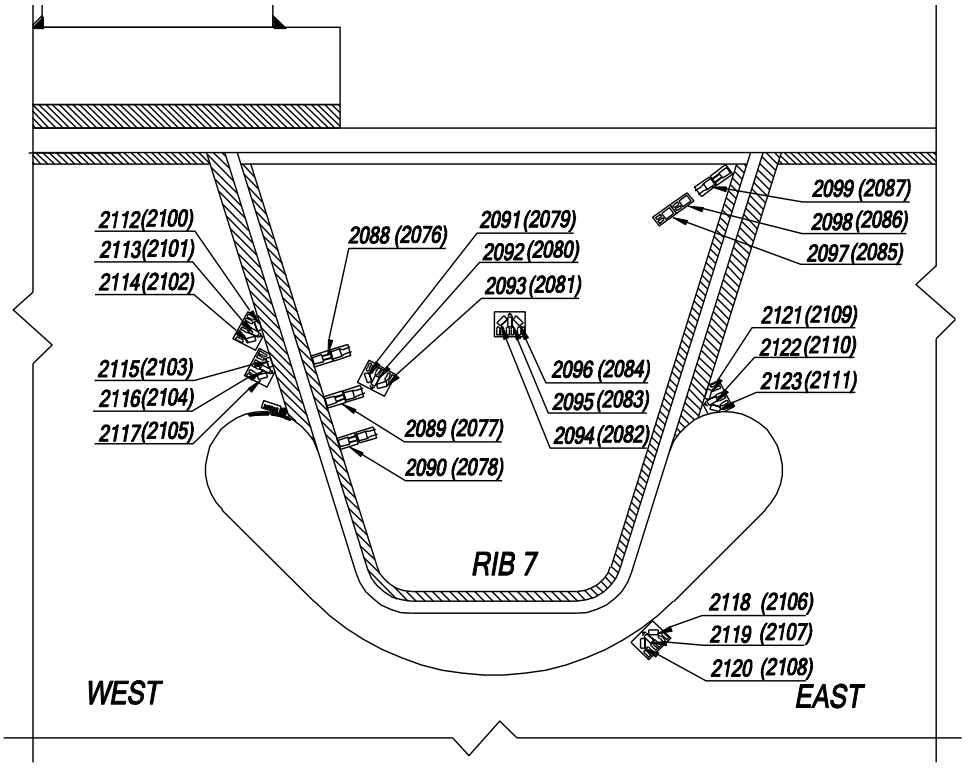

View looking north (showing south face); Gauges on the north face are identified in parentheses

West of Rib 7			
North face		South face	
CH	Measured Value (ksi)	CH	Measured Value (ksi)
2100	1.6	2112	1.3
2101	2.5	2113	2.1
2102	1.9	2114	1.2
2103	3.3	2115	3.0
2104	5.3	2116	5.0
2105	5.9	2117	4.5

East of Rib 7			
North face		South face	
CH	Measured Value (ksi)	CH	Measured Value (ksi)
2106	4.7	2118	5.1
2107	0.5	2119	0.6
2108	3.2	2120	2.6
2109	2.8	2121	3.0
2110	4.3	2122	7.0
2111	7.9	2123	9.4

Bulkhead Plate			
North face		South face	
CH	Measured Value (ksi)	CH	Measured Value (ksi)
2076	3.5	2088	3.0
2077	3.0	2089	2.6
2078	0.8	2090	0.9
2079	0.9	2091	1.2
2080	0.4	2092	1.4
2081	2.7	2093	2.7
2082	2.1	2094	1.6
2083	0.4	2095	1.2
2084	2.5	2096	2.1
2085	3.9	2097	4.2
2086	4.4	2098	5.0
2087	6.4	2099	Bad

Figure 163 Measured stress ranges on SFB2a around Rib 7 cutout and on the bulkhead plate in Rib 7 during the initial static test (looking north) of November 1, 2010

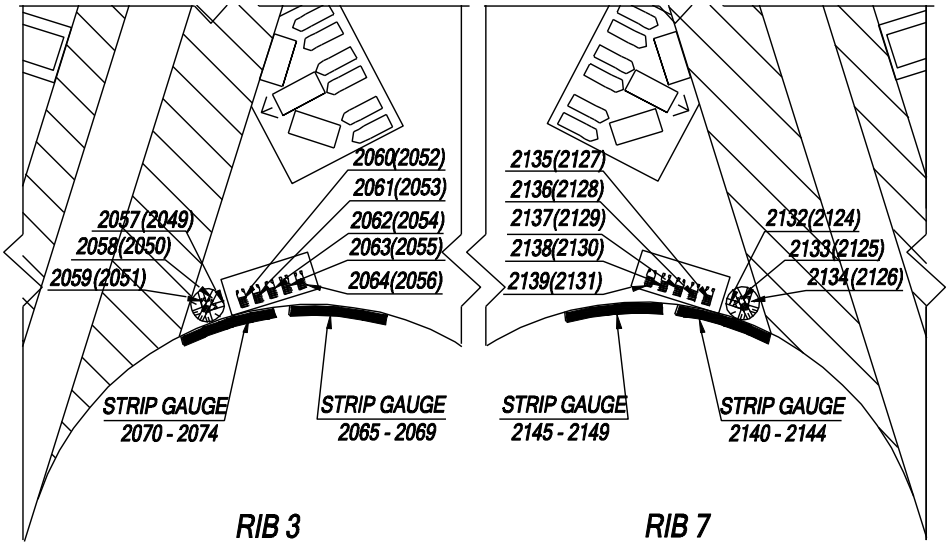

View looking north (showing south face); Gauges on the north face are identified in parentheses

Rib 3 Cutout			
North face		South face	
CH	Measured Value (ksi)	CH	Measured Value (ksi)
2049	9.6	2057	14.6
2050	15.9	2058	7.5
2051	8.2	2059	1.8
2052	14.5	2060	14.3
2053	12.9	2061	13.4
2054	12.1	2062	12.7
2055	11.4	2063	11.8
2056	12.3	2064	11.6

Rib 7 Cutout			
North face		South face	
CH	Measured Value (ksi)	CH	Measured Value (ksi)
2124	7.2	2132	14.1
2125	12.0	2133	6.8
2126	7.1	2134	1.2
2127	12.3	2135	11.4
2128	11.6	2136	13.1
2129	11.4	2137	10.9
2130	10.2	2138	10.2
2131	10.6	2139	9.5

Rib 3 Cutout Face	
CH	Measured Value (ksi)
2065	17.2
2066	18.4
2067	18.5
2068	18.3
2069	18.8
2070	14.4
2071	13.5
2072	12.8
2073	12.8
2074	12.8

Rib 7 Cutout Face	
CH	Measured Value (ksi)
2140	13.2
2141	14.2
2142	15.7
2143	16.7
2144	16.5
2145	15.7
2146	15.0
2147	15.4
2148	14.5
2149	14.2

Figure 164 Measured stress ranges on SFB2a around Rib 3 and Rib 7 cutout during the initial static test (looking north) of November 1, 2010

Figure 165 Orientation of gauges at the cutout - Rib 3 south face

Figure 166 Orientation of gauges at the cutout - Rib 3 north face

Figure 167 Orientation of gauges at the cutout - Rib 7 south face

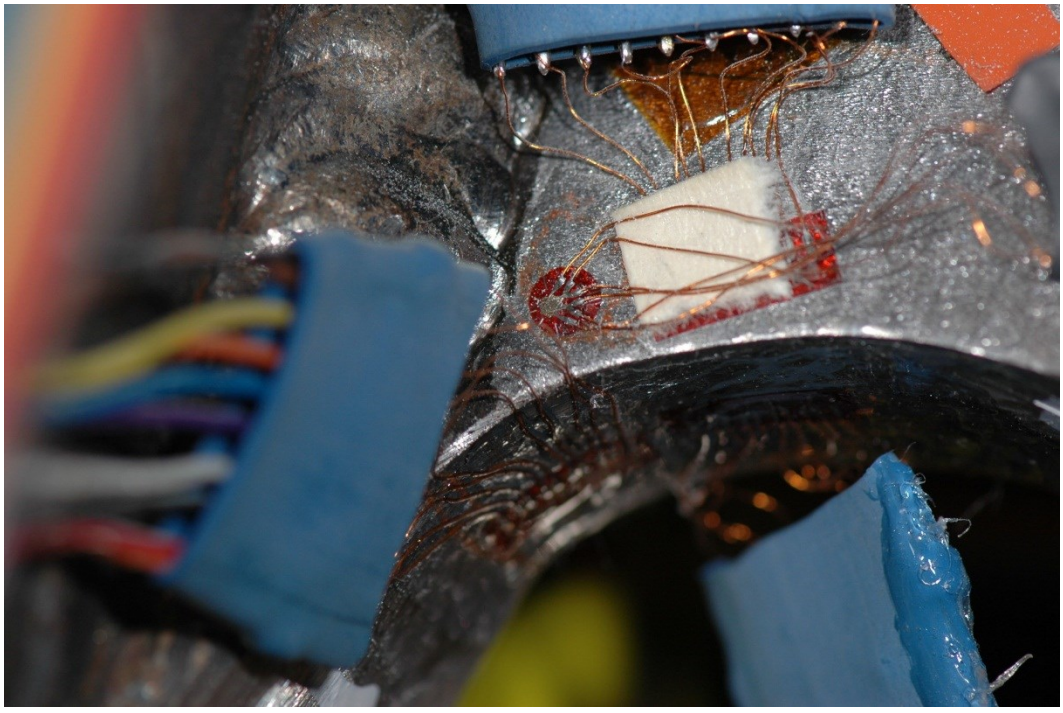

Figure 168 Orientation of gauges at the cutout - Rib 3 north face

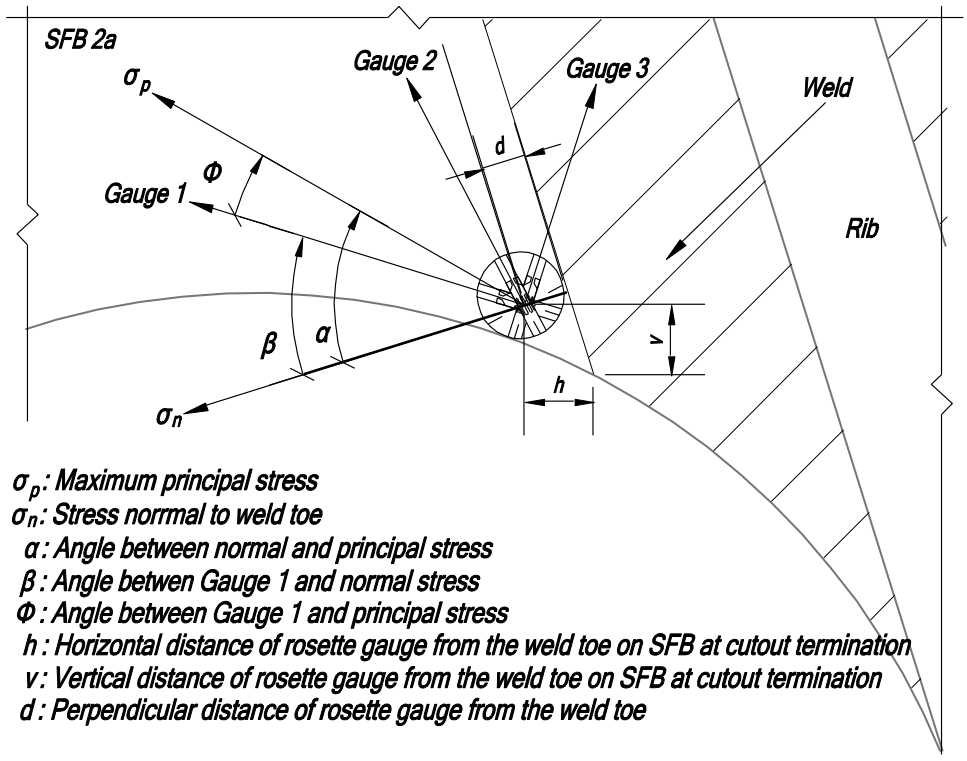

Figure 169 Parameters measured from rectified images

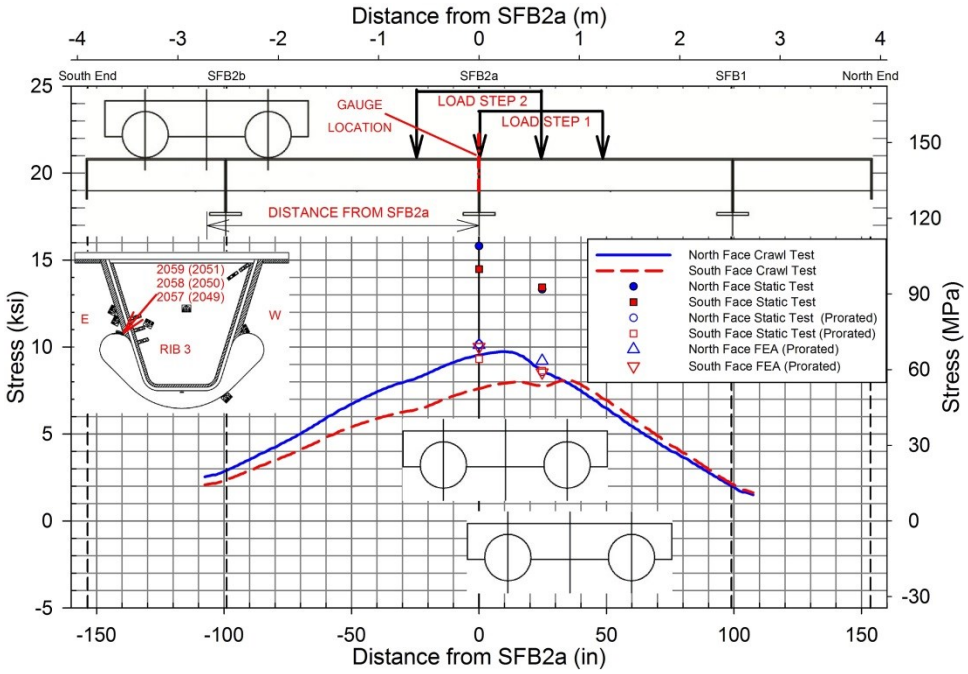

Figure 170 Maximum principal stress in SFB2a to the east of Rib 3 at the cutout termination during static and crawl tests with FEA results

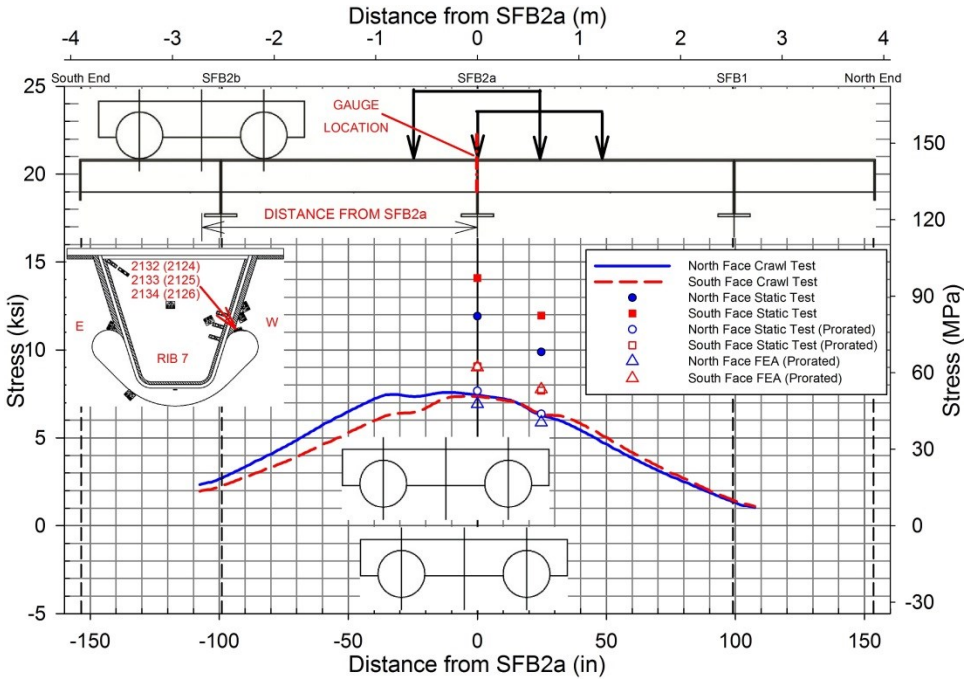

Figure 171 Maximum principal stress in SFB2a to the west of Rib 7 at the cutout termination during static and crawl tests with FEA results

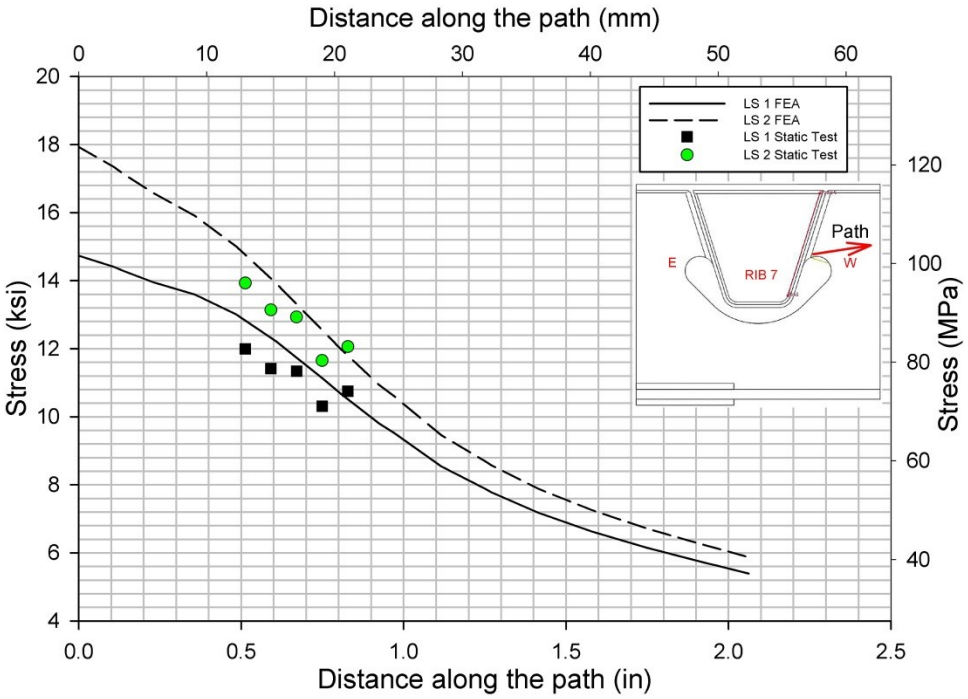

Figure 172 Stress gradient along the shown path at Rib 7 north face with FEA and static test measurements

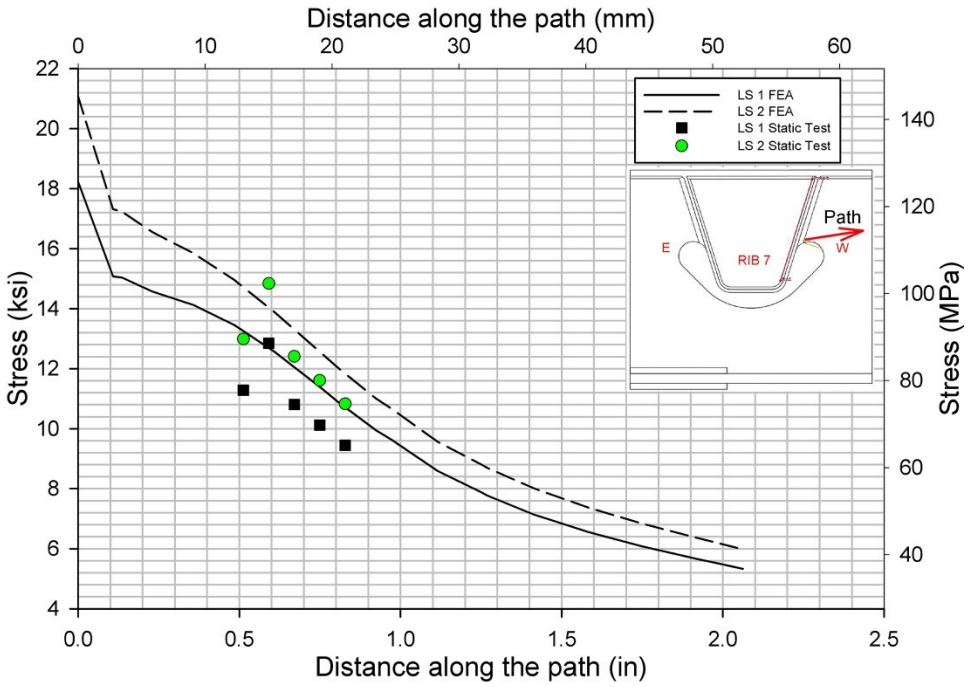

Figure 173 Stress gradient along the shown path at Rib 7 south face with FEA and static test measurements

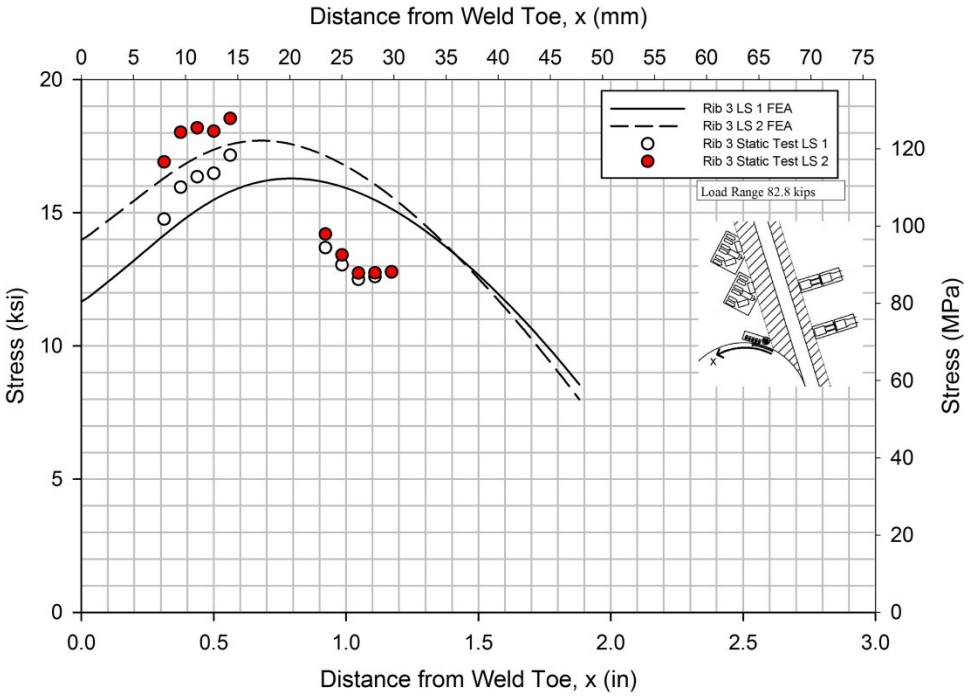

Figure 174 Stresses measured by on the rib 3 cutout edge along the direction shown

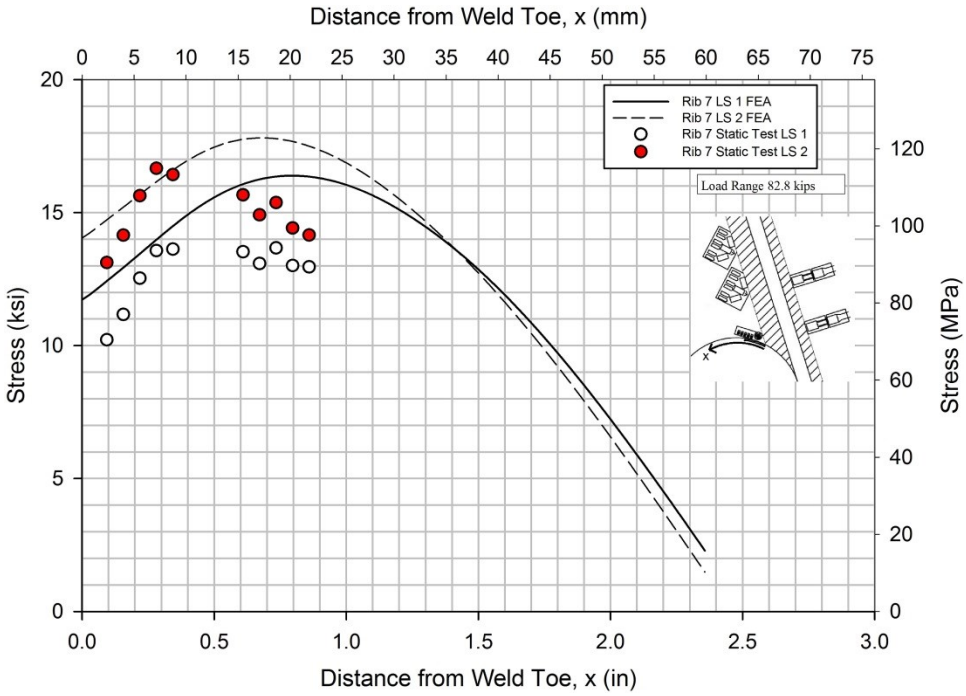

Figure 175 Stresses measured on the rib 7 cutout edge along the direction shown

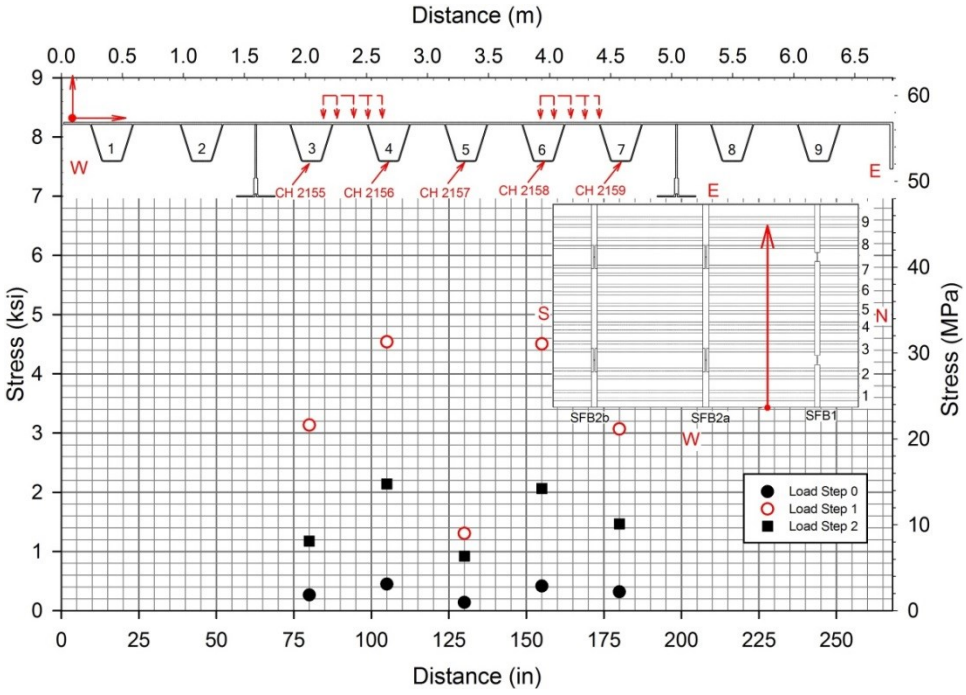

Figure 176 Measured longitudinal stress at the rib soffits on section Y-Y for each load step during the static test of Sept 28, 2011

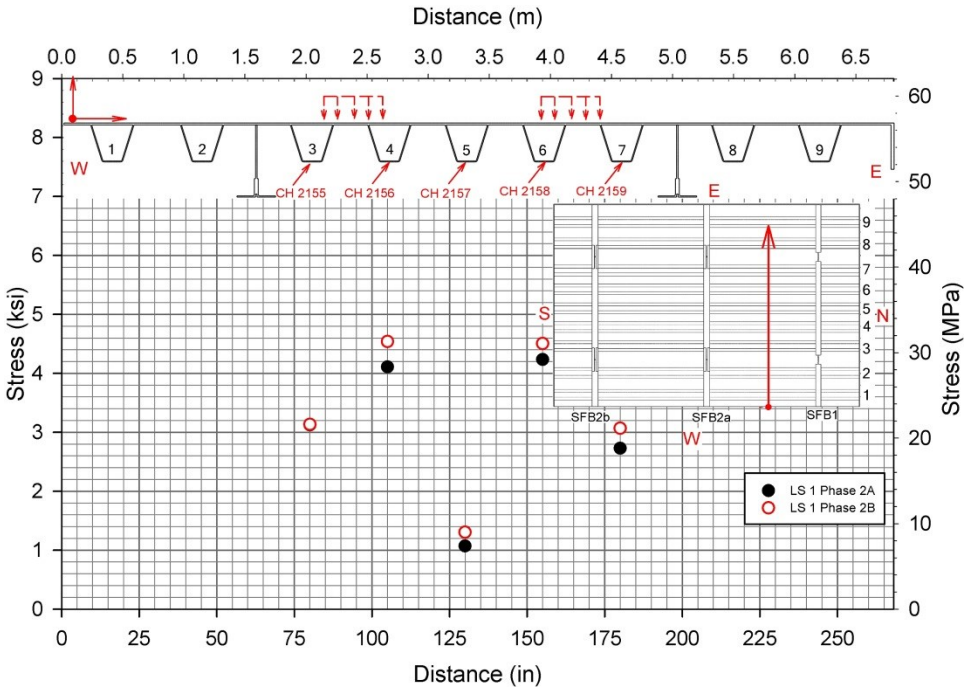

Figure 177Comparison of longitudinal stresses of Phase 2A and Phase 2B at the rib soffits on section Y-Y for LS-1

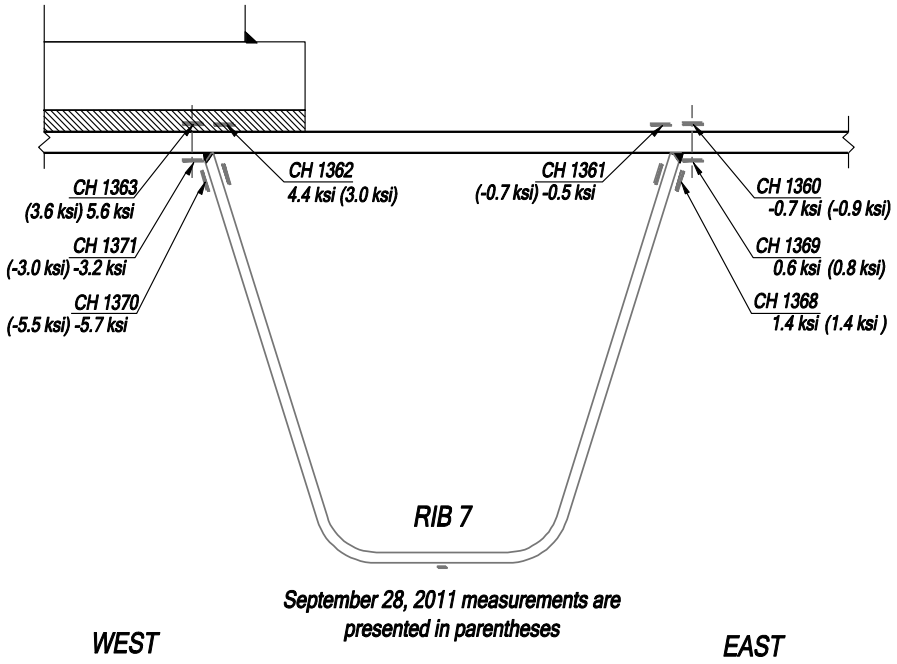

Figure 178 Comparison of maximum stresses in the deck plate and rib wall of Rib 7 at section Y-Y for static test of November 1, 2010 and September 28, 2011

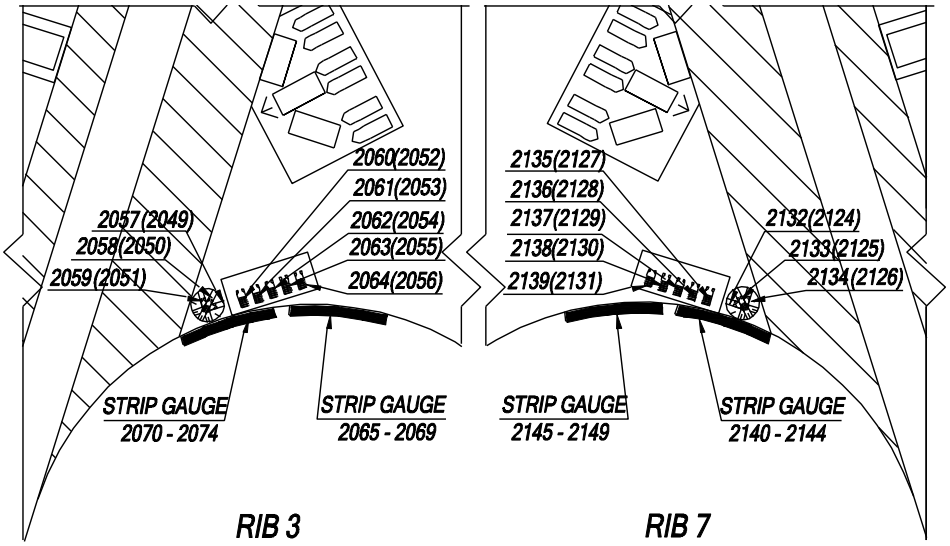

View looking north (showing south face); Gauges on the north face are identified in parentheses

Rib 3 Cutout			
North face		South face	
CH	Measured Value (ksi)	CH	Measured Value (ksi)
2049	10.5	2057	15.7
2050	17.3	2058	7.9
2051	8.8	2059	1.9
2052	15.8	2060	15.5
2053	14.1	2061	14.8
2054	13.3	2062	14.3
2055	12.5	2063	13.0
2056	13.3	2064	12.9

Rib 7 Cutout			
North face		South face	
CH	Measured Value (ksi)	CH	Measured Value (ksi)
2124	8.2	2132	16.5
2125	13.8	2133	8.0
2126	8.2	2134	1.4
2127	14.2	2135	13.3
2128	13.4	2136	15.3
2129	13.1	2137	12.7
2130	11.8	2138	11.9
2131	12.2	2139	11.0

Rib 3 Cutout Face	
CH	Measured Value (ksi)
2065	18.7
2066	19.9
2067	20.2
2068	20.1
2069	20.7
2070	16.1
2071	15.2
2072	14.5
2073	14.5
2074	14.7

Rib 7 Cutout Face	
CH	Measured Value (ksi)
2140	15.4
2141	16.6
2142	18.3
2143	19.5
2144	BAD
2145	18.3
2146	17.3
2147	17.9
2148	16.7
2149	16.3

Figure 179 Measured maxima of stresses on SFB2a around Rib 3 and 7 cutouts in Rib 3 from September 28, 2011 static test

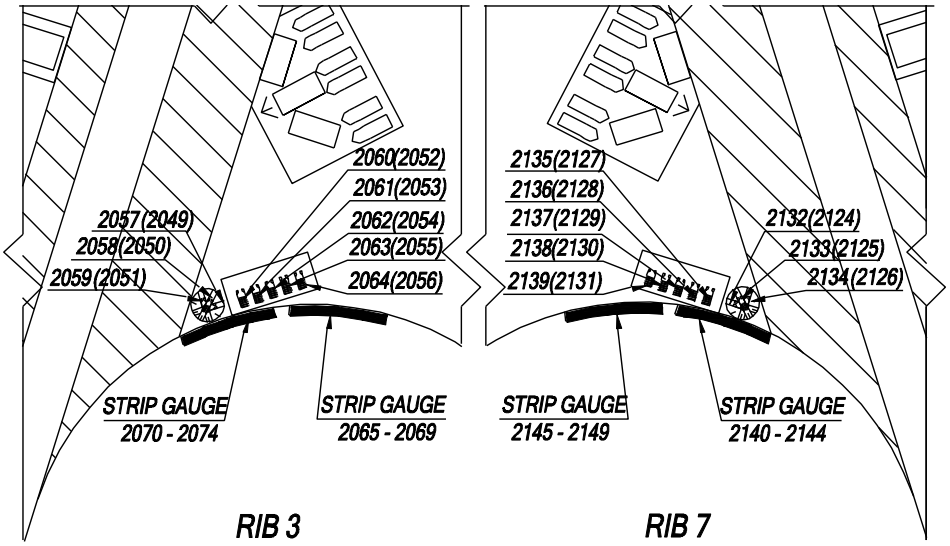

View looking north (showing south face); Gauges on the north face are identified in parentheses

Rib 3 Cutout			
North face		South face	
CH	Measured Value (ksi)	CH	Measured Value (ksi)
2049	9.3	2057	13.9
2050	15.4	2058	7.1
2051	7.8	2059	1.7
2052	14.0	2060	13.7
2053	12.5	2061	13.1
2054	11.7	2062	12.6
2055	11.1	2063	11.5
2056	12.0	2064	11.4

Rib 7 Cutout			
North face		South face	
CH	Measured Value (ksi)	CH	Measured Value (ksi)
2124	7.2	2132	14.4
2125	12.2	2133	7.0
2126	7.2	2134	1.3
2127	12.4	2135	11.6
2128	11.7	2136	13.3
2129	11.5	2137	11.1
2130	10.4	2138	10.4
2131	10.7	2139	9.6

Rib 3 Cutout Face	
CH	Measured Value (ksi)
2065	16.5
2066	17.6
2067	17.9
2068	17.8
2069	18.3
2070	14.2
2071	13.4
2072	12.7
2073	12.8
2074	12.9

Rib 7 Cutout Face	
CH	Measured Value (ksi)
2140	13.5
2141	14.6
2142	16.1
2143	17.1
2144	15.4
2145	16.0
2146	15.1
2147	15.6
2148	14.6
2149	14.2

Figure 180 Stress ranges on SFB2a around Ribs 3 and 7 cutouts for September 28, 2011 static test

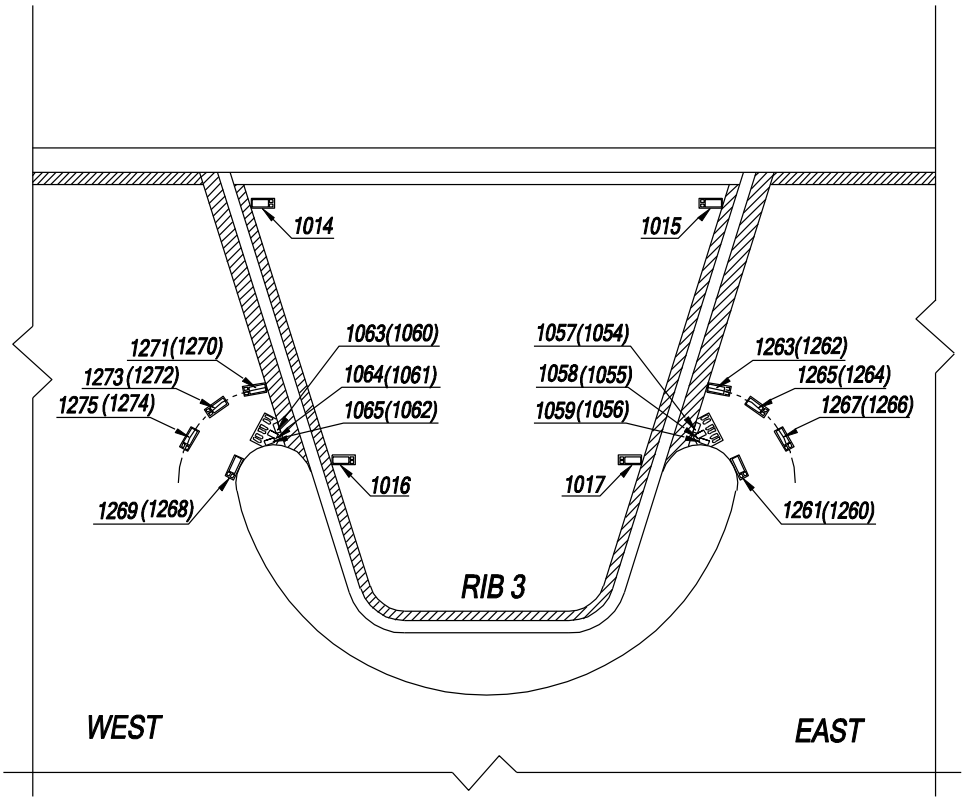

View looking north (showing south face); Gauges on the north face are identified in parentheses

West of Rib 3			
North face		South face	
CH	Measured Stress (ksi)	CH	Measured Stress (ksi)
1060	-2.6	1063	-3.0
1061	-4.2	1064	-4.4
1062	-5.6	1065	-8.2
1268	-2.8	1269	-5.5
1270	-0.2	1271	-1.3
1272	-0.6	1273	-1.6
1274	-0.1	1275	-1.6

Bulkhead Plate	
South face	
CH	Measured Stress (ksi)
1014	2.9
1015	-3.2
1016	-2.6
1017	2.3

East of Rib 3			
North face		South face	
CH	Measured Stress (ksi)	CH	Measured Stress (ksi)
1054	3.6	1057	3.9
1055	5.4	1058	6.2
1056	7.4	1059	5.4
1260	1.9	1261	-1.2
1262	0.6	1263	0.5
1264	0.7	1265	-0.7
1266	0.4	1267	-1.2

Figure 181 Measured maxima of stresses on SFB1 around Rib 3 cutout and on the bulkhead plate in Rib 3 for Phase 2B static test

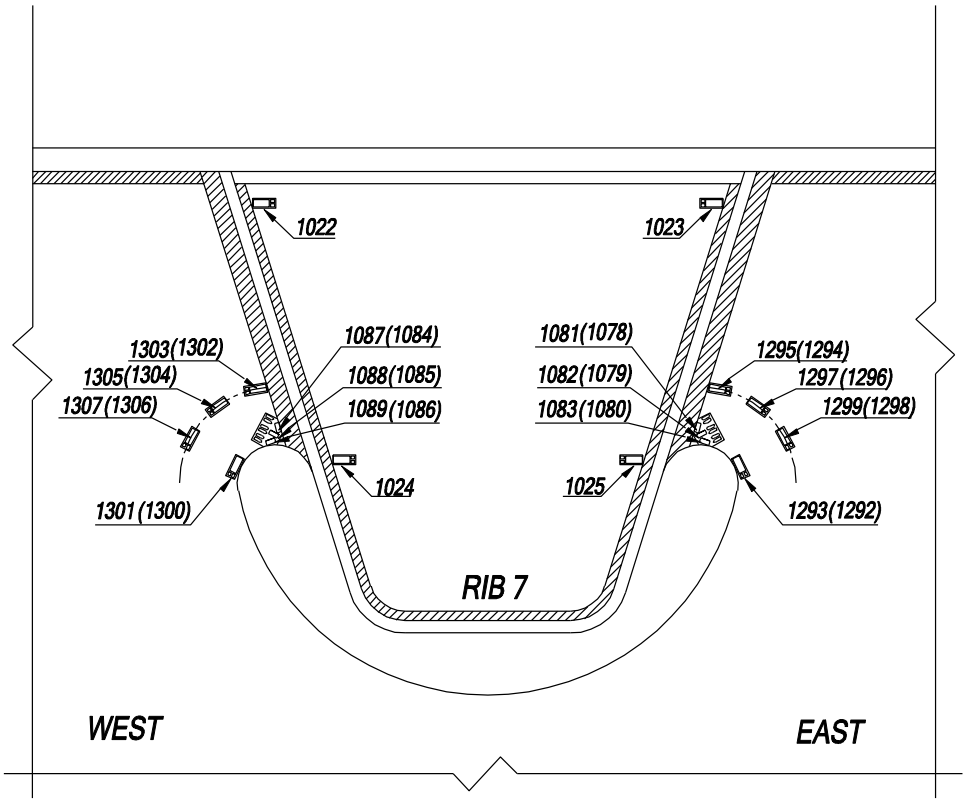

View looking north (showing south face); Gauges on the north face are identified in parentheses

West of Rib 7			
North face		South face	
CH	Measured Stress (ksi)	CH	Measured Stress (ksi)
1084	2.6	1087	2.0
1085	3.2	1088	2.8
1086	3.8	1089	0.7
1300	0.3	1301	-2.8
1302	0.4	1303	-0.2
1304	0.6	1305	-1.3
1306	0.4	1307	-1.3

Bulkhead Plate	
South face	
CH	Measured Stress (ksi)
1022	-2.2
1023	1.6
1024	-0.6
1025	-1.1

East of Rib 7			
North face		South face	
CH	Measured Stress (ksi)	CH	Measured Stress (ksi)
1078	-2.5	1081	-2.8
1079	-4.3	1082	-4.2
1080	-5.5	1083	-7.4
1292	-2.4	1293	-4.5
1294	N/A	1295	-0.4
1296	N/A	1297	-1.7
1298	N/A	1299	-1.3

Figure 182 Measured maxima of stresses on SFB1 around Rib 7 cutout and on the bulkhead plate in Rib 7 for Phase 2B static test

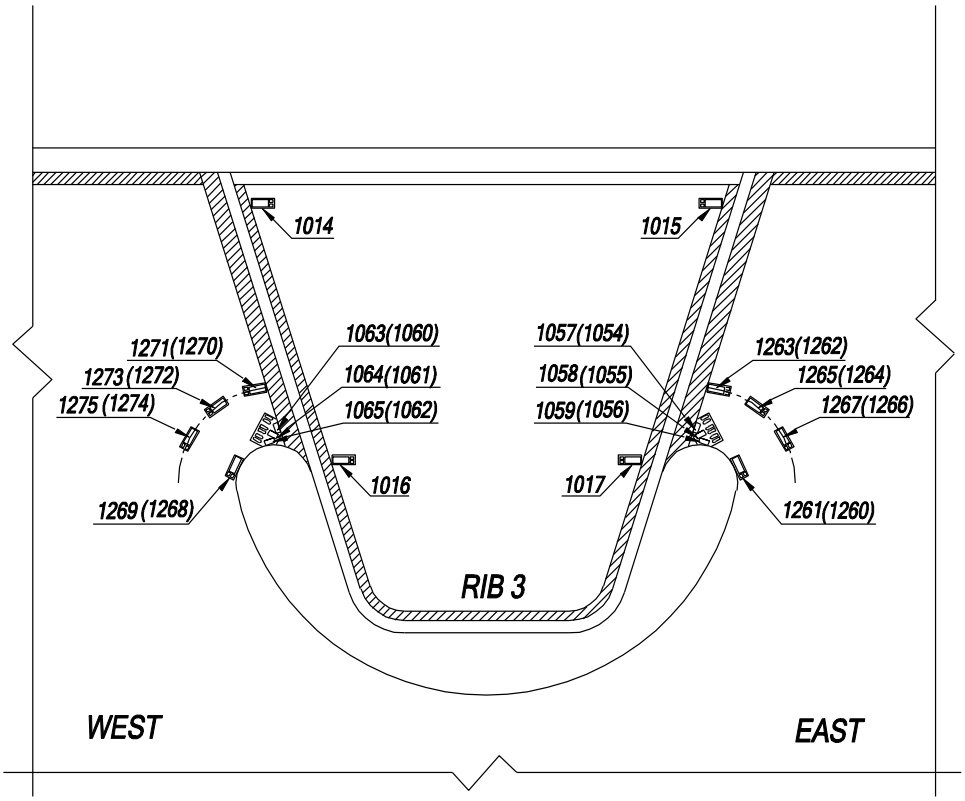

View looking north (showing south face); Gauges on the north face are identified in parentheses

West of Rib 3			
North face		South face	
CH	Measured Stress (ksi)	CH	Measured Stress (ksi)
1060	2.4	1063	2.7
1061	3.8	1064	3.9
1062	5.0	1065	7.3
1268	2.6	1269	4.9
1270	0.2	1271	1.1
1272	0.5	1273	1.4
1274	0.1	1275	1.5

Bulkhead Plate	
South face	
CH	Measured Stress (ksi)
1014	2.7
1015	2.6
1016	2.1
1017	2.2

East of Rib 3			
North face		South face	
CH	Measured Stress (ksi)	CH	Measured Stress (ksi)
1054	3.2	1057	3.4
1055	4.9	1058	5.5
1056	6.6	1059	4.9
1260	1.7	1261	1.1
1262	0.5	1263	0.4
1264	0.6	1265	0.6
1266	0.3	1267	1.1

Figure 183 Measured stress ranges on SFB1 around Rib 3 cutout and on the bulkhead plate in Rib 3 for Phase 2B static test

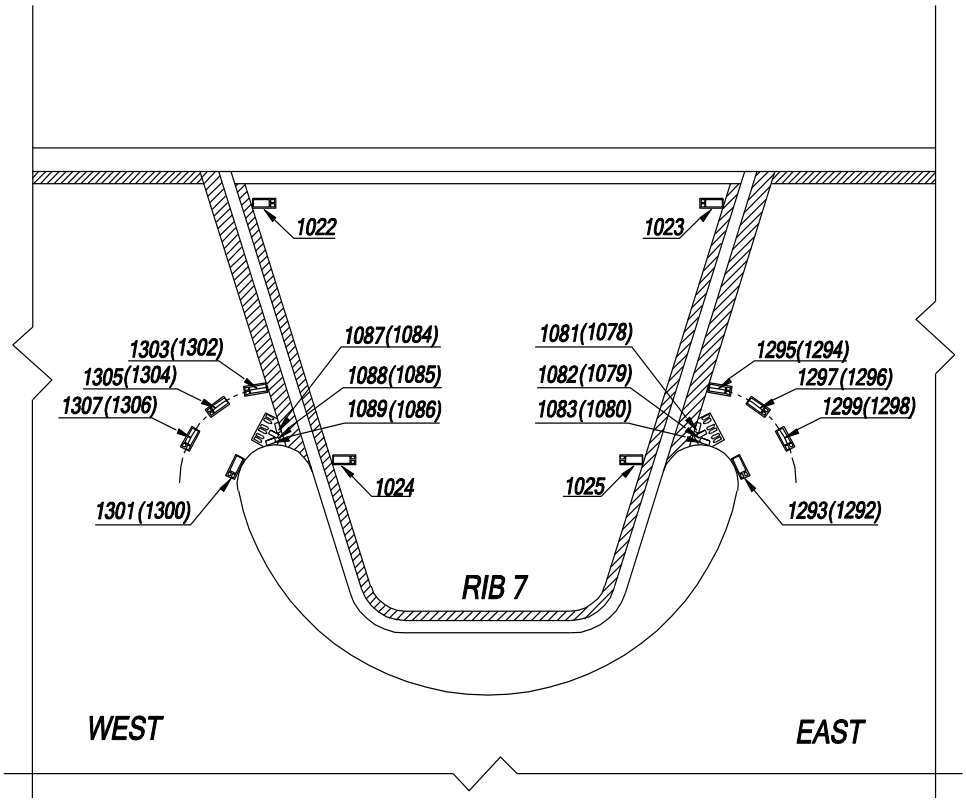

View looking north (showing south face); Gauges on the north face are identified in parentheses

West of Rib 7			
North face		South face	
CH	Measured Stress (ksi)	CH	Measured Stress (ksi)
1084	2.3	1087	1.8
1085	2.8	1088	2.5
1086	3.3	1089	0.6
1300	0.3	1301	2.5
1302	0.4	1303	0.1
1304	0.5	1305	1.2
1306	0.4	1307	1.1

Bulkhead Plate	
South face	
CH	Measured Stress (ksi)
1022	1.7
1023	1.6
1024	0.4
1025	0.8

East of Rib 7			
North face		South face	
CH	Measured Stress (ksi)	CH	Measured Stress (ksi)
1078	2.2	1081	2.4
1079	3.8	1082	3.7
1080	4.8	1083	6.5
1292	2.2	1293	4.0
1294	N/A	1295	0.3
1296	N/A	1297	1.5
1298	N/A	1299	1.2

Figure 184 Stress ranges on SFB1 around Rib 7 cutout and on the bulkhead plate in Rib 7 for Phase 2B static test

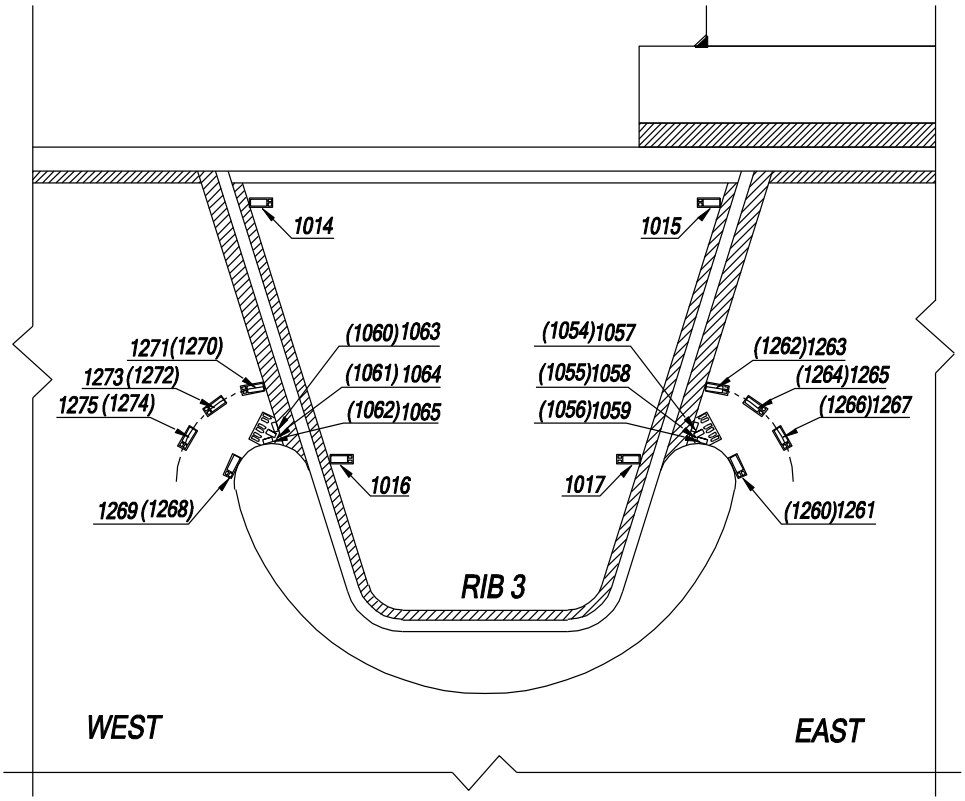

View looking north (showing south face); Gauges on the north face are identified in parentheses

West of Rib 3			
North face		South face	
CH	Measured Value (ksi)	CH	Measured Value (ksi)
1060	-7.0	1063	-6.4
1061	-11.2	1064	-10.7
1062	-16.5	1065	-17.2
1268	-7.4	1269	-9.7
1270	-1.8	1271	-2.3
1272	-2.4	1273	-2.8
1274	-1.3	1275	-2.5

Bulkhead Plate	
South face	
CH	Measured Value (ksi)
1014	7.1
1015	-7.0
1016	-5.0
1017	4.9

East of Rib 3			
North face		South face	
CH	Measured Value (ksi)	CH	Measured Value (ksi)
1054	6.8	1057	7.7
1055	10.6	1058	12.7
1056	14.2	1059	15.2
1260	2.8	1261	1.7
1262	1.0	1263	1.9
1264	0.9	1265	0.6
1266	-1.9	1267	-1.7

Figure 185 Measured maxima of stresses on SFB1 around Rib 3 cutout and on the bulkhead plate in Rib 3 for January 29, 2009 static test

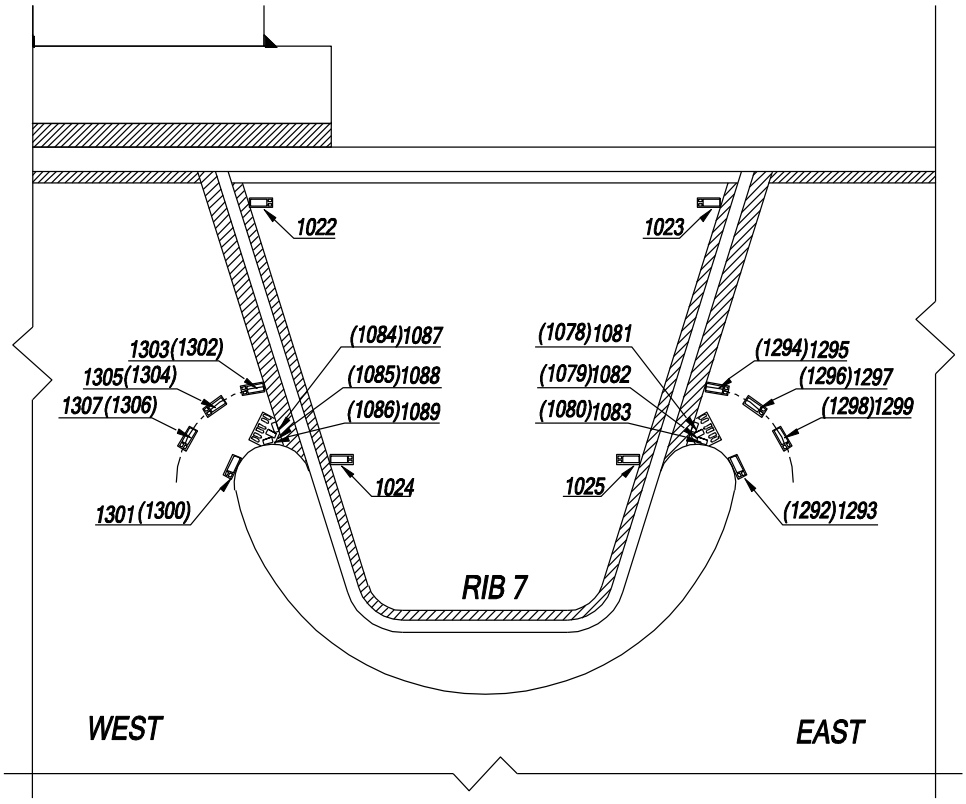

View looking north (showing south face); Gauges on the north face are identified in parentheses

West of Rib 7			
North face		South face	
CH	Measured Value (ksi)	CH	Measured Value (ksi)
1084	6.5	1087	6.4
1085	10.6	1088	10.2
1086	13.3	1089	13.0
1300	2.3	1301	1.9
1302	1.4	1303	1.1
1304	0.9	1305	-1.3
1306	-1.6	1307	-1.2

Bulkhead Plate	
South face	
CH	Measured Value (ksi)
1022	-7.1
1023	4.9
1024	2.2
1025	-1.4

East of Rib 7			
North face		South face	
CH	Measured Value (ksi)	CH	Measured Value (ksi)
1078	-6.4	1081	-6.1
1079	-10.8	1082	-9.7
1080	-15.3	1083	-13.9
1292	-6.8	1293	-6.8
1294	-2.7	1295	-0.7
1296	-2.7	1297	-2.4
1298	-1.2	1299	-1.5

Figure 186 Measured maxima of stresses on SFB1 around Rib 7 cutout and on the bulkhead plate in Rib 7 for January 29, 2009 static test

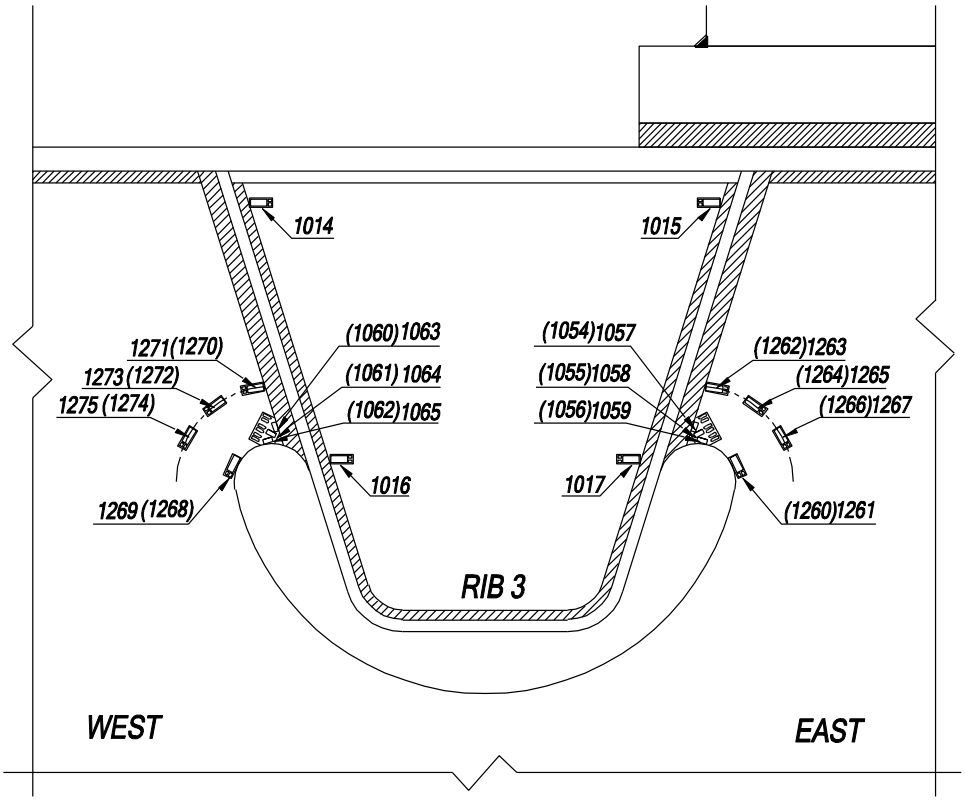

View looking north (showing south face); Gauges on the north face are identified in parentheses

West of Rib 3			
North face		South face	
CH	Stress Range (ksi)	CH	Stress Range (ksi)
1060	-6.2	1063	-5.6
1061	-10.0	1064	-9.4
1062	-14.8	1065	-15.3
1268	-6.8	1269	-8.8
1270	-1.8	1271	-2.1
1272	-2.2	1273	-2.5
1274	-1.6	1275	-2.3

Bulkhead Plate	
South face	
CH	Stress Range (ksi)
1014	6.4
1015	-6.2
1016	-4.4
1017	4.4

East of Rib 3			
North face		South face	
CH	Stress Range (ksi)	CH	Stress Range (ksi)
1054	6.0	1057	6.9
1055	9.4	1058	11.3
1056	12.6	1059	13.8
1260	2.5	1261	2.8
1262	0.9	1263	1.7
1264	1.1	1265	1.2
1266	-2.4	1267	-1.5

Figure 187 Stress ranges at gauges on SFB1 around Rib 3 cutout and on the bulkhead plate in Rib 3 for January 29, 2009 static test

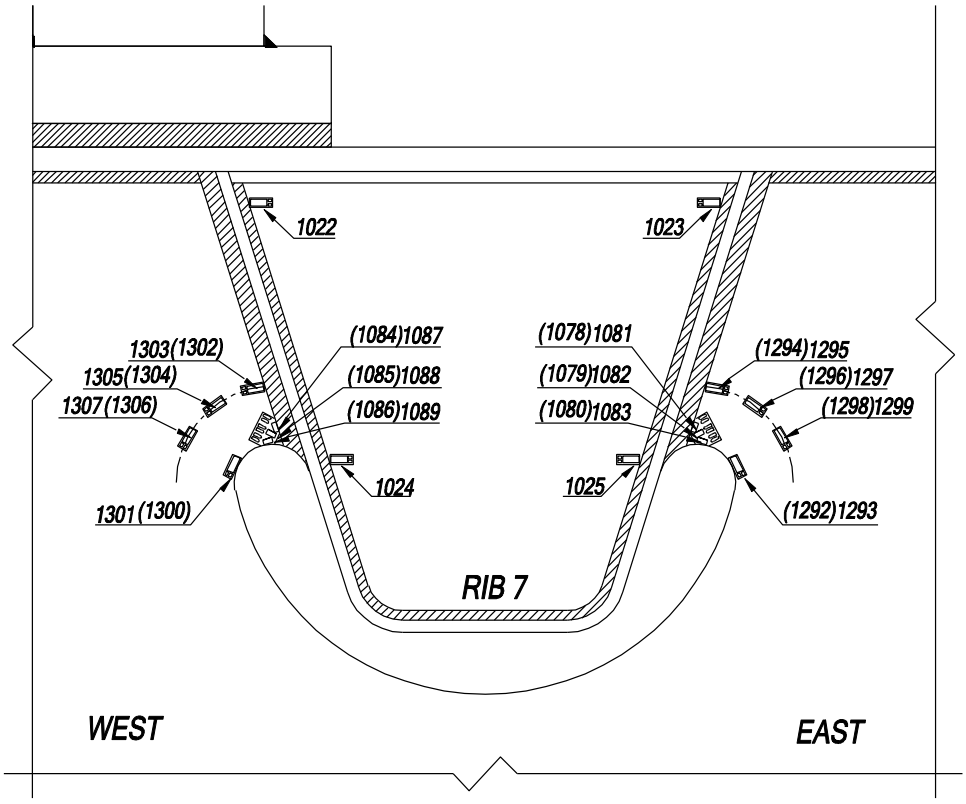

View looking north (showing south face); Gauges on the north face are identified in parentheses

West of Rib 7			
North face		South face	
CH	Stress Range (ksi)	CH	Stress Range (ksi)
1084	5.7	1087	5.7
1085	9.3	1088	9.1
1086	11.8	1089	11.8
1300	2.3	1301	3.3
1302	1.3	1303	1.1
1304	1.0	1305	-1.1
1306	-2.1	1307	-1.2

Bulkhead Plate	
South face	
CH	Stress Range (ksi)
1022	-6.4
1023	4.3
1024	2.1
1025	-1.3

East of Rib 7			
North face		South face	
CH	Stress Range (ksi)	CH	Stress Range (ksi)
1078	-5.7	1081	-5.4
1079	-9.1	1082	-8.6
1080	-13.7	1083	-12.2
1292	-6.5	1293	-6.1
1294	-2.4	1295	-0.6
1296	-2.5	1297	-2.2
1298	-1.6	1299	-2.0

Figure 188 Stress ranges at gauges on SFB1 around Rib 7 cutout and on the bulkhead plate in Rib 7 for January 29, 2009 static test

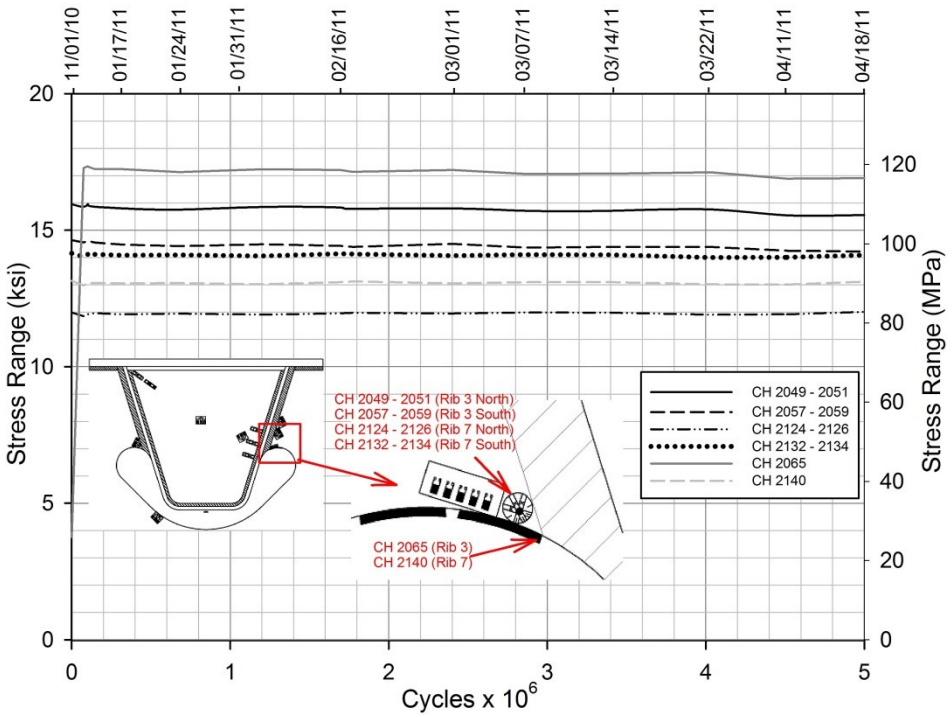

Figure 189 Change in stress ranges at the cutouts for ribs 3 and 7 obtained from the intermittent static tests during Phase 2A testing

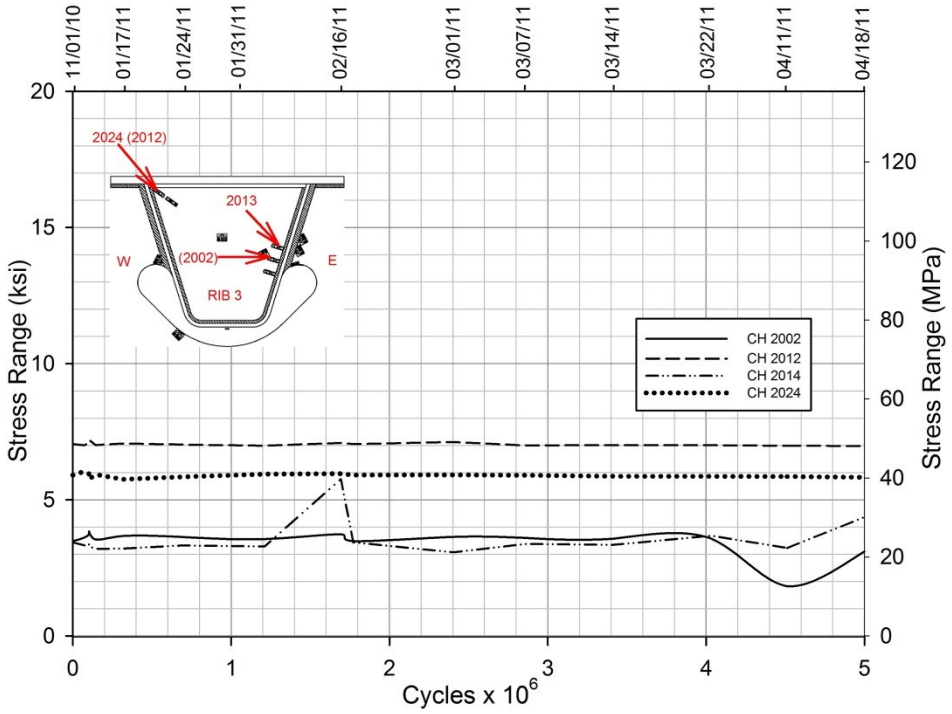

Figure 190 Change in stress ranges at Rib 3 bulkhead plate obtained from the intermittent static tests during Phase 2A testing

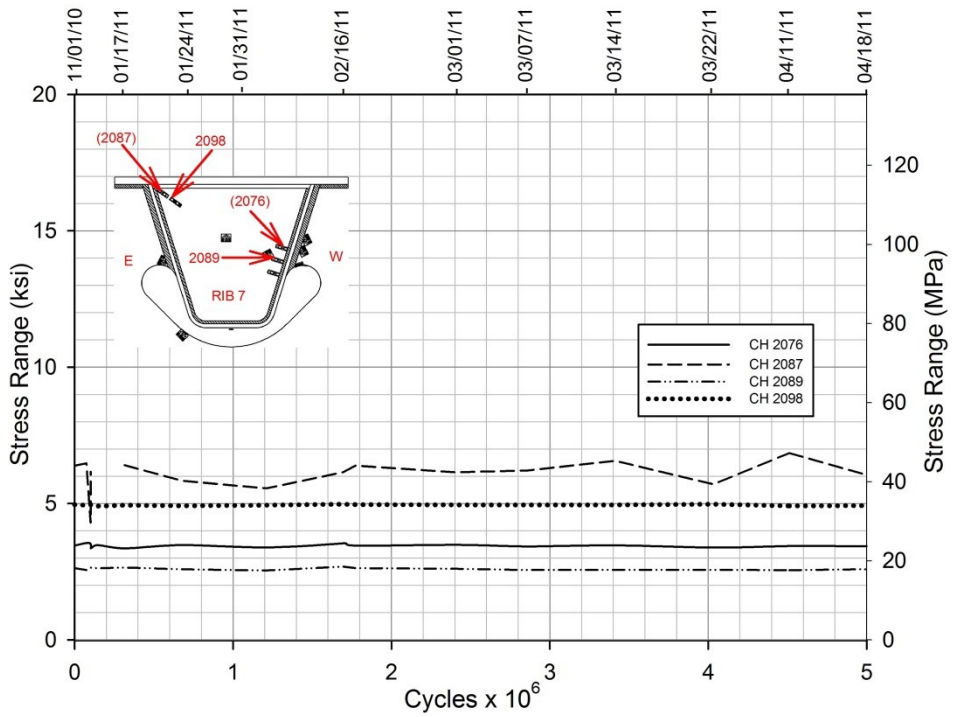

Figure 191 Changes in stress ranges at Rib 7 bulkhead plate obtained from the intermittent static tests during Phase 2A testing

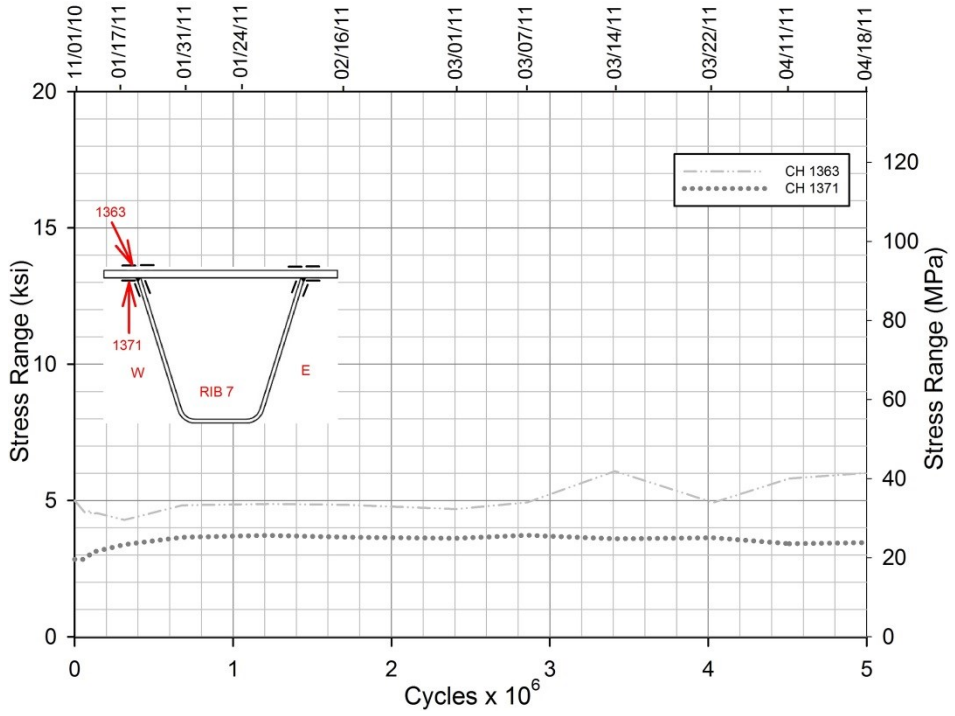

Figure 192 Change in stress ranges at the deck plate gauges to the west of Rib 7 obtained from the intermittent static tests during Phase 2A testing

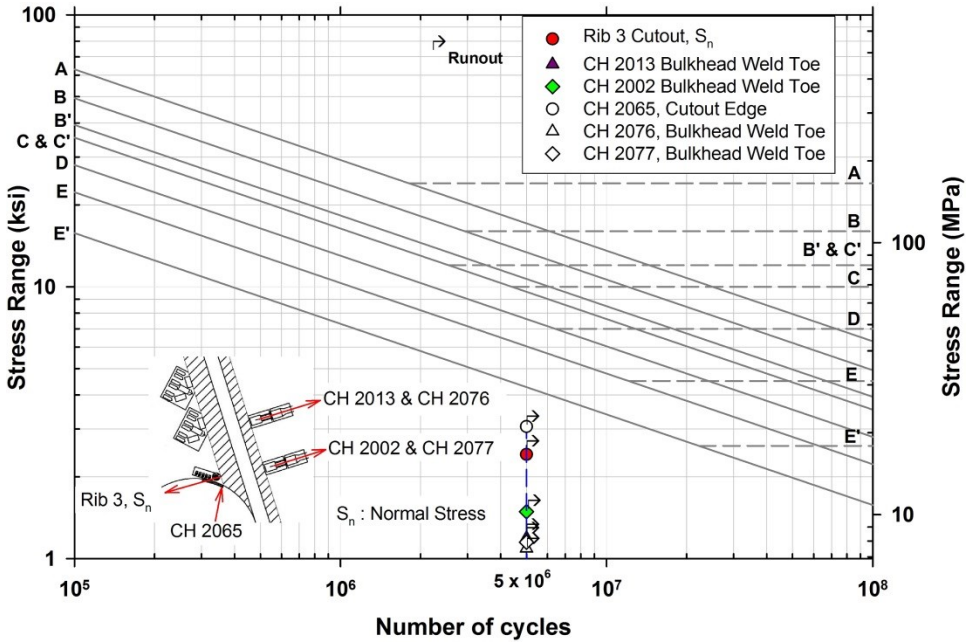

Figure 193 SN plot for Phase 2A fatigue test results at the critical details

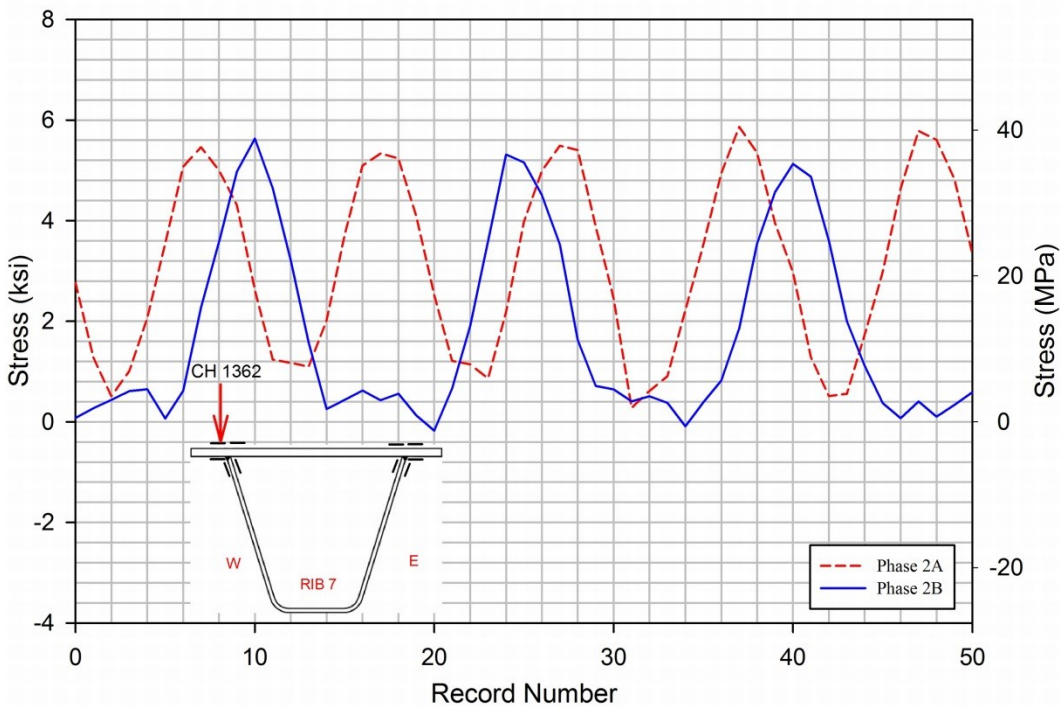

Figure 194 Comparison of normal stress at the gauge on top of the deck plate between Phase 2A and Phase 2B

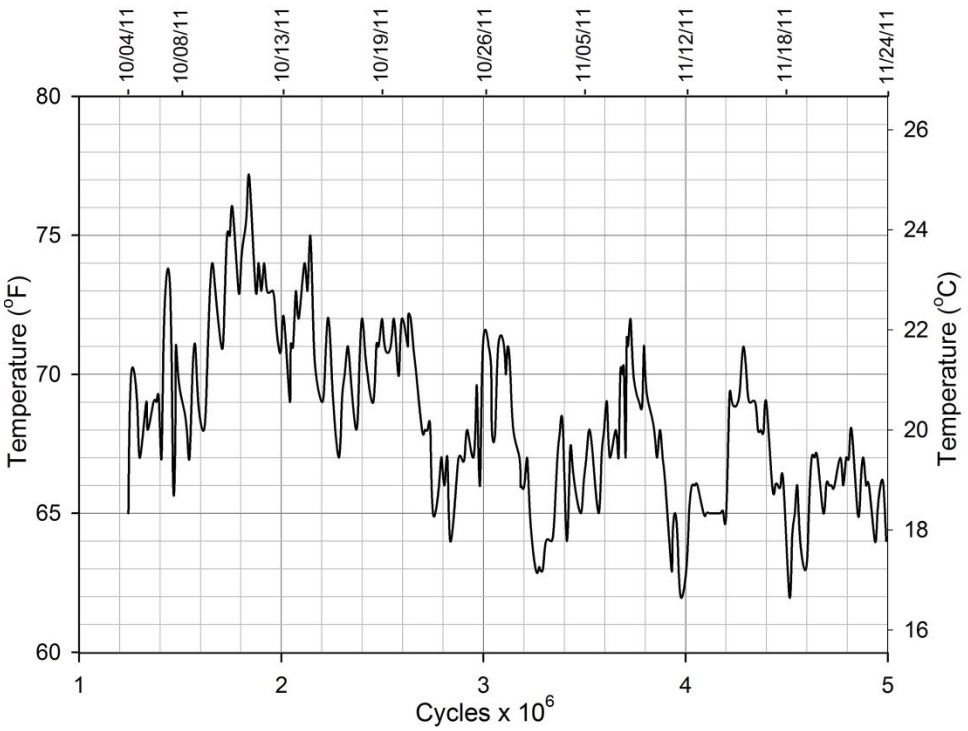

Figure 195 Temperature variation of the deck specimen in Phase 2B

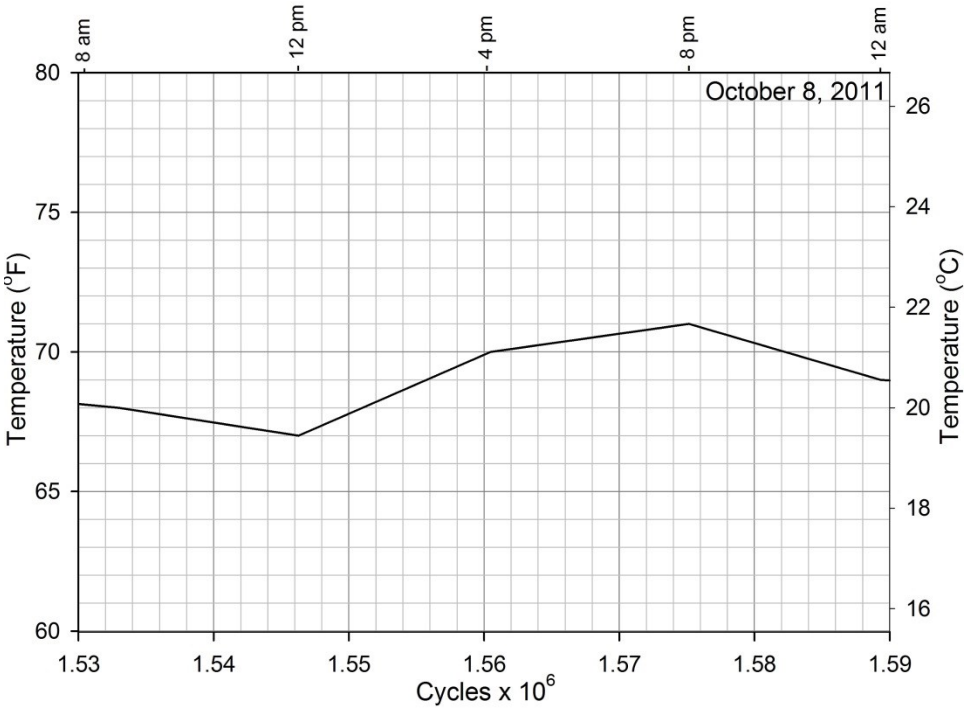

Figure 196 Temperature variation of the deck recorded on October 8, 2011

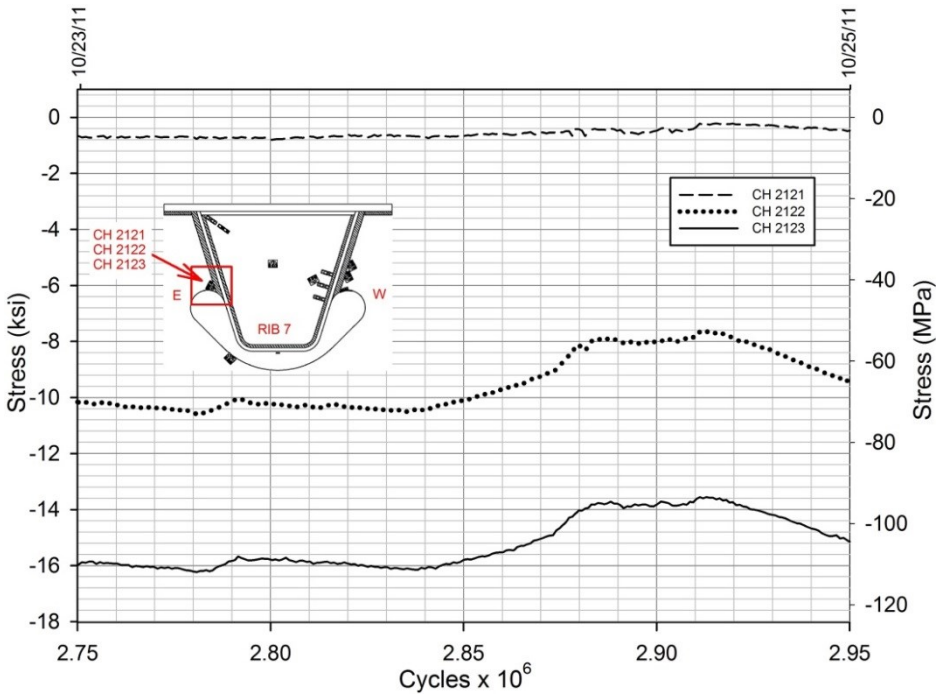

Figure 197 Fluctuations observed at the rosette gauge to the east cutout for Rib 7 on south face of SFB2a

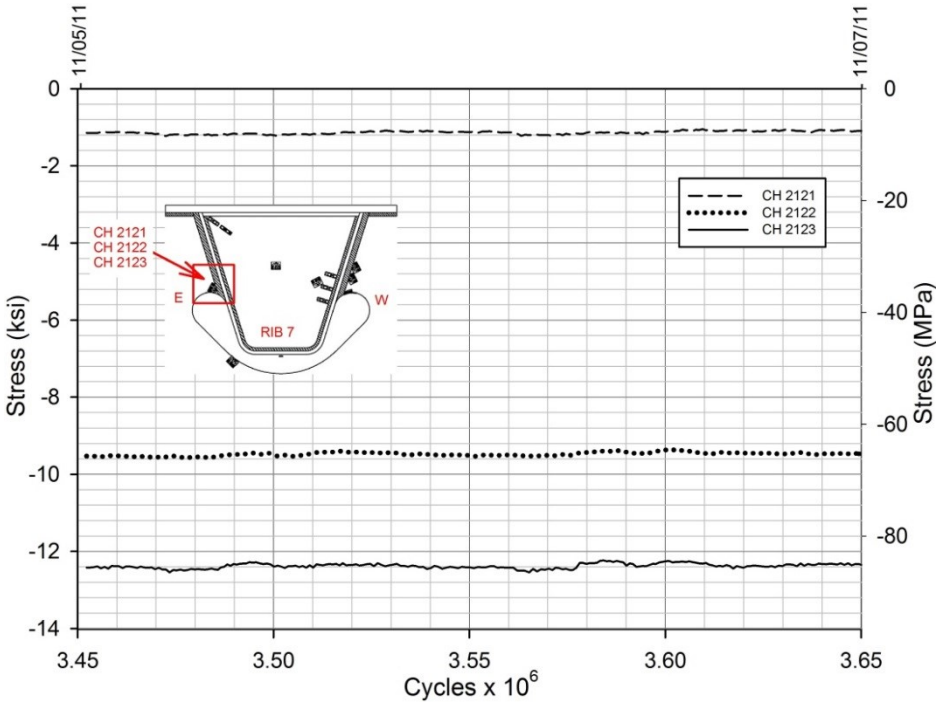

Figure 198 Response of the rosette gauges to the east of cutout for Rib 7 on south face of SFB2a after replacement

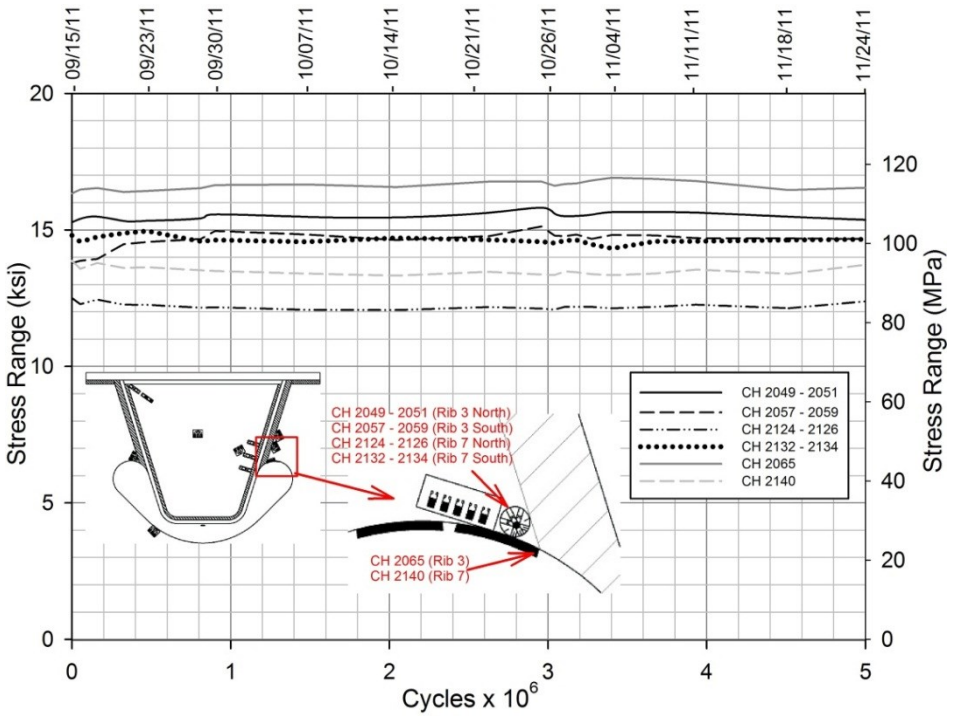

Figure 199 Change in stress ranges at the rosette gauges and strip gauges adjacent to the cutouts for ribs 3 and 7 during Phase 2B testing

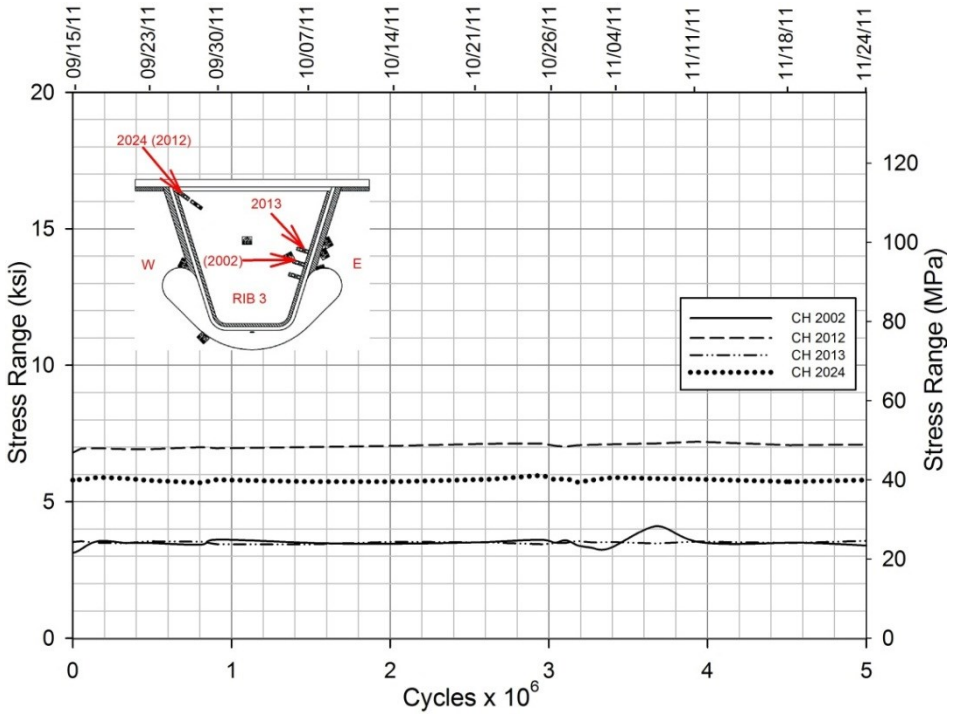

Figure 200 Changes in static test stress ranges on the bulkhead plate gauges at Rib 3 during Phase 2B testing

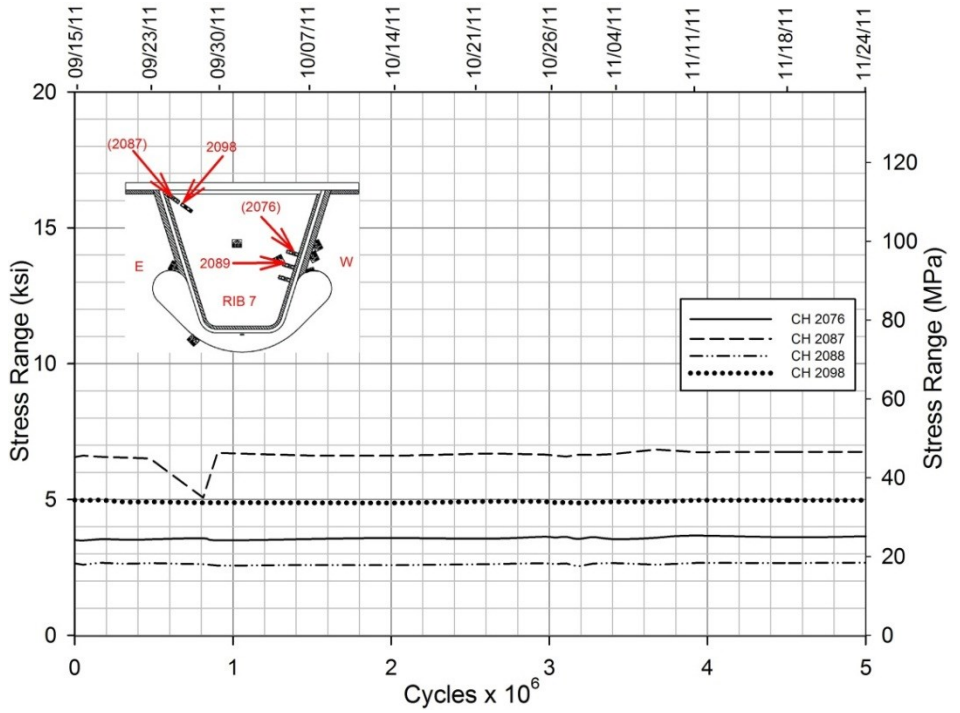

Figure 201 Changes in static test stress ranges on the bulkhead plate gauges at Rib 7 during Phase 2B testing

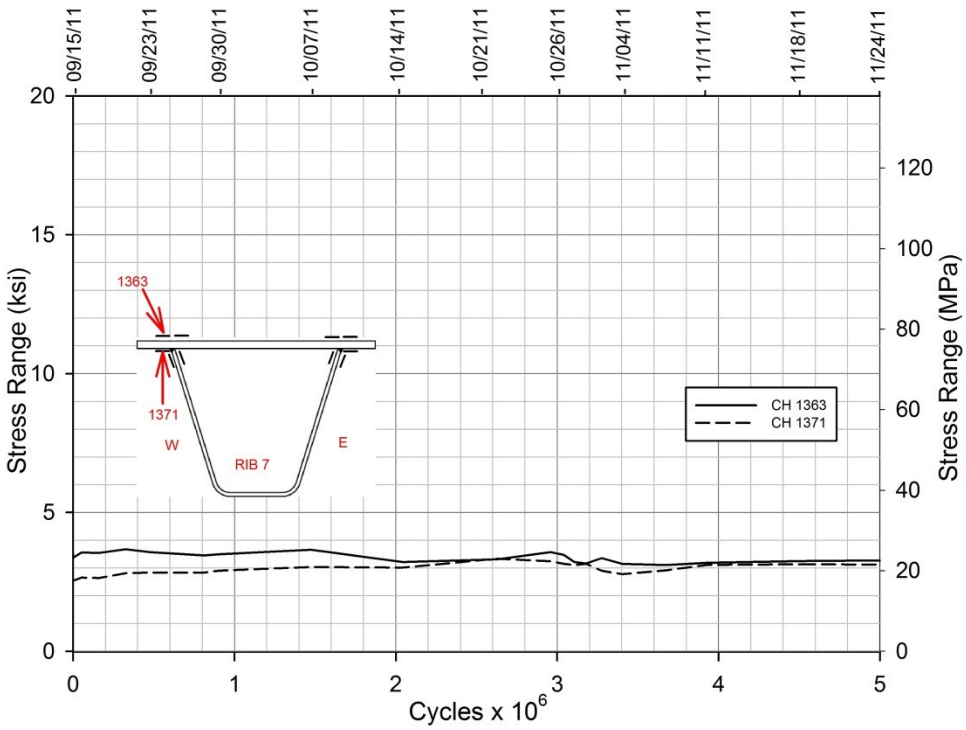

Figure 202 Changes in static test stress ranges at the deck plate gauges to the west of Rib 7 during Phase 2B testing

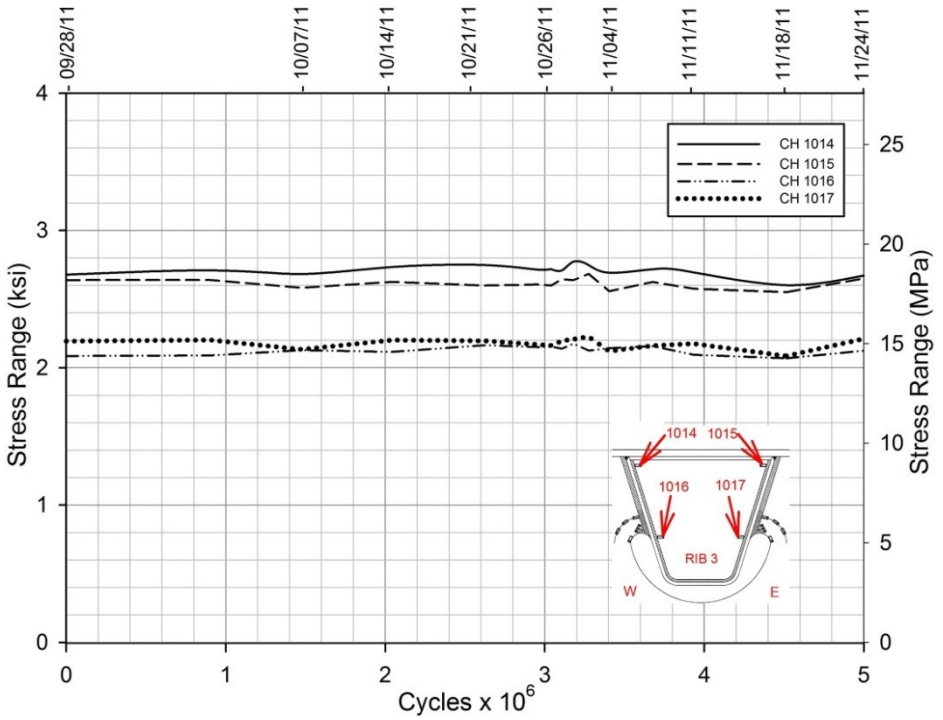

Figure 203 Changes in static test stress ranges on the bulkhead plate gauges on SFB 1 at Rib 3 during Phase 2B testing

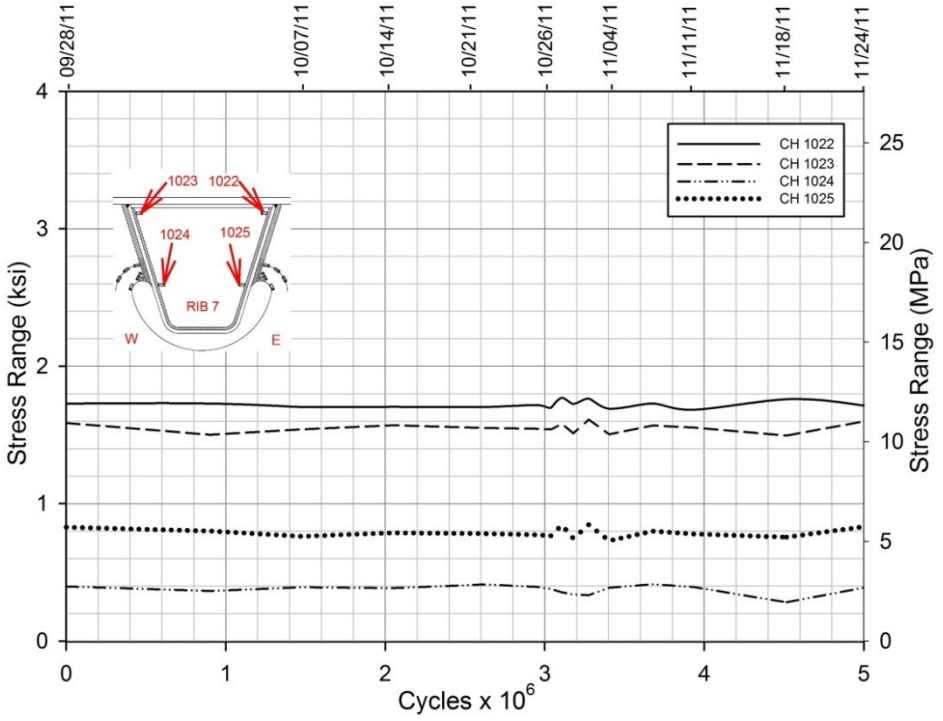

Figure 204 Changes in static test stress ranges on the bulkhead plate gauges on SFB1 at Rib 7 during Phase 2B testing

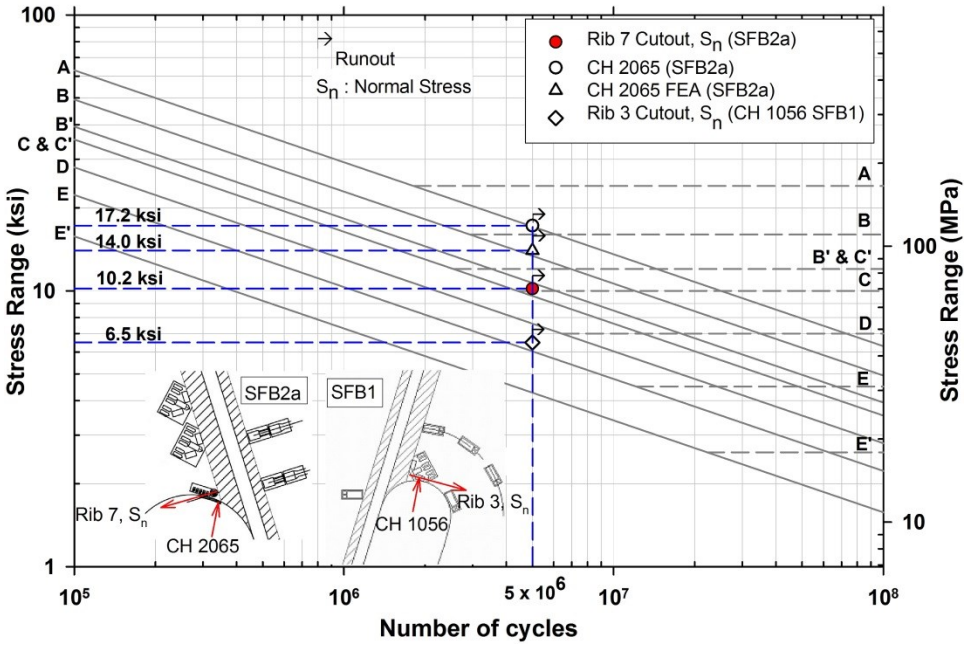

Figure 205 Assessment of fatigue performance of the rib-to-SFB2a connection

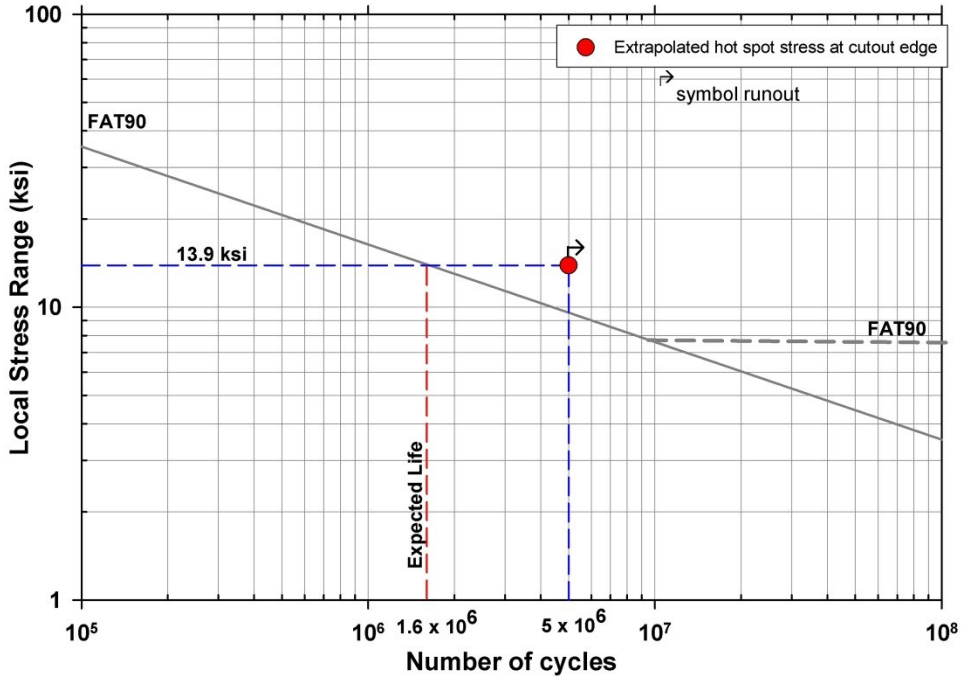

Figure 206 Evaluation of fatigue performance of cutout edge at the rib-to-SFB2a connection

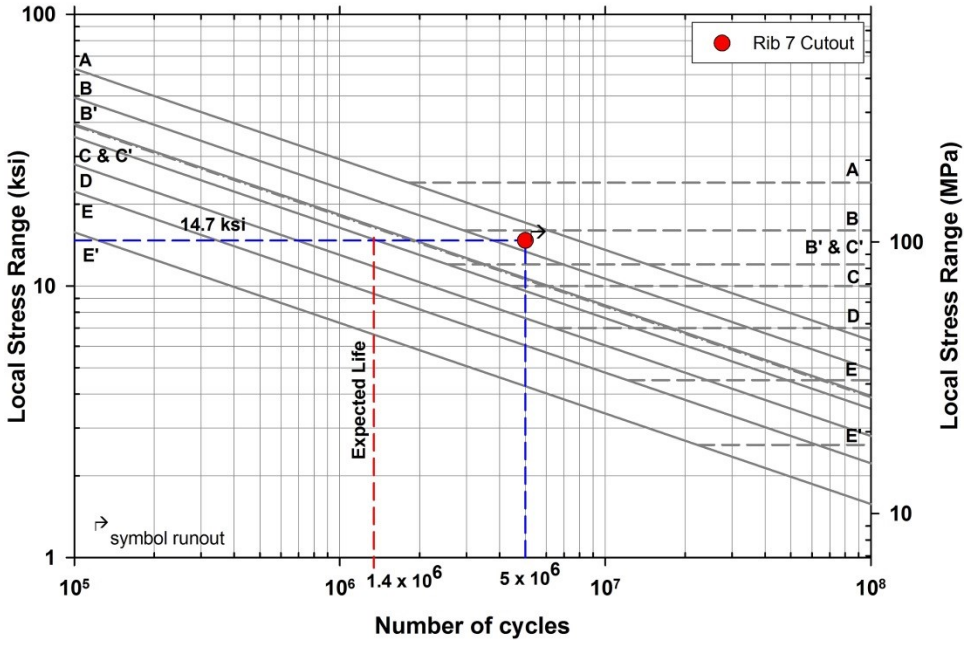

Figure 207 Evaluation of fatigue performance of rib-to-SFB2a weld connection as per AASHTO recommendations

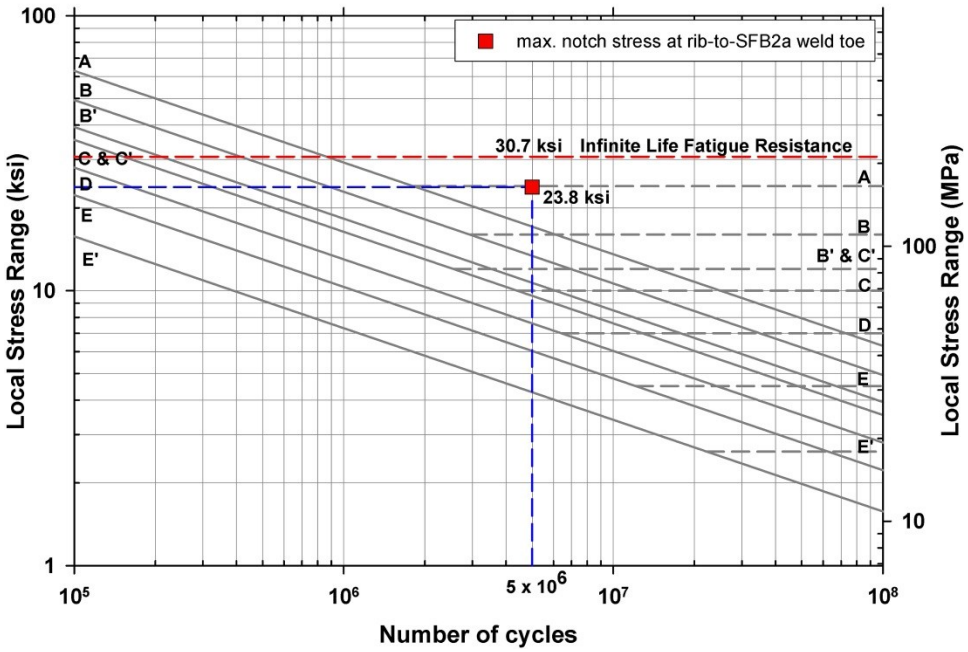

Figure 208 Evaluation of fatigue performance of rib-to-SFB2a weld connection using notch stress approach

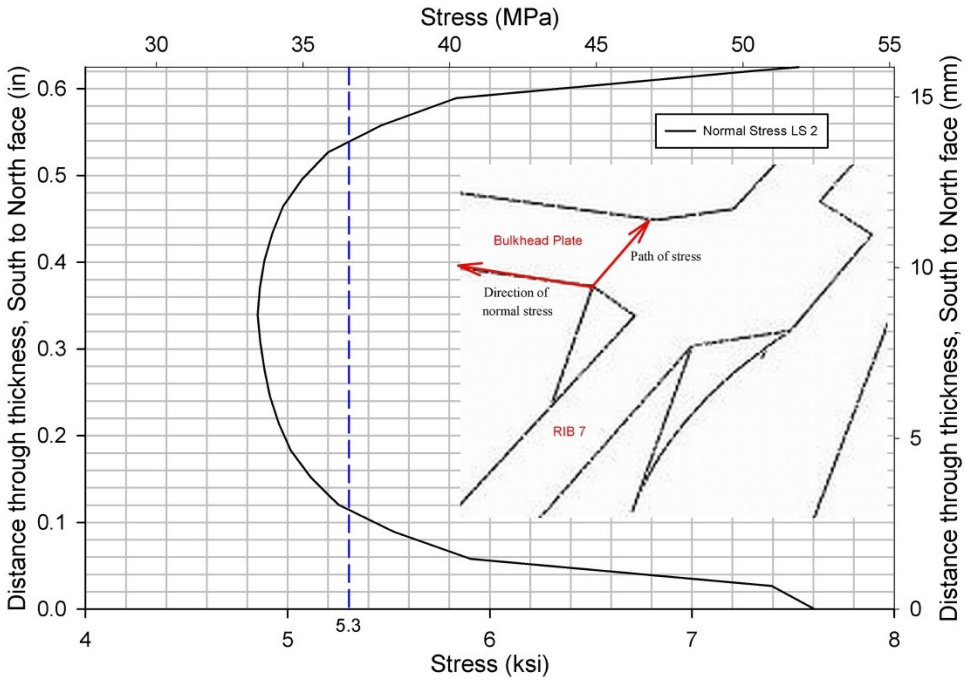

Figure 209 The through thickness stress distribution at Rib 7 rib-to-bulkhead plate weld toe showing mean stress

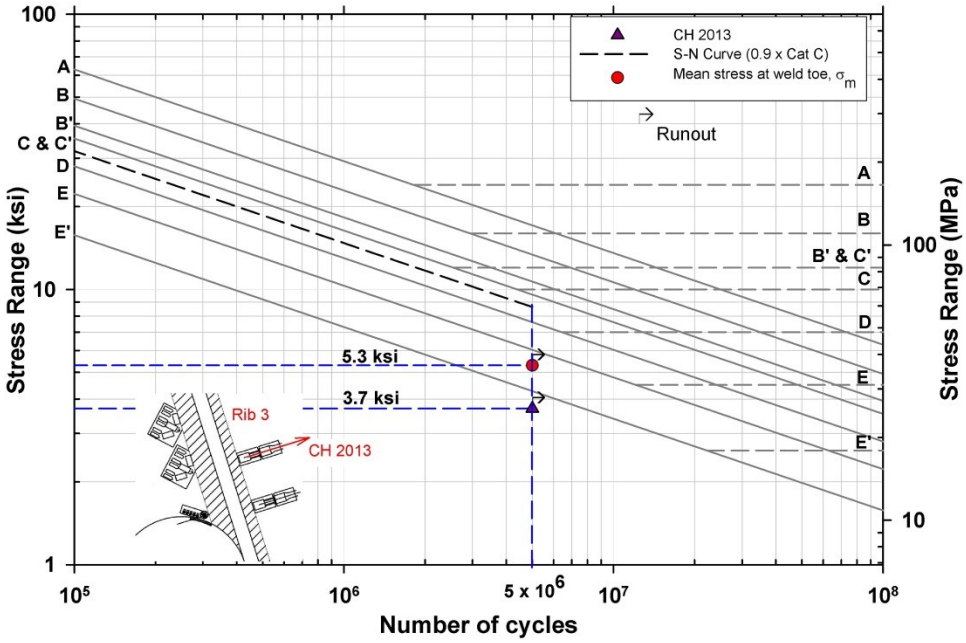

Figure 210 Assessment of fatigue performance of the rib-to-bulkhead plate connection at the intermediate subfloor beam

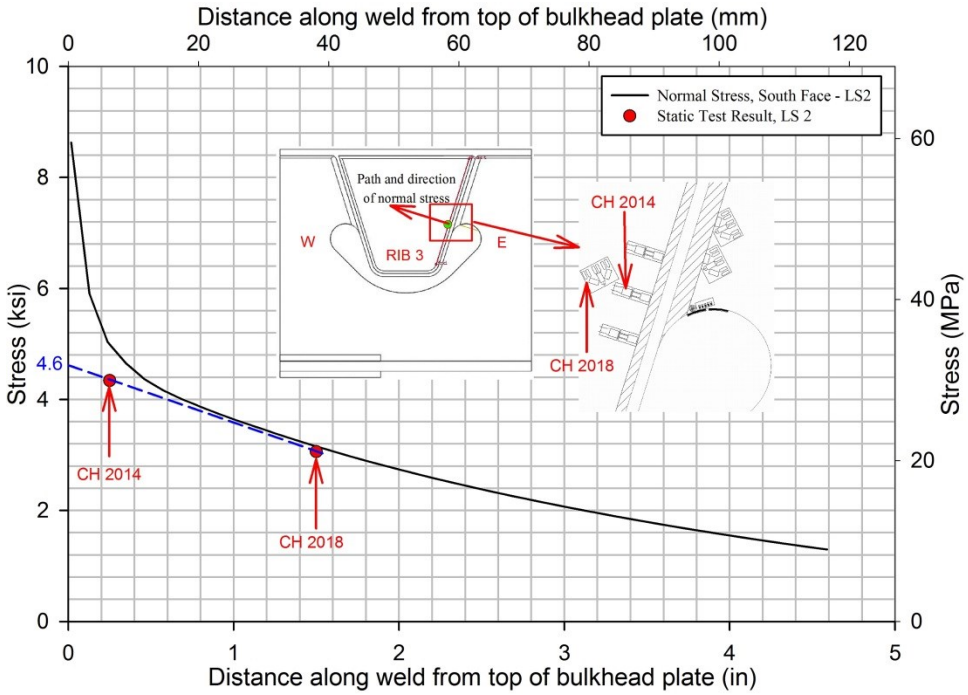

Figure 211 Comparison of measured stresses with the FEA results at Rib 3 for static LS-2

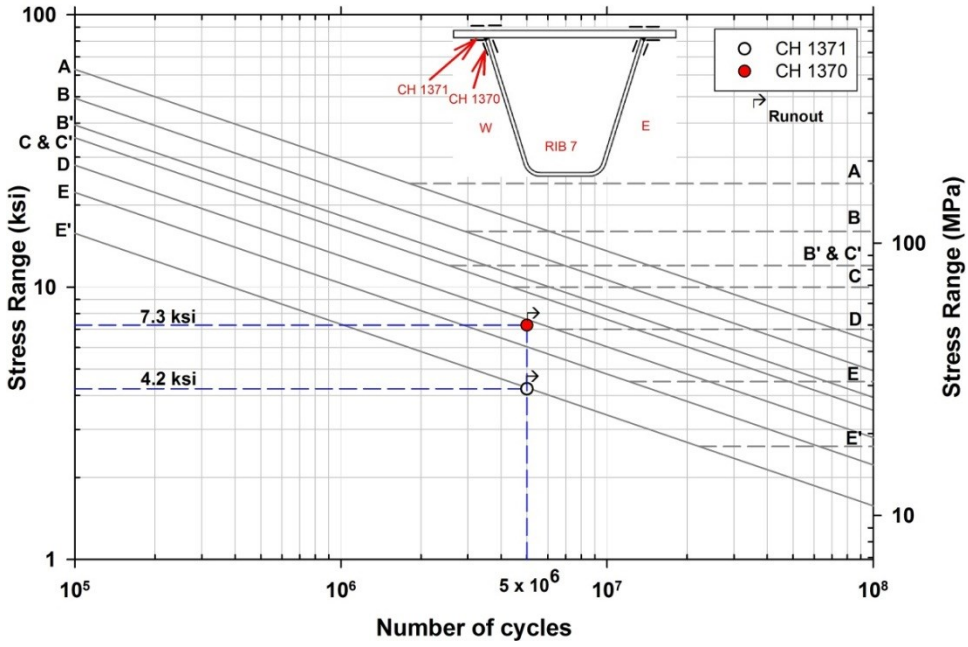

Figure 212 Assessment of fatigue performance of rib-to-deck plate connection for Phase 1 testing

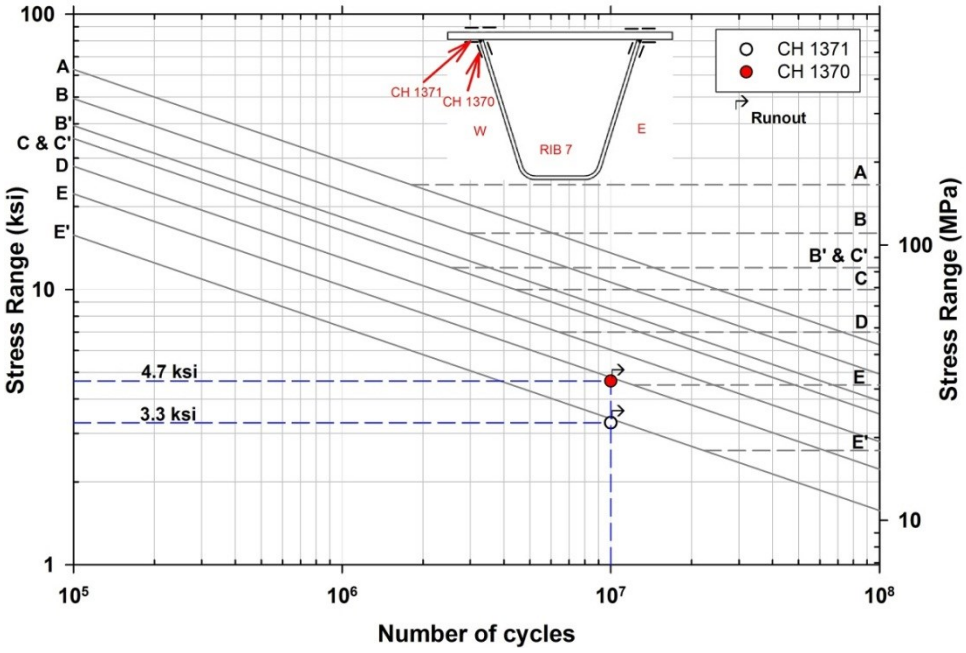

Figure 213 Assessment of fatigue performance of rib-to-deck plate connection for Phase 2 testing

REFERENCES

Alapati, R. S. D. (2012), Fatigue Evaluation of Replacement Orthotropic Deck for a Signature Bridge, M.S. Thesis, Department of Civil and Environmental Engineering, Lehigh University, Bethlehem, PA.

American Association of State Highway and Transportation Officials (AASHTO). LRFD Bridge Design Specifications. Washington D.C., 2010

Banantine, J. A., Comer, J. J., Handrock, J. L. (1990), *Fundamentals of Metal Fatigue Analysis*, Prentice Hall, Inc., Engelwood Cliffs, NJ.

Cook, R. D., Malkus, D. S., Plesha, M. E., Witt, R. J., (2002), *Concepts and Applications of Finite Element Analysis, 4th ed.*, John Wiley & Sons, Inc., Hoboken, NJ.

Fricke, W., Bogdan, R. (2001), Determination of Hot Spot Stress in Structural Members with In-Plane Notches Using a Coarse Element Mesh: IIW document XIII-1870-01

Fricke, W., Sabel, A. (2000). *Hot spot stress analysis of five structural details and recommendations for modeling, stress evaluation and design S-N curve. (Report No. FF99.188)*, Germanischer Lloyd, Germany

Healy, B. (2004), *Hot Spot Stress Analysis of a Side Shell Connection Using Surface Extrapolation and the Battelle Structural Stress Method*, Paper No. OMAE-FPSO'04-0022, Proceedings of OMAE Specialty Conference on Integrity of Floating Production, Storage & Offloading (FPSO) Systems, Aug. 30-Sept. 2, 2004, Houston, TX

Higgins, C., and Nguyen, Q.D. (2009), *Digital image rectification tool for metrification of gusset plate connections in steel truss bridges*. Oregon State University, Corvallis, OR

Hobbacher, A. 2007. *Recommendations for Fatigue Design of Welded Joints and Components*, IIW document XIII-2151-07 / XV-1254-07, ex XIII-1965r18-03 / XV-1127r18-03.

Kaczinski, M.R., Stokes, F.E., Lugger, P., and Fisher, J.W. 1997. *Williamsburg Bridge orthotropic deck fatigue test. ATLSS Report No. 97-04.* Bethlehem, PA: ATLSS Engineering Research Center, Lehigh University.

Logan, D. L. (2007), *A First Course in the Finite Element Method, 4th ed.*, Thomson, Toronto, Ontario, Canada.

Marshall, P.W., and Wardenier, J. 2005. *Tubular versus non-tubular hot spot stress methods*. *Proceeding of the 15th International Offshore and Polar Engineering Conference*, ISOPE-2005, June 19-24, Seoul.

Radaj D., Sonsino C.M., Fricke, W. (2006), *Fatigue Assessment of Welded Joints by Local Approaches, 2nd ed.*, Woodhead Publishing Limited, Cambridge, England.

Roy, S. and Fisher, J.W. 2005. *Enhancing fatigue strength by Ultrasonic Impact Treatment*. *International Journal of Steel Structures*, 5(3), 241–252.

Roy, S., Alapati, R.S.D., Manandhar, N.K., Molina, M.A. (2012), *Fatigue Resistance Investigation for the Replacement Orthotropic Deck at the Verrazano Narrows Bridge – Phase 1, ATLSS Report No. 12-01*, Lehigh University, Bethlehem, PA.

Tsakopoulos, P.A., and Fisher, J.W. 2003. *Full-scale fatigue tests of steel orthotropic decks for the Williamsburg Bridge*. *Journal of Bridge Engineering,* 8(5), 323-333.

Tsakopoulos, P.A., and Fisher, J.W. 2005. *Full-scale fatigue tests of steel orthotropic deck panel for the Bronx-Whitestone Bridge rehabilitation*. *Bridge Structures,* 1(1), 55.

Vishay Micro-Measurements Tech Note TN 515 (2007), *Strain Gage Rosettes: Selection, Application and Data Reduction*, www.vishaymg.com

APPENDIX A Determination of Correct Placement of Gauges at Sub-floor Beam Cutout Termination

A.1 Background

As discussed in Chapter 4, a multi-axial stress state including a high stress concentration existed in the subfloor beams, adjacent to the cutout terminations on the rib wall, which rendered the subfloor beam-to-rib welded connection at the cutout termination sensitive to fatigue cracking. To quantify the tensile stress concentration and the principal stresses, stacked rosette gauges of 1 mm gauge length were planned to be installed in a back-to-back configuration, adjacent to the cutout terminations to the west of Rib 7 and to the east of Rib 3 as close to the weld toe and the cutout as possible (Figures Figure 81and 83). One of the rectangular rosette arms (identified as Gauge 1 in Figure 85) was planned to be at 55^{o} with respect to the rib-to-subfloor beam weld toe. This would provide a reference frame for the measured principal stresses and would allow estimation of the stresses normal to the weld toe by transformation.

Inadvertently, however these 1 mm rosettes were installed in arbitrary orientations (Figures 165 to 168). While this arbitrary orientation of the rosettes did not have any impact on the measured principal stresses and their directions (due to invariance), the reference frame for the principal stress direction was lost and the stress normal to the rib-to-subfloor beam weld toe could not be readily determined. In addition, since the gauges were installed in a stress field of high gradient, accurate determination of the gauge location was necessary for improved correlation with the FEA results. As such, further investigation was necessary to determine the as-installed location and orientation of these rosette gauges.

Three distances and an angle with respect to a fixed reference frame were needed for accurately determining the as-installed location and orientation of the gauges. As shown in Figure 169, the horizontal distance from the weld termination on the cutout (h), the vertical distance from the weld termination on the cutout (v), and the perpendicular distance of the gauge center from the weld toe (d) were chosen for determining the as-installed location of the gauges. The angle, β, between the normal to the weld toe and the first arm of the rosette gauge (identified as Gauge 1) was considered for determining the as-installed orientation of the gauges.

The relationships used to estimate the principal stresses, and their directions from the measurements are shown in the following (Vishay 2007). The maximum and minimum principal strains (ε_P and ε_Q, respectively) were calculated from the measured strains at the rosette gauges as:

$$\varepsilon_{P,Q} = \frac{\varepsilon_1 + \varepsilon_3}{2} \pm \frac{1}{\sqrt{2}} \sqrt{(\varepsilon_1 - \varepsilon_2)^2 + (\varepsilon_2 - \varepsilon_3)^2} \tag{A1}$$

where, ε_1, ε_2 and ε_3 are respectively the strain measurements at Gauge 1, Gauge 2 and Gauge 3 of the rosette.

The maximum and minimum principal stresses (σ_P and σ_Q) were then calculated as:

$$\sigma_P = \frac{E}{1-\nu^2}\left(\varepsilon_P - \nu\varepsilon_Q\right) \tag{A2}$$

$$\sigma_Q = \frac{E}{1-\nu^2}\left(\varepsilon_Q - \nu\varepsilon_P\right) \tag{A3}$$

where, E is the modulus of elasticity and v is the Poisson's ratio.

The direction of principal stresses ($\phi_{P,Q}$) with respect to Gauge 1 was obtained as:

$$\phi_{P,Q} = \frac{1}{2}\tan^{-1}\left(\frac{2\varepsilon_2 - \varepsilon_1 - \varepsilon_3}{\varepsilon_1 - \varepsilon_3}\right) \quad \text{(A4)}$$

The principal stress angle was measured from the first gauge arm (Gauge 1 counted in counterclockwise direction. If $\phi_{P,Q}$ was positive the principal stress direction was counterclockwise, and if negative, it was clockwise. To identify whether the direction given by $\phi_{P,Q}$ was the direction of maximum (ϕ_P) or minimum (ϕ_Q) principal stress direction, the following rules were followed:

(a) If $\varepsilon_1, > \varepsilon_3$, then $\phi_{P,Q} = \phi_P$

(b) If $\varepsilon_1, < \varepsilon_3$, then $\phi_{P,Q} = \phi_Q$

(c) If $\varepsilon_1, = \varepsilon_3$ and $\varepsilon_1, < \varepsilon_3$, then $\phi_{P,Q} = \phi_P = -45°$

(d) If $\varepsilon_1, > \varepsilon_3$ and $\varepsilon_1, > \varepsilon_3$, then, $\phi_{P,Q} = \phi_P = +45°$

(e) If $\varepsilon_1, = \varepsilon_2 = \varepsilon_3$, then $\phi_{P,Q}$ is indeterminate

The stresses in any other direction could be calculated after the magnitude and direction of principal stresses are determined. Once the orientations of the as-installed gauges with respect to the weld toe were known, the directions of principal stresses could be determined and the stresses normal to the weld toes could be estimated.

The location and orientation of the as-installed gauges could be roughly estimated from physical measurements; however, measuring instruments could not be used due to limited access at the densely gauged location. As such, measurements were made from photographic images of the gauged location. Initially, photographs of the locations of interest were imported into AutoCAD®, a commercially available CAD software. These images were scaled to size and the desired dimensions were measured. Although it was relatively convenient, the measurements

were not accurate due to parallax as it was not possible to photograph gauged locations with the camera positioned normal to the gauges. Accordingly, an image rectification code developed by Higgins and Nguyen (2009) for collecting dimensional data of gusset plates in truss bridges, was suitably modified and used for rectifying the skewed images. The location and orientation of the gauges were then measured from the rectified images after importing them into AutoCAD®. The original code for image rectification of gusset plates was developed in MATLAB®, a commercially available technical computing language, utilizing the Image Processing Toolbox for MATLAB®. The code was provided by the lead author Dr. Christopher C. Higgins of Oregon State University for the current study (personal communication with Dr. Sougata Roy)

The image rectification algorithm implemented by Higgins and Nguyen (2009) involved processing of generic digital images of any perspective to rectified images in normal projection from which dimensional data could be digitally extracted. Higgins and Nguyen implemented the image rectification technique for measuring large gusset plates located at a considerable distance from the camera. The methodology required specially designed cruciform reference targets of 8 in. (203 mm) or 24 in. (610 mm), superimposed on the photographed object. The current study, however, involved obtaining measurements of small rosette gauges from photographs taken at close ranges. The reference targets designed for measuring gusset plates were too large for the purpose. Accordingly, modifications were made to reference target and the MATLAB® code.

A.2 Technique Implemented by Higgins and Nguyen

The generic photographic images provide with the perspective view of the real world objects on a photographic plane with respect to the camera lens. The dimension and orientation

of the objects on the photographs are relative to their positions from the camera. Mathematical transformation of mapping elements on a desired plane of the photograph can be used to develop orthographically projected or rectified image by removing perspective. Higgins and Nguyen implemented one of the most common techniques for image rectification, the direct linear transformation (DLT) algorithm, which solves a set of variables with respect to a set of similarity relations for the rectification process.

DLT requires that certain geometrical characteristics be established between the desired plane or the real plane and the photographic or image plane. The image plane and the real planes (Figure A-1) are assumed to be homogeneous. Accordingly as shown in Figure A-2, corresponding points on the image plane are mapped onto the desired real plane based on central projection (Hartley and Zisserman, 2000). With this point to point mapping, a line in one plane is also mapped to a line in another. In homogenous coordinates on each plane, the central projection mapping can be expressed as follows:

$$x' = Hx \tag{A5}$$

where x and x' are points in real and image planes, respectively, and H is a non-singular 3×3 transformation matrix.

A minimum of four control points are needed (x and y coordinates each provide a degree-of freedom (DOF) for a total of eight DOFs and one more is provided by scale, thereby providing nine DOFs to solve for the matrix). If more points are available, error estimation can be made, as described subsequently.

Nine relationships are necessary to solve for the elements of the transformation matrix H.

Each mapped point provides two degrees of freedom (x and y coordinates). Three control points can provide six DOFs for an affine image rectification in which parallel lines are rectified but the angles between intersecting lines are not (eg. a square when rectified can look like a rhombus). Four points providing eight DOFs are necessary for rectifying the angles between the lines. The knowledge of scale is the extra DOF that provides the length ratios of the transformed lines. The scale is used to recover the metric properties from the image. Hence, a minimum four control points and scale are needed for solving the transformation matrix. If more control points are used, the relationships are over constrained and thus error in transformation can be estimated. DLT generates a two–dimensional transformation based solely on the control point coordinates, thus, camera parameters are not needed. Higgins and Nguyen implemented the DLT algorithm using nine control points and a scale for better accuracy and error estimation.

Cruciform reference targets of known scale, affixed on the gusset plates with magnets, were used to establish the geometrical and metric features. The effect of the offset of the reference target from the plane of the object on the true scale was corrected as:

$$Coff = \frac{L}{L-t} \tag{A6}$$

$$L_{cor} = Coff \times L_{mes} \tag{A7}$$

where, L_{mes} is the length measured from the transformed image, L_{cor} is the correct length measurement, L is the distance between the camera and the object, t is the thickness of reference target or the offset, and *Coff* is the scale correction factor..

The detailed step by step procedure for image rectification and measurements using custom reference targets and the MATLAB® code are reported in Higgins and Nguyen (2009).

A.3 Modification to Reference Target

The dimensional measurements to be made for the current study were much smaller than the gusset plates, being of the order of about 1 in. (25 mm). Accordingly, the reference targets had to be scaled down and the MATLAB® code needed to be modified. Due to limited access in the densely gauged region, the reference target was improvised as a 1 in. × 1 in. (25 mm × 25 mm) square with $^1/_4$ in. × $^1/_4$ in. (6 mm × 6 mm) grids printed on a plastic transparency sheet used for projector display. The nine control points were marked at the grid intersections on the axes of symmetry of the square, similar to the cruciform target configuration used by Higgins and Nguyen. As shown in Figure A-3, the transparent reference target was cut into size and mounted over the rosette gauge on the subfloor beam adjacent to the cutout with transparent adhesive tapes (eg. Scotch tapes), which resulted in a reference target practically imprinted on the object. A reference target of 2 in. × 2 in. (51 mm × 51 mm) square with $^1/_2$ in. × $^1/_2$ in. (13 mm × 13 mm) grids was also investigated but not used because the 1 in square reference target was found to be more suitable for the need.

Although reference targets were attached on the subfloor beam web, due to the presence of gauges underneath, a maximum offset of about 0.5 mm to 1 mm existed. As was demonstrated by Higgins and Nguyen and also evident from the hyperbolic relationship in Equation (A6), the effect of the offset is diminished significantly for a relatively larger distance of the object from the camera. For the current study, the distance between the camera and the target was about 13 in. (330 mm). The resulting scale correction factor *Coff* was about 1.002, which was negligible.

A.4 Modification to MATLAB Program

The image rectification algorithm coded in MATLAB® was modified to incorporate the changes made to the reference target. The distance between the control points was changed. In addition, the resolution of the rectified images was increased from 0.04 in/pixel to 0.002 in/pixel. In the code developed by Higgins and Nguyen, the rectified image was limited to 2500×2500 pixels, which produced a maximum image size of 100 in. (2.54 m). Since for the current study the image size was limited to about 1 in. (25 mm), the details on the rectified images were pixelated at the resolution of 0.04 in/pixel. Accordingly, the resolution of the rectified image was modified for more precise identification of the geometric features and accurate measurements thereof. A resolution of 0.002 in/pixel produced a rectified image of maximum 5 in. (127 mm).

A.5 Procedure

The transparent reference target was mounted over the rosette gauge locations of interest (Figure A-3). A Nikon D3000 single lens reflex (SLR) camera was used to photograph the targeted regions with the focal length of 105 mm, the aperture value of f/3.36, AF-S focus mode and 1× zoom. The resolution of the captured image was 6 megapixel. The camera was positioned perpendicular to the target region. The distance between the camera lens and the targeted surface was approximately measured with a measuring tape. As discussed earlier, a 0.02 in (0.5 mm) offset was considered for correction considering the presence of the rosette gauges underneath the reference target.

In the study conducted by Higgins and Nguyen, cameras with different quality lenses and resolutions were used. Photographs were taken at skew angles of 0°, 45° and 70° from the center

of the target. The study demonstrated that images rectified from photographs taken at 0° skew angle from the center of the target had the least error. The error percentages were least for camera with better quality lens and higher resolution. The results were in good correlation with the actual gusset plate measurements when the gusset plate covered the larger portion in the photograph and when the images were in sharp focus.

Following the procedure outlined by Higgins and Nguyen, the digital photographs of the targets were downloaded into the folder containing the modified image rectification code in MATLAB®. The filename, the size of the reference target and an approximate distance of the camera from the target was input interactively, when the image rectification program was executed. The size of the reference target has to be selected 1 in. The control points were interactively identified on the displayed image of the target. After the control points were identified, the code processed the target image to generate the rectified image. This image was saved in the same folder and could be used for measurements.

Although the MATLAB® code contained additional features for taking measurements such as distance, angle, and perimeter based on user selected points on the rectified image, measurements on imported images in AUTOCAD® were preferred in view of better accuracy and consistency. The imported images were scaled with respect to 1 in. × 1 in. (25 mm × 25 mm) reference target and the desired dimensions were digitally measured from the scaled image. An example of the rectified image with measurements is shown in Figure A-4.

The measurements obtained from images for each side of ribs 3 and 7 are tabulated in Tables A-1 to A-4 for β, h, v and d, respectively. The principal and normal stresses calculated based on the measurements are tabulated in Tables 14 and 15 for LS-1 and LS-2, respectively.

Tables

Table A-1 Measurements from rectified images for the orientation of rosette gauges with respect to weld toe "β"

		Image		
Location	Face	1	2	Average
	North	8.0	8.0	8.0
Rib 3	South	36.0	36.0	36.0
	North	20.0	20.0	20.0
Rib 7	South	40.0	40.0	40.0

Table A-2 Measurements from rectified images for the horizontal distance of rosette gauges from cutout termination "h"

		Image		
Location	Face	1	2	Average
	North	0.14	0.14	0.14
Rib 3	South	0.06	0.06	0.06
	North	0.14	0.14	0.14
Rib 7	South	0.17	0.17	0.17

Table A-3 Measurements from rectified images for the vertical distance of rosette gauges from the cutout termination "v"

		Image		
Location	Face	1	2	Average
	North	0.27	0.27	0.27
Rib 3	South	0.24	0.24	0.24
	North	0.36	0.37	0.37
Rib 7	South	0.25	0.25	0.25

Table A-4 Measurements from rectified images for the perpendicular distance of the rosette gauges from the weld toe "d"

		Image		
Location	Face	1	2	Average
Rib 3	North	0.14	0.14	0.14
	South	0.06	0.06	0.06
Rib 7	North	0.14	0.14	0.14
	South	0.17	0.17	0.17

Figures

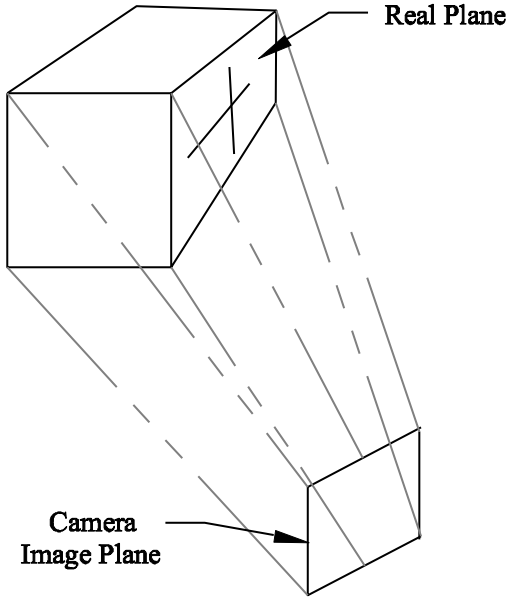

Figure A-1 A 3D object with real planes captured in a 2D camera image plane

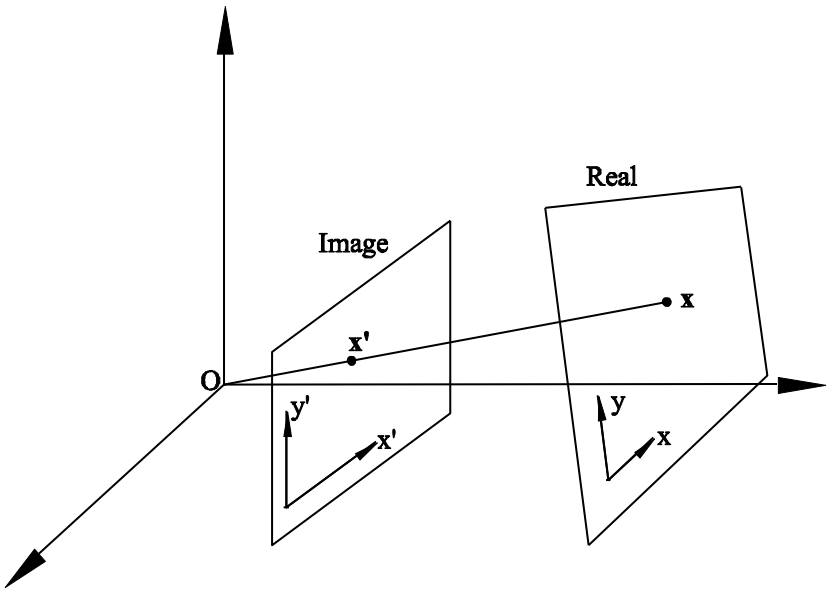

Figure A-2 Central projection maps image plane to real plane

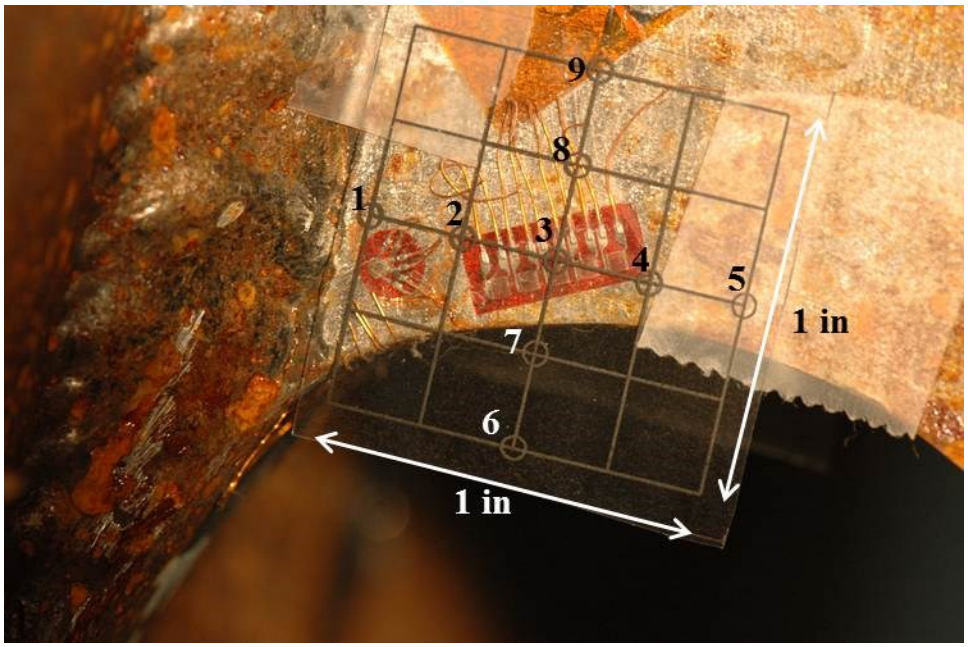

Figure A-3 A reference target with control points

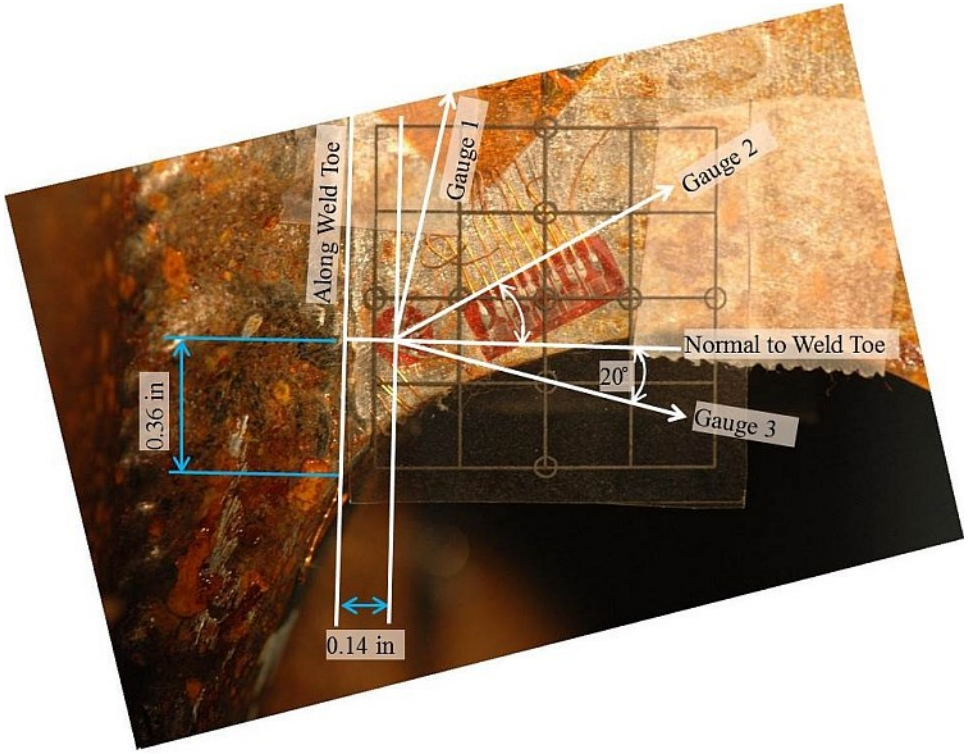

Figure A-4 Rectified image for Rib 3 north face showing measurements

VITA

Nirab Kumar Manandhar, the son of Nirmala Manandhar and Sushil Kumar Manandhar, was born on April 19, 1983. Nirab received his Bachelors of Science degree in Physics from Truman State University, Kirksville, Missouri in May 2008. Nirab joined ATLSS Research Center, Lehigh University as a Graduate Research Assistant since Fall 2009 and has worked on number of projects since. Nirab began graduate studies in the Department of Civil and Environmental Engineering at Lehigh University in Bethlehem, PA in August 2009 He will receive his Masters of Science in Structural Engineering from Lehigh University, Bethlehem, PA in September 2013.